Laboratory spectroscopic studies of interstellar ice analogues

Fabrizio Puletti

Thesis for the degree of Doctor of Philosophy

University College London

Chemistry

2014

I, Fabrizio Puletti, confirm that the work presented in this thesis is my own. Where information has been derived from other sources, I confirm that this is indicated in the thesis.

Signed: .....

Abstract

In recent years, the molecular chemistry in interstellar environments has proven to be far more complex than was initially expected. We live in a molecular universe that is rich with molecules formed both in the gas phase and on the surface of interstellar icy dust grains. Two important classes of interstellar molecules are sulphur-bearing species and complex organic molecules, *i.e.*, molecules containing carbon and containing more than 6 atoms. The former are relevant because of their potential utility in establishing the age of star forming regions. The latter are important because they are excellent probes of the physical conditions of the regions where they reside. Moreover, complex organic molecules are thought to be astrobiologically relevant.

To properly understand the chemical networks leading to the formation of astrochemical species, to date more than 170 have been conclusively identified, the integration of laboratory experimental data with existing computational models is paramount. Laboratory studies can be conducted in the gas phase or, as is the case for this work, in the solid state. Studies of the processing of ices, by thermal energy or by ultraviolet radiation, are particularly important in understanding solid phase chemistry in the interstellar medium.

In this thesis, the results of laboratory experiments aiming to mimic the physical/chemical reactions of ices on interstellar dust grains are presented. Specifically, temperature programmed desorption and reflection absorption infrared studies were carried out in an ultra high vacuum setup on H_2S (chapter 3) and on the $C_2H_4O_2$ isomer family (chapters 4 and 5) formed of acetic acid (CH_3COOH), glycolaldehyde ($HOCH_2CHO$) and methyl formate ($HCOOCH_3$). Ultraviolet irradiation studies of glycolaldehyde have also been performed, and the results of these are presented in chapter 6.

In order to put the laboratory results into an astrophysical context, computer simulations of the desorption of these species from interstellar grains were conducted. The results for H_2S are presented in chapter 3. Those for acetic acid, glycolaldehyde and methyl formate are presented in chapter 4.

The material shown in this thesis will be used for the publication of the following papers, to be submitted in the following months:

The adsorption and desorption of H_2S from model interstellar ices.
Fabrizio Puletti and Wendy A. Brown.

Studying the desorption of complex organic molecules in interstellar ices: temperature programmed desorption studies of glycolaldehyde and its isomers.
Daren J. Burke, **Fabrizio Puletti**, Paul Woods, Serena Viti, B. Slater, and Wendy A. Brown.

The effect of structure on the bonding and desorption of glycolaldehyde and its isomers.
Daren J. Burke, **Fabrizio Puletti**, Paul Woods, Serena Viti, B. Slater, and Wendy A. Brown.

Using infrared spectroscopy of interstellar ices to identify complex organic molecules.
Daren J. Burke, **Fabrizio Puletti**, Paul Woods, Serena Viti, B. Slater, and Wendy A. Brown.

Acknowledgements

Before thanking the people who contributed to this work and supported me in the past 3 years, I would like to acknowledge the LASSIE FP7 ITN network that financed this PhD and all the training events I attended.

Firstly, I would like to thank my supervisor, Professor Wendy Brown, for giving me the possibility to work on this research project. It was a bit of a jump into unknown waters, considering that I did not come from a strictly experimental background. I hope that after almost four years of ups and downs she is still convinced I was a good choice. I would like to thank Dr Daren Burke, for his help into all things laboratory and for his comments on my thesis draft. They were challenging and extremely helpful. I would also like to thank Dr Mike Parkes. He always lent me a hand whenever I needed, especially in the first year when I was by myself in the lab. A big thanks goes to Mark for his help in the lab, his humour and his friendship.

A lot of gratitude and affection go to all the extraordinary people I have met in the past years, if it were not for them, this PhD experience would have been incomparably less enjoyable. All the members of the LASSIE network, for making attending conferences and events a social and absolutely fun occasion. The people at UCL physics department, for adopting me, a stranded physicist in the chemistry department, and giving me the possibility to basically have a social life in London. Among them, I have to mention the super loudly energetic Angela, and Farah with whom I share the passion for Japan and, apparently, gossiping. A big thanks to Jas for allowing me to contribute to research that can actually save people's lives (project F) and to Derek because he is the G, and that is reason enough.

An enormous sense of gratitude goes to my family. Even though they are far away, they always support me and worry whether I am well and I am eating properly. No matter how far away I go or how long I am away, I will always bring them with me. Finally, I would like to thank Moumita. For loving me, for being there when I am discouraged, for the long walks in London, the afternoons spent reading, for putting up with my silences and … for all the little things.

List of Tables

List of Figures

1 Introduction

The general picture of the molecular universe has changed drastically since the first discovery of diatomic molecules back in the 1930s. After more than 80 years of ground-based and space-based observations, it has become clear that the presence of molecules, from simple diatomic molecules, like H_2 and CO, all the way to complex[1] organic molecules such as acetic acid and polycyclic aromatic hydrocarbons (PAHs), is ubiquitous throughout space. Space-based observatories, such as the Infrared Space Observatory, launched by the ESA in 1995, and the Spitzer Space Telescope, launched by NASA in 2005, show that complex molecules are also abundant and permeate a variety of environments in the interstellar medium (ISM) [1,2]. Our universe has a rich chemistry that produces molecules that influence the formation and evolution of stars. These molecules can also be used as probes for the age and physical conditions of certain regions. So called prebiotic organic molecules, such as acetic acid and its isomers, are also found that can potentially represent the first step towards the onset of life on our planet. Moreover, a wide variety of ions (CH^+, HCO^+, HCS^+…) and radicals (CH, OH, HCO…) are detected throughout the ISM [3].

The ISM comprises 10% of the mass of the entire galaxy and consists of 99% gas and 1% dust grains by mass. The gas phase is dominated by the presence of hydrogen (~89%), helium (~9%) and heavier elements (~2%) [4]. The ISM is also a very heterogeneous medium: the temperature can range from a few K to several thousands of K and densities can vary several orders of magnitude from 10 to 10^{12} molecules cm^{-3}.

At the beginning of astrochemical studies, it was thought that molecules formed mainly *via* gas phase processes. However, it soon became clear that purely gas phase processes could not entirely justify the presence and abundances of some of the identified molecules, such as molecular hydrogen, CH or CN [5]. Today there is ample evidence to show that the chemical reactions leading to the formation of interstellar molecules take place not only in the gas phase, but also in the solid phase, *i.e.*, on the surface of cosmic dust grains. Dust grains act therefore as molecule reservoirs and potential catalysts for chemical reactions [6].

[1] In astronomical terms, a complex molecule is any molecule that contains more than 5 atoms

This thesis describes laboratory experiments performed in order to investigate the adsorption and desorption of a range of astrophysically relevant ices on an interstellar dust grain. Specifically, temperature programmed desorption (TPD) and reflection absorption infrared (RAIR) studies have been performed on hydrogen sulphide (H_2S), acetic acid (CH_3COOH), methyl formate ($HCOOCH_3$) and glycolaldehyde ($HCOCH_2OH$). These studies have been performed in an ultra high vacuum environment (UHV) and at low temperatures (20 K) in order to mimic the extreme conditions found in the ISM. A thorough description of the setup and the experimental procedures can be found in chapter 2.

In this chapter, a general overview of the physical properties and of the molecular chemical reactions taking place in the ISM is given. Given the nature of the work described in this thesis, more emphasis is given to processes involving interstellar dust grains and to two particular classes of molecules: sulphur-bearing species and complex organic molecules. A brief review of the literature regarding laboratory studies in astrochemistry will also be presented.

1.1 The physical model of the ISM

The physical characteristics of the ISM are essentially determined by its interactions with the stars. In proximity to bright stars (O or B type in the main sequence), the ISM is subject to an intense electromagnetic bombardment able to ionise hydrogen and helium almost completely [7]. These regions expand for a distance of ≈10 Parsecs[2] from the star and are called HII[3] regions. In these regions, photons with energy higher than 13.6 eV are completely removed from the radiation field *via* interaction with H atoms. Photons with lower energy can escape and interact with other components of the ISM giving rise to an interstellar radiation field (ISRF) [8].

The commonly accepted three phase model of the ISM was theorised by Field *et al.* [9] and then improved by McKee *et al*. [10]. The general structure of the ISM is regulated by the injection of energy through stellar winds and supernovae shock waves. Supernovae are the dominant source of kinetic energy in the ISM. They heat up the gas, forming extremely hot ($T_k \approx 10^6$ K) and rarefied ($n \approx 10^{-3}$ cm^{-3})[4]

[2] 1 Parsec = 3.0856×10^{13} Km
[3] In astronomical notation HI is the neutral element, HII the first ionized one and so on…
[4] When not specified, density is referred to hydrogen atoms density.

"bubbles". These bubbles constitute the hot ionised medium (HIM), also referred to as hot coronal gas, due to the similarity of its temperature with our Sun corona's temperature. The HIM expands, forming a net embedding two other denser and colder phases. The intermediate phase ($T_k \approx 10^4$ K and $n \approx 10^{-3}$ cm^{-3}) is formed of an ionised part and a neutral part, respectively known as the warm ionised medium (WIM) and the warm neutral medium (WNM). The WIM is mainly composed of HII regions. The last phase of the ISM is the coldest and densest ($T_k \approx$ 10-100 K and $n \approx$ 10-100 cm^{-3}) and is known as the cold neutral medium (CNM). The CNM is the most relevant for the formation of complex molecular species. Due to its low temperatures and high density, molecules can form and survive for a long enough time to interact with other molecules, and this gives rise to rich and complicated chemical networks. The CNM is structured in discrete entities know as interstellar clouds, which are mainly divided into two types: diffuse clouds and molecular or dense clouds. The separation is not so clear, since diffuse clouds show a broad mass and size distribution, which joins into those of molecular clouds [11]. Moreover, clouds with intermediate characteristics can also be found. These are called translucent clouds [4].

Diffuse clouds are regions with density $n \approx 50$ cm^{-3} and temperature $T_k \approx 80$ K. Their typical sizes and masses are ≈ 10 Parsecs and 500 $M_\odot$ (solar masses). As the name implies, diffuse clouds are quite transparent to the interstellar radiation field. Therefore, UV radiation plays an important role in determining the physics and chemistry of these regions. In diffuse clouds, several kinds of relatively simple molecules have been detected. The most abundant is molecular hydrogen, observed directly through the Lyman and Werner Bands in the UV [1]. Diatomic radicals, such as CH, CH^+ and CN, with electronic transitions in the visible, were already observed back in the 1930s [12]. Later on, many more species were added to the list: C_2, C_3, CO, OH, NH, H_3^+ and a variety of polyatomic species such as HCN. This chemical simplicity is due to the harsh conditions inside diffuse clouds, such as the intense UV field.

Molecular clouds are formed by dense and cold molecular gas with temperatures in the 10-20 K range and density $n \approx 10^4$ - 10^6 cm^{-3}. Observations along the CO J=1-0 transition have shown that most of the molecular gas in the Milky Way is localized in discrete giant molecular clouds with typical sizes around

40 Parsecs and masses of 4×10^5 $M_\odot$ [13]. Molecular clouds are self-gravitating, rather than in pressure equilibrium with the surrounding medium. This can lead to the collapse of the molecular clouds and the formation of prestellar cores, namely, star-forming regions. The presence of star formation and the shielding from external UV due to the clouds own density makes molecular clouds the regions with the richest chemistry in the ISM. A wide variety of molecules, including large organic species, has been detected in molecular clouds [1,6].

The various regions of the ISM are all interconnected. The material is initially released into the ISM in the explosions of the star or in the form of stellar wind. This material circulates in the diffuse and molecular clouds. When the molecular clouds collapse due to their own gravity, this material ends up being part of the newly formed star and the associated planetary system. The new star eventually dies and re-ejects part of its gases, enriching the ISM, and the cycle starts anew [1,4].

1.2 Interstellar dust grains

The story of interstellar dust started long ago in 1784 when the astronomer William Herschel noted the presence of dark regions in the sky where there seemed to be a complete absence of stars [14]. As we now know, the cause of these "holes in the sky" (figure 1.1) is small sub-micrometer dust grains that absorb and scatter the visible radiation. The absorbed radiation heats the dust and is re-emitted in the infrared wavelength region.

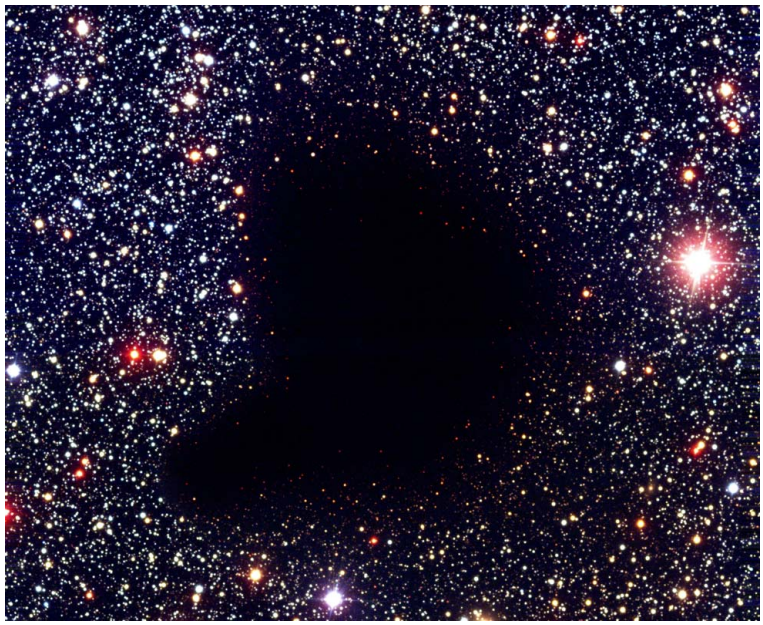

Figure 1.1. Molecular cloud Barnard 68. Image credit: NASA.gov.

This combination of absorption and scattering is called extinction. The presence of dust grains and their physical and chemical characteristics can be inferred by several phenomena [15]:

- General extinction of starlight in the visible and UV wavelength range. The extinction curve is studied as a function of wavelength and models are created to produce a suitable fit to the curve (figure 1.2).
- Scattering and polarization of starlight. In some circumstances, the light reflected by dust clouds close to bright stars can be detected. Starlight is usually a few percent linearly polarized, and this is considered to be due to the interaction with elongated dust grains that are aligned with the interstellar magnetic field.
- Infrared absorption and emission features.
- Collection/analysis of interplanetary dust particles. Samples of cosmic dust can be found in primitive meteorites. However, it is important to recognize that the chemical analysis techniques used to probe the samples and the same formation of the meteorite can alter the composition and the structure of these dust grains. Cosmic dust grains can also be collected in the high atmosphere (figure 1.3).

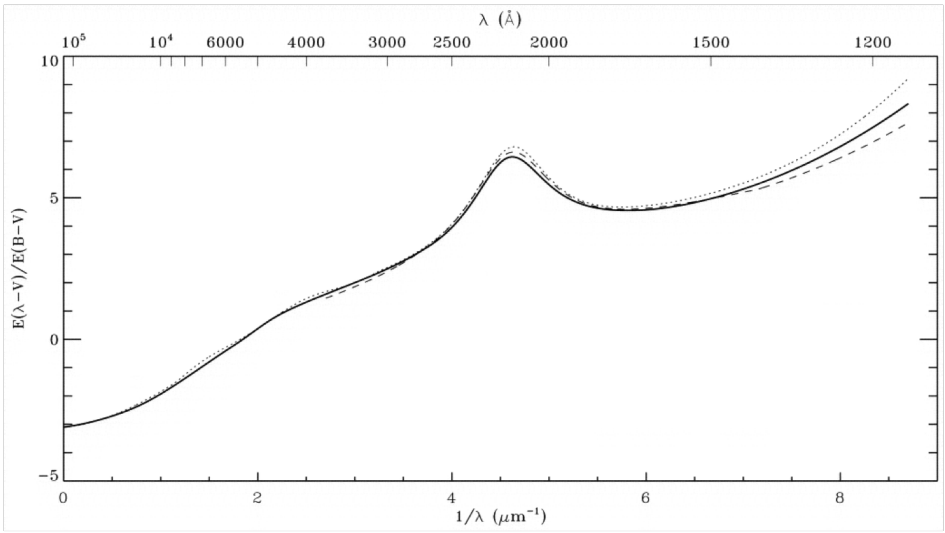

Figure 1.2. Dependence of the interstellar extinction on the wavelength, figure adapted from [16]**. The different curves represent different estimates of the extinction as discussed in** [16]**.**

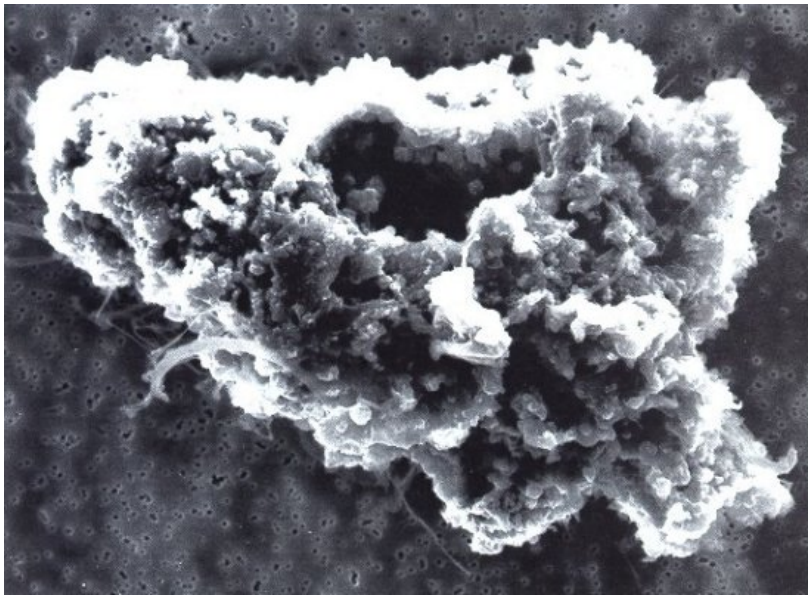

Figure 1.3. Cosmic dust grain collected by high altitude aircraft. Photograph credit: NASA.

It is thought that dust grains originate in the outer layers of stars at the end of their lives. These kinds of stars (giants and super giants) develop an extended atmosphere that may be cool and dense enough for solid nuclei to form. Atoms and molecules can then attach to those nuclei, forming solid particles. Finally, the newly formed dust grains can be accelerated by perturbations coming from the star (solar winds, outflows…) and ejected into interstellar space [17].

The composition of interstellar dust grains is still a matter of debate, but based on observations, the most likely candidates seem to be silicate and carbonaceous materials. More rare materials include SiC, and carbonates like calcite ($CaCO_3$) and dolomite ($CaMg(CO_3)_2$) [18].

The term carbonaceous indicates materials formed predominantly from C (by mass). Examples of these materials can be diamond, graphite, amorphous carbon, hydrogenated amorphous carbon, polycyclic aromatic hydrocarbons (PAHs) and chainlike hydrocarbons [18]. The feature at 2175 Å in the extinction curve in figure 1.2 indicates the presence of carbonaceous material in dust grains. The extinction curve also shows a series of weak features, know as diffuse interstellar bands (DIB). DIBs are usually assigned to PAHs.

There is little doubt that silicate material is also present in the composition of dust grains. A broad emission feature centred at 9.7 μm [18] is usually attributed to the Si-O stretch mode. Moreover, the Si abundance is strongly depleted compared to cosmic abundances, therefore it is generally assumed that the missing Si contributes

to the structure of dust grains. Observed gas-phase abundances of heavy species, such as Mg, Fe and Si, and their variations from cloud to cloud, suggest that silicate grains may have a Mg-rich mantle and a Fe-rich core [19].

1.3 Chemistry on dust grains

The importance of interstellar dust grains lies in the fact that molecules can condense onto the surface forming ices. Dust grains are therefore reservoirs of chemical species. The observational evidence for this is numerous. Ices have been detected in a variety of environments: molecular clouds, hot cores, young stellar objects and in the proximity of stars at different stages of their evolution [1,2,18,20]. In figure 1.4 the spectrum of the protostar W33A shows several ice features.

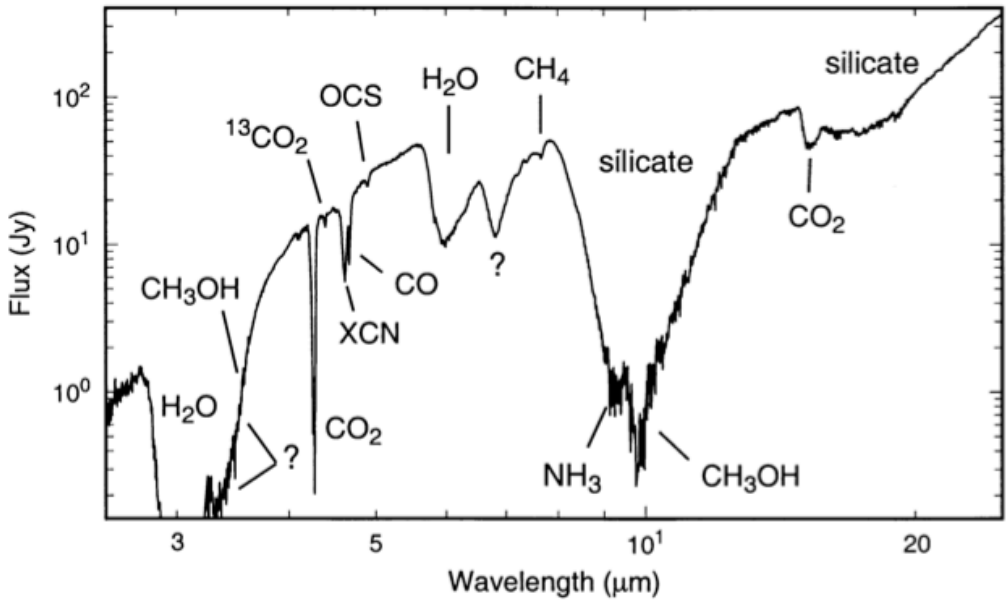

Figure 1.4. The mid-IR spectrum of the protostar W33A observed with the short wavelength spectrometer on board ISO. All the features, a part from the ones at 10 and 18 μ m, are due to molecules in ice mantles. Taken from [20]**.**

These ices can play an important role in the formation of other species on the surface of grains by increasing the probability of trapping other atoms/molecules, thereby increasing the time these species can stay on the surface. Dust grains can also act as a catalyst by providing an escape route for extra energy that some molecules possess immediately after formation, and that would otherwise lead to re-dissociation of the molecule. Moreover, dust grains can catalyse chemical reactions lowering the activation barrier. This was demonstrated theoretically, for example, in the case of OCS on coronene [21].

The number of positively identified molecules in space is nowadays higher than 170, see table 1.1 page 20. For many years, their possible routes of formation in the gas-phase have been investigated. This leads to the understanding that the dominant reactions observed in the ISM are exothermic ion-molecule reactions. However, simulations that just take into consideration gas-phase chemistry can explain the formation of only ~ 80% of the molecules observed in the gas phase [22,23].

Among the molecules in the remaining 20%, the most dramatic example is H_2. This species cannot be formed, in the observed abundance, when two hydrogen atoms collide in the gas phase because of the very low efficiency of this process. H_2 formed in the gas phase is, in fact, highly rovibrationally excited and would simply dissociate again due to the extra energy it possesses. The only viable solution is to consider a 3-body reaction in which the dust grain surface acts as a catalyst allowing for the extra energy to be dispersed [24].

Information regarding the composition of these ices can be gathered by analysing the infrared spectra of protostars embedded in molecular clouds, or of background stars behind these clouds. The complexity of the molecules found on dust grains is variable. Amorphous water ice is the most abundant ice component (60%-70% of the ice in most lines of sight [2]), while most of the carbon is divided between CO, CO_2 and CH_3OH [1] with abundances depending on the environment (*e.g.*, CH_3OH varies from 1% to 30% with respect to H_2O ice [6]). The majority of the species found on dust grains are highly hydrogenated, such as NH_3 and CH_4, because atomic hydrogen, which accretes from the gas and then diffuses very rapidly, is a very efficient reactant on surfaces.

Dust grain ices are also constantly bombarded by UV radiation and cosmic rays. These processes can induce further chemistry by breaking existing molecules (*e.g.*, photolysis) and encouraging the formation of radicals.

2	3	4	5	6	7	8
H_2	C_3	c-C_3H	C_5	C_5H	C_6H	CH_3C_3N
AlF	C_2H	l- C_3H	C_4H	l-H_2C_4	CH_2CHCN	$HCOOCH_3$
AlCl	C_2O	C_3N	C_4Si	C_2H_4	CH_3C_2H	CH_3COOH
C_2	C_2S	C_3O	l-C_3H_2	CH_3CN	HC_5N	C_7H
CH	CH_2	C_3S	c-C_3H_2	CH_3NC	CH_3CHO	C_6H_2
CH^+	HCN	C_2H_2	H_2CCN	CH_3OH	CH_3NH_2	$HCOCH_2OH$
CN	HCO	NH_3	CH_4	CH_3SH	c-C_2H_4O	l-HC_6H
CO	HCO^+	HCCN	HC_3N	HC_3NH^+	H_2CCHOH	CH_2CHCHO ?
CO^+	HCS^+	$HCNH^+$	HC_2NC	HC_2CHO	C_6H^-	CH_2CCHCN
CP	HOC^+	HNCO	HCOOH	NH_2CHO		H $_2CH_2CN$
SiC	H_2O	HNCS	H_2CNH	C_5N		CH_3CHNH
HCl	H_2S	$HOCO^+$	H_2C_2O	l-HC_4H		
NH	HNO	H_2CN	HNC_3	c-H_2C_3O		
NO	MgCN	H_2Cs	SiH_4	H_2CCNH (?)		
NS	MgNC	H_3O^+	H_2COH^+	C_5N^-		
NaCl	N_2H^+	c-SiC_3	C_4H^-	HNCHCN		
OH	N_2O	CH_3	HC(O)CN			
PN	NaCN	C_3N^-	HNCNH			
SO	OCS	PH_3 ?	CH_3O			
SO+	SO_2	HCNO	$NH4^+$			
SiN	c-SiC_2	HOCN				
SiO	CO_2	HSCN				
CS	H_3^+	C_3H^+ (?)				
HD	SiCN					
FeO ?	AlNC					
O_2	SiNC					
CF^+	HCP					
PO	AlOH	**9**	**10**	**11**	**12**	**>12**
OH^+	H_2Cl^+	CH_3C_4H	CH_3C_5N	HC_9N	c-C_6H_6	$HC_{11}N$
CN^-	KCN	CH_3CH_2CN	$(CH_3)_2CO$	CH_3C_6H	$C_2H_5OCH_3$?	C_{60}
SH^+	FeCN	$(CH_3)_2O$	$(CH_2OH)_2$	C_2H_5OCHO	n-C_3H_7CN	C_{70}
SH		CH_3CH_2OH	CH_3CH_2CHO	$CH_3OC(O)CH_3$		
HO_2		C_8H				
HCl^+		$CH_3C(O)NH_2$				
TiO_2		C_8H^-				
TiO		C_3H_6				

Table 1.1. List of detected interstellar medium molecules categorized according to the number of their atoms. Adapted from http://www.astro.uni-koeln.de/cdms/molecules. The highlighted molecules are the objects of this thesis. Molecules with more than 8 atoms are listed at the bottom of the table for clarity.

The importance of the chemistry activated by external bombardment is dependent on the intensity of the surrounding radiation and on the thickness and composition of the icy mantle. In some cases the conditions are optimal for the formation and survival of

large complex organic molecules. For this reason, and because of observational results, dust grains are considered a reservoir for complex organic molecules [6].

There are essentially three kinds of molecular formation processes that can occur on the surface of the dust grains, once two or more species are adsorbed[5] (figure 1.5):

- Diffusive or Langmuir-Hinshelwood mechanism. Two adsorbates are bonded to the surface. At least one of them must be weakly bonded in order to be able to diffuse (*via* quantum tunnelling or thermal hopping) and interact with the other one. When the reaction occurs, the energy produced can be transferred to the surface and the product can subsequently desorb.
- Eley-Rideal mechanism. One adsorbate is bound to the surface when a gas phase species lands atop and reacts with the adsorbate.
- Hot atom mechanism. In the previous processes, the species on the surface were thermalized. In this case, however, a gas-phase species lands on the surface, diffuses without thermalizing and then collides with the adsorbate.

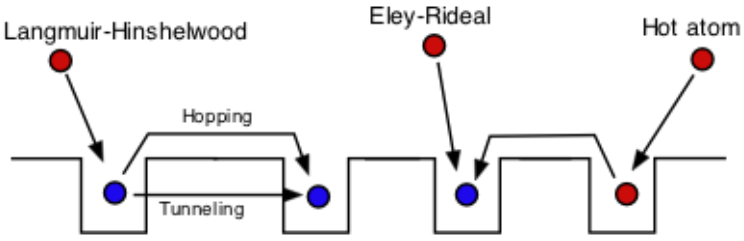

Figure 1.5. Three mechanisms of molecular formation: Langmuir-Hinshelwood, Eley-Rideal and hot atom. Blue circles represent thermalized species, red circles represent non-thermalized species. Image modified from [25]**.**

The Langmuir-Hinshelwood mechanism is generally the most likely process due to the long permanence of the adsorbates on the surface. However, in denser environments, the increase of impingement from the gas phase can favour the Eley-Rideal and the hot atom mechanisms.

Besides the aforementioned processes involving direct atom/atom or molecule/molecule interaction, the ices on the grains can go through further modification *via* exposure to ultraviolet (UV) [26] radiation, X-ray or cosmic ray (protons, heavy He nuclei) [27] radiation in addition to thermal processing. Bombardment of the ices can cause destruction and the formation of new molecules, and the modification of the ice morphology [27–29]. In regions where the temperature

[5] Note the difference between absorption and adsorption. The former presumes penetration of the species into the bulk. The latter implies that the species is bonded to the surface *via* a chemical (chemisorption) or physical (physisorption) bond.

of the grains rises, sublimation of the ices can take place. The ISM will then be enriched by the molecular species formed on the surface of the grains, which can drive new and more complex chemistry [4]. The artistic representation in figure 1.6 [30] shows the processes that the ice mantles can undergo in the ISM.

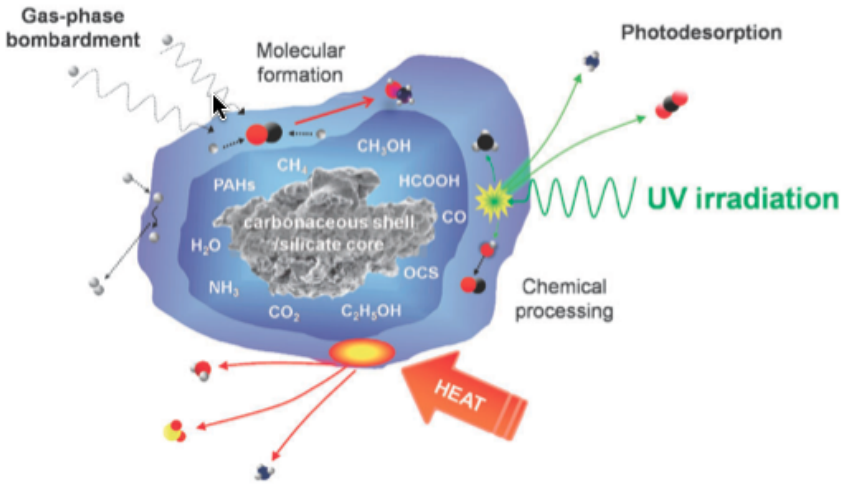

Figure 1.6. Schematic showing the main routes of interstellar ice processing that takes place in astrophysical environments. The molecular species labeled within the inner layer highlight the main constituents detected in interstellar ices. Picture and label are taken from [30]**.**

1.4 Laboratory ices

Laboratory studies in astrochemistry constitute a source of information complementary to observational and computational studies. They are roughly separated into gas phase experiments and solid phase experiments. This thesis focuses on the latter, therefore a brief overview of the range of laboratory studies of astrochemical ices will be given in this section. A comprehensive description of gas phase experiments, which is beyond the scope of this thesis, can be found in Smith [31].

The experimental setup used for laboratory ice studies consists of a high vacuum (HV) or ultra high vacuum (UHV) chamber in which ices are grown on a cold substrate. UHV chambers possess a better level of vacuum (~10^{-11} mbar compared to ~10^{-7} mbar), hence they are considered to be better at reproducing the extreme conditions in interstellar environments. The idea behind this kind of experiment is to reproduce the processes of adsorption, desorption, chemical synthesis and interaction with radiation that can take place on the surface of cosmic dust grains.

As mentioned in the previous section, the exact composition of dust grains is still a matter of debate. Although it is accepted that their constituents are essentially carbon

and/or silicate materials, the exact composition is not known precisely and it is reasonable to think that it will depend on the specific environment in which the grains are formed. Considering this uncertainty, a wide variety of materials have been used as dust grain analogues for laboratory experiments. These include silicates (amorphous [32] and crystalline [33]), carbonaceous materials such as highly oriented pyrolitic graphite (HOPG) [34,35], metal substrates including gold coated copper [36] and insulator surfaces like CsI [37].

Several surface science techniques are currently used in laboratory astrochemistry, such as time of flight mass spectroscopy (TOF) [38], resonance enhanced multi-photon ionization (REMPI) [39], temperature programmed desorption (TPD) [40] and infrared spectroscopy both in transmission [41] and in reflection (RAIRS) [42]. In the present work, TPD and RAIRS are used and a more extensive and detailed description of these techniques is provided in chapter 2. The desorption processes of molecules from the surface can be described with an Arrhenius type law (see chapter 2 for further details). TPD essentially provides desorption orders, desorption energies, and pre-exponential factors characteristic of the adsorbate in question. Astronomers, in turn, use this information to simulate the desorption of the investigated species under astronomical conditions. The results of this kind of simulations are shown in chapters 3 and 4. TPD can also provide indications on the trapping of a species in water ices and of phase transitions.

TPD of a variety of ices has been performed over the years, see for example [30,40]. These studies have shown that the composition and morphology of the ice affects both its adsorption and desorption.

Infrared laboratory studies are important because they can provide spectral fingerprints that, directly compared with astronomical observations, can shed light on the composition of the ice mantles in the ISM. From such comparisons, it was found that dust grains are covered by 50-100 monolayer thick ice mantles that are mainly formed of H_2O, but also other species like CO, CO_2, HCOOH, NH_3, CH_3OH and traces of more complex molecules. These ices are mainly amorphous and have a layered structure consisting of H_2O and CO dominated ice mixtures [25]. Laboratory IR studies can also provide information about the interactions between two or more adsorbates, by monitoring how the vibrational bands change in position and shape compared to when one or the other species is present alone. On metallic and semi-metallic sample surfaces, such as graphite, RAIRS can be used to give information about the orientation of the

adsorbate, by using the metal surface selection rule to identify the allowed vibrational modes for a given adsorbate geometry [30].

Dust grains and their associated mantles are found in very dynamic environments such as hot cores (regions of star formation). As a result the ices are irradiated by several sources, mainly UV photons originating from the evolving star or from the interstellar radiation field and cosmic rays. Cosmic rays are energetic particles (1-10 MeV) consisting of ~97-98% protons and 2-3% helium nuclei [7]. This constant bombardment can influence the chemical composition of the ice and its physical structure. Moreover, the energy released into the grain contributes to a change of temperature that can promote the sublimation of the species from the icy mantles.

Nowadays, the trend of laboratory studies of astrophysically relevant ices is moving towards the investigation of the chemical and physical modification of the ices due to the interaction with UV [43], protons (simulating the interaction with cosmic rays) [44,45] and with impinging atoms [46].

1.5 Sulphur in the ISM

In this thesis a complete study of the adsorption and desorption of H_2S on a dust grain analogue will be presented. An understanding of sulphur chemistry in the ISM, both in the gas phase and in the solid phase, is important to understand the motivation behind this work and the utility of the data produced.

Sulphur is a fairly abundant element in the ISM, its abundance is 4% that of carbon. Similarly to carbon, it has an ionization potential lower than that of hydrogen (10.4 eV) so in diffuse, thin HI regions sulphur is mostly ionized, while in dark regions it is predominantly neutral [47].

Currently, around 17 S-bearing species have been positively identified in the gas phase in a variety of environments in the ISM: including the diffuse ISM, star forming regions, translucent and molecular clouds, and shock regions. Their complexity goes from simple diatomic molecules, such as CS, SO, NS and SH to molecules like HNCS, CH_3SH and ions such as SO^+, SH^+ and HCS^+. In the condensed phase, only two species have been positively detected: SO_2 [48,49] and OCS [50,51]. H_2S has been suggested by Geballe *et al* [52], but that assignment is not fully supported in the literature. Van der Tak *et al.* [53] argued that infrared observations do not support the assumption that H_2S is the main sulphur reservoir in grain mantles [54]. Additionally, several S-bearing

molecules have been detected in comets. The most abundant among them is H_2S with abundances from 0.2 to 1.5% relative to H_2O [54].

The observed abundances of sulphur bearing molecules (*i.e.*, H_2S, SO, SO_2, H_2CS and OCS) in hot star forming regions differ significantly from the observed abundances in colder and quiescent regions, such as dark clouds. They also show spatial gradients within individual star forming regions [55]. These features imply a strong dependence of sulphur chemistry on the physical characteristics of the surrounding medium. For this reason, sulphur species have been proposed to be good evolutionary tracers and as molecular clocks for astrophysical environments such as hot cores and shock regions [55–57]. Recently, however, computational modelling showed that S-bearing molecular ratios depend very strongly on gas temperature and density, the abundance of atomic oxygen, and on the form of sulphur injected into the gas phase, which is very poorly known. This makes sulphur bearing molecular ratios difficult to use precisely as molecular clocks, but they can still be used to give hints on the age of the source and on the mantle composition [56].

Observations of interstellar SI and SII shows that sulphur is depleted when neutral, but not when ionized [58]. In some cases it can be depleted in molecular clouds by a factor of 1000 compared to its estimated cosmic abundances, while its abundance in the gas phase in the diffuse interstellar medium is comparable to the cosmic abundance [54]. This suggests two possible scenarios: either there is a form of sulphur, which is not observed in molecular clouds or sulphur chemistry on icy grains, which are formed exclusively in dense clouds, plays an important role.

This second hypothesis seems to be very probable. Duley *et al.* [58] suggested that sulphur can be depleted onto small oxide grains or alternatively onto icy mantles present on the surface of bigger grains. There is also compelling evidence that dust grains have an active role in the chemistry of S-bearing molecules. Chemical gas phase models are in fact unable to explain the abundances of species such as HCS^+ and OCS [59], or H_2S and CS [58]. It is therefore commonly accepted that grain surface reactions can provide efficient routes of formation for many of the observed sulphur bearing species.

1.6 Complex organic molecules in the ISM

By astrophysical standards, complex organic molecules are molecules containing carbon formed of more than 6 atoms. In this thesis, a complete study of the adsorption

and desorption of acetic acid (CH_3COOH), methyl formate ($HCOOCH_3$) and glycolaldehyde ($HOCH_2CHO$) along with a study of glycolaldehyde irradiation, will be presented. In this section, a brief introduction to complex organics in the ISM is therefore presented.

Most interstellar and circumstellar molecules are organic in nature. The preponderance of organic molecules is great for the larger molecules detected; 100% of species with more than 6 atoms are, in fact, organic. The sources of complex organic molecules are numerous: circumstellar envelopes around evolved stars, cold interstellar cores, hot cores and corinos, outflows and other regions [6]. However, the majority of complex organic molecules were identified from their rotational emission features in hot cores. Hot cores are defined as the regions around a young star that have reached levels of emission high enough to heat up the surrounding material. Temperatures in these regions reach 100 K. Hot cores are found essentially inside molecular clouds, where the regions of star formation have their origin [60]. Hot cores are small (< 0.1 Parsecs), dense ($> 10^6$ cm^{-3}) and hot regions, these characteristics are optimal for the development of a complex and rich chemistry.

The molecular inventory in hot cores is dominated by saturated molecules such as methanol, methyl formate, dimethyl ether (CH_3OCH_3) and propionitrile [6]. The richest source of complex molecules in the galaxy is located in the Galactic Centre giant cloud Sgr B2. Interferometric observations of this cloud show that it contains two hot clumps called Sgr B2 (M) and Sgr B2 (N) [61]. Further studies show that Sgr B2(N) is the richest in complex organic molecules, so much that this hot core is also referred to as the large molecular heimat [62]. In this region, species like acetone (CH_3COCH_3), ethylene glycol [$(CH_2OH)_2$], glycolaldehyde and methyl formate have been identified.

Molecules in hot cores can have three possible origins [63]:

- Cold gas phase chemistry, combined with accretion onto dust during the collapse of the core. This can account for the presence of CO, HCN and acetylene.
- Grain surface reactions. These processes can produce simple saturated compounds such as water, NH_3, HCOOH, CH_3OH and more complex ices. Laboratory experiments of UV irradiation of ices made of astronomically relevant mixtures showed also the formation of amino acids [64].

- Evaporation of simple molecular mantles drives gas phase complexity. This is an alternative to grain surface reactions for the production of complex organic molecules.

All of these processes contribute to the currently observed molecular abundances in hot cores. Dust grains have a fundamental role given the fact that they can provide an environment (icy mantles) where reactions can occur more efficiently and/or drive gas phase chemistry by releasing newly formed molecular species *via* evaporation of the mantles.

A very important class of organic molecules are the so-called prebiotic molecules. These are defined as molecules thought to be involved in the processes leading to the origins of life. Molecules in this category possess structural elements in common with molecules found in living organisms. The majority of the prebiotic molecules were identified in Sgr B2 (N-LMH), for example, glycolaldehyde [65], which is considered the simplest sugar, and ethylene glycol ($HOCH_2CH_2OH$) an hydrogenated sugar [66]. Both acetic acid and amino acetonitrile (NH_2CH_2CN) have also been detected. These two molecules are of biological importance because they are both considered as potential precursors of the simplest amino acid, glycine (NH_2CH_2COOH).

From what is described in this chapter, it appears evident that the laboratory investigation of the adsorption and desorption of H_2S, CH_3COOH, $HCOOCH_3$ and $HCOCH_2OH$, both in hydrous and anhydrous environments, is important in order to shed light on the role that these species have in their respective chemical networks. Experimental results reported in this thesis are not intended to be directly compared to astronomical observations. Rather, the combined use of TPD and RAIRS allows the study of the physical properties of the ices. Nonetheless, computer simulations have been performed to provide astronomers with astronomically meaningful desorption temperatures based on the results of the TPD data obtained.

2 Experimental Setup and Techniques

The main purpose of experimental setups used for laboratory astrochemistry is to emulate the extreme conditions of pressure (< 10^{-12} mbar) and temperature (< 10 K) existing in the interstellar medium (ISM). Recreating the exact level of vacuum characteristic of the ISM is not currently possible, however it is possible to reach pressures as low as 10^{-10} mbar. This level of pressure is defined as Ultra High Vacuum (UHV) and is low enough to ensure cleanliness of the sample during experimental procedures (*i.e.*, to avoid contamination due to atmospheric gases) and to allow experiments within practical timescales (maximum several hours). Low temperatures are easily achieved in the laboratory.

The experiments described in this thesis were executed on 2 UHV chambers that will be referred to as chamber 1 (CH1) and chamber 2 (CH2). In this work, a series of reflection absorption infrared spectroscopy (RAIRS), temperature programmed desorption (TPD) and ultraviolet (UV) irradiation experiments have been conducted on several molecules of astrophysical interest. A list of the molecules and of the experiments run on each chamber is shown in table 2.1.

Setup	H_2S	CH_3COOH	$HCOOCH_3$	$HCOCH_2OH$
CH1	TPD/RAIRS	RAIRS	RAIRS	RAIRS/I**
CH2	/	TPD	TPD	TPD

Table 2.1. List of the experiments executed on the different experimental setups.

**** I = UV irradiation**

CH1 and CH2 are similar in their basic configuration; the differences are in the general layout of the system and the sample mount. Experimental setup CH1 was the one used for the majority of the experiments presented in this work. For this reason, and because of the similarities between the two setups, CH1 will be described in detail section 2.1, while CH2 will be described with less detail in section 2.3.

2.1 Experimental chamber 1

Previous descriptions of CH1 are already in the literature [35], [67]. The main part of the experimental apparatus is the UHV chamber. This is a stainless steel vessel which can achieve, during non-operational time, a base pressure of ≈

2×10^{-10} mbar (measured by an uncalibrated ion gauge). During experiments, gases are introduced into the chamber and the pressure may increase up to 10^{-7} mbar.

Achieving such low levels of pressure is not a trivial task: different kinds of pumps must be used depending on what pressure is required inside the chamber. A schematic representation of the vacuum system is shown in figure 2.1.

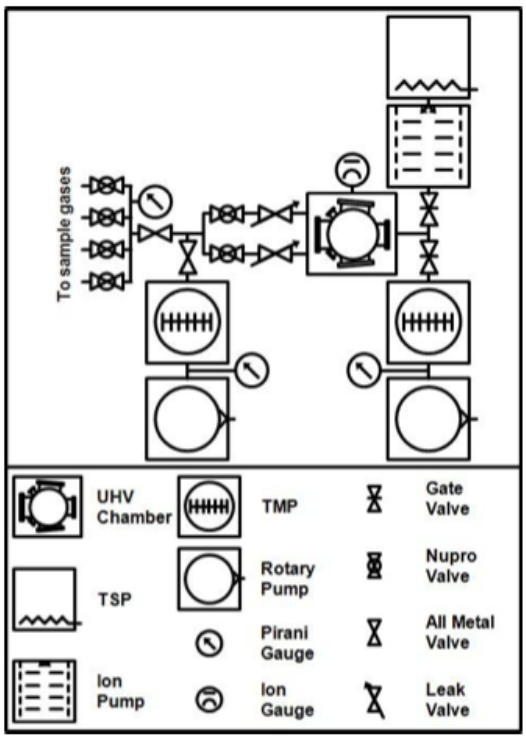

Figure 2.1. Schematic of the vacuum system in CH1. Taken from [67]**.**

The system is initially brought from atmospheric pressure (1 bar) down to $\approx 3\times10^{-3}$ mbar *via* a rotary pump (Trivac D5E, Leybold); this is very close to the limiting compression ratio for this kind of pump. Following this, the pressure is decreased *via* a turbo-molecular pump (Turbovac 151, Leybold Ltd.) to $\approx 1\times10^{-7}$ mbar.

The pressure is now so low that the total amount of gas inside the chamber becomes comparable to the amount of gas trapped on the internal surfaces of the chamber itself. This trapped surface gas is in dynamic equilibrium with the volume of the chamber, therefore it will statistically desorb from, and be re-adsorbed onto, the walls, affecting the vacuum. A bake out is thus necessary in order to properly degas the chamber walls. The whole setup is heated to 375 K for at least 24 hours. The most abundant molecular species present in the chamber before baking is water, for this reason a temperature around 375 K must be reached during baking. A bake

out is executed whenever the internal pressure of the chamber degrades, either because it does not go back to UHV pressure or it takes too long to recover after experiments. The pressure usually degraded after several weeks of experiments had taken place, due to water and other gases accumulating on the chamber walls and on the sample mount.

After the bake out, the chamber is finally pumped down by an ion pump and a titanium sublimation pump (TSP). The former works by ionizing the residual gas and trapping it onto electrically charged metal plates. The latter is located inside the ion pump and plays an important role in removing H_2 and reactive gases such as CO_2 from the main chamber. The TSP consists essentially of titanium filaments that are electrically heated up to thousands of degrees. At these temperatures the titanium from the filaments coats the surrounding metal, and chemically reacts with residual gases, removing them from the gas phase.

After base pressure is reached, all of the pumps keep working simultaneously to preserve the vacuum. The TSP fires every three hours only if the pressure is higher than 1×10^{-9} mbar.

The chamber is connected to a stainless steel gas-dosing manifold through two high precision leak valves (LVM Series Leak Valve, VG). The manifold is pumped by a turbo-molecular pump (Turbovac 50, Leybold Ltd) down to $\approx 1\times10^{-3}$ mbar. A rotary pump backs the turbo-molecular pump. This configuration allows the simultaneous dosing of two gases into the chamber. This feature is necessary to study layered and mixed ices, *i.e.*, ices formed of more than one species. For example, in this work, layered systems and mixtures of all of the investigated molecules (H_2S, CH_3COOH, $HCOOCH_3$ and $HCOCH_2OH$) with water have been studied.

Pressure measurement of residual gases is achieved *via* Pirani gauges in the backing line and *via* an uncalibrated ion gauge (IG) inside the main chamber. The IG is also used to monitor the gas pressure during dosing for the experiments. No correction of the pressure is performed depending on the dosed species.

The chamber also includes an Ar^+ gun used for cleaning of metal samples, optics for low energy electron diffraction (LEED) and a quadrupole mass spectrometer (QMS) used to monitor which gases are inside the chamber and for temperature programmed desorption (TPD) and residual gas analysis.

Several windows are fitted on the experimental chamber to allow monitoring of the sample during its insertion and movement. Two differentially pumped KBr

windows are also installed on the chamber to allow the infrared beam used during RAIRS experiments, to pass through the chamber unmodified (KBr interacts only weakly with IR light). The RAIRS optics are described later in this chapter.

A quartz window is also located on the chamber to allow the UV beam to reach the sample during UV irradiation experiments. A schematic showing the positioning of the windows, the mercury cadmium telluride (MCT) detector, the Fourier transform spectrometer and the UV lamp is shown in figure 2.2.

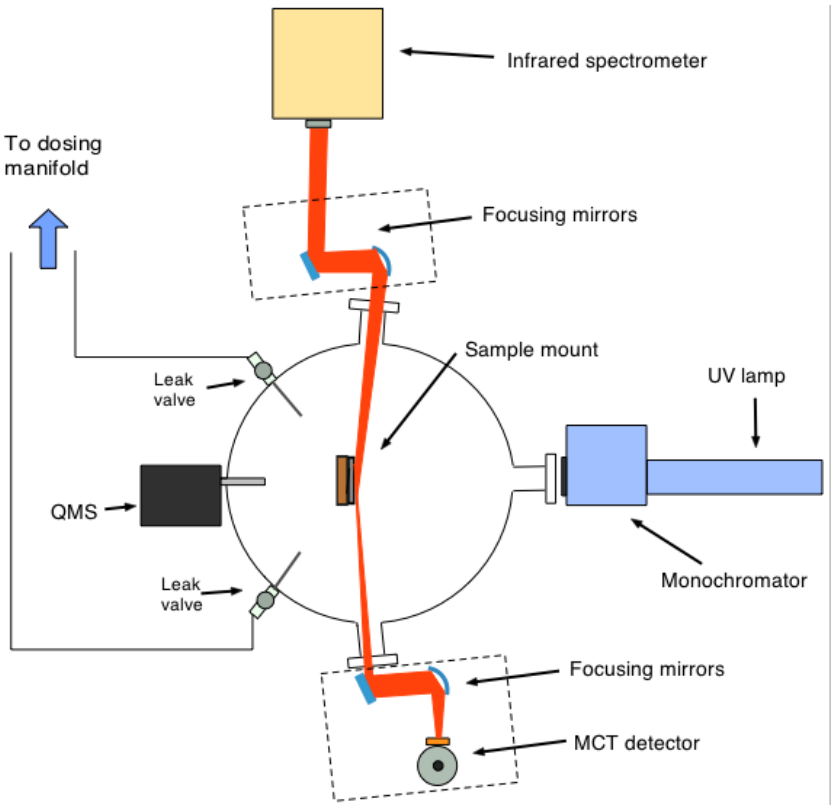

Figure 2.2. Schematic of the experimental level of CH1 showing the positioning of the MCT detector, spectrometers and UV generating setup. The representation is not to scale.

The core of the experimental apparatus is the HOPG (Highly Oriented Pyrolitic Graphite) sample, 20×10×2 mm (Goodfellow Ltd., UK), which is used as an interstellar dust grain analogue. HOPG is composed of sheets of graphene packed into a honeycomb crystal lattice and it can be considered to be a suitable analogue of interstellar dust grains. It has been previously used to investigate the formation of H_2 [68–70] and to study the adsorption and desorption of other molecular species [30,35]. The HOPG sample is mounted on an oxygen-free high conductivity copper rod, hereon called the "cold finger", connected to a closed cycle Helium refrigerator (HC-2D-1, SHI-APD Cryogenics Inc.) that can reach temperatures lower than 20 K. The sample temperature is monitored *via* an N-type thermocouple connected to a

temperature control module ($\epsilon 2408$, Eurotherm Ltd.). The cold finger is inserted into the chamber *via* a high precision manipulator combined with a differentially pumped bellows-sealed feedthrough. This ensures accurate control of the sample position along the three axes (x, y, z) and allows it to be rotated, when needed for RAIRS and TPD experiments.

2.1.1 The sample mount

The sample mount must satisfy several requirements in order to allow chemical reactions to occur in physical conditions similar to the ones found in the ISM. Firstly the ability to reach a very low temperature ($\leq$ 20 K) is needed. Hence an optimum thermal contact between the sample and the cooled sample mount must be ensured. An accurate control of the sample temperature is necessary to properly perform TPD experiments; therefore a heating circuit and a thermocouple must be placed in contact with the sample. Finally, during the heating of the sample, the temperature of the sample mount should not raise excessively so that desorption of gases adsorbed on its surface does not occur, it is easier to cool down the sample again and the sample mount itself is not damaged in the process.

In order to satisfy all these requirements the sample mount was designed by Dr D. J. Burke, as in figure 2.3.

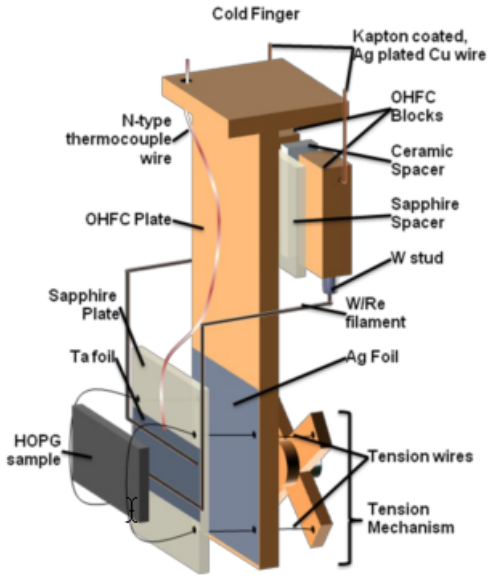

Figure 2.3. Diagram showing the sample mount and the tension wire mechanism used to position and stabilize the sample. Taken from [67]**.**

The sample mount is made of oxygen-free high conductivity copper (OFHC). It is directly connected to the end of the cold finger, *via* a few layers of silver foil, to improve thermal conductivity. The heating circuit passes through the back of the OFHC plate *via* two OFHC blocks isolated from the mount by a sapphire spacer and from each other by a ceramic layer. The insulating layers are necessary to avoid a short circuit between the heating circuit and the earthed parts, *i.e.*, the mount and the cold finger. Sapphire is chosen because its conductivity is high at low temperature and low at high temperature. This allows efficient cooling, while avoiding heat transfer from the heating elements to the mount (*e.g.*, during TPD). Kapton insulated Ag plated Cu wires are screwed into each OFHC block. They are connected to electrodes placed outside of the chamber *via* feed-throughs. The final part of the resistive heating circuit consists of 0.5 mm W/Re wires (75% W, 25% Re) silver soldered into holes bored into the OFHC blocks. The W/Re wires are then bent toward the front of the mount and placed underneath the HOPG sample.

Finally, at the end of the sample mount, a series of elements are assembled as follows, in order from top to bottom:

1. Four layers of Ag foil. These improve thermal conductivity between the OFHC plate and the sample. Tests have been conducted on which was the optimal number of layers to be used.
2. Sapphire plate. The purpose of this plate is to insulate the sample from the mount. The sapphire plate is blackened with amorphous carbon produced by the smoke of a wax candle, to eliminate any potential IR contribution from the sapphire surface during RAIRS experiments. Once the sapphire is blackened, in fact, its reflectivity is negligible.
3. Ta foil. The thermocouple is spot welded onto this foil. It contributes to close the heating circuit.
4. W/Re heating wires.
5. HOPG sample. Grooves are etched into the back of the sample to allow space for the W/Re wires. This is done in order to keep the back of the sample in contact with the Ta foil and consequently with the sapphire. This maximizes thermal transfer and therefore sample cooling.

The sample and all the underlying layers are held in place by a tension mechanism electrically insulated from the OFHC plate by ceramic sleeves. The tension mechanism is formed from an OFHC cross in which 4 holes have been made

to host the wires that go through the sapphire, the silver foil and the mount. The wires are held in position in the cross *via* screws. The cross rests behind the mount on a copper cap that is in contact with the sapphire plate and insulated from the copper mount by a ceramic ring. A stainless steal bolt is inserted in the centre of the cross, when this is tightened the cross moves away from the sample, pulling the tension wires.

The HOPG sample cleanliness must be ensured during all of the experimental operations. To achieve this the sample is cleaned, removing part of the surface layer of graphite prior to its placement on the mount. This is done by mechanical exfoliation using scotch tape [71,72]. Some of the residual gas inside the chamber will tend to condense onto the sample due to its low temperature. For this reason, before the beginning of a new experiment, the sample is cleaned by heating it to ~ 220 K for typically 1 minute. At this temperature all the residual gases, mainly water, will desorb. Moreover, at this temperature the heating of the cold finger is limited; this allows the sample to cool back to base temperature in ~ 5 min. The cleanliness of the sample after mechanical cleavage with scotch tape and further heating to 220 K has been checked numerous times by running test TPDs on the bare sample: no appreciable quantity of residual gases have been detected desorbing from the sample.

2.2 UV setup

Ultraviolet (UV) irradiation experiments were conducted on glycolaldehyde ices. A combination of a 150 W tuneable UV xenon arc lamp and a dual grating monochromator is used to generate a monochromatic UV beam that is then focused onto the sample *via* three quartz lenses. A schematic representing the UV setup and the sample is shown in figure 2.4.

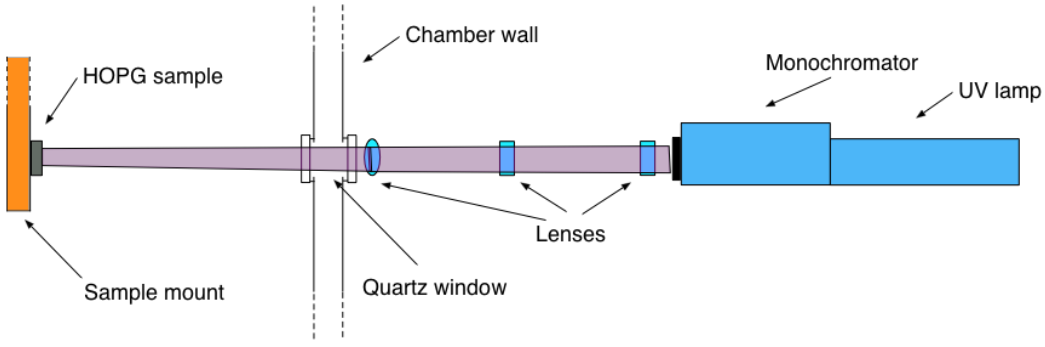

Figure 2.4. Schematic of the UV setup.

In order to be able to estimate the photon flux on the sample, a measurement of the power output of the system lamp + monochromator has been conducted. Figure 2.5 shows the power emitted as a function of the wavelength. The power was measured *via* a UV detector positioned immediately outside of the monochromator slit. The emission depends both on the wavelength selected and on the amount of power supplied to the Xenon arc lamp. However, the dependence on the frequency is the most relevant.

The glycolaldehyde irradiation experiments were conducted at a wavelength of 285±27 nm. The choice of this interval was based on [73], where the absorption cross section of gas phase glycolaldehyde was shown to have a maximum in the region between 280 and 300 nm. The uncertainty in the wavelength (27 nm) depends on the aperture of the slit outside the monochromator. In all experiments, a wide slit aperture of 6.5 mm was used. This choice of aperture was taken in order to maximise the output of the monochromator. This is necessary because, as shown in figure 2.5, the power emitted by the UV setup is very small at the 285 nm wavelength.

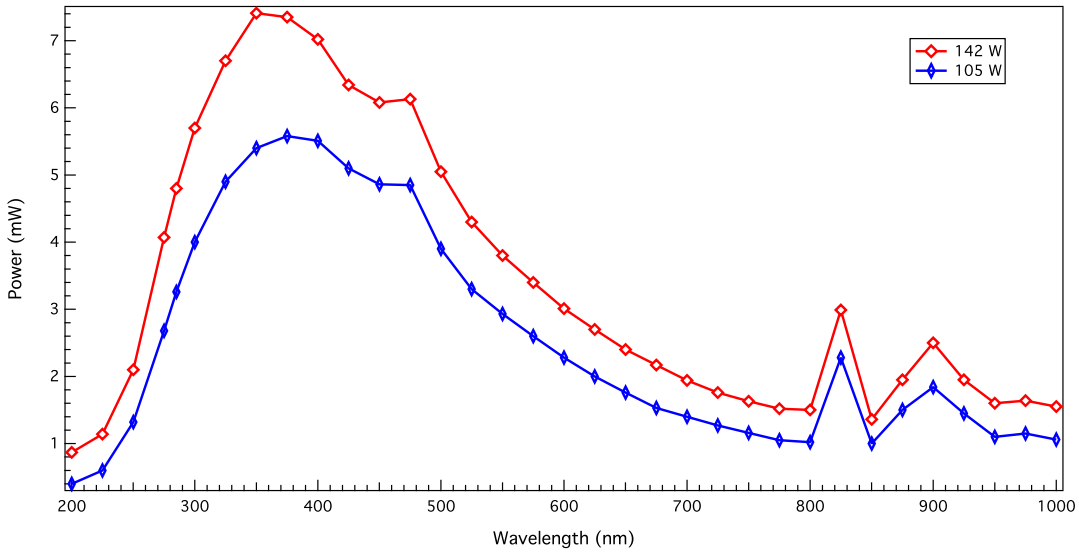

Figure 2.5. Power emission of the UV lamp + monochromator as measured outside of the monochromator slit. The two curves represent different supplied powers for the Xenon arc lamp, respectively 105 W and 142 W.

To calculate the power on the surface on the sample, an UV detector (Thorlab S3O2C) was placed at the same distance that the HOPG sample has with respect to the lenses. The configuration is analogous to the one shown in figure 2.4, with the only difference being that the detector is outside the chamber. The power detected in this configuration was 0.9 mW, which at a wavelength of 285 nm, and considering that the area of the sensor is ~0.7 cm^2, corresponds to a photon flux of

$\sim 1.9 \times 10^{15}$ cm^{-2} s^{-1}. The uncertainty comes from the variation that the flux goes through when the frequency changes throughout the bandwidth.

2.3 Experimental chamber 2

The configuration of CH2 is essentially analogous to that of CH1. The main differences are in the way UHV is reached and in the layout of the experimental level of the chamber. In CH1 UHV is achieved *via* a turbomolecular pump, an ion pump and a titanium sublimation pump (TSP). However, in CH2, UHV is achieved *via* two diffusion pumps and a TSP. The employment of diffusion pumps requires the use of a cold trap to stop the oil vapour from entering the main chamber. The cold traps (one for each diffusion pump) are cooled with liquid nitrogen.

Figure 2.6 shows a representation of the experimental setup CH2. The main differences compared to CH1 (figure 2.2) are the position of the leak valves with respect to the sample and the fact that there are two extra windows. These windows can be used for UV laser bombardment of the sample. However, no experiments of this kind are presented in this work.

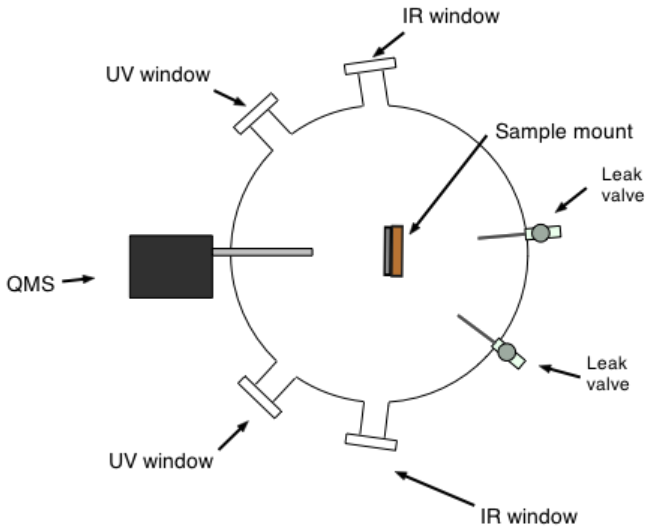

Figure 2.6. Schematic of the experimental level of CH2.

In both setups a Fourier transform infrared spectrometer and a quadrupole mass spectrometer are used to probe the species adsorbed onto, and desorbing from, the sample.

2.4 Experimental techniques

Experimental surface science techniques are essentially of two types: invasive and non invasive. In the first case, the material deposited onto the sample is removed

from the surface in the process of analysing it. In the second case, the adsorbate is probed directly on the surface without it being severely affected by the procedure.

The experimental techniques usable with the previously described setups are mainly two: RAIRS and temperature programmed desorption (TPD). The first is a non destructive method that allows us to qualitatively analyse which species are present on the surface and to monitor the formation of molecules in "real time". The latter is a destructive process and it is used to quantitatively analyse the species on the sample and the strength of their bonds to the surface.

2.4.1 RAIRS

RAIRS is a surface analysis technique that provides information on the adsorbate by measuring the difference in intensity between an incident and a reflected infrared beam. In this configuration, the infrared beam is generated by a Fourier transform infrared spectrometer. It is then focused onto the sample *via* a combination of a flat and a parabolic mirror. After reflection from the surface of the HOPG, the IR light is reflected by mirrors and focused onto a liquid nitrogen cooled mercury cadmium telluride (MCT) solid state detector.

The IR radiation crosses the chamber through the KBr windows. The optics, the MCT detectors (housed inside closed metal boxes) and the FTIR are purged with dry air to lower (and maintain constant) the amount of atmospheric CO_2 and H_2O, as both species are strong IR absorbers and would affect the beam.

The difference between the incident (I) and reflected (R) beam is due to the absorption of light by the adsorbate. The absorption occurs because of the coupling between the electric dipole moment of the adsorbate and the electric field of the radiation. The incident and the reflected beams can be separated into two components based on the polarisation with respect to the plane of incidence. The component perpendicular to the plane of incidence, s-polarised light, undergoes a 180° phase change upon reflection, resulting in a zero net vector. The parallel, p-polarised, component has a phase change that depends on the angle of incidence: for grazing angles of incidence it is such that this component is enhanced. Therefore, only adsorbates possessing a component of the dipole moment perpendicular to the surface can interact with the IR beam and be detected by RAIRS. This is the so called "metal surface selection rule" or pseudo selection rule. HOPG is not a metal surface, but it has been shown extensively that it still obeys this rule [74,75]. HOPG

is, in fact, a semimetallic, crystalline allotropic form of carbon. It possesses a reflectivity that is intermediate between a metal and a dielectric substrate. Similarly to metals, the p-polarized reflectivity rises rapidly towards the value of 1 (complete reflection) when the incidence angle is close to 90° (grazing incidence) [75].

RAIRS is used mainly to obtain information about the molecular composition of the ice deposited onto the sample. Every molecule possesses a characteristic IR fingerprint. If absorption bands belonging to different species do not overlap, unequivocal identification of the adsorbed species is usually possible. This is particularly useful in irradiation experiments, where the composition of the ice can change due to induced formation/destruction of new compounds. RAIRS can also provide indications about the ice phase changes in temperature variation experiments. During phase changes the intensity of the IR feature changes due to the reorientation of the molecules in the ice bulk. This usually appears as an intensification of the IR bands in the spectrum (*e.g.*, see H_2S behaviour in chapter 3). Potentially, RAIRS can also provide information about the orientation of the molecules with respect to the surface. If a particular vibrational mode does not possess a component of the dipole moment perpendicular to the surface of the sample, it will be invisible in a RAIR spectrum. This fact could be used to infer, at least qualitatively, the orientation of the molecules in the ice.

2.4.2 TPD

Temperature programmed desorption is an important experimental technique for the determination of kinetic parameters of desorption processes, such as: binding energy, desorption order and pre-exponential factor. TPD is also used to study layered and mixed ices, *i.e.*, ices formed by dosing one species on top of another species (layered) or by dosing two species at the same time. In these cases, TPD can provide information about where one species is bound to the other (*e.g.*, surface or bulk), and about porosity and the structure of the ice (*e.g.*, amorphous to crystalline phase transitions are sometimes visible in the spectrum). Furthermore, TPD provides a semi-quantitative indication of the coverage (or relative coverage) of the ice deposited onto the sample. The area underneath the TPD curve is, in fact, proportional to the amount of species adsorbed on the sample. In order to obtain a

fully quantitative estimation of the coverage, further assumptions on the impingement rate need to be made (more details at the end of the chapter).

In a typical TPD experiment, the sample covered with adsorbate is placed in front of the QMS. The temperature is increased linearly *via* the previously described heating circuit. Stable heating rates (usually 0.50 ± 0.01 K s^{-1}) are achieved *via* controlling software (Itools, Eurotherm Ltd.) and a power supply (Xantrex 30-70, Thurlby Thandar Ltd.); the whole procedure is regulated using a thermocouple feedback loop. The typical power loaded onto the sample during heating ranges from 0 to around 30 W, corresponding to a sample temperature change from 20 K (base temperature) to ≈200 K. As the sample is warmed, the energy of the adsorbate molecules in the ice increases until it eventually overcomes the bonding energy and any possible activation barrier. The adsorbate starts desorbing and its flux is recorded by the QMS, which is set to continuously scan the mass of the molecules of interest.

The TPD process is described by the Polyani-Wigner equation:

$$r_{des} = -\frac{d\theta}{dt} = A\theta^n exp\left(-\frac{E_{des}}{RT}\right) \tag{2.1}$$

where r_{des} is the rate of desorption, θ the coverage, t is the time, A the pre-exponential factor, E_{des} the desorption energy, R the gas constant and T the surface temperature. Equation (2.1) expresses the variation of the coverage as a function of time. However in TPD experiments, the coverage changes as a function of the temperature T. Using the relation:

$$-\frac{d\theta}{dt} = -\frac{d\theta}{dT} \times \frac{dT}{dt} = -\beta \frac{d\theta}{dT} \tag{2.2}$$

equation (2.1) can be rearranged as follows:

$$-\frac{d\theta}{dT} = \frac{1}{\beta} A\theta^n exp\left(-\frac{E_{des}}{RT}\right) \tag{2.3}$$

where β is the heating rate. In the manipulation of equation (2.3) the heating rate is treated as a constant, therefore it is important that it stays linear for the duration of the TPD experiment.

The intensity of the signal recorded by the mass spectrometer is proportional to the rate at which the coverage decreases as a function of temperature, hence we can write:

$$I(T) \propto \frac{1}{\beta} A\theta^n exp\left(-\frac{E_{des}}{RT}\right) \tag{2.4}$$

Several experimental values can be obtained by manipulating equation (2.4). This can be done in several ways. For a comprehensive description of the advantages and disadvantages for each method see King, 1975 [76]. The choice method for this work is the desorption isotherm analysis [77]. This method for calculating desorption order and desorption energy is based on the assumption that the desorption energy and pre-exponential factor do not vary with temperature and coverage. This assumption has been proven to be valid in numerous previous studies, see for example [35,78]. To obtain the desorption order we can rearrange (2.4) as follows:

$$\ln I(T) = n \cdot \ln(\theta_{rel}) + \mathrm{c}_1 \tag{2.5}$$

Where θ_{rel} is the relative coverage obtained from the area under the TPD curve. From equation (2.5) we can determine the desorption order (n) from the gradient of a plot of $\ln I(T)$ against $\ln(\theta_{rel})$ at a constant temperature, using TPD spectra with different initial coverages. Figure 2.7 shows a graphic example of this kind of analysis procedure: a temperature of 80 K has been selected in the leading edge of the curves. The relative coverage corresponding to a temperature T is given by the area under the curve for temperatures higher than T. This is shown in the figure for the case of 1 L of CO_2.

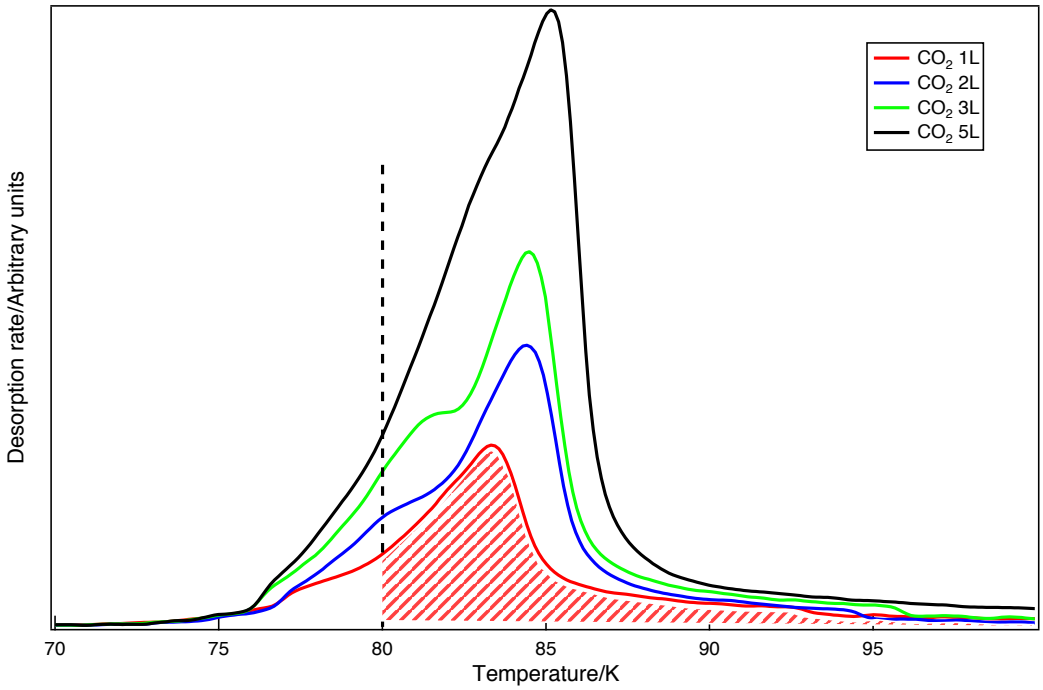

Figure 2.7. Example of TPD curves for different dosages of CO_2. The shaded area in the 1 L curve represents the relative coverage at a temperature of 80 K.

Desorption order provides information on how the molecules are bound and formed on the surface. Zero order desorption is characteristic of multi-layered systems, first order of non dissociative adsorption (monolayer regime) and second order of recombinative desorption.

Further manipulation of equation (2.4) leads to:

$$\ln I(T) - n \cdot \ln(\theta_{rel}) = -\frac{E_{des}}{RT} + c_2 \tag{2.6}$$

By plotting $\ln I(T) - n \cdot \ln(\theta_{rel})$ against $1/T$ for several TPD spectra, we can obtain E_{des} from the gradient. Desorption energy gives an indication of the binding energy within an adsorbate layer (multi-layer configuration) or between the adsorbate and the surface (single layer configuration).

Further information about the bonding can be inferred considering how the position of the peak maximum changes with the coverage. The maximum occurs when $dI/dT = 0$. Differentiating equation (2.4), after simple substitution, leads to:

$$\frac{E_{des}}{RT_p^2} = \frac{A}{\beta} exp\left(-\frac{E_{des}}{RT_p}\right) \cdot n\theta^{n-1} \tag{2.7}$$

From equation (2.7) we notice that the peak maximum temperature T_p behaviour changes depending on the desorption order.

From equations (2.3) and (2.7), the theoretical behaviour of TPD curves depending on the desorption order can be summarized as follows:

- $n = 0$. The desorption rate does not depend on coverage and it increases exponentially with T. Therefore the curves for different coverages share the leading edge and there is an abrupt drop when all the molecules have desorbed. T_p position is directly proportional to the coverage.
- $n = 1$. The desorption rate is proportional to the instantaneous coverage. T_p does not depend upon the coverage. The peak shape is characteristically asymmetric.
- $n = 2$. The desorption is rate proportional to the square of the instantaneous coverage. T_p is inversely proportional to the coverage, the peak moves toward lower temperature when the coverage is increased.

Occasionally fractional ($0 < n < 1$) desorption orders are observed, this is believed to indicate cluster formation on the surface and desorption from the edges of the clusters.

Finally, the pre-exponential factor can be calculated knowing the desorption order and the desorption energy. To determine this, the absolute coverage must be calculated. Assuming a sticking probability of 1, the number of molecules on the surface N_m is given by:

$$N_m = \frac{10^{-4} LA}{\sqrt{2\pi m k T_g}} \tag{2.8}$$

Where L is the dosage in Langmuirs ($1L = 10^{-6}$ mbar $\cdot$ 1 s), A is the surface area of the sample, m is the mass of the adsorbate species, k is the Boltzman constant and T_g is the temperature of the dosed gas (typically 300 K).

2.5 Setup calibration

Once the sample has been mounted and the UHV chamber, pumped down and baked so that the pressure is in the 10^{-10} mbar, TPD is used in order to assess the correct functioning of the setup. Specifically, TPD is used to assess the thermal contact between the sample and the cold finger, and the correct functioning of the

heating circuit. In order to achieve that, a run of water TPD is usually performed. Triply distilled and degassed (via multiple freeze-pump-thaw cycles) water is allowed into the chamber at different dosages and a series of TPD curves is obtained. These curves are then compared with previous data obtained on the same setup and with the existing literature. If the setup is operating correctly, the curves corresponding to high dosages of water should show characteristic of multilayer desorption and a plateau around 145 K corresponding to the amorphous to crystalline water transition (see figure 2.8).

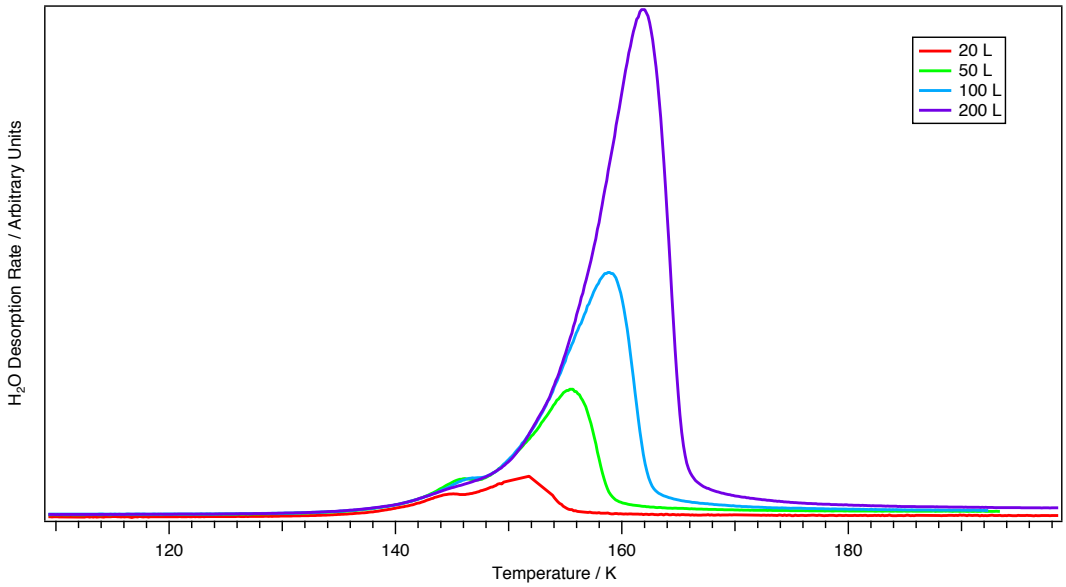

Figure 2.8. Example of water TPD curves.

3 TPD and RAIRS of H_2S bearing ices

3.1 Introduction

Hydrogen sulphide was detected in the interstellar medium for the first time in 1972 by Thaddeus *et al* [79]. Since then, the presence of H_2S in the gas phase has been confirmed multiple times in a variety of environments, including regions of star formation [47], dark clouds [80] and shock regions [57]. More recently it has also been observed in its doubly deuterated form (D_2S) towards young stellar objects [81].

Sulphur bearing molecules have important astrophysical relevance. As already mentioned in section 1.5 the abundances of sulphur bearing species in hot cores are dependent on the evolutionary stage of the object, hence sulphur-bearing species could be used as molecular clocks. Specifically, it is predicted by chemical models that during the evolution of hot cores, almost all of the original H_2S is converted to SO and SO_2. Sulphur monoxide is formed rapidly from H_2S at early times ($t < 10^5$ years) and at low temperatures when T < 230 K. Above this temperature most of the available reactive oxygen goes into the production of water, therefore SO_2 formation is inhibited. In hot cores, SO_2 is never more abundant than SO within the first 10^5 years. Therefore SO/H_2S and SO/SO_2 ratios are thought to be good evolutionary tracers [47].

Computational studies of magneto-hydrodynamic shocks in dense clouds have also shown that H_2S fractional abundance is enhanced by the passage of shock waves [56]. This suggests that H_2S could also be an important tracer for this type of astrophysical region.

Considering that H/H_2 are the most abundant species in space and also considering the amount of sulphur observed in diffuse environments, sulphur would be expected to react with the very abundant hydrogen to form H_2S, which should be the main reservoir of sulphur on dust grains in dense clouds. However, the observation of H_2S in icy grain mantles suggested by Geballe *et al.* [52] has never been completely confirmed. This is probably due to its main band being near 3.92 μm, where it overlaps with a feature of methanol [44] or due to some kind of processing of H_2S ice (photo processing or cosmic rays) that reduces the amount of

H_2S ice to below the limits of detection. Study of the irradiation of H_2S bearing ices points towards this conclusion: UV irradiation of H_2O/H_2S ices readily shows the formation of S_2 and S-chains up to S_8 [54], and proton bombardment of CO/H_2S ices shows formation of OCS, SO_2 and other sulphur bearing molecules [44]. Another possible explanation for the apparent lack of solid H_2S could be that the chemical networks used to model the interaction of sulphur bearing species and interstellar grains, predicting the presence of H_2S, are not completely understood. There are indications that this is part of the problem, for example an updated model has shown that the amount of H_2S on the surface of dust grains is strongly decreased in favour of polysulphanes H_2S_3 at temperatures higher then 10 K in dense clouds [82].

In order to help to solve the mystery of sulphur depletion in dense clouds, a through comprehension of the kinetics of H_2S adsorption and desorption on dust grain analogues is necessary. For this reason, a complete temperature programmed desorption study of H_2S in anhydrous and hydrous environments has been undertaken in the present work. A reflection absorption IR spectroscopy investigation has also been performed, to further corroborate and complement the TPD results.

3.2 Experimental

Experiments were performed in the UHV chamber (CH1) described in detail in chapter 2. Research grade H_2S (Sigma Aldrich, 99.5%) and distilled water were used in all experiments. Water was purified *via* multiple freeze-pump-thaw cycles to eliminate the gases trapped inside it.

Normally, ices are grown on the sample by backfilling the chamber *via* a precision leak valve. This is done to ensure a more isotropic growth of the ice and to avoid potential effects on the ice growth due to the deposition angle (see, for example, Stevenson *et al.* [83]). However, in the case of H_2S TPD studies, the ice growth was obtained by "direct" deposition. The sample faced the dosing line during deposition and was turned to face the mass spectrometer for the recording of a TPD spectrum. The choice of this unusual configuration was due to the "stickiness" of H_2S inside the chamber: the H_2S gas was pumped out of the chamber very slowly by the turbomolecular pump. This impeded an accurate control of the amount of ice

accreted onto the sample, making a quantitative analysis of the TPD curves impossible. Moreover it contributed to the degradation of the quality of the vacuum inside the chamber in the long term. Considering that during direct deposition the distance of the sample from the dosing line is around 10 cm, the effects of direct dosing on the structure and uniformity of the ice are assumed to be negligible. For the study of layered ices of H_2O and H_2S, the sample was turned alternatively towards each dosing line, and finally towards the quadrupole mass spectrometer, for the recording of a spectrum. In the case of binary mixtures (molecular species and water), the sample was turned to an intermediate position facing the quadrupole mass spectrometer, leaving it at an angle of $\approx 45°$ with respect to both dosing lines. During mixture dosing, the pressure of the most abundant molecule, usually water, is monitored *via* the ion gauge in the chamber, while the pressure of the secondary species is monitored *via* the QMS.

During RAIRS experiments the sample was positioned facing the opposite direction (the back of the sample faces the QMS) and the ice growth was obtained by background deposition. This is the only possible configuration for RAIRS experiments, due to the chamber design.

Exposures were measured in Langmuir, where 1 L = 10^{-6} mbar·s, and were not corrected for the ion gauge sensitivity. All TPD spectra were recorded at a heating rate of 0.5 K/s. RAIR spectra were taken at a resolution of 2 cm^{-1} and 256 scans were taken for each spectrum. For the temperature dependent RAIRS studies, the temperature was raised at a rate of 0.5 K/s to the set value and kept stable for 3 minutes; RAIR spectra were taken when the temperature had dropped.

TPD and RAIR spectra were recorded for H_2S bearing ices adsorbed on a highly oriented pyrolitic graphite (HOPG) surface at 25 K. Experiments with water and H_2S were executed in three different regimes: pure H_2S, layers of H_2S on top of H_2O and H_2O/H_2S mixtures. Additionally, in the case of TPD, investigations of H_2O adsorbed on top of H_2S were performed to study the porosity of water with respect to H_2S.

3.3 TPD of pure H_2S ices

Figures 3.1 and 3.2 show TPD spectra recorded for a range of exposures of pure H_2S adsorbed on HOPG at 20 K. Figure 3.1 shows the spectra for low dosages,

from 0.05 to 0.2 L. Figure 3.2 shows the spectra for high exposures, from 0.2 to 5 L. The curves have been divided into two graphs because, as will be shown later, they are characteristic of two different adsorption regimes corresponding to submonolayer and monolayer coverage, and the multilayer regime respectively. The 0.2 L exposure marks the transition between the two regimes and is shown on both figures as a comparison.

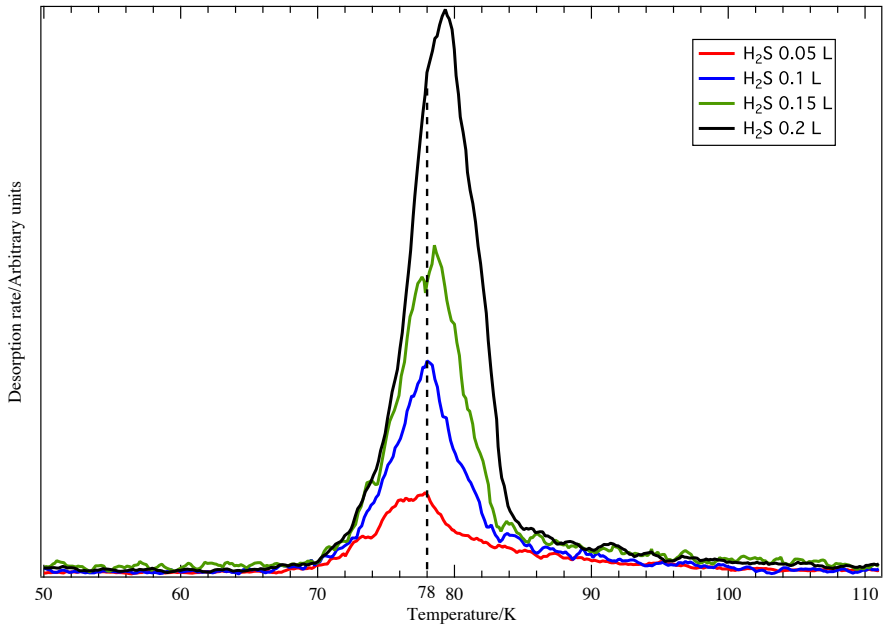

Figure 3.1. TPD spectra of low exposures of H_2S, up to 0.2 L, adsorbed on a bare HOPG surface at 20 K.

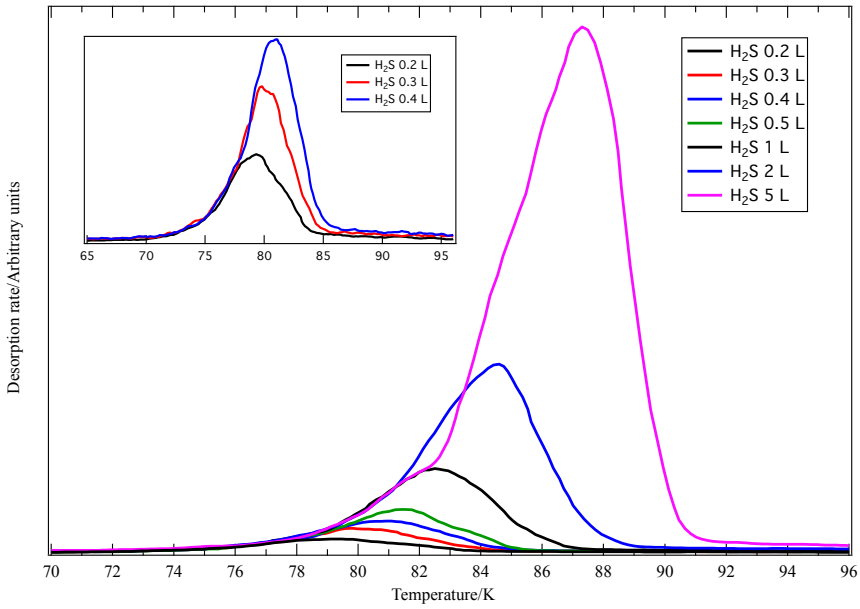

Figure 3.2. TPD spectra of high exposures of H_2S, above 0.2 L, adsorbed on a bare HOPG surface at 20 K. The inset magnifies the curves from 0.2 L to 0.4 L for clarity.

At the lowest H_2S exposure of 0.05 L, a peak is observed in the TPD spectrum at ≈ 78 K. Increasing the H_2S exposure to 0.1 L and further to 0.15 L does not appreciably change the TPD peak position, which remains stable at ≈ 78 K.

At higher exposures (figure 3.2) above 0.2 L and up to 5 L, the peak position increases consistently with the amount of H_2S dosed. The peak temperature increases from 78 K, for 0.2 L, to 87 K for 5 L. The curves show a common leading edge in the temperature range 74 to 79 K. Between 79 and 81 K the leading edge is shared only by dosages higher than 1 L.

A qualitative analysis of the TPD spectra at low exposures of H_2S (figure 3.1), from 0.05 to 0.15 L, shows that the peak temperature does not depend on the dosage, the curves do not share a leading edge and the peak shape is slightly asymmetric. These characteristics are an indication of 1^{st} order desorption which is common for monolayer and sub-monolayer desorbing species [8-9]. Higher dosages, above 0.3 L, show characteristics of 0^{th} order desorption: a highly asymmetric peak shape, shared leading edges and increasing peak temperature with increasing adsorbate coverage. This is common for multilayer desorbing species [77,78].

In figure 3.2, the curve corresponding to 5 L completely shares the leading edge with all the curves up to 1 L. Leading edge sharing is partial with the curve corresponding to 2 L because a kink/shoulder appears in the 5 L trace around 81 K. This feature is most probably associated with H_2S crystallization. This assignment is based on the similarity of this feature to the amorphous solid water to crystalline water ice phase transition (150 K) feature [84] and it is further confirmed by temperature dependent RAIR spectra which show a sharpening of the H_2S vibrational bands at around 70 K (discussed later in section 3.6). Crystallization is not clearly observed at dosages lower than 5 L probably because the feature is too small compared to the main peak. Crystallization is a bulk process, therefore the intensity of the transition depends on the ice thickness. Also in the case of water, crystallization is not observed for lower dosages.

The RAIRS study shown later does not show appreciable differences between low dosage and high dosage spectra showing that the monolayer and multilayer cannot be distinguished by infrared spectroscopy. However, the intensity of the H_2S infrared signal is very low (0.5 % for the highest dosage), therefore it is very difficult to clearly distinguish any features at low dosages.

In figure 3.3, a linear correlation is observed when comparing the integrated area of each TPD spectrum as a function of the exposure of H_2S; this shows that the deposition of H_2S on HOPG is constant as is the sticking probability of H_2S on HOPG. The linear deposition curve does not saturate at high dosages, this is expected in the case of multi-layered, physisorbed systems. The assignment of TPD due to monolayer desorption for low dosages and multilayer desorption for high dosages is confirmed in the quantitative analysis that follows in this chapter.

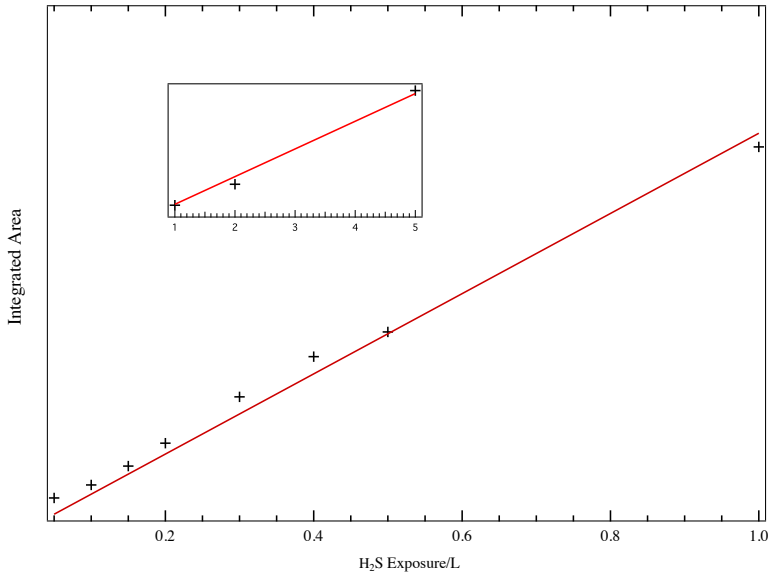

Figure 3.3. Integrated area of the TPD spectra shown in figure 3.1 and figure 3.2 as a function of H_2S exposure. The line represents a linear fit to the data. The inset shows higher dosages from 1 to 5 L. Error bars are absent because errors on the integrated area are considered negligible.

3.3.1 Quantitative analysis of TPD data

A quantitative analysis of the TPD data obtained for H_2S desorption from HOPG is necessary to further understand the dynamics of this process and to provide numerical information for astrochemical models. The methods used in this section have been described in detail in chapter 2.

Desorption orders. The desorption order can be determined from the gradient of a plot of $\ln I(T)$ against $\ln \theta_{rel}$ at a fixed temperature, using a set of TPD curves

corresponding to different H_2S coverages (eq. 2.5). Monolayer desorption orders were calculated from the TPD spectra for H_2S exposures between 0.05 and 0.15 L (figure 3.1). Figure 3.4 shows, as an example, the result of one of the plots for the determination of the monolayer desorption order. The relative coverage is calculated as the area under the curve in the interval that spans from the selected temperature to the high temperature end of the spectrum. In this way, only the contribution of the adsorbate still present on the surface is actually considered. The temperatures were chosen on the leading edge of the curves at a range of fixed temperatures between 73 and 76 K, in 0.5 K intervals. The results of the determination of the desorption orders for each temperature are shown in table 3.1. The average monolayer desorption order was found to be 0.9 ± 0.1. Considering that the uncertainties on I(T) and θ_{rel} are negligible, the uncertainty was taken as twice the standard deviation (σ) of the mean of the obtained gradients from table 3.1. A 2σ uncertainty ensures a more reliable confidence interval given the relatively small amount of experimental points.

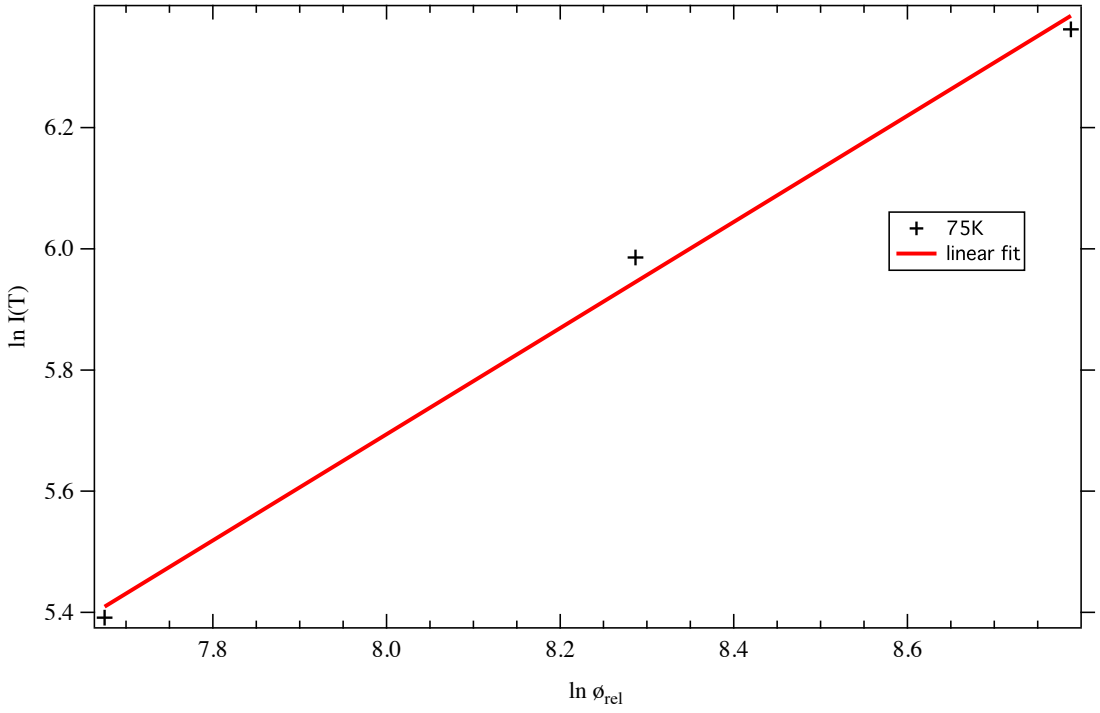

Figure 3.4. Plot of $ln\ I(T)$ versus $ln\ \theta_{rel}$ at a fixed temperature of 75 K producing a gradient for the determination of monolayer desorption order. Error bars are absent because errors on I(T) and θ_{rel} are considered negligible.

Temperature/K	Desorption order, n
73.0	0.7
73.5	1.0
74.0	0.8
74.5	1.0
75.0	0.8
75.5	0.7
76.0	0.9

Table 3.1. Calculated desorption orders for monolayer H_2S, adsorbed on HOPG.

The same procedure was applied to the high dosage curves (figure 3.2) in the temperature range from 76.5 to 79 K, and results are shown in table 3.2. The choice of the temperatures to be used is, in this case, limited by the lowest dosage (0.3 L). Temperatures higher than 79 K fall after the peak temperature, therefore the associated area does not represent the relative coverage. The average desorption order in this case is 0.06 ± 0.02, where the error is again taken as twice the standard deviation of the mean.

Temperature/K	Desorption order, n
76.5	0.02
77.0	0.01
77.5	0.07
78.0	0.08
78.5	0.03
79.0	0.05

Table 3.2. Calculated desorption orders for multilayer H_2S, adsorbed on HOPG.

Both the obtained values are very close, within the errors, to the expected values for monolayer $(n = 1)$ and multilayer desorption $(n = 0)$. Other sulphur-bearing species desorption orders, calculated for desorption from HOPG, are available in the literature. SO_2 desorption orders were found to be 0.65 ± 0.02 and 0.05 ± 0.04 respectively for monolayer and multilayer regimes, while CS_2 orders were found to be 0.88 ± 0.07 and 0.14 ± 0.05 [67]. H_2S desorption orders are comparable to CS_2 for monolayer desorption and to SO_2 in the case of multilayer desorption.

An intermediate dosage of 0.2 L was also recorded. Visually the curve seems to belong to the monolayer family, but further analysis showed that when included in the desorption order calculation it contributed to considerably lower the value of n. Likewise, if included in the multilayer family it increased the value of n well above 0. This indicates that 0.2 L presents characteristics of both monolayer and multilayer desorption and for this reason it has been excluded from the final calculations for the orders of desorption.

Desorption energies. Knowing the desorption orders we can calculate the corresponding desorption energies by plotting $\ln \mathrm{I(T)} - \mathrm{n}\ln \theta_{\mathrm{rel}}$ against $1/\mathrm{T}$ and taking the gradient as $-E_{des}/R$ (equation 2.6). Figure 3.5 shows an example of such a plot in the case of 2 L exposure of H_2S.

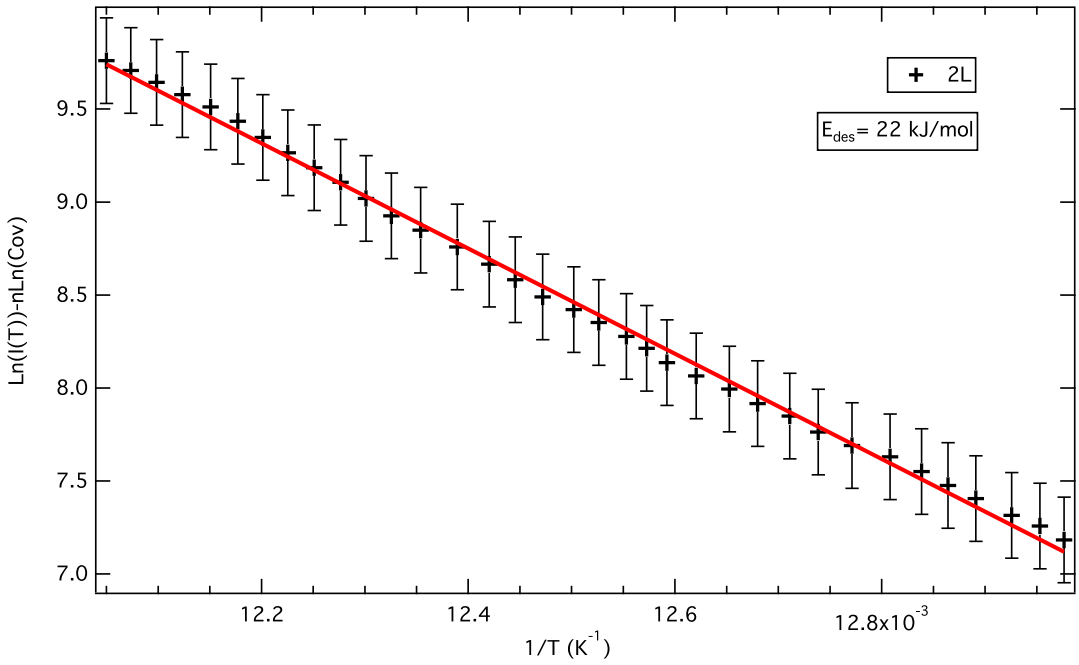

Figure 3.5. Plot of $ln\ I(T) - n ln\ \theta_{rel}$ against $1/T$ from the TPD spectrum following 2 L of exposure of H_2S.

Using the series of TPD spectra between 0.05 and 0.15 L, from figure 3.1, monolayer desorption energies were obtained for n = 0.9. The values obtained for each curve are shown in table 3.3. The average monolayer desorption energy was found to be 19 ± 3 kJ mol^{-1}. The uncertainty has been calculated as twice the standard deviation (σ) of the mean. This choice is based on the fact that the uncertainty on the desorption energy associated with the fluctuation of the desorption order within its uncertainty interval was considerably smaller (0.2 versus 3). Considering that there is a certain degree of variability in the calculation of the desorption order, depending on what

portion of the leading edge is used during the analysis, and considering that the average is performed over a small amount of points, a 2σ uncertainty represents a more cautious estimation of the errors.

H_2S exposure/L	Desorption Energy/kJ mol^{-1}
0.05	16.2 ± 0.5
0.10	19.1 ± 0.3
0.15	20.6 ± 0.4

Table 3.3. Calculated desorption energies for monolayer H_2S adsorbed on HOPG.

Applying the same procedure to the curves in figure 3.2, the desorption energy for the case of multilayer desorption can be obtained. The values obtained for each curve are shown in table 3.4. The average multilayer desorption energy was found to be 22 ± 1 kJ mol^{-1}, for n = 0.06. The error was calculated as in the previous case.

H_2S exposure /L	Desorption Energy /kJ mol^{-1}
0.3	20.4 ± 0.3
0.4	21.1 ± 0.2
0.5	22.7 ± 0.5
1.0	22.1 ± 0.2
2.0	23.8 ± 0.2
5.0	23.0 ± 0.5

Table 3.4. Calculated desorption energies for multilayer H_2S adsorbed on HOPG.

Desorption energies for monolayer H_2S tend to increase with an increase of the dosage (table 3.3). Considering that desorption energies for multilayer H_2S are higher than the monolayer ones, it can be assumed that the growth trend in the monolayer desorption energies is due to the influence of multilayers, which begin to already grow at lower exposures. This influence can potentially take place as island formation, *i.e.*, H_2S adsorbs onto H_2S whilst the first monolayer is still to be completed.

To the best of the author's knowledge, no previous values of H_2S desorption energies are available for monolayer desorption of H_2S from HOPG. However the interaction of high dosages of H_2S with other carbon surfaces has been studied. Values

for the desorption energy ranged from 20.6 kJ mol^{-1}, for H_2S on carbon black [85,86], to 30-39 kJ mol^{-1} for H_2S on amorphous carbon films, and finally 39-47 kJ mol^{-1} for H_2S on commercially activated carbon [87]. The very high desorption energies for commercially activated carbons is potentially due to their microporosity [87]. The value found in this work falls in the range of the previously determined desorption energies. Furthermore, desorption energy data are available for a plethora of molecules on HOPG and the values determined for molecules desorbing at temperatures comparable to H_2S, such as CO_2, are in good agreement with those found in the present work [88]. The fact that the multilayer desorption energy is higher than the monolayer one is compatible with the observed desorption temperatures, and suggests that H_2S binds more favourably with itself than with the HOPG. The reported value for the sublimation enthalpy of H_2S, ΔH_{sub} = 23.01 kJ mol^{-1} [85], is compatible with the desorption energy of multilayer H_2S (22 ± 1 kJ mol^{-1}) found in this work. This further supports the hypothesis that the interaction of H_2S/HOPG is weaker than the H_2S/H_2S interaction.

Pre-exponential factors. Finally the pre-exponential factors ν_n can be calculated using the values obtained for the desorption orders and the desorption energies. This is achieved using the procedure described in chapter 2. The first step is calculating the rate of impingement of H_2S molecules on the HOPG surface. According to equation 2.8, the impingement rate on a 2×1 cm surface, as a function of H_2S exposure, is 5.22×10^{14} molec L^{-1}. This value can be used to convert the relative coverage and relative intensity (*i.e.* the area under the TPD curve and the desorption rate respectively), into absolute coverage and absolute intensity. This is performed by scaling, using the relationship between the integrated TPD peak area and the actual H_2S exposure. From figure 3.3, the area under each TPD curve against H_2S exposure produced a linear fit with a gradient of 6.78×10^4 L^{-1}, producing a scaling factor of 7.7×10^9 molec.

To determine the pre-exponential factors, the Polanyi-Wigner equation is simply rearranged to give an expression for ν_n. The pre-exponential factors are calculated for a range of points on the leading edge of each TPD trace. For consistency, the same ranges of points as in the calculation of the desorption energy have been chosen. The values obtained in this way are then averaged to obtain the final ν_n for each TPD curve. The average values of n and E_{des} were used for the calculations. The results are shown in tables 3.5 and 3.6.

H_2S exposure/L	Pre-exponential factor /$(molec \cdot m^{-2})^{0.1} s^{-1}$
0.05	$10^{11\pm2}$
0.10	$10^{13\pm2}$
0.15	$10^{14\pm2}$

Table 3.5. Calculated pre-exponential factors for monolayer H_2S adsorbed on HOPG.

The variation of the pre-exponential factor due to the fluctuation of the desorption order and desorption energy, within their uncertainty intervals, is in this case the major source of uncertainty. Therefore, n and E_{des} were varied within their uncertainty intervals and the corresponding maximum variation on the pre-exponential factor was taken as its uncertainty.

The average monolayer and multilayer pre-exponential factors were found to be $10^{13\pm2}$ $(molec \cdot m^{-2})^{0.1} s^{-1}$ and $10^{27\pm1}$ $(molec \cdot m^{-2})^{0.94} s^{-1}$. These values were found averaging the values of the exponents in tables 3.5 and 3.6. Units are given as $(molec \cdot m^{-2})^{1-n} s^{-1}$.

H_2S exposure/L	Pre-exponential factor /$(molec \cdot m^{-2})^{0.94} s^{-1}$
0.3	$10^{25\pm1}$
0.4	$10^{26\pm1}$
0.5	$10^{27\pm1}$
1.0	$10^{26\pm1}$
2.0	$10^{28\pm1}$
5.0	$10^{27\pm1}$

Table 3.6. Calculated pre-exponential factor for multilayer H_2S, adsorbed on HOPG.

As in the case of the desorption energies, the values of the pre-exponential factors in the monolayer regime increase when the dosage increases. This is probably a further confirmation of the fact that multilayers start forming at a lower exposure than 0.3 L.

Pre-exponential factors for a variety of molecules are available in the literature. Their values for multilayer desorption have been found to vary from 8×10^{25} molec m^{-2} s^{-1} for NH_3 [42] to 2×10^{32} molec m^{-2} s^{-1} for CH_3OH [34]. The value found in this work falls in this interval and is comparable to the pre-exponential factor for H_2O which has been found to be 1×10^{27} molec m^{-2} s^{-1} [30]. Typical values of the pre-exponential factor for monolayer desorption are often taken as the vibrational frequency of a

molecule on a surface: $1 \times 10^{12\text{-}13}$ s^{-1} [89]. The pre-exponential factor found for H_2S monolayer desorption is fairly close to this range of values and similar values have been found for CO, CO_2 and H_2O [30].

3.4 TPD of binary H_2S/H_2O ice

Considering that water is one of the most abundant molecules in space and a fundamental component of the icy layers formed on interstellar dust grains, it is important to study the adsorption and desorption of H_2S in the presence of water. There is evidence that different molecules can stick to dust grains forming a layered structure or mixtures of ices. Understanding how layered ices behave is also key to understanding how mixed ices desorb. For this reason, experiments on both standard (H_2S on H_2O) and reverse (H_2O on H_2S) layered ices, as well as mixtures, have been performed.

In the case of binary-layered experiments, H_2S was deposited on top of 1 L of pre-deposited H_2O ice. The dosage of 1 L was chosen because it was experimentally found to be enough to properly coat the HOPG, 1 L of H_2O is in fact enough to form a solid multi-layered ice. In this way, the H_2S deposited on top of the water is not interacting with the HOPG substrate and the H_2S/H_2O interaction can be properly studied. In experiments where water was deposited on top of 0.5 L of pre-deposited H_2S ice (termed here as reverse layers) the amount of pre-deposited H_2S was chosen using the same rationale as the pre-deposited H_2O in the standard layered experiments. All the ices were grown at a temperature of 20 K. At this temperature and in UHV conditions water is found in its amorphous solid (ASW) phase [90]. If the temperature is raised (*e.g.*, during TPD) water goes through a phase transition into cubic crystalline ice (CI) [90]. This transition has visible effects both on TPD and RAIR spectra.

3.4.1 H_2S deposited on H_2O ice

Figure 3.6 shows TPD spectra for a range of exposures of H_2S on a pre-deposited 1 L layer of H_2O on HOPG at 20 K. Both at low (from 0.05 to 0.15 L) and at high (from 0.2 to 0.5 L) exposures of H_2S, three main features can be distinguished: a broad peak in the 70-105 K temperature range (α), a sharp peak in the 140-155 K region (β) and finally a very broad and small peak in the 155-175 K region (γ). For reference, the H_2O

TPD spectrum is also shown with the dashed red trace. The H_2O trace has been scaled by a factor of 100 for clarity.

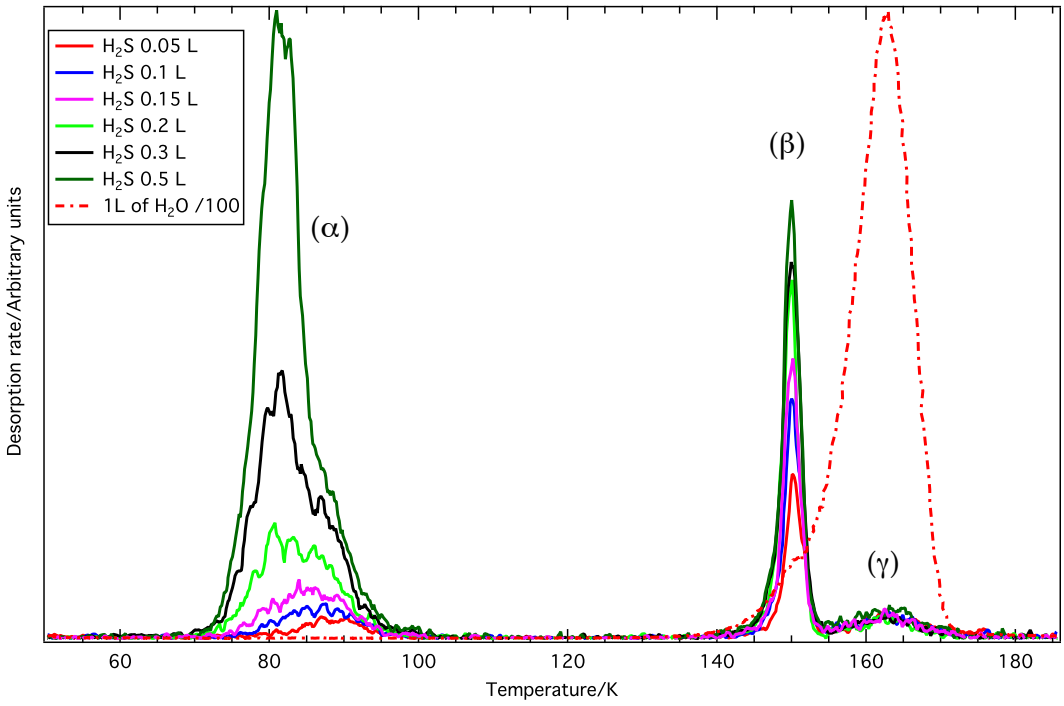

Figure 3.6. TPD spectra of low to high exposures of H_2S on 1 L of pre-deposited H_2O ice on HOPG at 20 K. The dashed red line shows the desorption of 1 L of H_2O, the trace has been scaled for ease of fit into the graph.

Peak α shows a very broad and complex (rich with sub features and irregularities) structure at all dosages. However, the broadness and complexity decrease with increasing dosage. Eventually, at an exposure of 0.5 L, peak α shows a defined "central" structure, which shows a maximum at ≈ 81 K, and a broadening at higher temperatures starting at ≈ 86 K. This broadening tapers down, forming a shoulder that disappears at ≈ 100 K. Figure 3.7A shows the comparison between the TPD of 0.15 L of pure H_2S adsorbed on HOPG and the low dosages (0.05 to 0.15 L) of H_2S deposited on top of H_2O. This clearly shows that for low exposures the maximum of peak α is shifted to higher temperatures compared to pure H_2S desorption. The peak maximum tends to move towards lower temperatures with increasing dosages. For a dosage of 0.5 L, the peak maximum is comparable to that for the equivalent dosage of pure H_2S ice. This can be seen in figure 3.7B, where the TPD of 0.5 L of pure H_2S ice and the TPD of 0.5 L of H_2S adsorbed on water have been plotted for comparison.

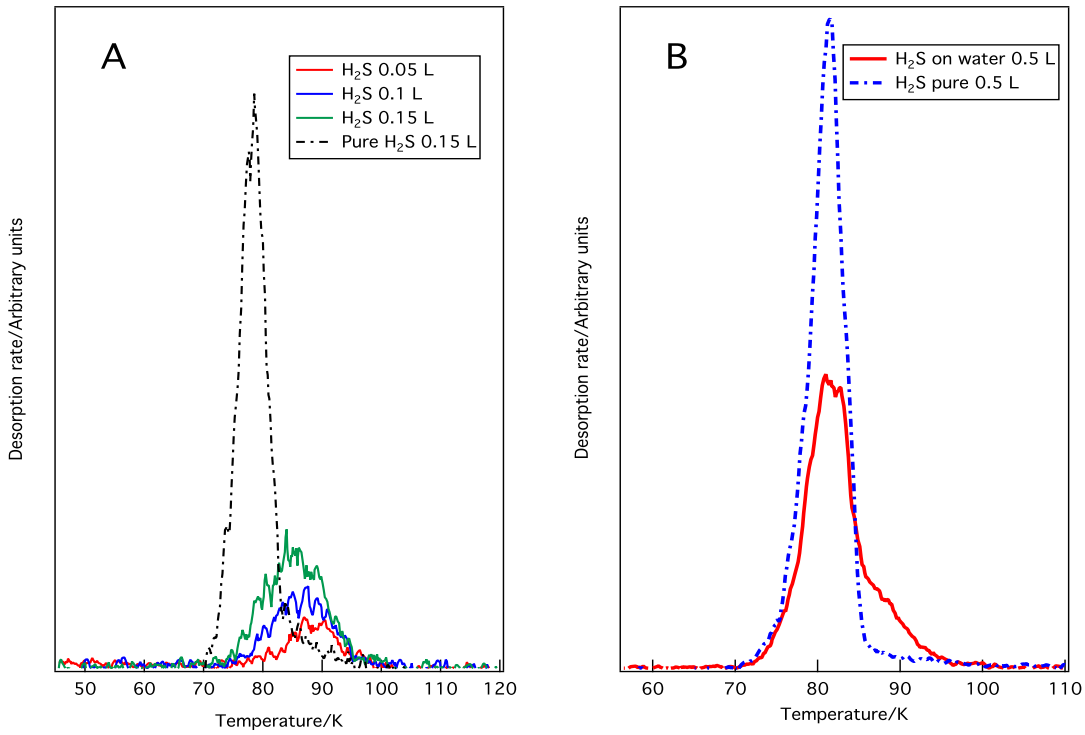

Figure 3.7. A) TPD spectra of low exposures of H_2S onto 1 L of pre-deposited H_2O ice on HOPG at 20 K. The dashed black line shows the desorption of pure H_2S after an exposure of 0.15 L. B) TPD of 0.5 L of pure H_2S ice compared to TPD of 0.5 L of H_2S on 1 L of pre-deposited H_2O on HOPG at 20 K.

The fact that peak α appears at temperatures comparable to the ones corresponding to desorption of pure H_2S from HOPG is an indication that it could be associated with desorption of H_2S from the surface of H_2O. As mentioned before, water deposited in this range of pressure and temperature is amorphous and therefore porous and rich with surface irregularities. At low dosages (< 0.15 L), in the monolayer regime, H_2S interacts directly with the surface layer of water. When the temperature increases enough, H_2S is released from this irregular and porous surface. This explains the broadening of peak α and its complexity. When the dosage increases above 0.15-0.2 L, according to the pure H_2S study, H_2S starts adsorbing in multilayers. Therefore the H_2S/H_2S interaction becomes predominant over the H_2S/H_2O interaction. In figure 3.6, this is noticeable by the fact that peak broadening and complexity decrease for higher dosages and the peak maximum moves to lower temperatures which are characteristic of pure H_2S desorption (figure 3.7A). Eventually, for 0.5 L of H_2S dosage, the temperature of the peak maximum is comparable for both the pure and layered system (figure 3.7B). For all these reasons, peak α is assigned to H_2S desorption from the surface of ASW.

Peak β is characteristically sharp at all dosages and its maximum stays at around 150 K for all dosages. In coincidence with peak β, a discontinuity in the form of a small plateau is noticeable in the water TPD (see figure 3.6). This plateau indicates the temperature at which water undergoes the ASW to CI phase change [84,91]. During the phase change, when water is rearranging itself into the new structure, H_2S molecules trapped in the water matrix can escape. Peak β is therefore assigned to the so called "volcano desorption" [84] of H_2S molecules trapped inside the water matrix. The rapidity of the transition and the fact that H_2S is well above its temperature of desorption gives peak β its characteristic sharpness. Volcano desorption is a well documented physical effect for a variety of molecules such as CS_2, SO_2, CO_2 and CO [40,91].

Finally peak γ appears in coincidence with the main desorption peak of H_2O, see figure 3.6. It is fairly broad and its peak maximum does not change visibly at different exposures. For these reasons peak γ is assigned to the codesorption of residual H_2S still trapped inside the water matrix following the phase change of ASW to CI. Interestingly, the intensity and the area of peak γ are comparable for all exposures. This implies that the great majority of H_2S is released from the surface (peak α) and during volcano desorption (peak β).

3.4.2 H_2O deposited on H_2S ice

The study of reverse layers is important to gain a better understanding of the trapping and diffusion of H_2S in an ASW matrix. Figure 3.8 shows the TPD spectrum of 1 L of H_2O adsorbed onto 0.5 L of H_2S. For comparison the standard layered ice equivalent is also shown in a red dashed line. By analogy with pure H_2S ice adsorbed on water we can assign the peaks as follows: peak α is assigned to the diffusion of H_2S through ASW, peak β is assigned to volcano desorption of H_2S and peak γ is assigned to co-desorption of H_2S with CI.

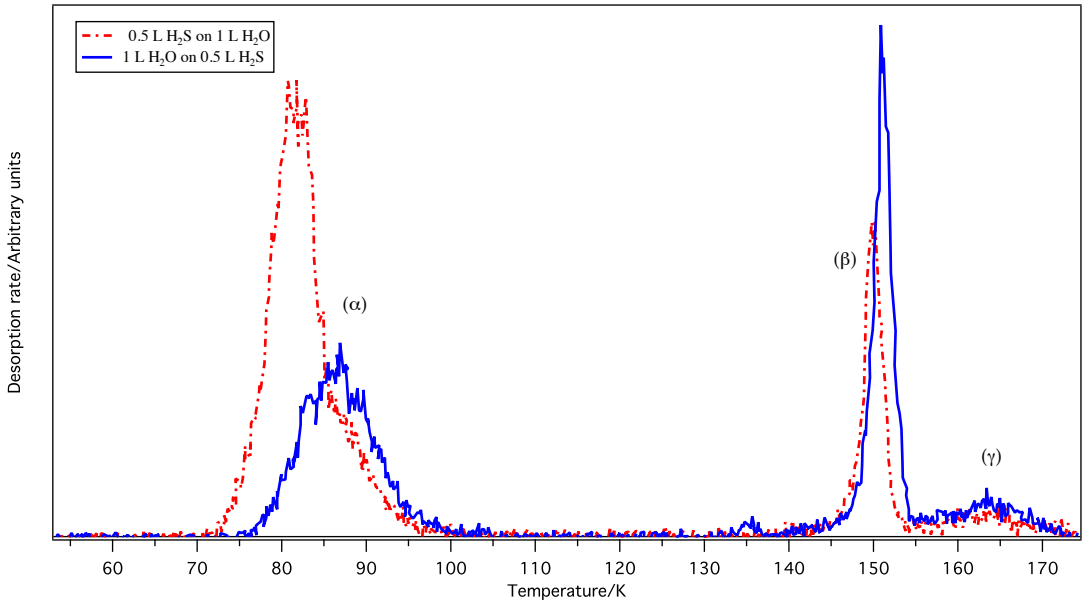

Figure 3.8 TPD spectra of a 1 L exposure of H_2O adsorbed onto 0.5 L of pre-deposited H_2S compared to 0.5 L of H_2S deposited onto 1 L of H_2O (dashed red line).

The most interesting feature in this case is peak α because it demonstrates that the ASW structure is porous enough to allow for H_2S diffusion. The peak maxima for both peaks α and β are shifted towards higher temperatures compared to the binary ice case. This is consistent with the fact that H_2S requires statistically more energy and time to percolate through the ASW matrix because it is initially underneath the water ice. Peaks α and β have a remarkably different relative height compared to the binary case, this is due to the fact that while H_2S is diffusing through the water ice layer part of the molecules get trapped in the ASW itself. For this reason peak α is shorter and broader in the reverse configuration, and the volcano peak β is higher.

3.5 TPD of H_2S:H_2O mixtures

TPD spectra were obtained for a range of H_2S and H_2O ice mixtures. In the different mixtures the dosage of water was kept constant at 1 L. The amount of dosed H_2S was changed accordingly to obtain a range of mixture varying from 15% to 46% of H_2S in water. The abundance of H_2S ice compared to H_2O ice is estimated to be around 1/32 in [54]. The amount of H_2S in the mixtures used for this work is evidently much higher. The choice of such high concentrations is due to limits of detection: for mixtures with a percentage of H_2S inferior to 15 %, the QMS signal for H_2S becomes too low to clearly distinguish features such as H_2S surface desorption from the ice and H_2S/H_2O codesorption. This can be clearly observed in figure 3.9 that shows the TPD spectra of a

series of H_2S:H_2O mixtures ranging from 15% to 46% of H_2S (curves represent the H_2S signal). Although executed with concentrations much higher than the ones characteristic of the ISM, the study of mixtures is still relevant to understand the behaviour of H_2S when it is embedded in ASW.

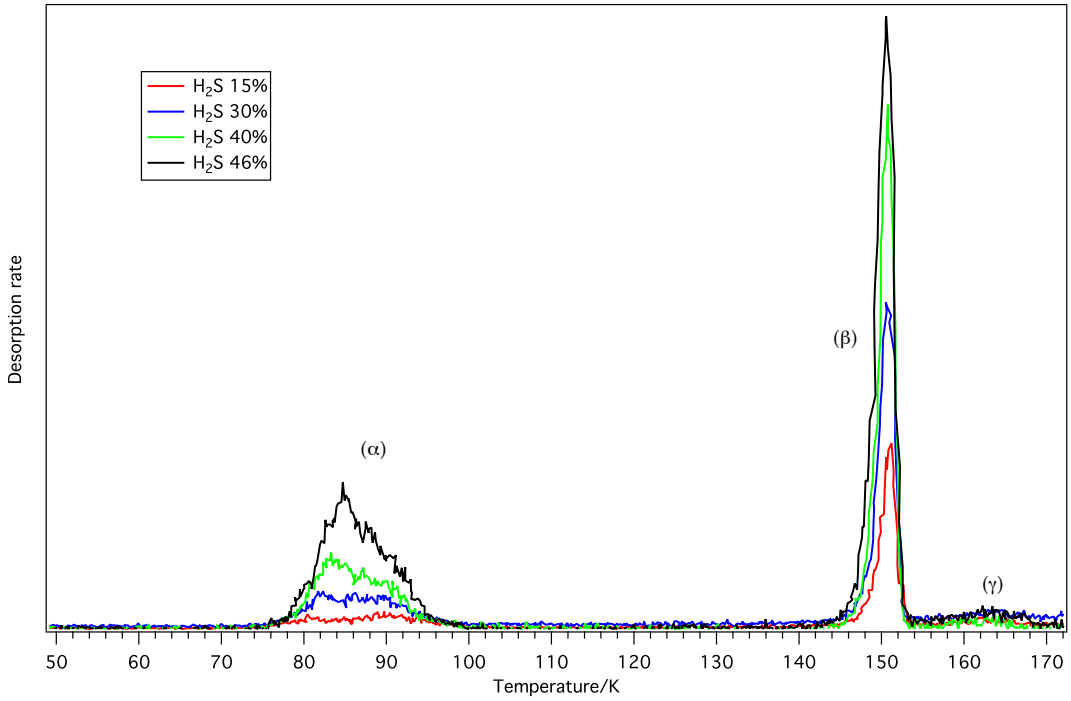

Figure 3.9. TPD spectra of 100 L of H_2S:H_2O mixtures, ranging from 15% to 46% of H_2S in water. The mixed ice was formed at 20 K.

Similarly to the layered configurations, three main peaks can be distinguished in the H_2S signal. These are assigned by comparison with the previous cases (layered and pure). Peak α is assigned to both desorption of H_2S close to the surface of the ice and desorption of H_2S after diffusing through the ice matrix (in agreement with the results from the reverse layer study). Peak β is assigned again to volcano desorption and, finally, peak γ is assigned to co-desorption of CI and H_2S.

Figure 3.10 shows a comparison of ≈ 0.5 L deposition of H_2S in the four configurations explored in the quantitative analysis of the TPD curves. The case of H_2S/H_2O mixtures does not show striking differences compared to the standard and reverse layered configurations. The three features α, β and γ are shown in all configurations containing water, although the relative size of the peaks changes.

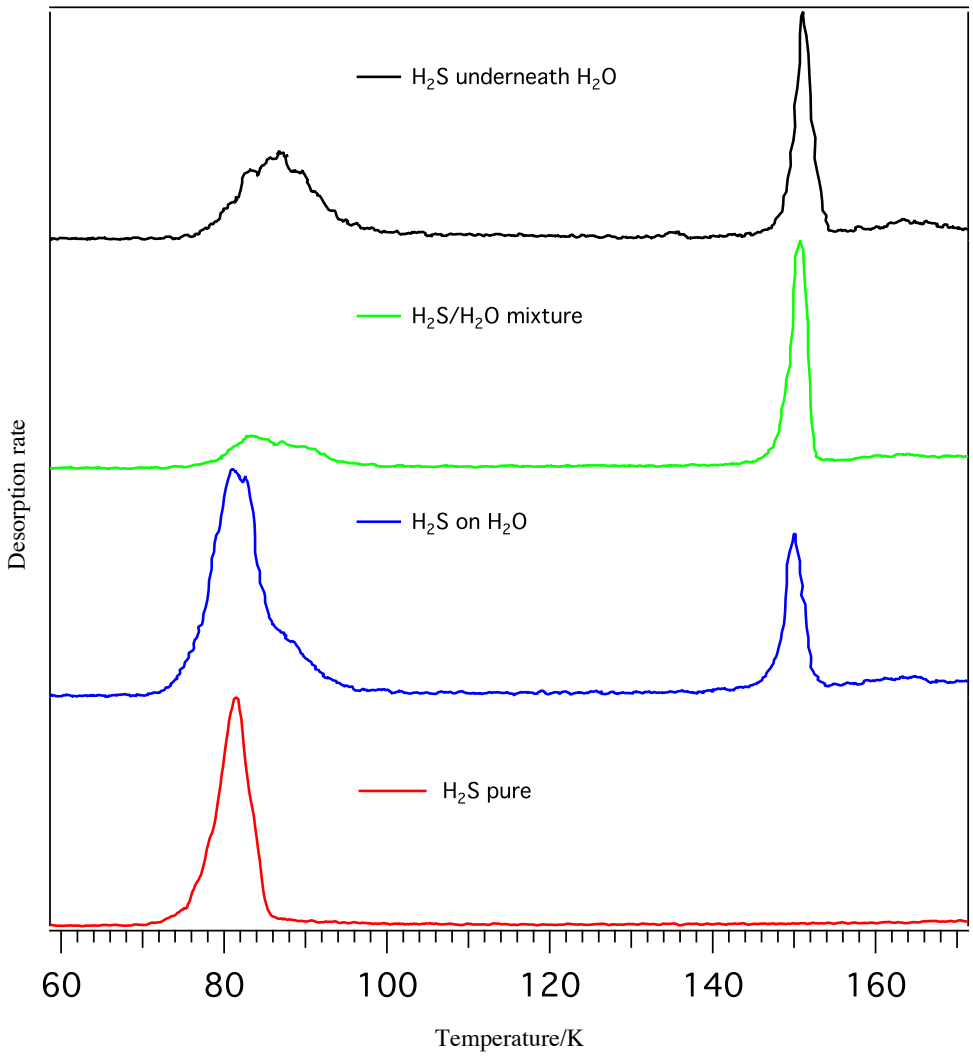

Figure 3.10. Comparison of H_2S TPD curves of 0.5 L of H_2S deposited on HOPG, on ASW, under 5 L of ASW and in a mixture with 1 L of ASW. Traces are offset, vertical axis values do not increase from top to bottom.

Peak α is most prominent in the standard layered configuration (H_2S on top of H_2O), as expected given that it represents desorption from the surface of the water substrate. In the reverse configuration (H_2O on top of H_2S), peak α gets broader and smaller due to H_2S having to percolate through the water ice layer to reach the surface and desorb. Peak β (volcano) is comparable in sharpness in all cases. Its intensity is higher than the peak α intensity in the H_2S/H_2O mixture and in the reverse layer configuration, while in the standard layered configuration the opposite is true. In the latter configuration, the amount of H_2S trapped in water is necessarily smaller than in the former configurations. Finally, peak γ (codesorption) is the smallest in all 3 cases.

From all the TPD experiments, important information concerning the desorption of H_2S was determined. H_2S can effectively diffuse through ASW, the small amount of H_2S still trapped within the ASW matrix at temperatures higher than the natural

desorption temperature will mostly escape during the ASW to CI transition. The amount that desorbs with water is very small.

3.6 RAIRS of pure H_2S ice

As already discussed, for RAIRS experiments the sample was not facing the dosing line and ices were deposited *via* background dosing. The amounts of H_2S dosed into the chamber were increased up to 100 L (the maximum in the TPD configuration was 0.5 L) to compensate for the diminished rate of adsorption. 5 L of directly dosed H_2S equals 20 L of background dosed H_2S. This was determined by comparing TPD curves obtained after H_2S direct dosing with TPD curves obtained after H_2S background dosing. All depositions were made at the base temperature of 20 K (see chapter 2 for details).

Figure 3.11 shows RAIR spectra for a range of exposures of H_2S adsorbed on a bare HOPG surface.

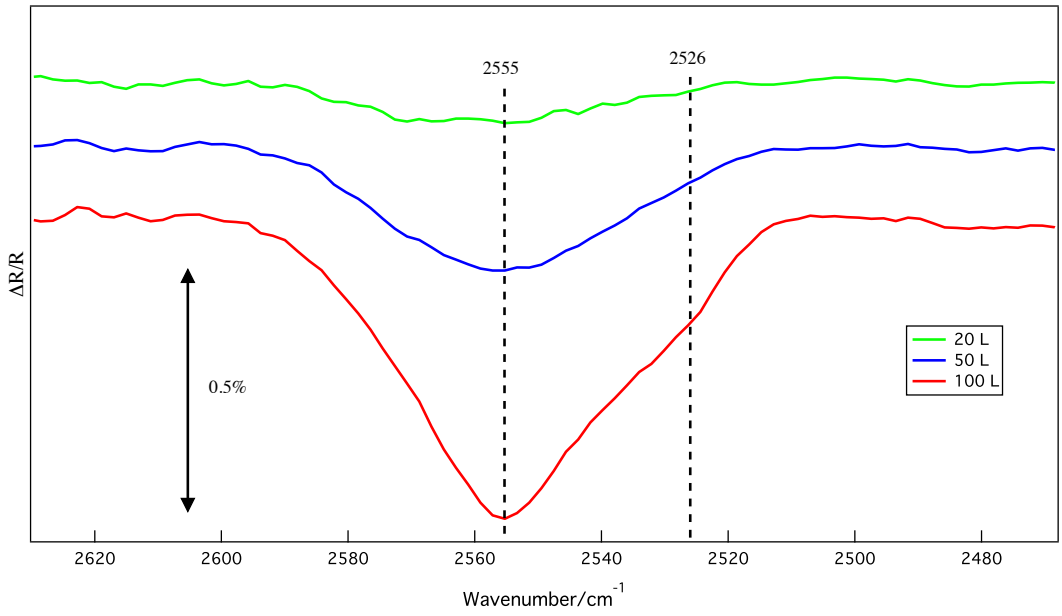

Figure 3.11. RAIR spectra of a range of exposures of H_2S adsorbed onto HOPG at 20 K.

Exposures lower than 20 L were recorded, but the H_2S infrared signal is so low that clearly distinguishing any feature was impossible. The H_2S dipole moment intensity is 0.97 D, which is small compared to, for example, the H_2O dipole intensity (1.85 D) [92]. This could be part of the reason why the H_2S signal is so faint. Alternatively, the orientation of H_2S molecules respect to the surface of the sample is such that the

component of the dipole moment interacting with the IR beam is small. This could be due to a very disordered structure of the H_2S ice.

With the increasing of the dosage a dominant band appears around 2555 cm^{-1}. The broadness of this feature supports the hypothesis that the ice structure is very amorphous. By comparison with gas phase data and the existing literature (see table 3.7), the asymmetric feature at 2555 cm^{-1} is associated with the overlapping of two strong vibrational bands of H_2S: the HS asymmetric stretch (2551 cm^{-1}) and the HS symmetric stretch (2526 cm^{-1}). For a dosage of 100 L a faint shoulder is observed between 2520 and 2530 cm^{-1}, this is likely due to the emergence of the HS symmetric stretch band. The H_2S infrared signal is very weak (0.5 %) even at dosages as high as 100 L.

TPD curves presented in section 3.3 showed the occurrence of H_2S crystallization at temperatures around 82 K. This is shown in figure 3.2, where the curve corresponding to 5 L dosage shows a plateau at around 81 K. To further investigate this phenomenon, the behaviour of H_2S ice after heating has been recorded with RAIRS. Figure 3.12 shows the RAIR spectra of 100 L of H_2S after progressive heating from 20 to 80 K.

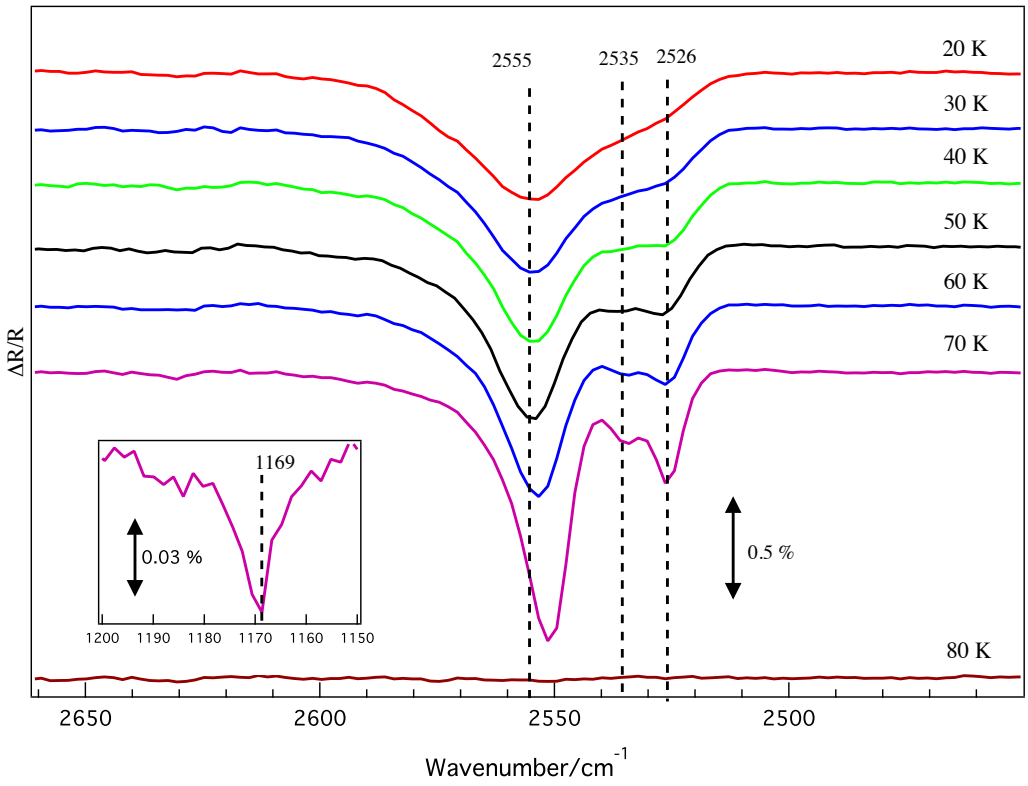

Figure 3.12. RAIR spectra of 100 L of H_2S ice at different temperatures during warming up. The inset shows the H_2S bending mode at 1169 cm^{-1} which appears at a temperature of 70 K.

During warm-up, crystallization of H_2S takes place and, as a result, the vibrational bands become more defined. The sharpening and increased intensity of the vibrational bands during crystallisation is due to the alignment of the electric dipole moments of the H_2S molecules. This alignment occurs because of the ordered nature of crystalline ice. Crystallization of H_2S was also previously observed in the literature [54,93]. In the crystalline structure, as described in [94], each H_2S molecule is hydrogen bonded to 4 neighbours, forming a quasi-bidimensional network of zigzag chains.

As a result of crystallization, the peak at 2555 cm^{-1} becomes more pronounced as the temperature increases and around 50 K a shift of this peak toward lower wavenumbers begins to take place. At 70 K the peak maximum has moved to ≈ 2551 cm^{-1}, closer to the natural HS asymmetric stretch frequency in the solid phase [54,93]. The faint shoulder observed for 100 L exposure, which was assigned to the HS symmetric stretch, develops into a full peak at 70 K, at around 2526 cm^{-1}.

A very small, but still observable, peak appears around 2535 cm^{-1} at a temperature of 70 K. This is assigned to remaining amorphous H_2S, in agreement with [54]. This assignment is done by comparison with results shown in [54]. A peak at 1169 cm^{-1} (inset in figure 3.12) is visible only at 70 K for 100 L of dosage. This peak is assigned to the H_2S bending mode, in agreement with previous studies [54,93,95]. The bending mode is very weak [95], and for this reason it becomes visible only at high doses for crystalline H_2S ice. All of the band assignments and comparisons with previous work are shown in table 3.7. At 80 K all H_2S has desorbed, in agreement with the previously collected TPD data.

Vibrational mode	On HOPG*	On ASW*	Jiménez-Escobar *et al.* [54]	Salama *et al.* [93]	Gas Phase [95]
ν_{as}, antisym. str.	2551	2551	2551	2633	2626
H_2S amorphous	2535	/	2539	/	/
ν_s, sim. str.	2526	2526	2528	2548	2615
δ_s, bending	1169	/	1169	1167	1183

Table 3.7. Assignment of H_2S vibrational frequencies on HOPG and on ASW. Comparison with Jiménez-Escobar *et al.* (on KBr substrate), *Salama et al.* (on CsI substrate) and gas phase values. All values in cm^{-1}. *This work.

The TPD curve of 5 L of H_2S (figure 3.2) already showed evidence of crystallization in the form of a plateau between 81.5 and 82.5 K (see section 3.3). As

mentioned before, 100 L of background dosed H_2S is equivalent to ≈ 1 L of directly dosed H_2S, therefore RAIR spectra show evidence of crystallization at lower dosages compared to TPD spectra. This is likely due to RAIRS being more sensitive to phase changes compared to TPD. The detection of the crystallization occurs at different temperatures depending on the experimental procedure utilized: ≈ 70 K for RAIRS and ≈ 82 K for TPD. This is caused by the fact that during a RAIRS experiment the sample is kept at the assigned temperature for a prolonged period of time (3 minutes), compared to a TPD experiment which uses a continuous heating rate of 0.5 K/s. Furthermore, in the TPD spectrum at 5 L the shoulder marks the change from desorption of amorphous H_2S to desorption of converted crystallized H_2S. This indicates that crystallization begins at lower temperatures, in agreement with the RAIRS results.

3.7 RAIRS of binary H_2S/H_2O ice

The characteristics of the interaction between H_2S and water can also be probed by RAIRS. Figure 3.13 shows a range of exposures of H_2S adsorbed on 100 L of ASW. Similarly to the TPD study of H_2S on H_2O, this thickness of pre-deposited ASW ice is enough to fully cover the HOPG surface. This allows for the study of H_2S/H_2O interactions instead of H_2S/HOPG interactions.

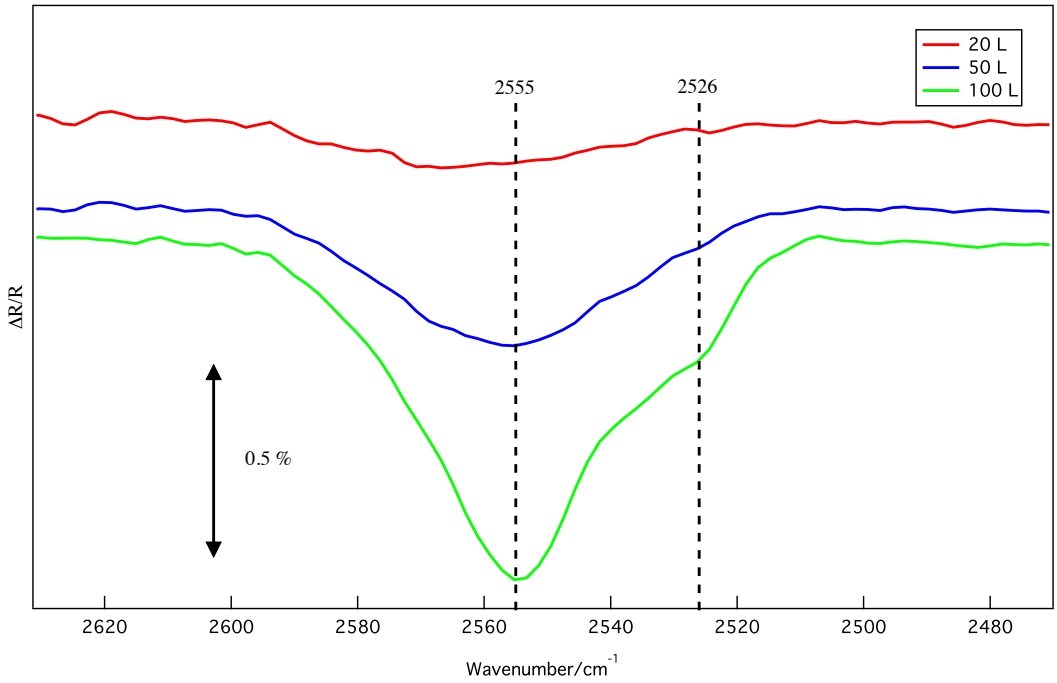

Figure 3.13. RAIR spectra of a range of exposures of H_2S adsorbed on 100 L of pre-deposited ASW at 20 K.

The main features of the H_2S peak are not substantially different compared to the case of pure H_2S ice adsorbed on HOPG (see figure 3.11 and table 3.7 for comparison): the maximum is still at 2555 cm^{-1} with a shoulder at 2526 cm^{-1}. This indicates that water does not have a prominent influence on multilayer H_2S ices compared to the corresponding ices deposited on a HOPG substrate. The only minor difference observed is in the shoulder at 2526 cm^{-1} which is slightly more pronounced, for 100 L of H_2S on ASW, than the respective peak for the same dose on bare HOPG. This could be due to the influence of the underlying water or to a small difference in exposure, the one onto ASW being slightly higher than the respective dose on bare HOPG.

Spectra at different temperatures for 100 L of H_2S deposited onto 100 L of ASW are shown in figure 3.14. No major differences were detected compared to the H_2S on HOPG case: crystallization still occurs at the same temperature and three prominent features can be identified at 2551 cm^{-1}, 2535 cm^{-1} and 2526 cm^{-1}. In the TPD studies, the crystallization was not visible for the H_2S on H_2O configuration. This was due to the curves being much broader and rich in complexity due to the interaction with ASW. As pointed out before, RAIRS seems to be more sensitive to phase changes compared to TPD.

In the H_2S on ASW configuration the effect of crystallization seems to be less prominent, namely, the peak height and sharpness are inferior and the peaks appear to be broader. This potentially implies an effect of water on adsorbed H_2S.

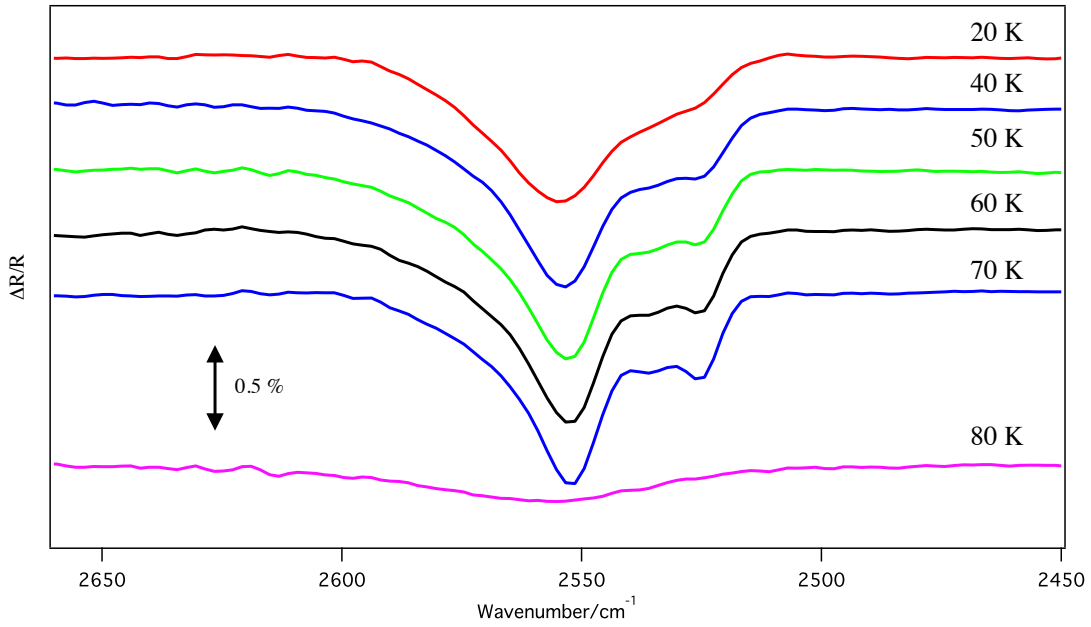

Figure 3.14. RAIR spectra of 100 L of H_2S adsorbed on 100 L of pre-deposited ASW, at different temperatures during warming up.

In figure 3.14, a small bump around 2555 cm^{-1} can be observed at 80 K, indicating that H_2S remains on ASW to higher temperatures compared to pure H_2S on HOPG. This is consistent with what is observed in the TPD study in which H_2S is present in the water matrix at temperatures higher than the natural sublimation temperature. However, TPD showed that in the H_2S on ASW configuration, there is desorption of H_2S in the form of volcano desorption and codesorption up to temperatures around 165 K. The difference in permanence of H_2S in water ice is too big to be completely explained by the different heating modalities between TPD and RAIRS. A possible cause of this difference can be that the orientation of the residual H_2S trapped inside the water matrix is such that the overall intensity of the IR signal becomes too low to be detected.

3.8 RAIRS of H_2S:H_2O mixtures

Figure 3.15 shows the thermal evolution of a 20% mixture of H_2S and H_2O deposited at 20 K. The overall thickness of the ice is 200 L. The choice for this high exposure is due to the fact that the intensity of the vibrational transitions for H_2S is very low, 100 L of pure H_2S produced a maximum intensity band of ~0.5%. Therefore in order to actually detect the signal of H_2S embedded in a water matrix, a thicker ice was needed. Even with a thick 200 L ice the intensity of the H_2S stretch band is of the order of 0.05%. The profile of the transition at 20 K is much more broad compared to the equivalent spectra for the case of pure H_2S ice (figure 1.12) or the case of H_2S deposited on the surface of water (figure 1.13).

No sub-features hinting to a distinction between symmetric and asymmetric stretch are distinguishable. The interaction with water causes the vibrational band to take the shape of a broad bump ranging from ~2460 to ~2640 cm^{-1}.

During the thermal processing of the ice, no visible effects of H_2S crystallization are present. This could be an indication that, once embedded in the ASW, the interaction with water impedes H_2S crystallization. Alternatively, it could be due to the low amount of H_2S in the ice. This could be too diluted in the water matrix to actually crystallize or its infrared absorption is simply to low to be able to distinguish any morphological change.

The signal from the H_2S stretch transition keeps decreasing with increasing temperature. At 90 K the signal is virtually undistinguishable from the background.

According to the TPD study of H_2S mixtures, the majority of H_2S desorption (62% in a 15 % H_2S/H_2O mixture) should desorb *via* volcano desorption, and around 30% *via* surface desorption (figure 1.9). Therefore, it would be expected for the IR signal of H_2S in the H_2S/H_2O mixture to be visible up to temperatures corresponding to the ASW to CI transition, around 140 K. Figure 3.15 suggests that this is not that this is not the case. The H_2S signal disappears at a temperature corresponding to surface/subsurface desorption (80-90 K). This is probably due to the low intensity of the signal. After the first amount of the H_2S is desorbed at ~90 K (peak α figure 1.9) the signal becomes simply too faint to be distinguished from the background.

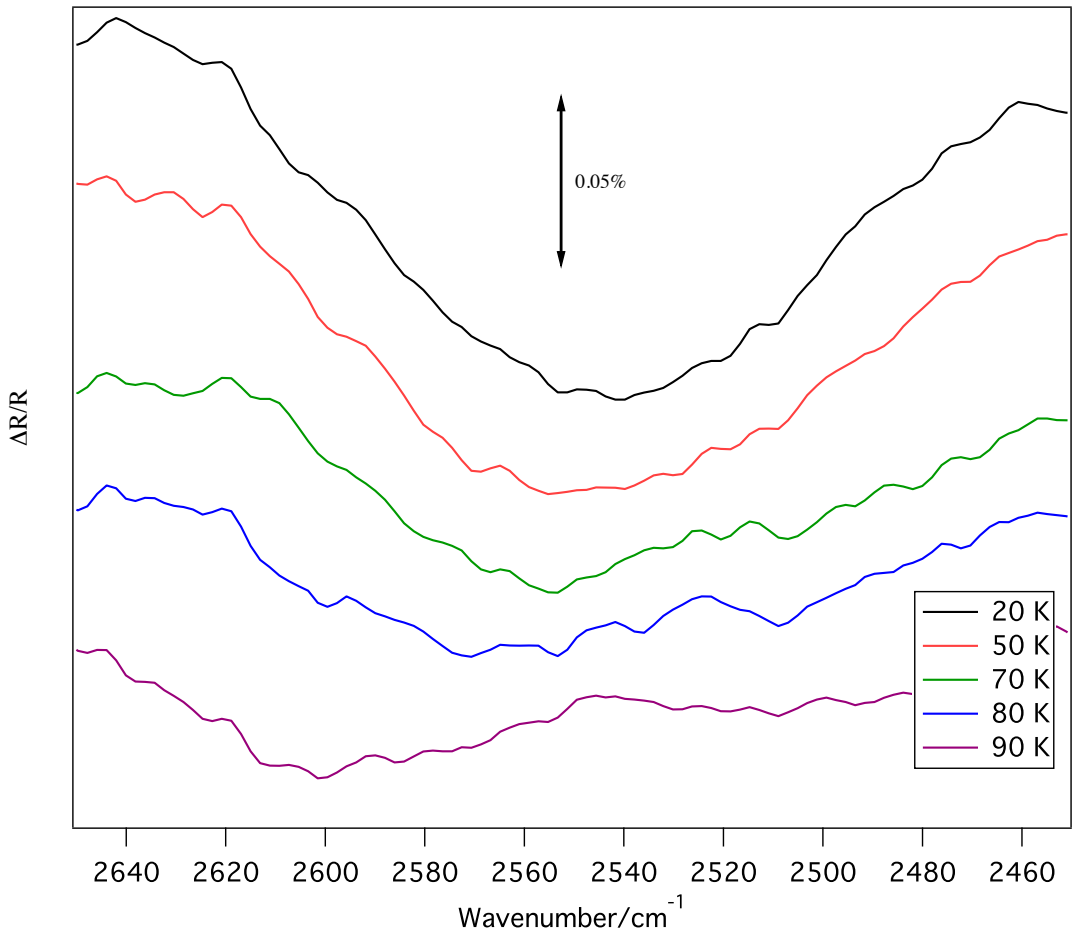

Figure 3.15. RAIR spectra of a 200 L 20/80% mixture of H_2S/H_2O. Temperature was changed from 20 to 90 K.

3.9 Astrophysical implications

The purpose of the quantitative analysis of the TPD results is ultimately to provide data for the modelling of astrophysical objects. Specifically, knowing the desorption energy, pre-exponential factor and the order of desorption for H_2S can be used to estimate when this species is desorbed from interstellar grains and becomes

available in the gas phase around a newly formed star. A thorough modelling of all the processes and of all the chemicals involved in the evolution of the environment surrounding a young stellar object is beyond the scope of this work. However, a simple model can be used to roughly estimate how H_2S desorbs in the proximity of an evolving star.

In the model the desorption process is described by the Polyani-Wigner equation:

$$r_{des} = -\frac{d\theta}{dt} = A\theta^n exp\left(-\frac{E_{des}}{RT}\right) \quad (2.9)$$

During the experiments a linear heating rate of 0.5 K/s is applied to the sample, but this is obviously very different from what happens in an astrophysical environment. Astronomical heating rates are not linear and the heating rates are considerably lower, of the order of a fraction of K per thousands of years. This is simulated in the model using the following heating rate:

$$\mathrm{T} = \mathrm{k} \times \mathrm{t}^{\mathrm{b}} \quad (2.10)$$

where k and b are parameters depending on the mass of the evolving star and t is the time in years [96]. The model describes the behaviour of a mixed H_2S/H_2O ice, the mixture in this case has been taken as 95% H_2O and 5% H_2S. The initial coverage is taken as 9.5×10^{21} molec m^{-2}. In the assumption that the density of the ice mixture is essentially equal to the density of ASW, this corresponds to an ice thickness of 0.3×10^{-6} m, comparable to the thickness of interstellar ice [97]. For the simulation of the H_2S desorption from the surface of the ice, the values of desorption energy, desorption order and pre-exponential factor for multilayer H_2S were used. However, the volcano desorption and water co-desorption of H_2S are processes driven by the change of phase and desorption of water. The values of desorption energy, pre-exponential factor and desorption order used to simulate the volcano desorption are the ones corresponding to amorphous ice desorption [98]. In the case of co-desorption, the values used were the ones corresponding to crystalline ice desorption, see for example [30]. The amount of H_2S that desorbs *via* surface desorption, volcano and co-desorption were determined using the data taken for the 15% H_2S/H_2O mixture (figure 3.9). The ratios of the areas under the H_2S curve corresponding to each mode of desorption were found to be 27% surface desorption, 62% volcano desorption and 11% co-desorption.

Figures 3.16 and 3.17 show the H_2S abundance in the gas phase is shown as a function of time for the case of a 5 solar masses and a 25 solar masses star. These two kinds of stars were chose as representatives of low mass and high mass stars. In both cases, the three kinds of desorption are clearly visible, the main difference between the two cases is the timescale. As expected, in the case of a high mass star the heating process is much faster and all the H_2S is desorbed in around 35000 years, while in the case of a low mass star the desorption continues up to 230000 years.

Figure 3.18 shows a comparison of the desorption of H_2S for the case of a high mass and a low mass star as a function of the temperature. In the case of the low mass star the desorption process takes place at slightly lower temperatures compared to the high mass star. However, due to the uncertainty on the pre-exponential factor, it is not possible to clearly separate low mass and high mass desorption at the temperatures corresponding to surface desorption.

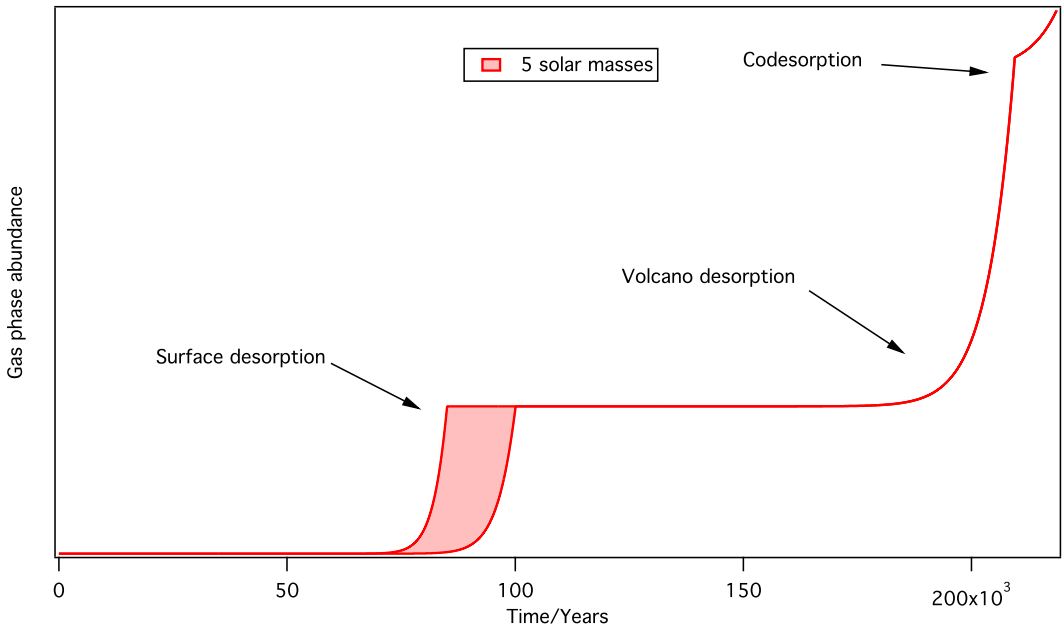

Figure 3.16. H_2S abundance in the surrounding of an evolving 5 solar masses star. Shaded area represent the effect of the uncertainty on H_2S pre-exponential factor.

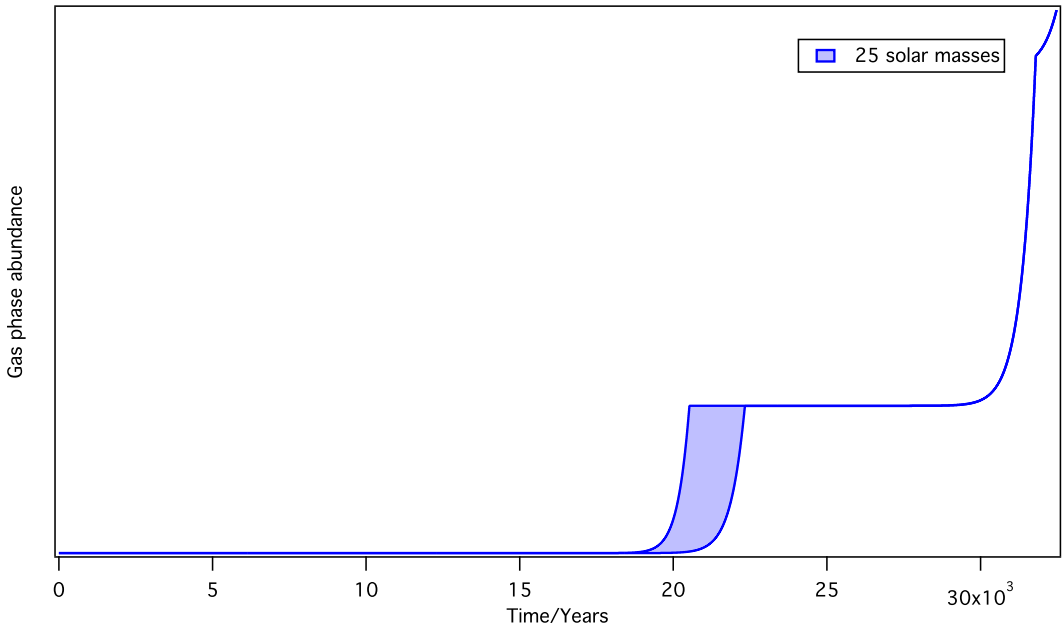

Figure 3.17. H_2S abundance in the surrounding of an evolving 25 solar masses star. Shaded area represent the effect of the uncertainty on H_2S pre-exponential factor.

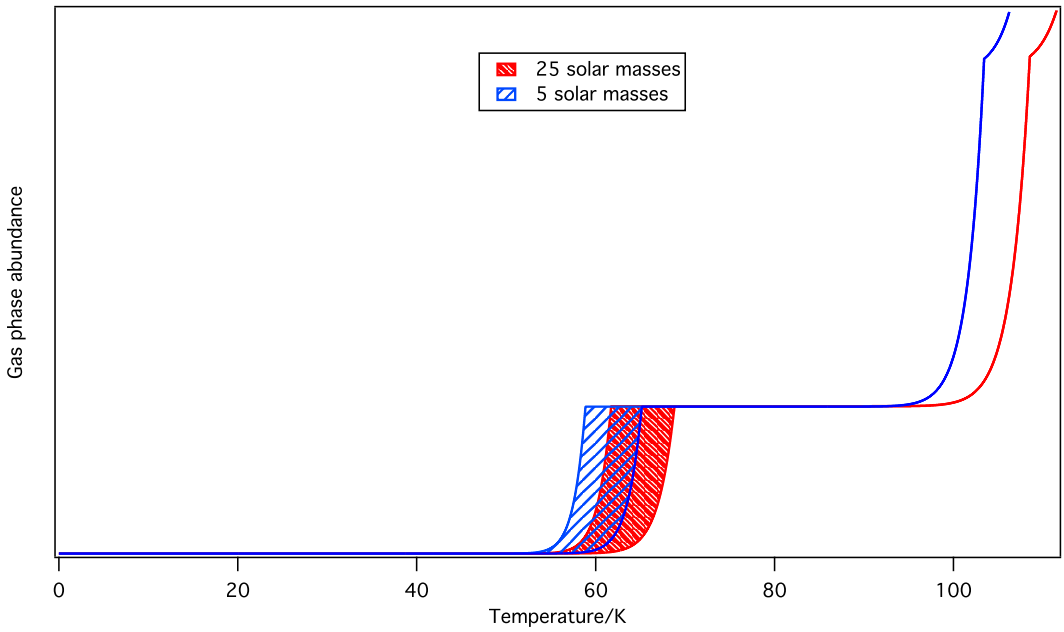

Figure 3.18. H_2S abundance in the surrounding of an evolving star as a function of the temperature. The two curves show the case of a 5 solar masses star and the case of a 25 solar masses star. Shaded area represent the effect of the uncertainty on H_2S pre-exponential factor.

3.10 Final remarks

In summary, the adsorption and desorption of H_2S from HOPG, from the surface of ASW and in a mixture with water were studied *via* TPD and RAIRS.

The TPD study has highlighted the difference between monolayer and multilayer desorption. It showed that sub/monolayers of H_2S desorb around a temperature of 80 K

and they possess a desorption energy of 19±3 kJ/mol, while multilayers of H_2S desorb at higher temperatures depending on the dosage and their desorption energy is 22±1 kJ/mol. Furthermore, the quantitative study of the TPD curves allowed the derivation of the pre-exponential factors for both monolayer and multilayer regime, respectively $1 \times 10^{14\pm1.6}\ (molec \cdot m^{-2})^{0.1} s^{-1}$ and $5 \times 10^{27\pm0.6}\ (molec \cdot m^{-2})^{0.94} s^{-1}$. The study of H_2S desorption from the surface of water and from H_2S/H_2O mixtures showed that H_2S desorbs in these configuration in three modalities: at low temperatures (80-90 K), because of volcano desorption when the ASW to CI phase change takes place (140 K) and in co-desorption with water at around 150 K.

The values of desorption energy and pre-exponential factor for multilayer desorption were then used to simulate the desorption of a H_2S/H_2O mixture under astronomical conditions.

The RAIR study showed the characteristic vibrational bands that H_2S exhibits when adsorbed on HOPG, ASW or when it is in a mixture with water. Pure, amorphous H_2S has been found to have a bulk vibrational band at 2535 cm^{-1} that evolves into two separate bands upon thermal annealing of the ice. The bands corresponding to symmetric and asymmetric stretches of the molecules appear at 2551 and 2526 cm^{-1}. A faint band, assigned to the bending mode, has been found in crystalline H_2S at 1169 cm^{-1}. The study of the IR spectrum of H_2S adsorbed on water did not show substantial differences compared to the spectrum of pure H_2S. The RAIR study of H_2S embedded in water showed instead that the band corresponding to the amorphous H_2S stretch was much broader than in the previous cases. No evidence of crystallization upon annealing was shown when the H_2S was embedded in water. Complete desorption of H_2S from the mixture seemed to take place, however, as discussed, this could effectively be due to the faintness of the H_2S signal in the H_2S/H_2O mixture.

4 TPD of $C_2H_4O_2$ bearing ices

The majority of the gas-phase molecules that have been detected in the interstellar medium are located in hot molecular cores (HMC). HMC are the birth sites of high (> 6 $M_\odot$[6]) mass stars and they are dense, compact and dusty regions with temperatures exceeding ~100 K [99]. Among all the species detected so far, particular attention has been paid to the formation of different isomers such as C_2H_4O (acetaldehyde, ethylene oxide, vinyl alcohol) and $C_2H_4O_2$ (glycolaldehyde, acetic acid, methyl formate, figure 4.1). Understanding their formation can provide insight into the physical and chemical evolution of the clouds and molecular cores, and about how complex molecules are formed [65,100]. There is strong evidence that the formation of complex organic molecules is linked to the evolution of chemical networks on icy grains [6]. Therefore understanding the physical behaviour of these species in their solid phase, both in the absence and in the presence of water, is of primary importance. This work focuses on the study of the adsorption and desorption of the $C_2H_4O_2$ isomers (figure 4.1) [65,101].

Acetic acid (CH_3COOH) is considered to be a molecule of astrobiological importance, acting as a precursor to the amino acid glycine (NH_2CH_2COOH) [101]. Acetic acid was first detected in 1997 in the hot molecular core Sgr B2(N-LMH) by Mehringer *et al.* [102]. Since then it has also been observed in a variety of other objects: other hot molecular cores [101], around low mass protostars [103], towards the proto-planetary nebula CRL 618 [104] and in the Murchinson meteorite [105].

Methyl formate ($HCOOCH_3$) was first detected in the hot molecular core Sgr B2(N)-LMH in 1975 by Brown *et al.* [106], but it has also been observed in low mass regions [103], in several galactic centre molecular clouds [107] and in the proto-planetary nebula CRL 618 [104]. Methyl formate seems to be fairly ubiquitous throughout the interstellar medium.

[6] $M_\odot$ = solar mass

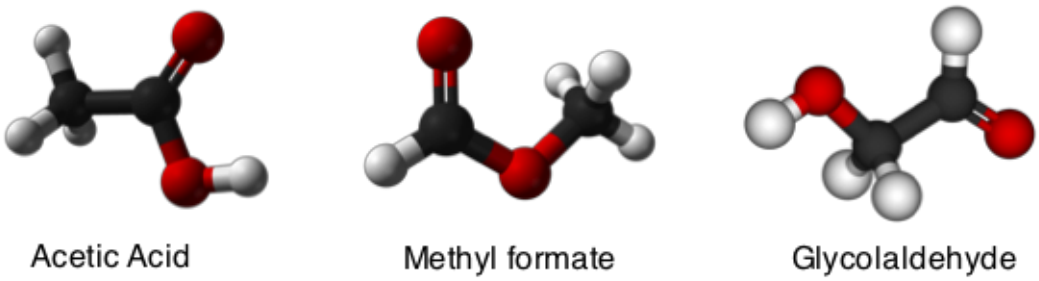

Figure 4.1. Three different $C_2H_4O_2$ molecules detected in the interstellar medium.

Glycolaldehyde ($HCOCH_2OH$) is a hydroxyaldehyde diose[7] and it is considered the simplest form of sugar. Glycolaldehyde could also be involved in the production of other important biomolecules, such as glycolaldehyde phosphate, amino acids and more complex monosaccharides like ribose, which is part of the structural backbone of RNA [108–110]. It is evident that glycolaldehyde could hold a great relevance as far as prebiotic chemistry in space is concerned. Glycolaldehyde was first identified by Hollis *et al.* (2000) [65] in Sgr B2 (N)-LMH and more recently has been detected towards a star forming region and hot molecular core, G31.41+0.31 [111].

Sgr B2 (N)-LMH is at the moment the only source where all three isomers have been positively detected. The relative abundances of the isomers and their spatial distribution inside LMH were reported by Hollis *et al.* (2001) [112]. Even though glycolaldehyde, methyl formate and acetic acid share a very similar atomic structure and identical composition, they show very different abundances (52:2:1, methyl formate: acetic acid: glycolaldehyde) and different spatial distributions. While methyl formate and acetic acid are confined inside LMH, glycolaldehyde extends far outside of it. It has been suggested that the conditions inside LMH favour glycolaldehyde destruction[8] and its survival outside of it [112]. Some authors have also speculated that isomerization could be an important factor in establishing the observed abundances and spatial distribution of the molecules [113]. However, the exact nature of the chemical reactions involved is not very well known.

The mechanism of formation of these molecules is still not completely clear, although it is becoming increasingly clear that the site of formation of large complex organic molecules is the icy surface of astronomical dust [114,115]. Chemical models that attempted to reproduce the abundances of these isomers based only on gas phase

[7] A monosaccharide formed by only two carbon atoms
[8] The authors speculate that this is due to the conditions of LMH favoring glycolaldehyde gas-phase chemistry over its isomers'.

chemical pathways failed by orders of magnitude [100]. In a recent work, Woods *et al.* (2012) and (2013) [116,117] modelled several chemical pathways and determined that some grain chemical networks could produce sufficient glycolaldehyde to match the observational estimates. Other encouraging experimental results showed that it is possible for both methyl formate and glycolaldehyde to be formed by electron irradiation of interstellar ices containing methanol and carbon dioxide [100] and acetic acid can be produced in mixtures of methane and carbon dioxide [118]. Methyl formate has also been shown to form in icy mixtures of methanol and carbon monoxide after irradiation by energetic protons [28].

Both theoretical and experimental work seems to point towards the icy origin of complex molecular organics in general and of the $C_2H_4O_2$ isomeric group in particular. A thorough understanding of the adsorption and desorption of these isomers on dust grains is therefore necessary to reproduce the chemistry that leads to their formation. These, in turn, could shed further light on the physical and chemical evolution of hot cores. For this reason, this work focused on the study of the adsorption and desorption of acetic acid, methyl formate and glycolaldehyde on a dust grain analogue (HOPG) and on/in amorphous solid water (ASW). This study was carried out in an ultra high vacuum (UHV) environment *via* TPD and RAIRS.

Experimental and theoretical studies on $C_2H_4O_2$ isomers are available in the literature. Bertin *et al.* [119] performed a TPD and RAIRS study of acetic acid and methyl formate on crystalline and amorphous water ice. Their findings drew similar (differences will be highlighted) conclusions, as far as the desorption of these species is concerned, to those delineated in this study. However, they did not perform a full quantitative analysis of the TPD spectra. Bahr *et al.* and Allouche & Bahr studied the interaction of acetic acid with solid water, deposited on metals, *via* computational modelling (density functional theory), TPD, electron spectroscopy, UV photoelectron spectroscopy and Fourier transform infrared spectroscopy [120,121]. Their findings concerning the stability of acetic acid and acetic acid/water configurations will contribute to the interpretation of the results of the TPD study of acetic acid in the next section. The thermal desorption of methyl formate from metals like silver, nickel and copper has also been studied *via* RAIRS and TPD [122–124]. While these studies are useful to qualitatively interpret the desorption of methyl formate, they do not provide a quantitative analysis of its desorption. Studies involving gas phase glycolaldehyde are available due to its relevance in atmospheric chemistry [73,125], however studies

involving glycolaldehyde ices adsorption and desorption are generally missing. In particualr, quantitative TPD studies of glycolaldehyde ices are not currently available in the literature. The characterization of the IR spectrum of glycolaldehyde has been object of several studies, such as that by Hudson *et al.* [126]. IR spectroscopic studies of glycolaldehyde, in the vapour phase, as a crystalline solid and in solution have also been performed [127].

4.1 Experimental

All TPD experiments involving the $C_2H_4O_2$ isomers were performed in the UHV setup CH2 described in chapter 2. Research grade high purity acetic acid, methyl formate and glycolaldehyde were used (Sigma Aldrich). Acetic acid and methyl formate come in liquid form, making dosing their vapours into the chamber straightforward. The liquids were freeze-pump-thawed before each experimental session to get rid of unwanted gases trapped inside of them. Glycolaldehyde was pumped down to 10^{-3} mbar for at least 1 hour to remove all H_2O trapped inside of it. Glycolaldehyde exists as a dimeric solid at room temperature, therefore needs to be heated up to ~370 K in order

for the vapour pressure to increase enough for dosing. This was achieved by putting the glycolaldehyde inside a custom made metal container and then heating it *via* resistive filaments. The temperature was controlled *via* a K-type thermocouple located on the outside of the container. Once the doser had reached the desired temperature, it was maintained for at least 30 minutes in order for glycolaldehyde to sublimate. For the experiments involving water (layered systems and mixtures), triply distilled water was used. The water was also purified *via* multiple freeze-pump-thaw cycles in order to remove undesired gases trapped inside it.

Ices were grown *in situ* by backfilling the chamber through a high precision leak valve. All exposures are measured in Langmuirs, where 1 L = 10^{-6} mbar·s. All TPD spectra were recorded at a heating rate of 0.5 K/s. The TPD curves shown below only exhibit the signal related to the most intense ion signal recorded by the mass spectrometer for each species. These signals correspond to the following ionic fragments: $H_3C_2O^+$ ($m = 43$ a.m.u.) for the acetic acid, H_3CO^+ ($m = 31$ a.m.u.) for methyl formate and H_2COH^+ ($m = 31$ a.m.u.) for glycolaldehyde. Mass 60 a.m.u., corresponding to the unbroken molecule, was also monitored for all isomers. Its

behaviour is consistent with the behaviour of the main fragments, but the signal is much less intense compared to the main fragment signal.

The TPD of methyl formate and glycolaldehyde were collected by Dr Daren Burke. TPD data collection for acetic acid, along with the general interpretation of the data and the quantitative analysis of all of the data have been performed by the author of this work.

4.2 TPD of pure Acetic Acid ices

Figure 4.2 shows TPD spectra recorded for a range of exposures of pure acetic acid (AA) adsorbed on HOPG at 20 K. Exposures start from 1 L and go up to 50 L. Exposures lower than 1 L were not considered because the signal to noise ratio degrades quite rapidly.

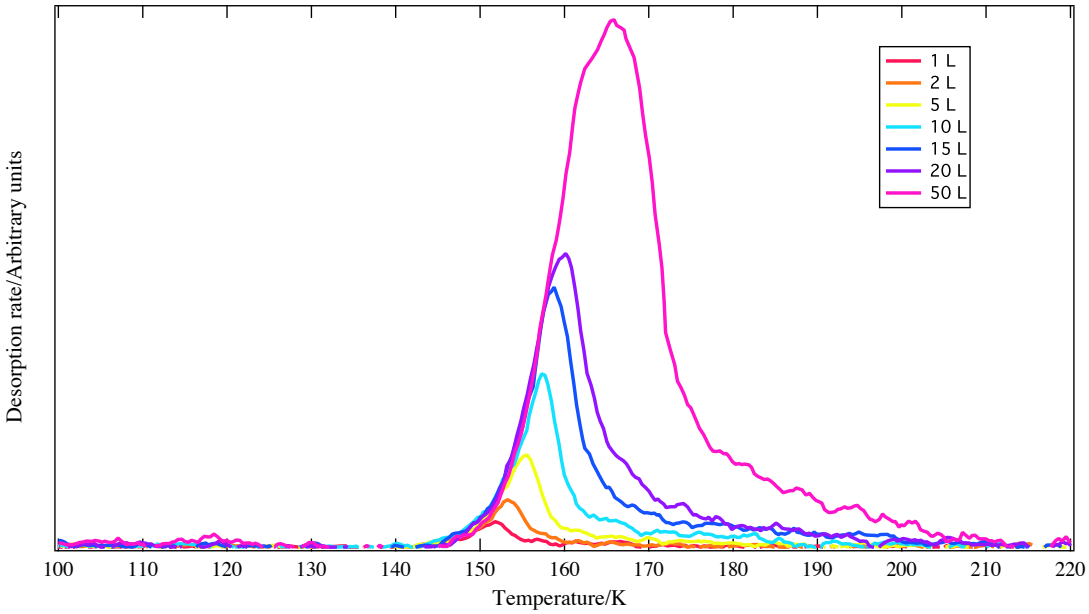

Figure 4.2. TPD spectra of CH_3COOH up to 50 L, adsorbed on a bare HOPG surface at 20 K.

On inspection, all curves seem to be sharing the leading edge and the peak temperature increases proportionally to the amount of acetic acid dosed. Specifically the peak temperature goes from ~152 K, for 1 L of exposure, to ~166 K for 50 L of exposure. Additionally, all the curves show asymmetric peak shapes; particularly at higher dosages. The shared leading edge, the proportionality of the peak temperature to the amount of acetic acid dosed and the asymmetric peak shapes are all characteristics of 0^{th} order desorption, which is associated with desorption of multi-layered systems (see chapters 2 and 3). The assignment of multi-layered desorption to all of the curves in figure 4.2 is confirmed in the quantitative analysis following in this section.

One would expect acetic acid to adsorb onto the HOPG surface and, when the first layer is complete, to begin the formation of multilayers. This does not seem to be happening in this case. Potential explanations for this are as follows: either sub-monolayer/monolayer formation is taking place, but it is not detected due to the poor signal to noise ratio below 1 L, or acetic acid prefers to bond with itself immediately, forming multi-layered islands on the sample.

In figure 4.3, a linear correlation between the amount of acetic acid dosed and the area under the TPD spectra is shown. This confirms that the deposition of acetic acid and the sticking coefficient are constant. The linear deposition curve does not saturate at high dosages, as is expected for multi-layered, physisorbed systems.

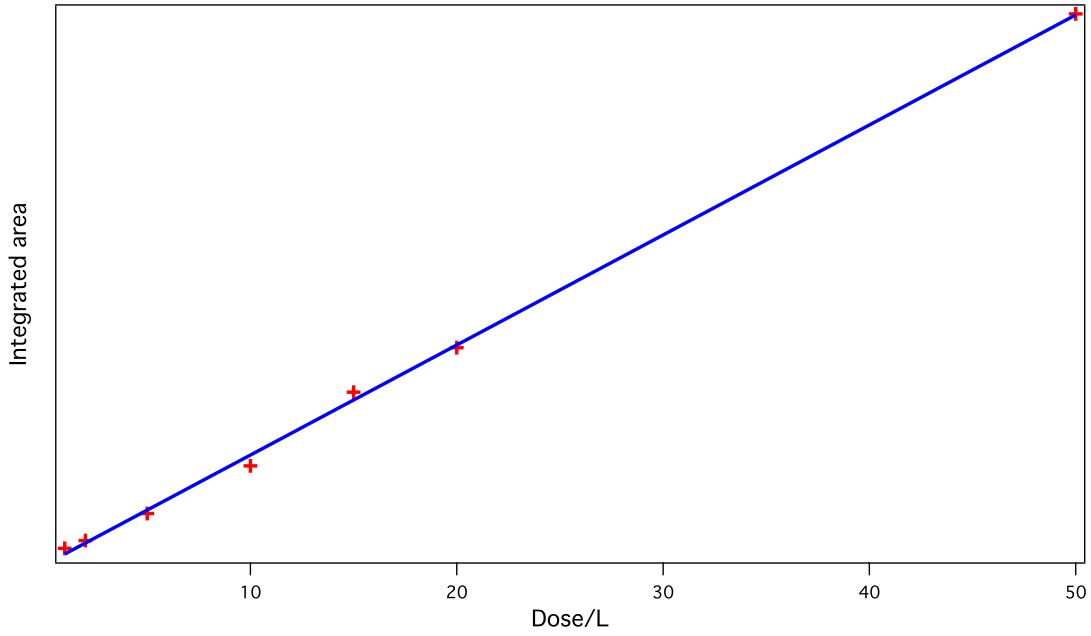

Figure 4.3. Integrated area of the TPD spectra shown in figure 4.2 as a function of CH_3COOH exposure. The blue line represents a linear fit to the data. Error bars are absent because errors on the integrated area are negligible.

4.2.1 Quantitative analysis of TPD data

A quantitative analysis of the TPD spectra is necessary to extract the kinetic information that is required to fully comprehend the dynamics of the acetic acid desorption and to create meaningful astrochemical models. The methods used in this section were theoretically described in chapter 2 and were applied to H_2S in chapter 3.

Desorption orders. The desorption order is determined from the gradient of a plot of ln I(T) against ln (θ_{rel}), where I(T) is the intensity recorded by the mass spectrometer at temperature T and θ_{rel} is the relative coverage at the temperature T,

using a set of TPD curves corresponding to different coverages (chapter 2, eq. 2.5). Considering that no differences between monolayer and multilayer regimes are visible from figure 4.2, all the curves were grouped together for the calculation of the desorption order. However, figure 4.2 shows that the amount of leading edge shared by the curves decreases with increasing dosage, and high dosages (from 10 to 50 L) share a consistent part of the leading edge at higher temperatures compared to the low dosages (from 1 to 10 L). For this reason the calculation of the desorption order has been performed over two ranges of temperatures: from 146.5 K to 148.5 K for all the curves, and from 153.0 K to 155.0 K for high coverages from 10 to 50 L. The results of the calculation of the desorption order for each temperature are shown in tables 4.1 and 4.2.

Temperature/K	Desorption order, n
146.5	0.0
147.0	0.0
147.5	0.1
148.0	0.1
148.5	0.2

Table 4.1. Calculated desorption orders for 1 to 50 L exposures of CH_3COOH, adsorbed on HOPG at 20 K.

Temperature/K	Desorption order, n
153.0	0.0
153.5	0.0
154.0	0.1
154.5	0.2
155.0	0.0

Table 4.2. Calculated desorption orders for 10 to 50 L exposures of CH_3COOH, adsorbed on HOPG at 20 K.

The overall average value of the desorption order (over all temperatures) is 0.07±0.03, where the error has been taken as the standard deviation of the mean. The essentially constant value of the desorption order over all the considered temperatures confirms that the TPD curves are characteristic of multilayer desorption [77].

Desorption energy. Knowing the desorption order, we can calculate the corresponding desorption energies by plotting $\ln I(T) - n\ln \theta_{rel}$ against $1/T$ and taking

the gradient as $-E_{des}/R$ (equation 2.6). Table 4.3 shows the results of the calculation for the desorption energies for each exposure.

The average desorption energy is 55 ± 2 kJ/mol, where the uncertainty has been calculated by propagating the uncertainties of the single desorption energies. No particular trend is evident in the desorption energies. This is consistent with multilayer desorption.

CH_3COOH exposure (L)	Desorption Energy (kJ mol^{-1})
1	56 ± 8
2	56 ± 7
5	53 ± 6
10	56 ± 3
15	54 ± 2
20	54 ± 2
50	55 ± 2

Table 4.3. Calculated desorption energies for multilayer CH_3COOH adsorbed on HOPG, at 20 K.

No previous values of the desorption energy of acetic acid from HOPG are available in the literature. However a certain number of TPD [119,120,128] and theoretical [121,128] studies of acetic acid adsorption and desorption from a water surface have been performed. TPD studies of acetic acid on water did not provide desorption energies for multi-layered desorption for two reasons. Firstly, the desorption of CH_3COOH from the water surface is complex and happens at temperatures comparable with the water desorption (*e.g.*, [119] and next section) therefore making it impossible to apply standard TPD analysis. Secondly, the aforementioned studies focused on the interactions of water and acetic acid and therefore only studied sub-monolayer desorption. However, some indication of the goodness of the energy derived in this study can still be inferred from the results of computational studies. Density functional theory (DFT) studies showed that acetic acid bonds to water with adsorption energies ranging from 38 kJ/mol, in the case of a single acetic acid molecule, to ~68 kJ/mol, in the case of the most likely acetic acid dimer configuration (cyclic dimer) [121,128]. The bonding with water happens *via* the sharing of a double hydrogen bond in any configuration, whether a single acetic acid molecule or a dimer is involved. In the case of acetic acid physisorbed onto HOPG, the bonding is due to van der Waals type

interactions, therefore it has to be weaker compared to the hydrogen bond. Hence, the adsorption energy of acetic acid on HOPG is most likely less than 38 kJ/mol. The desorption energy value obtained from the analysis of the multi-layer desorption, 55 kJ/mol, is even higher than some of the acetic acid/water configurations. This suggests that the bonding between acetic acid molecules is stronger than the simple van der Waals interaction with the HOPG. This supports the hypothesis that the lack of evidence of sub-monolayer desorption is due to the fact that acetic acid prefers to bond with itself compared to bonding with the HOPG surface. Allouche & Bahr [121] calculated also the cohesive energy of a series of acetic acid/water configurations, including monomers, dimers, trimers and hydrates and they all are in the range 55-56 kJ/mol, which is remarkably similar to the value of desorption energy found in this work. This is expected because both acetic acid/acetic acid and water/acetic acid share double hydrogen bonds. This similarity, and the fact that the value of desorption energy calculated in this work supports the lack of sub-monolayer desorption, suggests that 55 kJ/mol is a valid estimation of the multilayer desorption energy of acetic acid. The desorption energy of acetic acid multilayers is also comparable to that of ethanol (CH_3CH_2OH) [34] (56.3 kJ/mol), which is structurally similar to acetic acid.

The RAIR study of acetic acid adsorption on HOPG (next chapter) at 20 K showed that acetic acid adsorbs mostly as dimers. However, acetic acid polymers and monomers are also present at this temperature. Therefore it can be assumed that 55 kJ/mol is the energy associated with the desorption of a mixture of acetic acid dimers (mostly), polymers and monomers.

Pre-exponential factor. Once the desorption order and the desorption energy are know, the pre-exponential factor can be calculated. The procedure is described in chapter 2 and has already been used for H_2S in chapter 3. The impingement rate on the HOPG sample is calculated *via* equation 2.8 and is equal to 3.9×10^{14} molecules/L. The relationship between the area under the TPD curves and the actual CH_3COOH exposure is given by the slope of the fit line in figure 4.3. This is equal to 5.1×10^3 L^{-1}. The final scaling factor is therefore 7.7×10^{10} molecules.

The pre-exponential factors are calculated for a range of points on the leading edge of each TPD trace, rearranging the Polyani-Wigner equation to give an expression for ν_n. For consistency, the same ranges of points as in the calculation of the desorption energy have been chosen. The values obtained in this way are then averaged to obtain

the final ν_n for each TPD curve. The desorption order has been considered to be 0 and the desorption energy has been taken as 55 kJ/mol. Table 4.4 shows the results of these calculations. The uncertainties on the pre-exponential factors are obtained by varying the desorption energy within its uncertainty interval. The final multilayer desorption pre-exponential factor for CH_3COOH was found to be $8 \times 10^{33\pm2}$ molecules · m^{-2} s^{-1}.

CH_3COOH exposure/L	Pre-exponential factor /$(molec \cdot m^{-2})$ s^{-1}
1	$10^{33\pm2}$
2	$10^{33\pm1}$
5	$10^{32\pm2}$
10	$10^{32\pm2}$
15	$10^{33\pm1}$
20	$10^{32\pm1}$
50	$10^{33\pm1}$

Table 4.4. Calculated pre-exponential factor for multilayer CH_3COOH, adsorbed on HOPG at 20 K.

In the literature, pre-exponential factors for multilayer desorption are found to generally vary from 8×10^{25} molec m^{-2} s^{-1} for NH_3 [42] to 2×10^{32} molec m^{-2} s^{-1} for CH_3OH [34]. Molecules that exhibit strong intermolecular interactions, such as ethanol, have shown a multilayer pre-exponential factor higher than this interval ($2 \times 10^{37\pm2}$) [34]. The value of multilayer pre-exponential factor for acetic acid found in this work is quite high. This is another indication of the intensity of the acetic acid/acetic acid interaction.

4.3 TPD of CH_3COOH deposited on ASW

After the TPD of pure acetic acid on top of the HOPG sample, the TPD of acetic acid on top of a thick layer of amorphous solid water was investigated. Understanding the interactions of the molecule with water is important considering that, as mentioned before, water is the most abundant ice in the ISM.

Figure 4.4 shows the TPD curves of CH_3COOH deposited on top of 50 L of H_2O ice. For reference, the scaled TPD curve of water (mass 18) is also shown (dashed trace). 50 L of background-dosed water guarantees a complete coverage of the sample in the experimental setup CH2.

At first glance, several striking features are immediately apparent. Firstly, even though acetic acid has been deposited on top of H_2O, for high dosages above 15 L it desorbs from the sample at higher temperatures than water does. Dosages in the range 20-50 L desorb from the surface at temperatures around ~168 K, while water desorbs completely before ~160 K. Secondly, while the desorption from the HOPG sample could be described simply in terms of multilayer desorption, this is not the case any more for desorption from the water surface. Three main peaks appear at different temperatures, depending on the amount of acetic acid dosed onto the water. This behaviour is consistent with what is observed in other experimental studies [119].

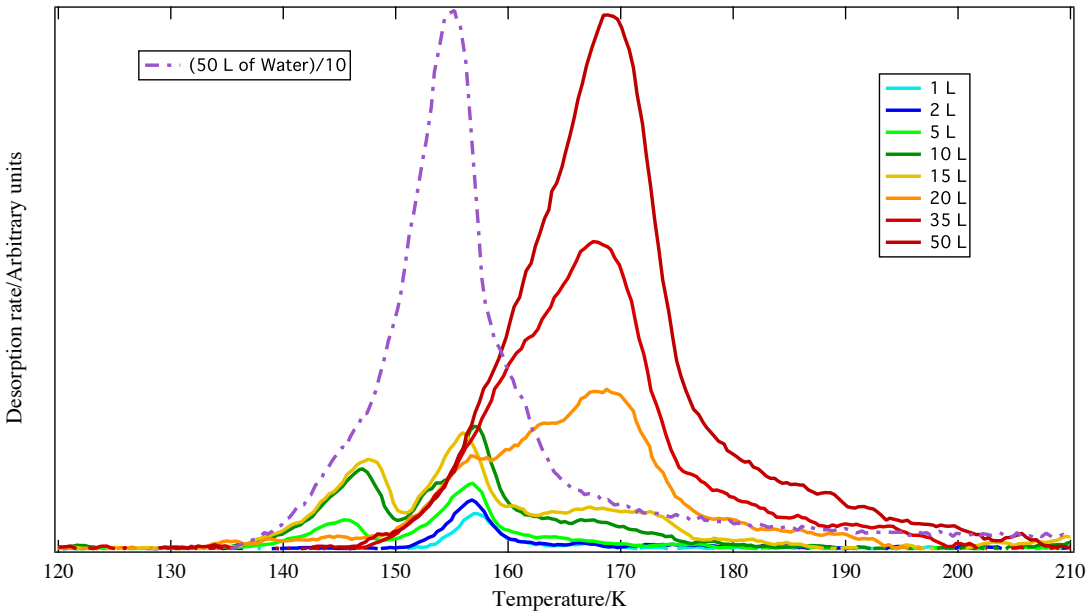

Figure 4.4. TPD spectra of low to high exposures of CH_3COOH on 50 L of pre-deposited H_2O ice on HOPG at 20 K. The dashed purple line shows the desorption of 50 L of H_2O corresponding to the 50 L CH_3COOH desorption. The trace has been scaled for ease of fit onto the graph.

It is well known that evaporating CH_3COOH liquid mostly produces, in the gas phase, cyclic acetic acid dimers formed *via* hydrogen bonding of the carboxylic groups of two CH_3COOH molecules [119,121]. It is predicted that when deposited on a water surface, these dimers form double hydrogen bonds with the surface with an adsorption energy in the same range as the cohesion energy of the ice itself [120]. The acetic acid multilayers forming afterward have also been shown to favour the cyclic dimer configuration. When the temperature increases, the thick acetic acid layer undergoes a phase transition from cyclic dimers to chainlike hydrogen bonded polymers [120,121,129]. This transition happens at temperatures comparable to the desorption temperature of water, allowing the underlying water to desorb almost freely. This explains why acetic acid deposited on top of water can desorb at higher temperatures

compared to water. The acetic acid phase transition was not visible in the TPD spectra in the case of pure acetic acid deposited on top of the HOPG (see section 3.2). However, it is clearly evident in RAIR studies performed on pure acetic acid ices (see next chapter).

In the case of pure acetic acid ice adsorbed on HOPG there was no evidence of further structure in the TPD spectra. The spectra only consisted of one main peak evolving as expected for multilayer desorption. However, the nature of the bond (hydrogen bond) of the acetic acid dimers with water is much more intense than the one between acetic acid and HOPG (van der Waals interaction). It is therefore reasonable that while acetic acid preferred bonding with itself when adsorbed on HOPG, it finds favourable bonding with water for low to medium dosages (up to 5 L). This begins to explain the reason for the drastic difference in the TPD spectra of acetic acid deposited on ASW, compared to the case of pure acetic acid ice.

In order to make the evolution of the peaks evident, the TPD curves of acetic acid have been divided into two graphs: figure 4.5 shows the low dosages, from 1 L to 15 L, while figure 4.6 shows the high dosages from 15 L to 50 L. TPD curves in these graphs are offset for clarity.

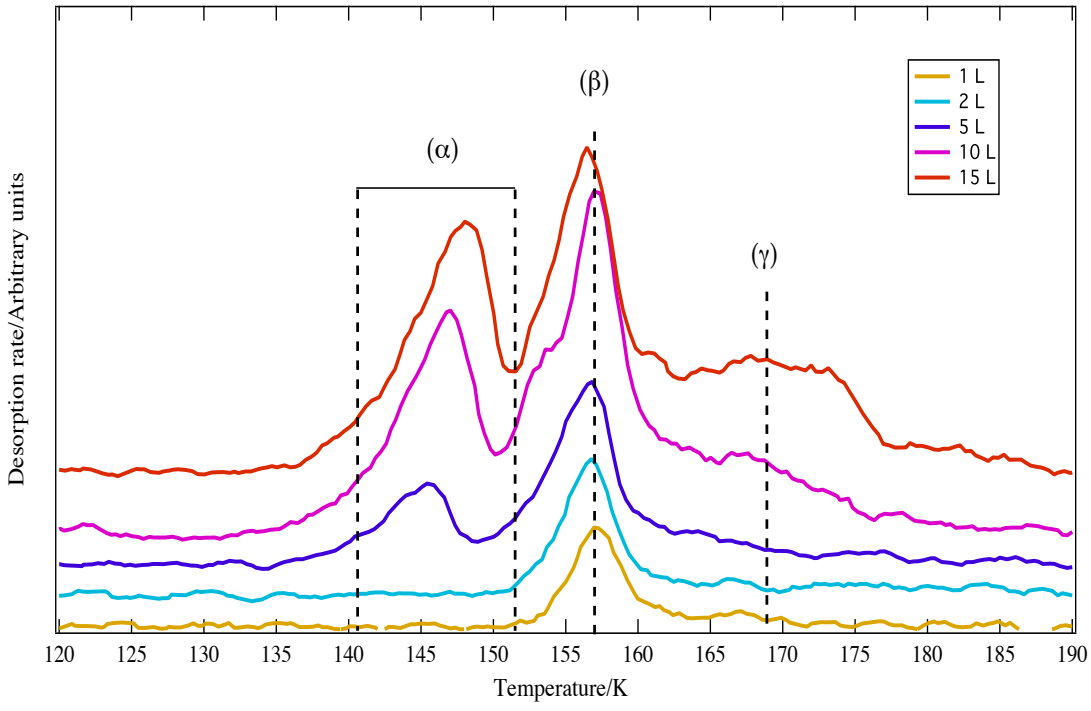

Figure 4.5. TPD spectra of low exposures of CH_3COOH on 50 L of pre-deposited H_2O ice on HOPG at 20 K. The curves are offset for clarity.

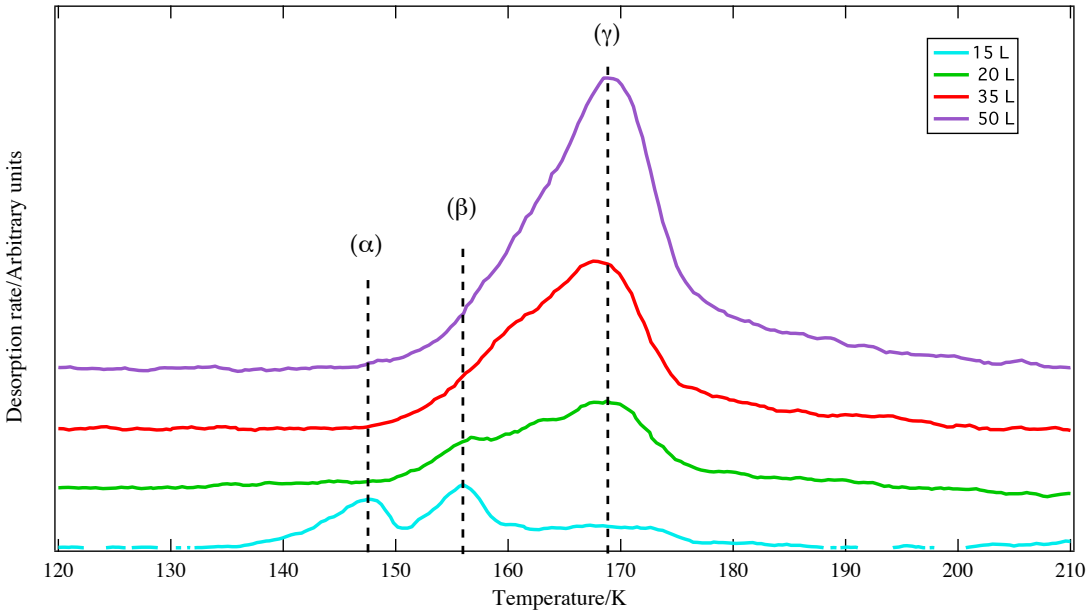

Figure 4.6. TPD spectra of high exposures of CH_3COOH on 50 L of pre-deposited H_2O ice on HOPG at 20 K. The curves are offset for clarity.

In figure 4.5, the evolution of the three features characterizing the desorption of acetic acid from water can be clearly appreciated. The first peak to appear is labelled β. At the lowest acetic acid exposures (≤ 2 L) it is the only peak in the spectrum. It appears and remains at around ~157 K from 1 L to 15 L of exposure. It then disappears or is absorbed by feature γ (figure 4.4 and 4.6). The fact that peak β is the only peak visible for low dosages and the fact that its peak temperature is constant seems to suggest that it is connected to sub-monolayer/monolayer desorption. However, peak β is clearly visible up to 20 L of dosages, which is a quite high dosage to be still producing monolayer desorption. This, and the appearance of the peak in correspondence with water desorption (figure 4.4), suggests that peak β could be related to co-desorption of acetic acid during water desorption. This would imply that, when dosed on top of ASW, part of the acetic acid strongly bonds to the porous surface of ASW and is embedded into it. ASW crystallization can contribute to "seal" this embedded acetic acid in the water matrix.

The second feature to become evident is labelled as α. It appears at lower temperatures compared to the other peaks, in the 145-147 K region, from 5 L to 15 L of exposure. It then disappears for higher exposures. The assignment of peak α is slightly more complex. A potential interpretation of peak α is that it is due to the desorption of acetic acid/water clusters desorbing from the surface of the ice. This is suggested by the

fact that peak α appears when water starts desorbing, at a temperature that is lower compared to the natural desorption temperature of acetic acid.

Finally, for high exposures from 15 L to 50 L the last peak (γ) appears around ~168 K. Peak γ is the dominant peak at higher temperature (above the water desorption temperature) and at higher dosages. Its peak temperature is also similar to the high dosage peak temperature for pure CH_3COOH ices. For these reasons, and considering that acetic acid crystallization occurs between 140-160 K, it is assigned to multilayer chain-like hydrogen bonded polymer desorption.

To summarize, at low dosages acetic acid strongly bonds directly to water and is somehow, due to the ASW porosity, to the ASW to CI transition or the sheer strength of the bonding, embedded into the water matrix. When water desorbs, this acetic acid desorbs producing peak β. When the amount of dosed acetic acid increases, the amount of acetic acid on the outer layer of the ice increases and, due to the strength of its interaction with water, it desorbs when the external layers of the ASW desorb (prior to the ASW to CI phase change). This creates peak α at medium dosages. When the dosed acetic acid increases, multilayers start forming and acetic acid crystallization can take place. This produces peak γ. The acetic acid on the external layers of ASW starts effectively interacting with itself, compared to water. This could explain why peak α disappears for high dosages (> 20 L).

The desorption of water (figure 4.4, dashed line) shows essentially two features: the ASW to CI phase transition around 148 K and the main desorption peak at around 155 K. The water curve in figure 4.4 was recorded during the desorption of a 50 L exposure of acetic acid. In this case a third feature in the water desorption is visible as a shoulder around 161 K. This feature becomes visible only for exposures ≥ 35 L (figure 4.7) and is assigned to desorption of water bonded to acetic acid. The stability of water/acetic acid hydrates has been computationally studied and it has been found that they can have cohesion energies around 57 kJ/mol [121], similar to the desorption energy of multilayer acetic acid.

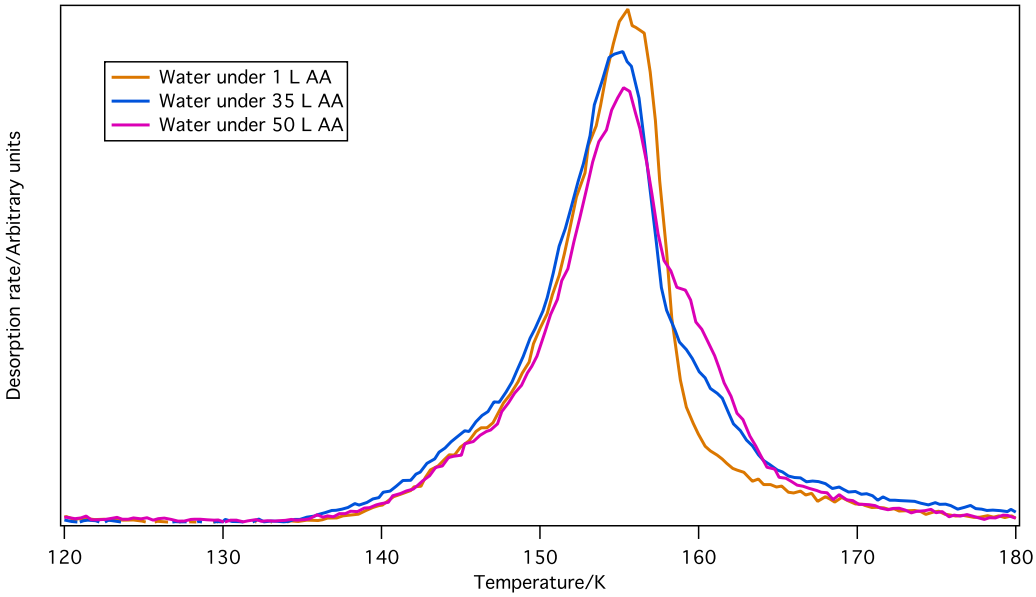

Figure 4.7. TPD curves of 50 L of water desorbing from under several dosages (1-50 L) of acetic acid.

4.4 TPD of CH_3COOH:H_2O mixtures

TPD spectra of acetic acid and water mixtures were also obtained. In figure 4.8 the TPD curves of CH_3COOH/H_2O mixtures (100 L) containing 12 % and 20 % of acetic acid are shown.

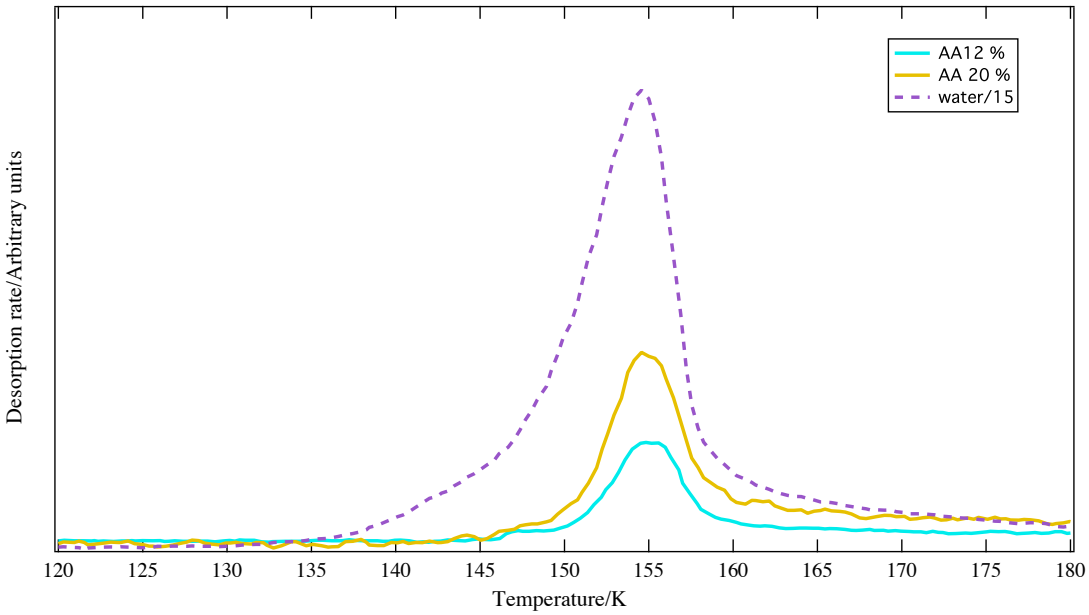

Figure 4.8. TPD spectra of 100 L of 12% and 20% CH_3COOH:H_2O mixtures, adsorbed on HOPG at 20 K. The percentage refers to the amount of acetic acid in the mixture. The TPD curve of 50 L of ASW has been scaled and included for comparison (dashed purple trace).

The desorption of acetic acid from the mixed ice is remarkably simple, especially if compared to the desorption of acetic acid from an ASW surface. Acetic acid desorbs simultaneously with water from ~145 to 160 K. The fact that all the acetic acid co-desorbs with water indicates that it is tightly bound to the ice matrix. Even during the transition from ASW to CI (~147 K) there is no evidence of acetic acid release in the form of volcano desorption, which is observed for a great range of molecules that are not strongly associated with water [30,40]. This is not unexpected. The comparative analysis of the TPD of pure acetic acid and acetic acid on top of ASW showed the strength of the interaction between acetic acid and water. When on top of water ice, acetic acid forms two hydrogen bonds with the water on the surface. It is therefore plausible that when embedded in the water, acetic acid is kept in the matrix by the same kind of bonds with the surrounding water molecules. Moreover, the surrounding water hinders acetic acid polymerization when the dimer-polymer phase transition temperature is reached. This explains the lack of acetic acid desorption at high temperatures around ~170 K. Firmly trapped in the water, with no substantial polymerization taking place, acetic acid desorbs only when water itself desorbs.

4.5 TPD of pure Methyl Formate ices

Figures 4.9, 4.10 and 4.11 show pure methyl formate desorption from an HOPG surface. The amounts of $HCOOCH_3$ dosed onto the sample vary from 0.3 L to 35 L. The curves were organized into three graphs to better display the different modes of methyl formate desorption.

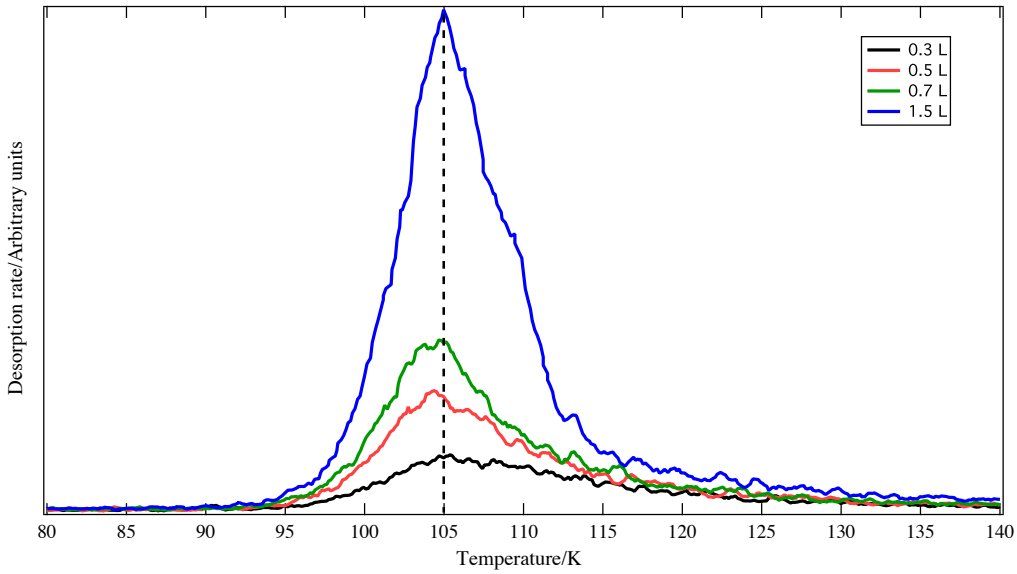

Figure 4.9. TPD spectra of low dosages of $HCOOCH_3$ up to 0.7 L, adsorbed on a bare HOPG surface at 20 K.

Figure 4.9 shows the desorption of methyl formate following exposures of 0.3 to 1.5 L. In this coverage range, methyl formate TPD curves peak at around 105 K. The position of the peak does not remarkably change depending on the amount of methyl formate dosed on the sample. The shape of the TPD peaks is slightly asymmetric. These characteristics indicate 1st order desorption, associated with the desorption of monolayer and sub-monolayer desorbing species, see for example, [35] and chapter 3 on H_2S desorption.

Figure 4.10 shows the desorption curves for 0.7 to 5 L of methyl formate. The behaviour displayed in this range of exposures is quite unexpected. Normally, one would expect the curves to simply show indications of multilayer desorption, *i.e.*, one single peak whose temperature increases as the dosage increases and a shared leading edge among the curves. However, this is not the case. In figure 4.10, it is evident that the shape of the peaks from 1.5 L to 5 L is the result of the superposition of two features, labelled α and β.

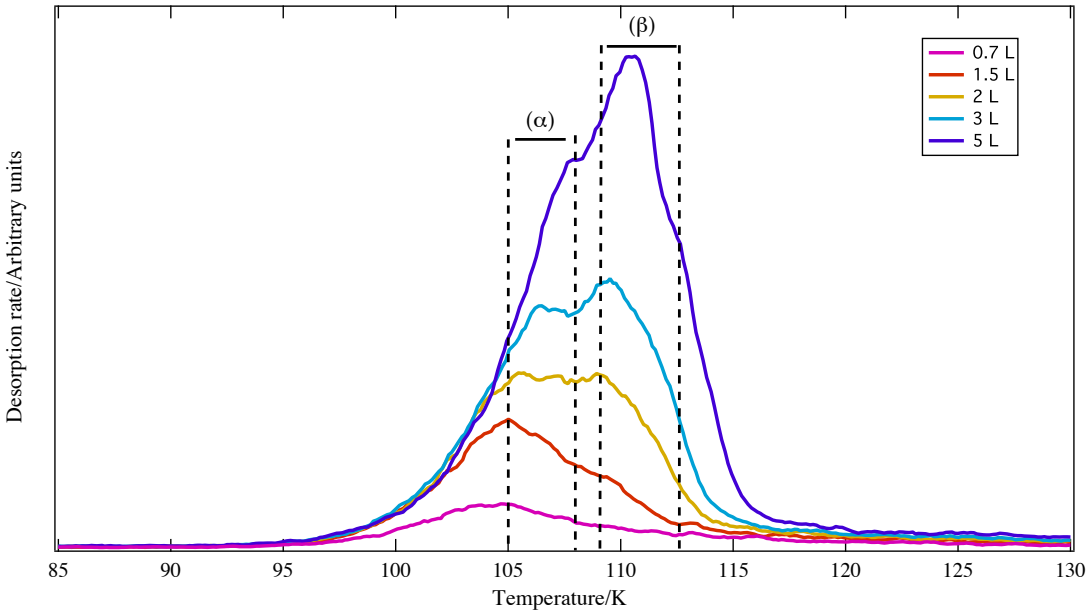

Figure 4.10. TPD spectra of medium dosages of $HCOOCH_3$ up to 5 L, adsorbed on a bare HOPG surface at 20 K.

At 1.5 L exposure, feature α is dominant, desorbing at ~105 K. Feature β starts being visible in the form of a slight shoulder at ~109 K. At 2 L exposure, feature β is as intense as feature α. Their peak temperatures are not easily distinguishable because the TPD curve has a broad shape. For a 3 L exposure, feature β becomes more intense than feature α. Both features peak positions move to higher temperature, ~106.5 K and 109.5 K, respectively for peak α and peak β. Finally, at 5 L, feature β becomes prominent

compared to peak α that has now almost merged into peak β. Again, both peak positions move to higher temperatures, ~108 K and 110.5 K, for peaks α and β respectively. The peaks in figure 4.10 show a common leading edge starting from 1.5 L and both α and β features exhibit a peak temperature dependence on methyl formate exposure. These are both indicators of multi-layer desorption [30], however the presence of 2 features instead of just one hints that a more complex form of desorption is occurring. In the existing literature, no evidence of this desorption behaviour for methyl formate is available. However, similar behaviour has been shown for the desorption of benzene from Cu [130]. In this case it was shown that benzene formed a metastable physisorbed state after ~2 layers have been deposited. The desorption of this metastable bilayer of benzene appears at a different temperature compared to the desorption of the bulk solid. The result of this is the co-existence of two desorption peaks above monolayer desorption. A similar behaviour, although with an even more complex peak configuration, was also reported for ethanol desorption from HOPG [34]. In the case of benzene on Cu, the reason for the formation of bilayers with different desorption energies compared to multilayers was assigned to a change in the adsorption geometry. In the case of ethanol desorbing from HOPG, the anomalous desorption was ascribed to the simultaneous formation of 2D (monolayers) and 3D (bilayers) clusters on the substrate prior to the formation of multilayers. From the similarities with benzene and ethanol desorption, feature α is assigned to the desorption of bilayers of methyl formate, while feature β is assigned to the desorption of multilayers of methyl formate.

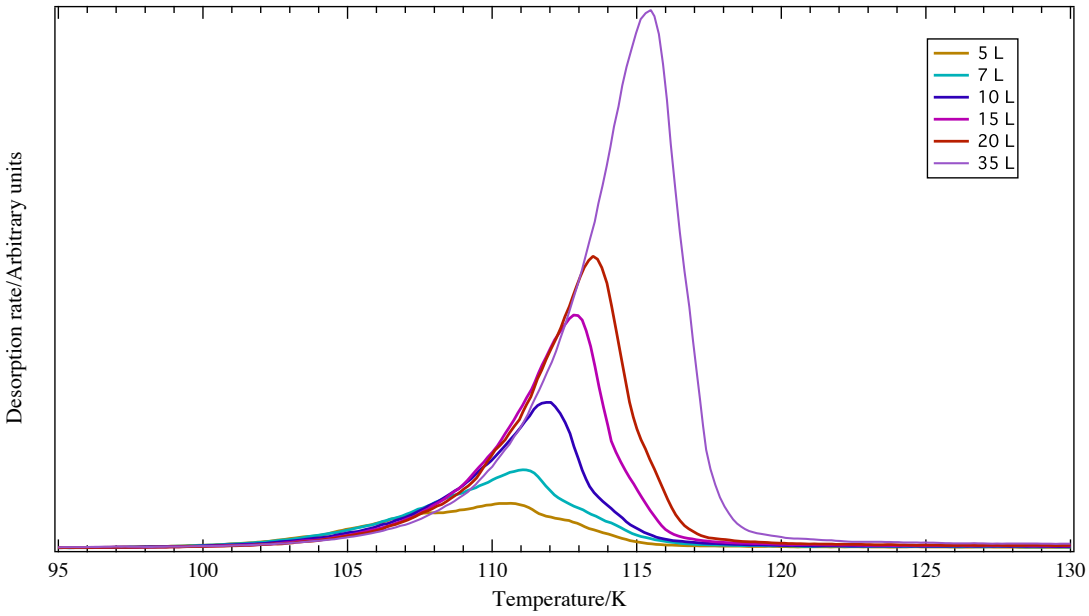

Figure 4.11. TPD spectra of high dosages of $HCOOCH_3$ up to 35 L, adsorbed on a bare HOPG surface at 20 K.

Figure 4.11 shows desorption curves from 5 to 35 L exposure of methyl formate. At high dosages (> 7 L), peak β is the only distinguishable feature. All curves have a shared leading edge and the peak temperature increases with the amount of methyl formate dosed, indicating multilayer desorption. This is consistent with the assignment of peak β to the desorption of multi-layered methyl formate at lower exposures.

In summary, the desorption of methyl formate seems to be happening in three modalities:

1. Monolayer desorption. Visible for low dosages (0.3-1.5 L), with a peak temperature around 105 K.
2. Bilayer desorption. Visible for intermediate dosages (1.5-5 L), with peak temperatures ranging from 105 to 108 K.
3. Multilayer desorption. Visible at intermediate and high dosages (2-20 L), with peak temperatures ranging from 109 to 113.5 K.

Figure 4.12 shows a linear correlation between the amount of methyl formate dosed and the area under the TPD curve. This shows that methyl formate uptake on the HOPG is constant throughout the dosing procedures.

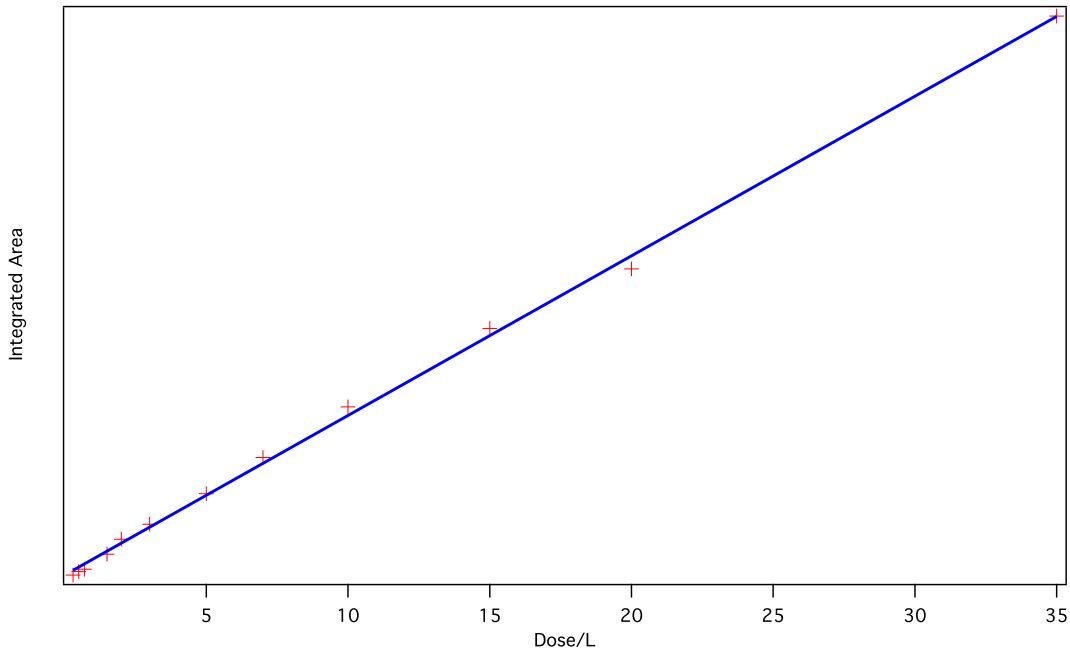

Figure 4.12. Integrated area of the TPD spectra shown in figures 4.9, 4.10 and 4.11, as a function of $HCOOCH_3$ exposure. The line represents a linear fit to the data. Error bars are absent because errors on the integrated area are considered negligible.

4.5.1 Quantitative analysis of TPD data

A quantitative analysis of the TPD curves has been performed to determine the characteristic kinetic parameters of methyl formate desorption from HOPG.

Desorption orders. For monolayer desorption, the curves representing desorption from 0.3 to 1.5 L of methyl formate have been considered (figure 4.9). Figure 4.10 shows that 1.5 L also possesses characteristics of multilayer (bi-layer) desorption, namely, shared leading edges with higher dosage curves. However, the determination of the monolayer desorption order showed that the inclusion of 1.5 L produced a value more in agreement with the expected theoretical value (1). The opposite was true when 1.5 L was included in the calculation for the multilayer desorption order. For this reason, 1.5 L was included in the calculations for monolayer desorption order.

The results for the calculation of the desorption order, for monolayer desorption, in the temperature range (100-103 K), are shown in table 4.5. The average desorption order for monolayer desorption of methyl formate from HOPG is 1.2 ± 0.1, where the error is taken as twice the standard deviation of the mean. This value of desorption order is marginally higher than the expected value for monolayer desorption, which is 1. This could be due to the contribution of bi-layers forming already at low dosages, since the formation of bilayers could potentially be considered a second order process.

Temperature/K	Desorption order, n
100.0	1.0
100.5	1.2
101.0	1.3
101.5	1.2
102.0	1.2
102.5	1.3
103.0	1.2

Table 4.5. Calculated desorption orders for 0.3 to 1.5 L exposures of CH_3COOH, adsorbed on HOPG at 20 K.

The same procedure was used for the calculation of multilayer desorption order using the TPD curves ranging from 5 to 20 L (figures 4.10 and 4.11). The range of temperature used was 107-110 K, where the curves show common leading edges. The results of the calculations of multilayer desorption orders are shown in table 4.6.

Temperature/K	Desorption order, n
107.0	0.2
107.5	0.1
108.0	0.1
108.5	0.0
109.0	0.1
109.5	0.1
110.0	0.2

Table 4.6. Calculated desorption orders for 5 to 35 L exposures of CH_3COOH, adsorbed on HOPG at 20 K.

The average desorption order for multilayer desorption of methyl formate from HOPG is 0.1 ± 0.1, where the uncertainty is was taken as twice the standard deviation of the mean.

The curves corresponding to 2 and 3 L desorption were not included in the final calculation of methyl formate multilayer desorption, even though they share part of their leading edge with higher dosage curves. This is due to the fact that, in the range of temperature of interest, the contribution of bilayers and multilayers distorts the shape of the curves creating plateaus (see figure 4.10). This affects the desorption order, although the final value of the multilayer desorption order including 2 L and 3 L is 0.2, which is still within the uncertainty associated with the final value.

Desorption energies. Table 4.7 shows the results of the calculations of the desorption energies for monolayer methyl formate.

$HCOOCH_3$ exposure (L)	Desorption Energy (kJ mol^{-1})
0.3	23 ± 1
0.5	29 ± 2
0.7	31 ± 1
1.5	33 ± 1

Table 4.7. Calculated desorption energies for monolayer $HCOOCH_3$ adsorbed on HOPG, at 20 K.

The average monolayer desorption energy is 29±5 kJ/mol, where the uncertainty has been calculated as twice the standard deviation of the mean. This choice is based on the fact that the uncertainty of the desorption energy associated with the fluctuation of

the desorption order within its uncertainty interval was considerably smaller (0.2 versus 5). The desorption energies for low exposures present a clear increasing trend. This is probably due to the increasing presence of bilayer structures accreting simultaneously with the monolayer structures. The overall effect is that the energy is moved to higher values that are characteristic of bilayer/multilayer desorption, which are shown in table 4.8.

Applying the same procedure for the exposures from 2 to 35 L, the desorption order for multilayer desorption has been calculated. The value of desorption order used was 0.1 for all exposures, including 2 L and 3 L that were not used for the actual calculation of the desorption order.

The results of the calculation of the desorption energy for exposure ranging from 2 to 35 L are shown in table 4.8. The average desorption energy is 35±5 kJ/mol, where the uncertainty is again taken as twice the standard deviation of the mean.

$HCOOCH_3$ exposure (L)	Desorption Energy (kJ mol^{-1})
2	34 ± 1
3	27 ± 1
5	26 ± 1
7	28 ± 1
10	35 ± 1
15	40 ± 1
20	41 ± 1
35	42 ± 1

Table 4.8. Calculated desorption energies for multilayer $HCOOCH_3$ adsorbed on HOPG at 20K.

The energies for the exposures ranging from 3 to 7 L appear to be markedly smaller compared to 2 L and to higher exposures (> 7 L). The reason for this is unclear. It could be due to the influence of the bilayer desorption on the multilayer desorption. However, this being the case, it would not be clear why this should act to lower the desorption energy, when it acted to increase it in the case of monolayer desorption. Moreover, the co-existence of bilayer and multilayer desorption is noticed also at 2 L exposure (figure 4.9), whose energy does not show anomalies.

Bertin *et al* [119] estimated the methyl formate multilayer desorption energy on ASW, under the assumption of n = 0, to be 37 ± 4 kJ/mol. This value is remarkably similar to the one obtained in the present work.

Pre-exponential factors. Once the desorption order and the desorption energy are known, the pre-exponential factor can be calculated. The impingement rate on the HOPG sample is calculated *via* equation 2.8 and is equal to 3.9×10^{14} molecules/L. The relationship between the area under the TPD curves and the actual $HCOOCH_3$ exposure is given by the slope of the fit line in figure 4.12. This is equal to 1.8×10^{4} L^{-1}. The final scaling factor is 2.1×10^{10} molecules. The calculation of the pre-exponential factors has been performed with the same method previously described for H_2S (chapter 3) and for acetic acid (section 4.2.1).

The pre-exponential factor calculations for monolayer and multilayer desorption are shown in table 4.9 and 4.10. The average values of the desorption order and desorption energy, for monolayer and multilayer desorption, have been used.

$HCOOCH_3$ exposure/L	Pre-exponential factor /$(molec \cdot m^{-2})^{-0.8} s^{-1}$
0.3	$10^{11\pm2}$
0.5	$10^{12\pm2}$
0.7	$10^{12\pm2}$
1.5	$10^{13\pm2}$

Table 4.9. Calculated pre-exponential factors for monolayer $HCOOCH_3$ adsorbed on HOPG at 20 K, for n = 1.2 and E_{des}= 29 kJ/mol

$HCOOCH_3$ exposure/L	Pre-exponential factor /$(molec \cdot m^{-2})^{0.9} s^{-1}$
2	$10^{29\pm1}$
3	$10^{25\pm1}$
5	$10^{25\pm1}$
7	$10^{26\pm1}$
10	$10^{29\pm1}$
15	$10^{32\pm1}$
20	$10^{32\pm1}$
35	$10^{32\pm1}$

Table 4.10. Calculated pre-exponential factor for multilayer $HCOOCH_3$, adsorbed on HOPG at 20 K, for n = 0.1 and E_{des}=35 kJ/mol.

The final monolayer and multilayer pre-exponential factors were found to be $10^{12\pm2}$ $(molec \cdot m^{-2})^{-0.2} s^{-1}$ and $1 \times 10^{29\pm3}$ $(molec \cdot m^{-2})^{0.9} s^{-1}$. Units are given as $(molec \cdot m^{-2})^{1-n} s^{-1}$. In the literature, values for monolayer pre-exponential factors are found to vary in the 10^{12}-10^{13} s^{-1} range [89], while the values for multilayer pre-exponential factor are in the range 10^{25}–10^{32} molecules m^{-2} s^{-1} [34,42]. Both the values found in this work fall into the expected intervals.

4.6 TPD of $HCOOCH_3$ deposited on ASW

Figure 4.13 shows the TPD spectra of a range of exposures, from 1 L to 20 L, of methyl formate adsorbed on ASW, at 20 K. The scaled TPD curve of water is shown in the bottom of the figure as a comparison.

As was the case for acetic acid, the desorption of methyl formate from ASW is complex and shows several contributions depending on the amount of adsorbate on the water substrate. Compared to methyl formate desorption from HOPG, methyl formate desorption from ASW immediately shows two extra features, γ and ϵ, associated with water driven desorption.

Feature δ occurs simultaneously with the ASW to CI phase transition, as is shown by the water TPD curve at the bottom of figure 4.12. Therefore peak δ is assigned to volcano desorption of methyl formate trapped inside the water matrix. This behaviour is observed for a variety of astrophysically relevant molecules [30,40], however it is still

remarkable that a molecule the size of methyl formate can desorb through the ice during water crystallization.

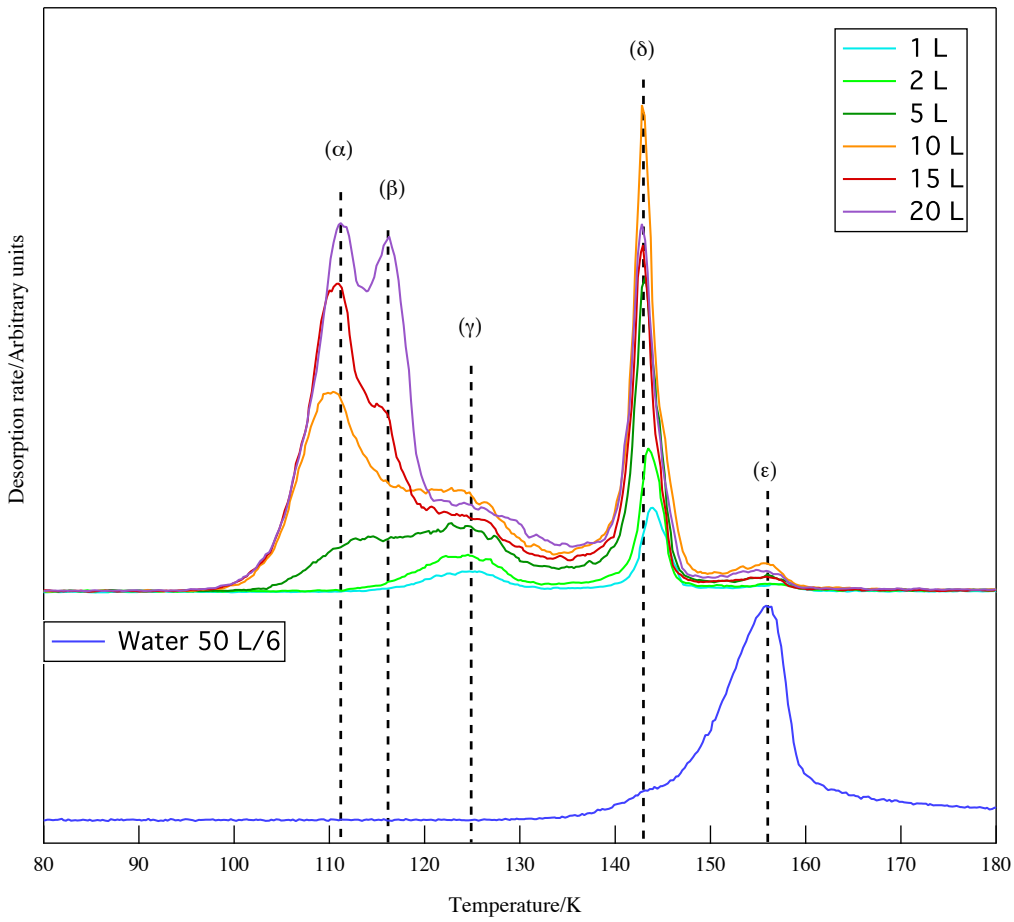

Figure 4.13. TPD spectra of 1 to 20 L exposures of $HCOOCH_3$ on 50 L of pre-deposited H_2O ice on HOPG at 20 K. The scaled TPD of 50 L of ASW is shown for comparison.

A small bump, feature ϵ is also visible in the methyl formate spectra, mostly for higher dosages (≥ 10 L), in the range 150-160 K. This is assigned to co-desorption of water and methyl formate.

At exposures from 1 to 2 L, 2 main desorption features are visible: one at 125 K (γ) and the other at ~143 K (δ). At 2 L, a new peak starts appearing at 111 K (α) which then increases constantly up to 20 L. Finally, from 15 to 20 L, a fourth peak appears around 116 K (β).

The position of peak γ does not change noticeably when the dosage is increased. Its intensity increases up to 5 L, then the contributions from features α and β tend to influence the shape of peak γ. It becomes, therefore, more complicated to clearly understand the behaviour of peak γ for dosages higher than 5 L. Apparently, feature γ tends to increase up to 10 L exposure and then seemingly saturates for higher exposures. Considering that this feature is the first to appear (together with the ones associated with

water desorption), it seems natural to assign it to the desorption of sub/monolayer methyl formate from the upper layers of the ASW. The desorption temperature of pure monolayer methyl formate from HOPG is 105 K. The peak temperature of feature γ is however much higher, 125 K. This is an indication that the bonding between methyl formate and water is stronger than the bonding between methyl formate and HOPG. This is not entirely surprising, because methyl formate could potentially hydrogen bond with water *via* the oxygen in the aldehyde group. Also, acetic acid showed the same kind of enhanced bonding strength with water compared to HOPG. The fact that feature γ saturates at higher dosages is also consistent with it being due to a sub/monolayer desorption.

Features α and β are both assigned to the desorption of multi-layered methyl formate. Comparing figure 4.13 to figure 4.10 displaying the desorption of pure methyl formate from HOPG), one can notice that the behaviour of features α and β in figure 4.13 is analogous to the behaviour of features α and β in figure 4.10. Therefore, feature α is assigned to the desorption of bi-layers of methyl formate, while feature β is assigned to the desorption of multi-layers of methyl formate.

The assignments of peak α to δ are in agreement with the only TPD study of methyl formate desorption from ASW, Bertin *et al.* [119]. However, in their study Bertin *et al.* did not explicitly assigned peak β to bilayer desorption. They simply assigned it to multilayer desorption.

For dosages higher than 20 L (figure 4.14), peak β (multilayer desorption) becomes prominent with respect to the other features. This is consistent with the assignment of peak β to multilayer desorption of methyl formate.

The intensity of feature γ seems to be higher for 10 L exposure compared to 15 and 20 L. This could be due to a direct influence of feature α (up to 15 L) and/or feature β (at 20 L) extending into the temperature range characteristic of γ. Alternatively, for high exposures the formation of multilayers is slightly favoured compared to the formation of sub/monolayer structures. This could be the case since a similar behaviour can be seen for feature δ. At 10 L, the peak for volcano desorption is higher than the respective peak for 15 and 20 L exposures. If the interaction between methyl formate molecules becomes dominant, compared to the methyl formate/water interaction, after a high enough dosage is reached the amount of methyl formate trapped in the water will tend to decrease. This is to be distinguished from the simple case of saturation of the water matrix (or the superficial layers of it) with methyl formate. This would appear as

a saturation of the volcano peak, *i.e.*, the volcano peak would remain constant after a high enough dosage has been reached.

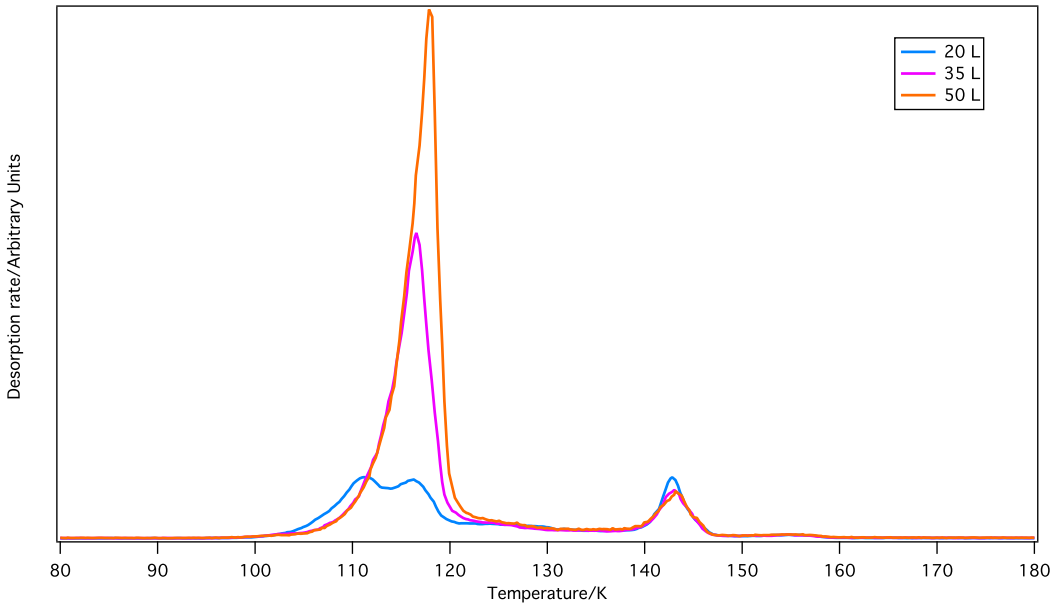

Figure 4.14. TPD spectra of 20 to 50 L exposures of $HCOOCH_3$ on 50 L of pre-deposited H_2O ice on HOPG at 20 K.

4.7 TPD of $HCOOCH_3$:H_2O mixtures

Figure 4.15 shows the TPD spectra of methyl formate desorbing from $HCOOCH_3/H_2O$ mixtures. Mixtures ranging from 10% to 30% of methyl formate in water are shown. The overall amount of species dosed (ice thickness) is 50 L. The curve corresponding to the TPD of water is also shown, scaled by a factor of 2.

The majority of the methyl formate desorbs during the ASW to CI phase change, as volcano desorption. The peak temperature of the volcano feature moves to lower temperatures when the percentage of methyl formate in the ice increases, from 147.3 K for a 10 % mixture to 146.0 K for a 30 % mixture. A potential explanation for this phenomenon is that when the amount of methyl formate in the mixture increases, the amount of it being close to the boundaries of the ice increases as well. This "peripheral" methyl formate desorbs more easily (lower temperature) and therefore shifts the peak temperature of the volcano peak to lower temperatures.

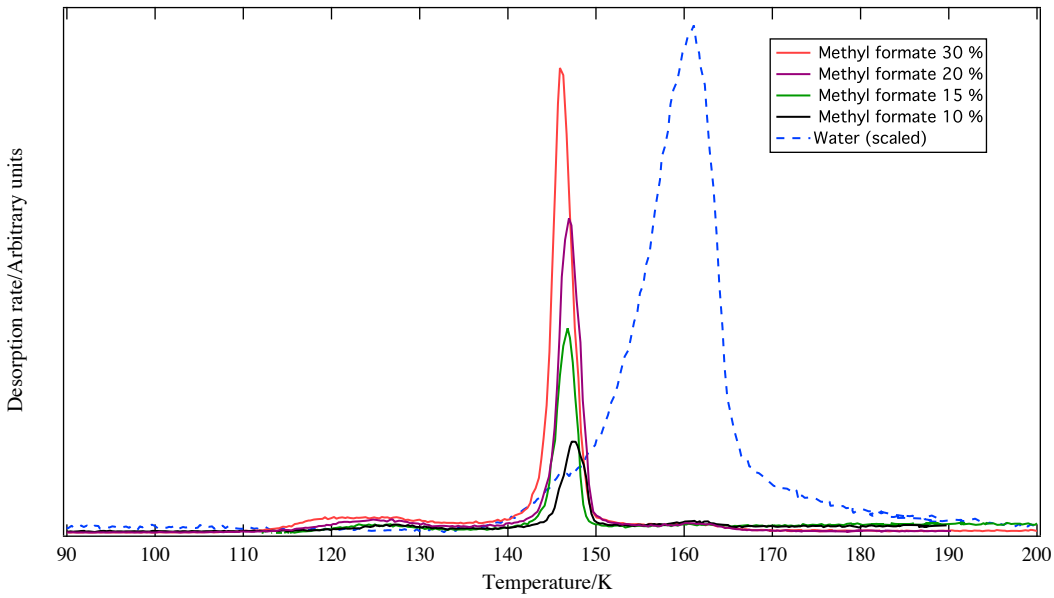

Figure 4.15. TPD spectra of 50 L of 10 %, 15 %, 20 % and 30 % $HCOOCH_3$:H_2O mixtures adsorbed on HOPG at 20 K. The percentage refers to the amount of methyl formate in the mixture. The dashed curve shows the scaled TPD desorption of water.

A small bump in the region between 120 K and 130 K indicates the desorption of sub/monolayer methyl formate from the surface layers (surface desorption) of ASW. This assignment is based on the similarity of this feature with feature γ observed in the case of methyl formate deposited on top of ASW.

Another very weak feature is visible at ~160 K. This feature appears in correspondence with water desorption. It is therefore assigned to co-desorption of methyl formate with water.

Figure 4.16 shows the percentile amount of desorbed methyl formate, for each desorption mode, as a function of methyl formate concentration. The fact that methyl formate desorbs almost entirely as volcano desorption indicates that, even though methyl formate is a fairly big molecule, it possesses a lot of mobility in the ice matrix.

Figure 4.16 shows that the amount of methyl formate co-desorbing with water is higher than the amount of methyl formate desorbing as surface desorption, for the 10 % mixture. However, as the concentration of methyl formate increases, the co-desorbed methyl formate peak becomes smaller than the surface desorbed methyl formate. This is probably due to the high mobility of methyl formate in the ASW. When the temperature is high enough to break the $HCOOCH_3$/H_2O bonding (120 K -130 K), a good amount of the methyl formate trapped in the bulk of ASW is freed and can desorb together with the methyl formate close to the surface of the ASW. As the concentration of methyl

formate increases the amount of it escaping as surface desorption increases relatively to the amount of methyl formate co-desorbing with water.

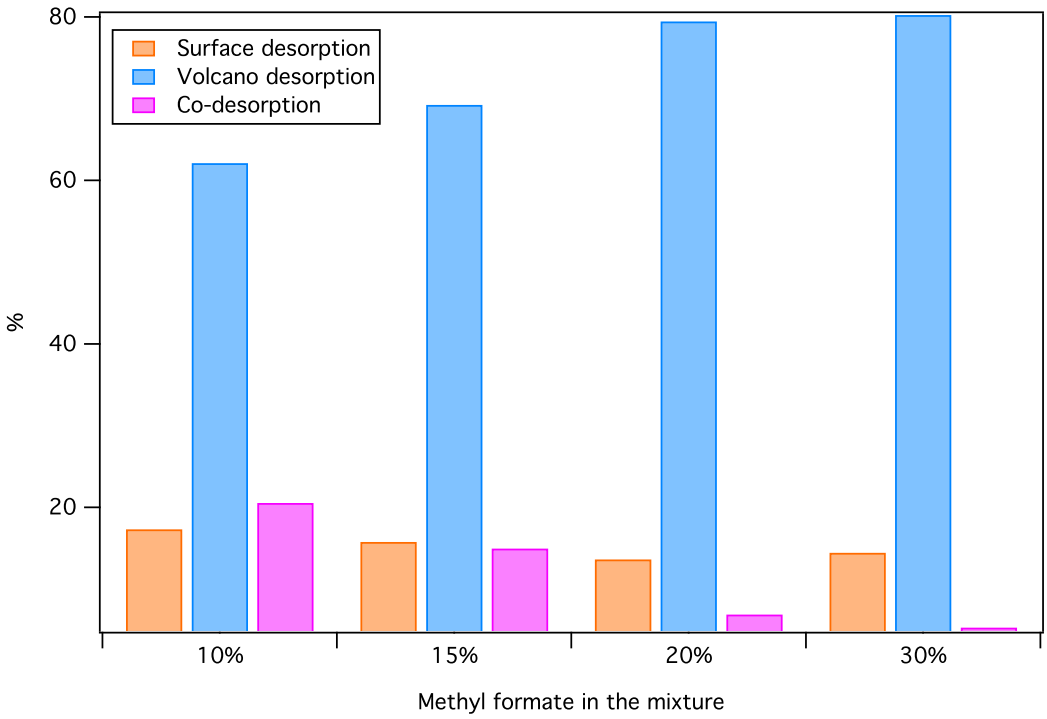

Figure 4.16. Plot showing the relative percentages of methyl formate desorbing for each desorption mode as a function of methyl formate concentration.

4.8 TPD of pure glycolaldehyde ices

Figure 4.17 shows the TPD curves of low dosages of glycolaldehyde, from 1 to 15 L. The curves from 1 to 15 L (figure 4.17) share leading edges and the peak temperature increases with glycolaldehyde exposure. The peak temperature ranges from 143 K, for 1 L, to 152 K for 15 L. The shared leading edge and the variation of the peak temperature as a function of the amount of adsorbate are an indication of multilayer desorption of glycolaldehyde. Similarly to the case of acetic acid (section 4.2), no sub/monolayer desorption seems to be shown.

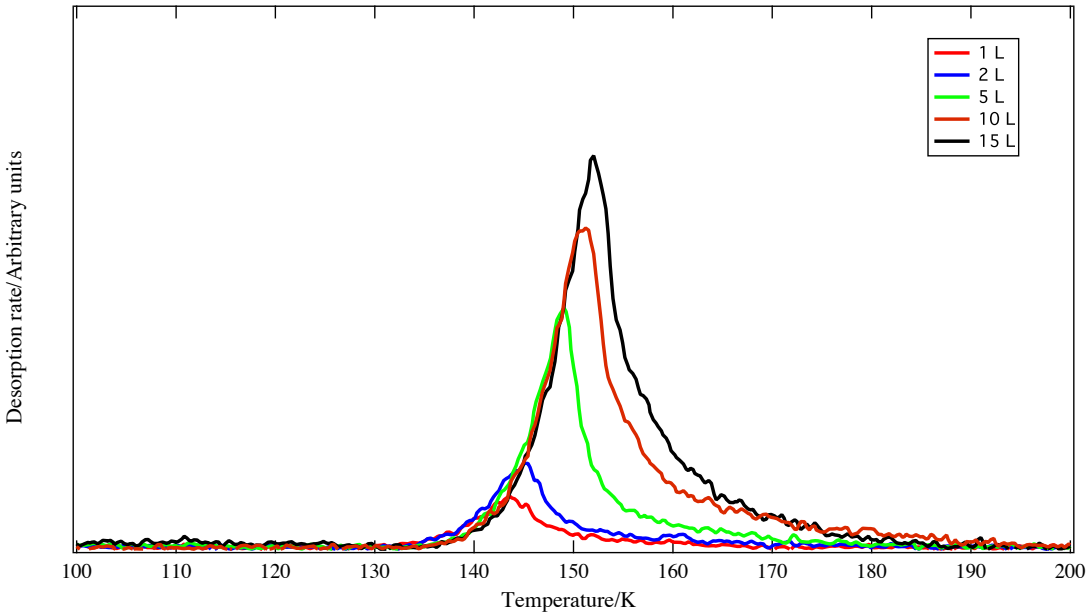

Figure 4.17. TPD spectra of $HCOCH_2OH$ from 1 to 15 L, adsorbed on a bare HOPG surface at 20 K.

Figure 4.18 shows the TPD spectra for higher exposures of glycolaldehyde ranging from 15 to 50 L.

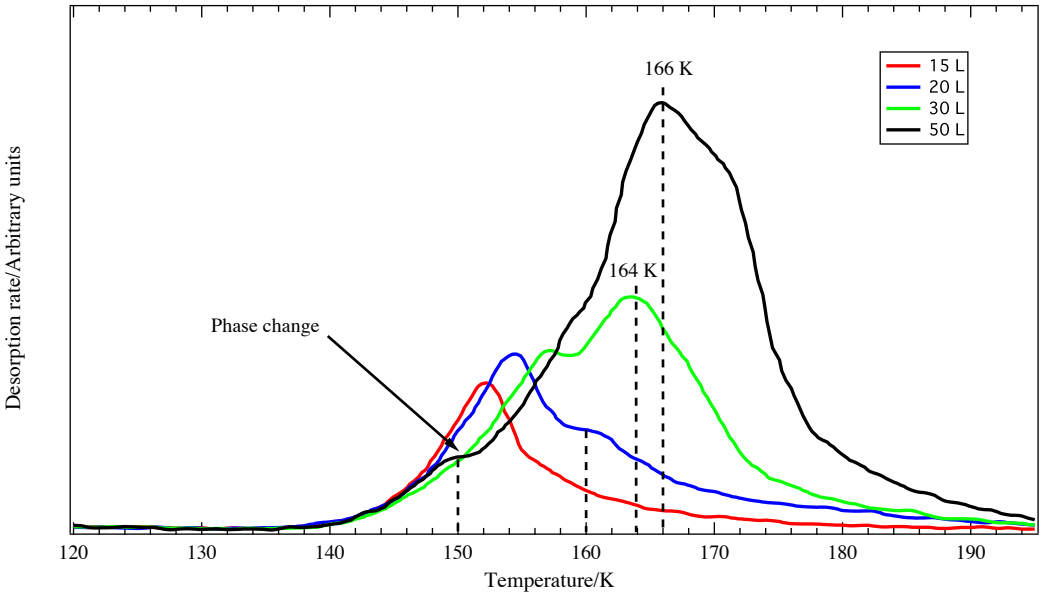

Figure 4.18. TPD spectra of $HCOCH_2OH$ from 15 to 50 L, adsorbed on a bare HOPG surface at 20 K. The black dashed line indicates the desorption of crystallized $HCOCH_2OH$.

The desorption at higher dosages is markedly different compared to the simple desorption behaviour at low exposures. All the TPD curves up to 50 L maintain a shared leading edge and the peak temperature continues to increase proportionally with the amount of adsorbate. However, it becomes evident at 20 L that an additional contribution to the overall shape of the peaks emerges. The 20 L curve, in fact, shows a

shoulder at ~160 K, seemingly indicating the desorption of a different "variety" of glycolaldehyde. At 30 L, two contributions are clearly visible. One is peaking at 157 K, while the other one is peaking at around 164 K. At 50 L of exposure, the high temperature feature has evolved into the prominent contributor to the peak shape, while the low temperature feature is not clearly distinguishable. At the same time, at 50 L, a plateau is suddenly visible at ~150 K (marked with a blue dashed line).

The behaviour shown in figure 4.18 can be rationalised in the context of glycolaldehyde crystallization. Examination of the 50 L exposure shows that a plateau exists at lower temperatures, followed by a main peak. This is very similar to what water desorption shows. In the case of water the plateau represents the ASW to CI transition. Considering this similarity with water desorption and the fact that Hudson *et al.* [126] showed evidence of a glycolaldehyde phase change, the feature appearing at ~150 K is assigned to an amorphous to crystalline glycolaldehyde transition. Evidence of crystallization is also shown in the RAIR study of glycolaldehyde adsorbed onto HOPG (next chapter).

The question is now: why is there no evidence of this transition at lower dosages? To address this problem, one has to consider that the overall shape of the peaks is given by the sum of two contributions, *i.e.* the contribution given by the desorption of amorphous glycolaldehyde (AG) and the contribution given by the desorption of crystalline glycolaldehyde (CG). Low dosages (figure 4.18), from 1 to 5 L, desorb entirely before the crystallization can take place (150 K). Therefore what is observed for low dosages is entirely AG desorption. 10 and 15 L desorption curves peak at 151 and 152 K respectively. Although their desorption temperature is higher than the crystallization temperature (150 K), the amount of AG that can actually be converted to CG in the space of just 2 K is very limited, since most of the AG has already desorbed. Therefore, the 10 L curve does not show any sign of CG desorption, while the 15 L curve only shows a very faint contribution in the shape of an inflexion (~155 K) in the descending edge of the desorption peak (visible only in figure 4.18). Starting from 20 L, whose peak temperature is ~154.5 K, the amount of AG converted into CG becomes relevant and the high temperature feature appears in the shape of a shoulder at ~160 K. The amount of AG to CG conversion is still not high enough to cause the representative plateau at 150 K. However, due to the contribution of crystallization, the leading edge of the desorption curves starts separating at around 150 K. This is due to the phase change and does not indicate a change in the mode of desorption (still multilayer).

At 30 L the AG desorption contribution peaks at 157 K. As expected, the peak temperature still increases (multilayer desorption), but the leading edge is visibly not shared with the lower dosage curves, for temperatures higher than ~150 K. The CG desorption contribution is now prominent and it peaks at ~164 K.

At 50 L, the relative intensities and positions of the CG and AG features, and the overall amount of ice are such that, for the first time, an almost complete AG to CG conversion can happen at 150 K. The 150 K plateau therefore becomes visible for the first time.

To be noticed, the temperature at which the CG feature maximum is located increases from 160 K, for 20 L, to 166 K for 50 L. This is indicative of the fact that the desorption mode is still multilayer, as expected.

Figure 4.19 shows a linear correlation between the amount of glycolaldehyde dosed and the area under the TPD spectra. This confirms that the deposition of glycolaldehyde and the sample uptake of glycolaldehyde are constant. The linear deposition curve does not show saturation at high dosages, as is consistent for multi-layered physisorbed systems.

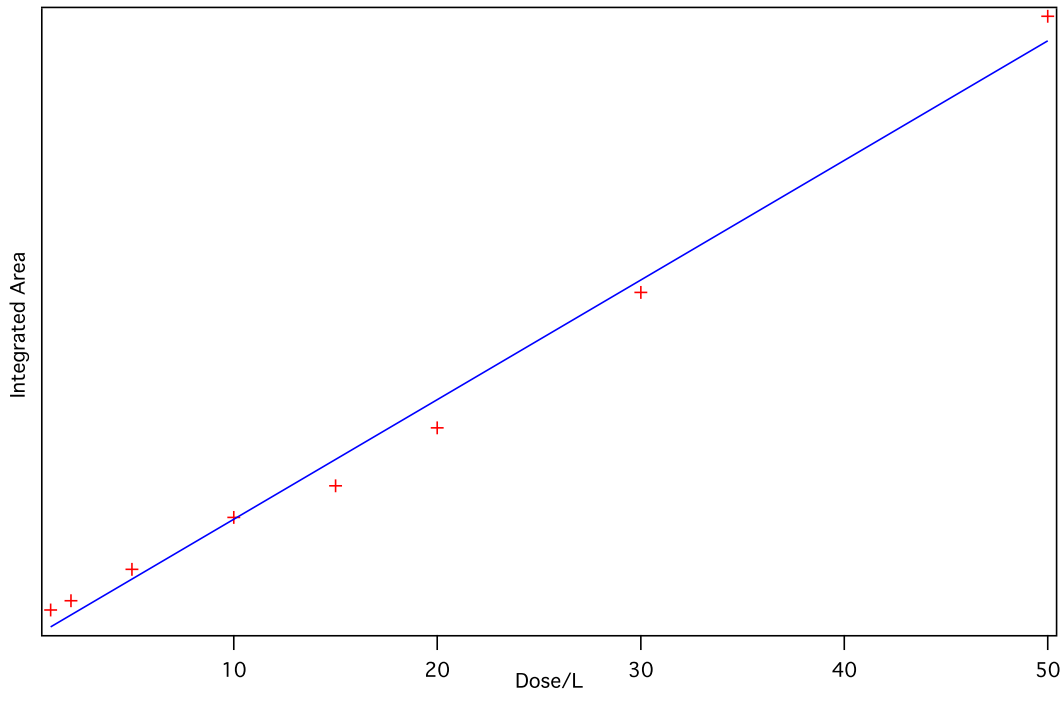

Figure 4.19. Integrated area of the TPD spectra shown in figures 1.14 and 1.15, as a function of $HCOCH_2OH$ exposure. The line represents a linear fit to the data. Errors bars are absent because errors on the integrated area are considered negligible.

4.8.1 Quantitative analysis of TPD data

Desorption order. The desorption order is determined from the gradient of a plot of ln I(T) against ln (θ_{rel}), where I(T) is the intensity recorded by the mass spectrometer at the temperature T and θ_{rel} is the relative coverage at the temperature T, using a set of TPD curves corresponding to different coverages (chapter 2, eq. 2.5).

Considering that the TPD curves of glycolaldehyde desorbing from HOPG show an indication of multilayer desorption, the desorption order can in principle be calculated utilizing all curves at the same time. However, considering that very low exposures share a very limited part of their leading edge with those at high exposure, the curves have been separated into the following ranges: 1 to 5 L, 5 to 20 L and 10 to 20 L. The curves corresponding to 30 and 50 L have not been used for the calculations because they share only a small amount of their leading edge at the very beginning of their desorption. For each range of exposure, the desorption order has been calculated over a specific range of temperatures. The details and the results of the calculations are shown in table 4.11. The average desorption order for glycolaldehyde desorption from a HOPG sample has been found to be 0.1 ± 0.1, where the uncertainty has been taken as the standard deviation of the mean. This value of desorption order refers to amorphous glycolaldehyde.

As the leading edges in the TPD spectra for multilayer glycolaldehyde do not perfectly overlap (figure 4.17), rigorous analysis of these spectra produces in most cases small, negative, desorption orders. This happens in all sets of curves (table 4.11) used for the calculation of the desorption order. A negative desorption order does not have a physical meaning; it is a direct result of the behaviour of the leading edges. In the literature, an example of negative desorption order has been reported for the case of multilayer CO_2 desorption [67]. In this situation the author, based on the qualitative characteristics of the curves, took the desorption order as 0. In the present work, whenever a negative value of desorption order appeared, its modulus was instead considered. This was done in order to still be able to associate an uncertainty to the value of the desorption order. The expected theoretical value, zero, is still included in the uncertainty interval.

Temperature/K	Desorption order, n
TPD curves: 1 to 5 L	
138.5	0.1
139.0	0.2
139.5	0.3
140.0	0.1
140.5	0.0
TPD curves: 5 to 20 L	
145.5	0.2
146.0	0.3
146.5	0.2
147.0	0.2
147.5	0.1
148.0	0.0
TPD curves: 10 to 20 L	
149.0	0.1
149.5	0.2
150.0	0.1

Table 4.11. Calculated desorption orders for several exposures of CH_3COOH, adsorbed on HOPG at 20 K. For each range of temperatures, the curves used in the calculation are indicated in the table.

Desorption energy. Table 4.12 shows the results of this calculation for the desorption energies for each dosage, when n = 0.1.

$HCOCH_2OH$ exposure (L)	Desorption Energy (kJ mol^{-1})
1	37 ± 4
2	50 ± 3
5	51 ± 2
10	55 ± 2
15	53 ± 2
20	56 ± 2

Table 4.12. Calculated desorption energies for multilayer $HCOCH_2OH$ adsorbed on HOPG, at 20 K.

The average desorption energy is 50 ± 6 kJ/mol, where the uncertainty is taken as twice the standard deviation of the mean. The uncertainty on this value is mostly due to the desorption energy associated with the 1 L exposure being very different from the desorption energies associated with the other exposures. The reason for the anomalous value for 1 L desorption energy could be related to noise in the leading edge of the curve due to the low signal to noise ratio. Excluding the value of 1 L desorption energy from the calculation of the average desorption energy, the latter becomes 53 ± 3 kJ/mol. This value is included within the uncertainty interval of the initial desorption energy, 50 ± 6 kJ/mol. The final average desorption energy for amorphous glycolaldehyde multilayers has therefore been taken as 50 ± 6 kJ/mol.

Pre-exponential factor. The impingement rate on the HOPG sample is calculated *via* equation 2.8 and is equal to 3.9×10^{14} molecules/L. The relationship between the area under the TPD curves and the actual $HCOCH_2OH$ exposure is given by the slope of the fit line in figure 4.19. This is equal to 1.2×10^4 L^{-1}. The final scaling factor is 3.3×10^{10} molecules. Table 4.13 shows the results of the pre-exponential factor calculation for exposures of glycolaldehyde ranging from 1 to 20 L. The calculations used n = 0.1 and E_{des}= 50 kJ/mol.

$HCOCH_2OH$ exposure/L	Pre-exponential factor /$(molec \cdot m^{-2})^{0.9} s^{-1}$
1	$10^{29\pm2}$
2	$10^{29\pm2}$
5	$10^{30\pm2}$
10	$10^{31\pm2}$
15	$10^{30\pm1}$
20	$10^{31\pm2}$

Table 4.13. Calculated pre-exponential factor for multilayer CH_3COOH, adsorbed on HOPG at 20 K.

The average multilayer desorption pre-exponential factor for $HCOCH_2OH$ was found to be $10^{30\pm2}$ (molecules · m^{-2})$^{0.9}$$s^{-1}$. Units are given as $(molec \cdot m^{-2})^{1-n} s^{-1}$. The uncertainty was calculated by varying both the desorption order and the desorption energy within their uncertainty intervals. In the literature, the values for multilayer pre-exponential factor are in the range 10^{25}–10^{32} molecules m^{-2} s^{-1} [34,42]. The value of the pre-exponential factor found for glycolaldehyde desorbing from HOPG is within this interval of values.

4.9 TPD of $HCOCH_2OH$ deposited on ASW

Figure 4.20 shows the desorption of 1 to 50 L of glycolaldehyde deposited on top of 50 L of water. The desorption of the underlying water ice is also shown on the bottom part of the plot. Contrary to what was observed for acetic acid and methyl formate, glycolaldehyde desorption from the surface of ASW shows only one main feature, whose peak is at the same temperature as the desorption of water (Figure 4.20).

Figure 4.21 shows a comparison between the TPD spectra of glycolaldehyde deposited on ASW and the TPD spectra of glycolaldehyde deposited on HOPG.

At 1 L, the glycolaldehyde desorption peak from ASW corresponds almost exactly to the water desorption peak (figure 4.20). The same amounts of glycolaldehyde deposited directly on HOPG desorb at ~143 K (figure 4.21), while in the case of glycolaldehyde on top of water, the desorption temperature is around 158 K. The fact that low dosages of glycolaldehyde stick to water until it starts desorbing suggests that the $HCOCH_2OH/H_2O$ bonding is stronger than the $HCOCH_2OH$/HOPG bonding.

As the amount of glycolaldehyde on top of ASW increases, the leading edge becomes more pronounced. At 10 L, desorption starts around 150 K. For dosages higher

than that, desorption begins at even lower temperatures (< 145 K). For higher dosages, the leading edge of the TPD spectra of glycolaldehyde desorbing from ASW extends towards the temperature region that is characteristic of glycolaldehyde desorption from HOPG. This is expected, since when the layers of glycolaldehyde build up, the influence of the water ice on the upper layers of glycolaldehyde is reduced and the desorption becomes more similar to glycolaldehyde desorption from HOPG. At 20 L the broad and flat shape of the peak is due to the interaction of the desorption of the upper layers of glycolaldehyde (started at ~145 K) and the glycolaldehyde/water co-desorption.

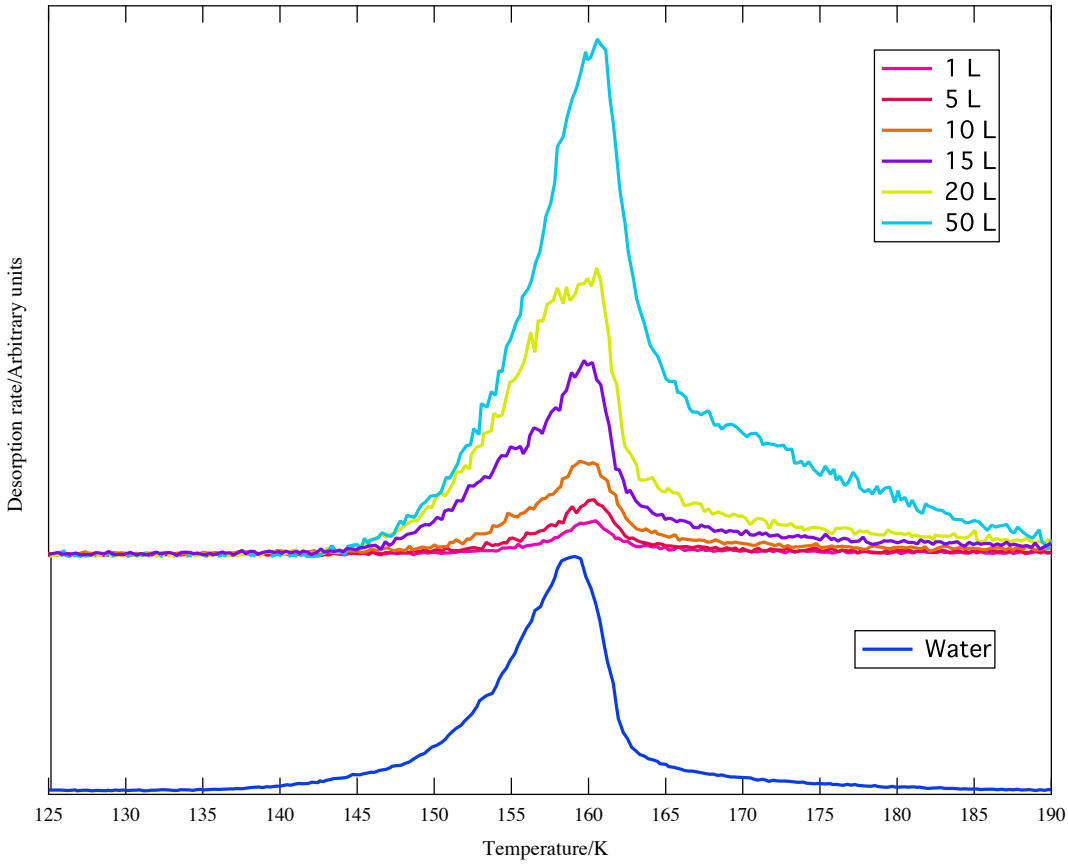

Figure 4.20. TPD spectra of 1 to 50 L exposures of $HCOCH_2OH$ on 50 L of pre-deposited H_2O ice on HOPG at 20 K. The TPD of 50 L of ASW has been shown, for comparison, on the bottom section of the graph.

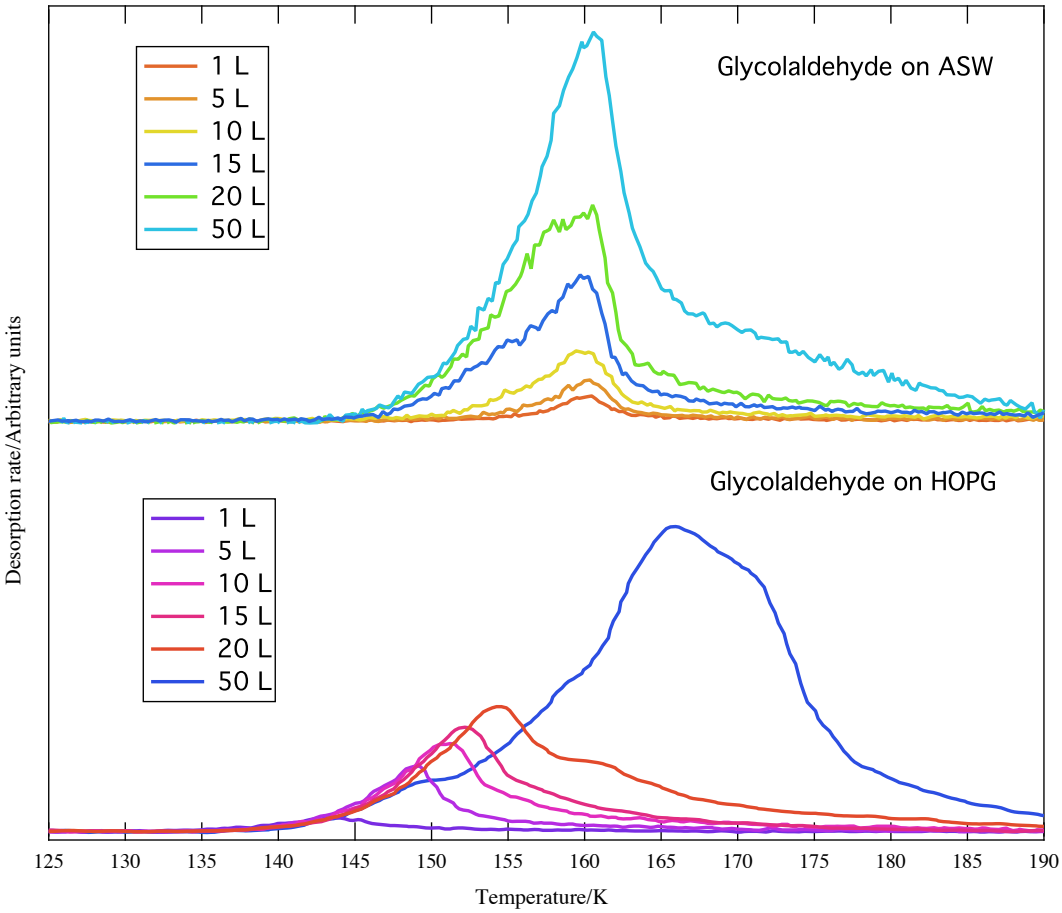

Figure 4.21. Comparison between TPD spectra of glycolaldehyde adsorbed on HOPG and glycolaldehyde adsorbed on ASW.

4.10 TPD of $HCOCH_2OH$:H_2O mixtures

Figure 4.22 shows the TPD spectra of glycolaldehyde desorbing from a range of glycolaldehyde/water mixed ices. The curves were offset for ease of display. The water TPD is also shown (scaled) in the bottom part of the plot. Glycolaldehyde desorbs from the mixed ices mostly as water desorbs. At low concentrations, 5 % and 15 %, a small bump is visible at 149 and 147 K respectively. This is indicative of volcano desorption. The intensity of the volcano desorption peak with respect to the co-desorption peak decreases as the concentration increases. At 20 % concentration, the residual volcano desorption appears as a shoulder at ~146 K.

The fact that glycolaldehyde desorbs mostly with water is a further indication of its strong bonding to water. This is most likely due to hydrogen bonding between glycolaldehyde and water. Glycolaldehyde can potentially form up to two hydrogen

bonds with water, *via* the hydrogen in the hydroxyl group and *via* the oxygen in the aldehyde group.

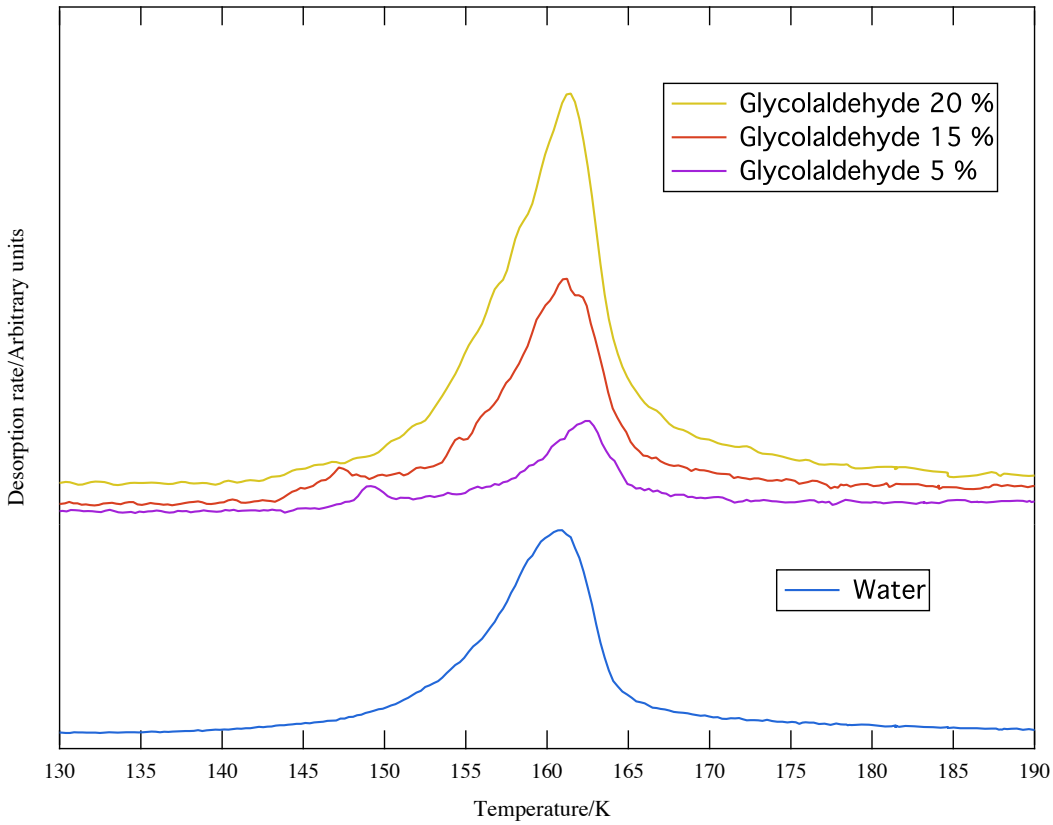

Figure 4.22. TPD spectra of 50 L of 20% CH_3COOH:H_2O mixture, adsorbed on HOPG at 20 K. The percentage refers to the amount of glycolaldehyde in the mixture. The curves are offset. The TPD of ASW has been shown, for comparison, on the bottom section of the graph.

4.11 Astrophysical implications

Using a similar model to that employed for H_2S in chapter 3, the desorption rates for acetic acid, methyl formate and glycolaldehyde have been calculated under astrophysical conditions. The model used for the simulations applies a heating rate characteristic of the evolution of a low mass (5 solar masses) or of a high mass (25 solar masses) star to the Polyani-Wigner equation. The model describes the behaviour of all mixed X/H_2O ice, where X is the selected species. The mixture in this case has been always taken as 95% H_2O and 5% X. The initial coverage is taken as 9.5×10^{21} molec m^{-2}. In the assumption that the density of the ice mixture is essentially equal to the density of ASW this corresponds to an ice thickness of 0.3×10^{-6} m, comparable to the thickness of interstellar ice [97]. For the simulation of the desorption of X from the surface of the ice, the values of desorption energy, desorption order and pre-exponential factor for multilayer X were used. However, the volcano desorption and water co-

desorption of X are processes driven by the phase change and desorption of water. The values of desorption energy, pre-exponential factor and desorption order used to simulate the volcano desorption are therefore the ones corresponding to amorphous ice desorption [98]. While in the case of co-desorption, the values used were the ones corresponding to crystalline ice desorption, see for example [30]. The percentage of each species that desorbs *via* surface desorption, volcano desorption and co-desorption were taken as the ratios of the areas under the X TPD curve corresponding to each mode of desorption. The spectra of the lowest concentration mixtures were used. Considering that acetic acid entirely co-desorbs from mixtures with water, its behaviour is identical (as far as the model can discern) and mirrors the desorption of crystalline water. Methyl formate, in a 10 % mixture, desorbs *via* surface desorption (17%), volcano desorption (62%) and co-desorption (21%). While glycolaldehyde, in a 5 % mixture, desorbs *via* volcano desorption (10 %) and *via* co-desorption (90 %).

Figure 4.23 shows the evolution of the abundances of the $C_2H_4O_2$ isomers in the surroundings of a 5 solar masses star and a 25 solar masses star, as a function of temperature. As mentioned before, acetic acid co-desorbs with water. Therefore the curves associated with acetic acid do not show features (such as plateaus) indicative of surface or volcano desorption. On the contrary, methyl formate shows evidence of all modes of desorption, the most prominent being volcano desorption, and glycolaldehyde shows a very faint inflexion due to volcano desorption. Figure 4.23 shows also the difference in desorption temperature between the case of a 5 solar masses star and the case of a 25 solar masses star. In the case of the more massive star, the desorption ends at 113 K, while in the case of the 5 solar masses star, it ends at ~104 K.

Figures 4.24 and 4.25 show the evolution of the abundances of the $C_2H_4O_2$ isomers in the surrounding of a 5 solar masses star and a 25 solar masses star, as a function of time. In terms of shape, the curves are analogous to the ones shown in figure 4.23. One can notice that in the case of the 25 solar masses star, the desorption of the ices is much faster compared to the case of the 5 solar masses star. This is expected, since high mass stars have typically a faster evolution (and a shorter life-span) compared to low mass stars.

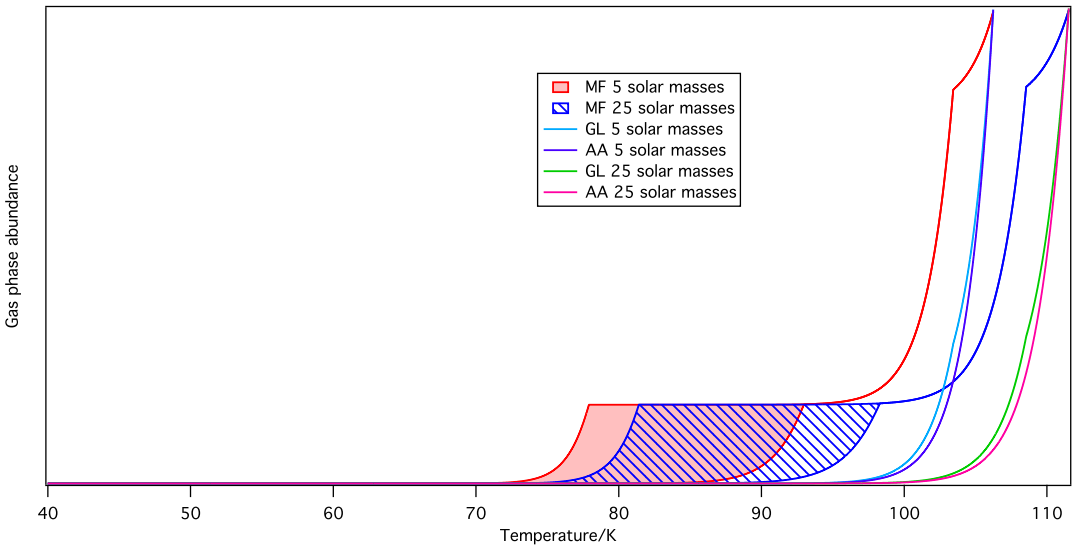

Figure 4.23. Comparison of the acetic acid (AA), methyl formate (MF) and glycolaldehyde (GL) abundances in the surroundings of a 5 and a 25 solar masses stars, as a function of temperature. Shaded area represent the effect of the uncertainty on $HCOOCH_3$ pre-exponential factor.

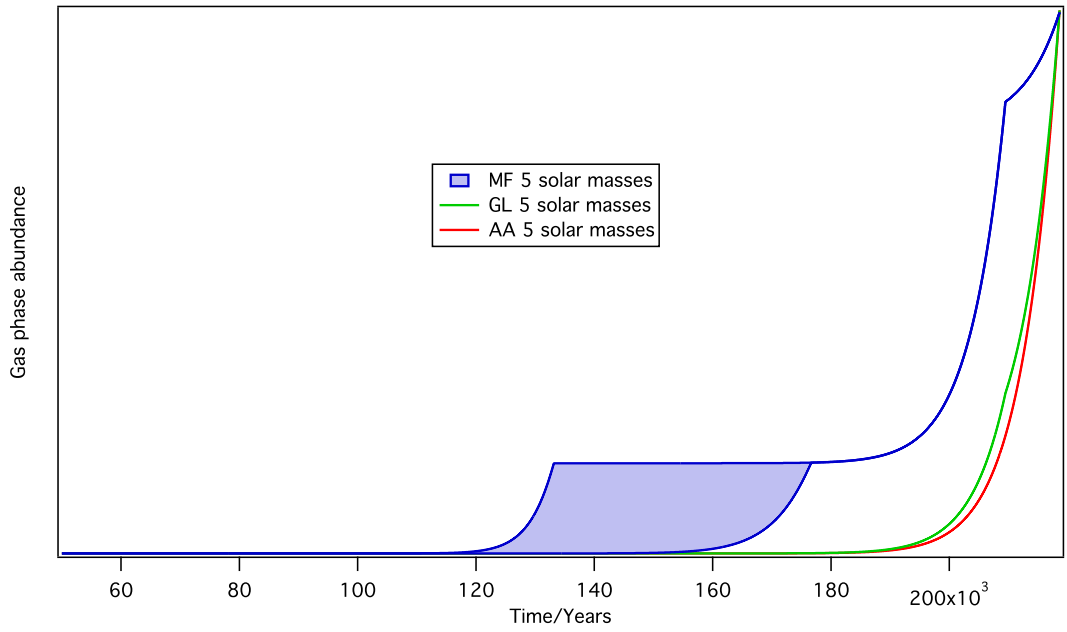

Figure 4.24. Comparison of the acetic acid (AA), methyl formate (MF) and glycolaldehyde (GL) abundances in the surroundings of a 5 solar masses star, as a function of time. Shaded area represent the effect of the uncertainty on $HCOOCH_3$ pre-exponential factor.

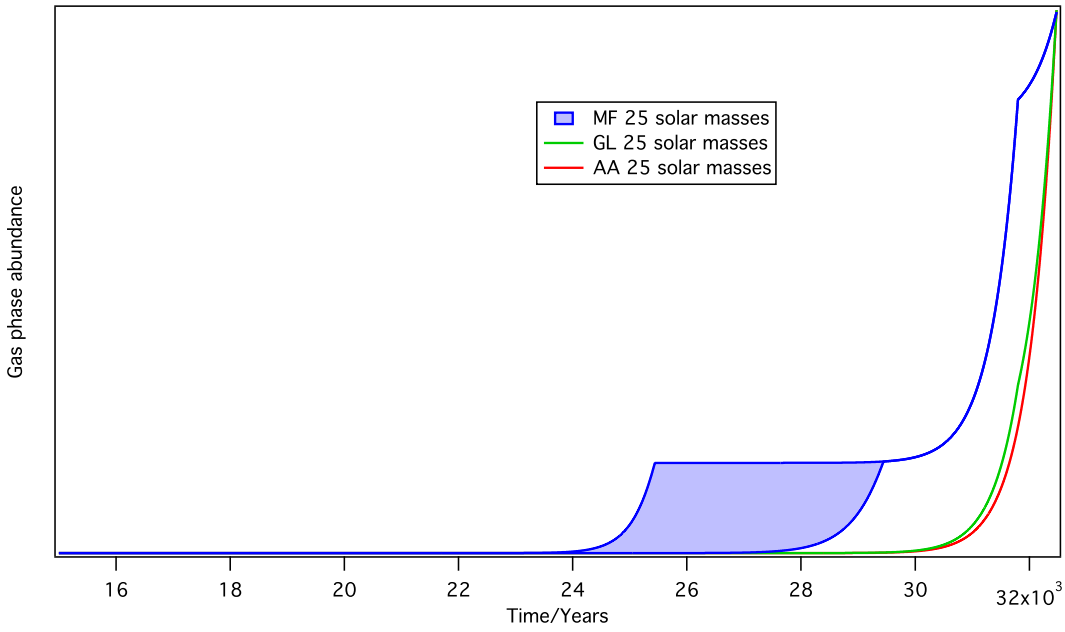

Figure 4.25. Comparison of the acetic acid (AA), methyl formate (MF) and glycolaldehyde (GL) abundances in the surroundings of a 25 solar masses star, as a function of time. Shaded area represent the effect of the uncertainty on $HCOOCH_3$ pre-exponential factor.

4.12 Final remarks

A complete TPD study of acetic acid, methyl formate and glycolaldehyde adsorbed on HOPG has been performed. The study provided both qualitative results, and quantitative (kinetic parameters) results *via* the analysis of the behaviour of the TPD curves as a function of different dosages. Moreover, the qualitative study of the desorption of each isomer from an ASW surface and from a mixture with water has also been performed.

Acetic acid and glycolaldehyde did not show any indication of monolayer desorption, when desorbing from HOPG. On the contrary, methyl formate showed evidence of sub/monolayer desorption. This is potentially due to the geometry of the single molecules. Acetic acid and glycolaldehyde can both establish two hydrogen bonds. Acetic acid can do this *via* the oxygen and the hydrogen of the carboxylic group, while glycolaldehyde can do it *via* the hydrogen in the hydroxyl group and the oxygen in the aldehyde group. This could make the acetic acid-acetic acid and the glycolaldehyde-glycolaldehyde bonding more intense compared to the acetic acid-HOPG and the glycolaldehyde-HOPG bonding. This can explain why methyl formate, that can only potentially form one hydrogen bond with another methyl formate

molecule, is the only one to show monolayer desorption. All the results of the quantitative analysis of the TPD curves, for each isomer, are shown in table 4.14.

	Acetic acid	Methyl formate		Glycolaldehyde
		Monolayer	Multilayer	
n	0	1.2	0.1	0.1
E_{des} (kJ/mol)	55	29	35	50
Pre-exponential	8×10^{32}	4×10^{12}	1×10^{32}	8×10^{30}

Table 4.14. Summary of the kinetic parameters found for acetic acid, methyl formate and glycolaldehyde.

When adsorbed on ASW, acetic acid and methyl formate show complex desorption, in which multiple features appear depending on the amount of adsorbate deposited. In the case of acetic acid, features assigned to monolayer, multilayer and acetic acid hydrate desorption are visible. In the case of methyl formate, there is evidence of monolayer, bi-layer and multilayer desorption. The complex behaviour shown by both species, when desorbing from ASW, is an indication of an intense interaction between the molecules and the water substrate. Most significant is the case of acetic acid that shows features that were not evident from the study of its desorption from HOPG. This suggests, especially in the case of acetic acid, that most likely hydrogen bonding between these species and water is taking place.

Glycolaldehyde, on the contrary, only shows evidence of multilayer desorption when adsorbed on top of water. This is somewhat surprising because it is in theory capable of hydrogen bonding with water. Part of the reason why glycolaldehyde is showing only one broad feature when desorbing from water is that its temperature of desorption is very close to that of water. However, this cannot be the only reason because also acetic acid possesses a desorption temperature in the same range as that of water. Therefore, a more subtle reason involving the dynamics of the glycolaldehyde/water bonding could be the cause of this behaviour. Further studies, such as comparative computational simulations of the interaction of the isomers with water, would be necessary in order to provide an exhaustive explanation of this behaviour.

When acetic acid and glycolaldehyde are mixed with water, they tend to co-desorb entirely with water. This is not so surprising since they are fairly big molecules

and they could form hydrogen bonds with water. It is unexpected that methyl formate desorbs, from mixtures with water, mostly during the ASW to CI transition (volcano desorption). Methyl formate has been shown to interact intensely with water when deposited on top of ASW. Given this fact and the size of the molecule it would be expected to mostly co-desorb with water, as the other two molecules do. Again the reason for this behaviour is not clear and further investigations are needed to fully explain it.

Finally, using all the information gathered *via* the TPD study, basic simulations of the desorption of the isomers in an astrophysical environment have been performed.

5 RAIRS of $C_2H_4O_2$ bearing ices

A series of reflection absorption infrared spectroscopy (RAIRS) experiments have been performed on the $C_2H_4O_2$ isomers: acetic acid (CH_3COOH), methyl formate ($HCOOCH_3$) and glycolaldehyde ($HCOCH_2OH$). These were conducted in the experimental setup CH1 described in chapter 2. The purpose of these studies is to provide detailed IR spectra for the isomer ices, both in their pure form and in the presence of water (the species of interest is deposited on top of water or in mixtures with water). Studying the infrared emission of the $C_2H_4O_2$ isomers in the presence of water is important because water is the most abundant molecule in interstellar ices [2], therefore if the formation of these molecules occurs on the dust grains, it is reasonable to expect it to happen in an hydrous environment [131]. Knowing the IR spectra of these molecules both in their pure form or in the presence of water could help identification of these species in an astronomical environment. Furthermore it provides information which complements the TPD results discussed in the previous chapter. In the literature IR studies of acetic acid, methyl formate and glycolaldehyde ices are available. RAIR studies of acetic acid and methyl formate deposited on crystalline and amorphous water were performed by Bertin *et al* [119]. The interaction of water and acetic acid was the focus of studies such as that performed by Bahr *et al.* [120] and Allouche & Bahr [121] who complemented their studies with density functional theory calculations. As far as methyl formate is concerned, RAIR studies on its behaviour when deposited on Ni(111) and Ag(111) surfaces were performed by Zahidi *et al*. [123] and Schwaner *et al* [122]. Studies focusing on glycolaldehyde ice and its interaction with water are not very numerous in the literature. Glycolaldehyde photolysis is relevant to atmospheric chemistry [73,125], therefore most of the literature on glycolaldehyde deals with gas-phase glycolaldehyde. However, mostly due to its relevance in the interstellar chemistry [116,117], studies involving glycolaldehyde and glycolaldehyde irradiation have been performed [126,132].

These studies provide important information concerning the IR spectra of these molecules and their adsorption on water or metal substrates. However, RAIR studies of the adsorption of these three isomers on HOPG, or other dust grain analogues, in their pure or hydrous forms are still currently unavailable. Moreover, a comparative study including the three isomers has yet to be performed.

All species were dosed onto the sample at cryogenic temperatures (20 K). For the thermal studies, the temperature was increased slowly to the target temperature with a heating rate of 0.5 K/s. The sample was then maintained at the temperature for 3 minutes and subsequently the RAIR spectrum was acquired. RAIR spectra were taken with a spectral resolution of 4 cm^{-1} and are the result of the co-addition of 256 scans. The formation of the layered and mixed ices was performed with the same procedures detailed in the previous chapters.

In this chapter, the RAIR studies of acetic acid, methyl formate and glycolaldehyde, in their pure form and in presence of water, are presented. In all the plots shown in this chapter, RAIR spectra were manually offset for ease of display.

5.1 RAIRS of pure Acetic Acid Ices

Figure 5.1 shows a comparison of RAIR spectra of 20 and 100 L of acetic acid deposited on HOPG, at a temperature of 20 K. These exposures form multi-layered ice on the HOPG, as suggested by the TPD study in the previous chapter. The vibrational properties of sub-monolayer acetic acid ices have been studied [119] and show no significant differences compared to the ones described in the present study. Figure 5.1 shows that the intensity of the transitions at a dosage of 20 L is very low. The most intense transition at 1735 cm^{-1} is less than 1%. In order to properly show the vibrational bands, and their modifications during the heating of the ice, this study focused on thicker ices of 100 L.

The main vibrational features are shown in figure 5.1. Four main regions can be identified: CH_3 rocking (1000-1070 cm^{-1}), C–O stretch (1250-1333 cm^{-1}), CH_3 and OH bending (1340-1500 cm^{-1}) and C=O (1650-1800 cm^{-1}). Comparison with previous studies [119,120,129] allows the assignment of all vibrational features. A list of the assignments is detailed in table 5.1. Acetic acid can exist in several different forms in the condensed phase. In the liquid phase, acetic acid exists mostly as cyclic dimers [133], although evidence of open-chain polymers is also reported [134]. In the solid phase, according to the TPD studies discussed in the previous section and to previous IR studies [129,135], acetic acid exists mainly in a combination of cyclic dimers and chainlike polymers. The dimer configuration is dominant when acetic acid is deposited at low temperatures [119], while the polymeric configuration is favoured when the deposition occurs at higher temperatures (typically above 120-130 K) [119,129]. When the transition from low to high temperature has been monitored, whether in TPD or IR

studies, evidence of a phase change from the cyclic dimer configuration to a crystalline chainlike polymer structure has been found [119,129,135].

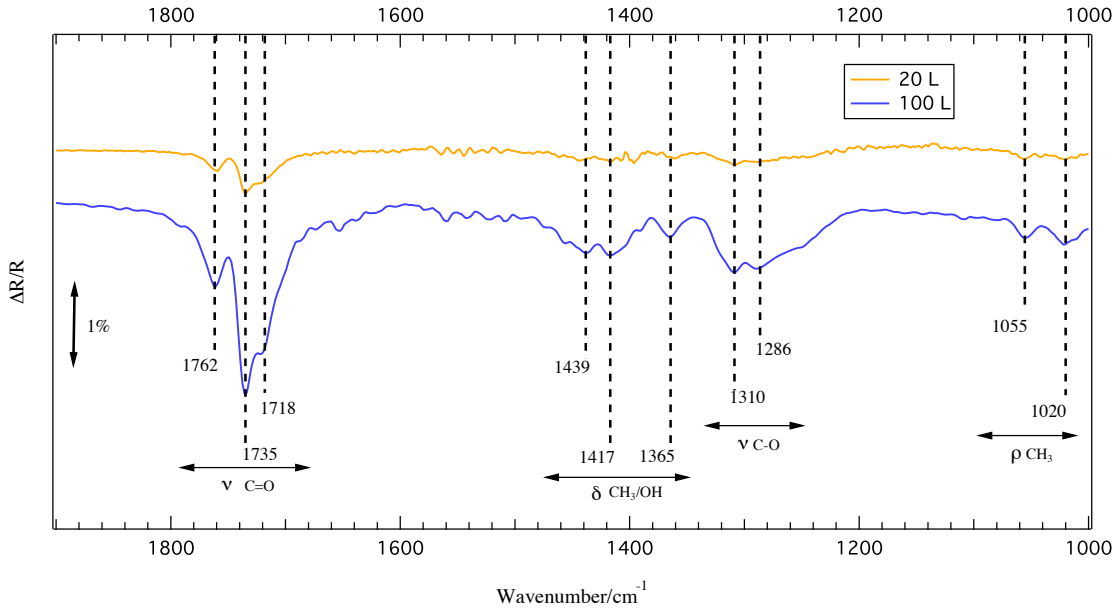

Figure 5.1. RAIR spectrum of CH_3COOH deposited on HOPG at 20 K. Comparison of two exposures: 20 L and 100 L. Abbreviations/symbols: ρ, rocking, ν, stretching, δ, bending, τ, twisting.

Assignment	CH_3COOH on HOPG This work	CH_3COOH on crystalline water [119]	CH_3COOH on Cu [129]	Solid phase [135]
ρ_s CH_3	1020			1019
ρ_{as} CH_3	1055			1049
ν C–O (c)	1286	1285	1284	1269
ν C–O (d)	1310	1302	1314	
δ_s CH_3	1365	1364	1363	1365
δ_{as} CH_3	1417	1415	1418	
δ COH	1439	1445	1436	1406
ν C=O (c)	1718	1640-1700	1646	1659
ν C=O (d)	1735	1720	1732	1715
ν C=O (m)	1762-1749	1750	1749-1790	
	1794			
2ν(C–O)	2582		2576	2519
ν(C–O)+δ_s(CH_3)	2642-2628		2640	2614
ν(C–O)+δ_s(OH)	2692-2679		2691	2664
ν_s(CH_3)	2929		2924	
ν (OH)	3103		3028	3028

Table 5.1. Assignment of the spectral features of multilayers of CH_3COOH adsorbed onto HOPG at 20 K, as seen in figures 5.1 and 5.3. All values are in cm^{-1}. Abbreviations/symbols: ρ, rocking, ν, stretching, δ, bending, s, symmetric, as, asymmetric; (c), related to crystalline CH_3COOH, (d), related to CH_3COOH cyclic dimers, (m), related to CH_3COOH monomers. In red, features that appear after heating of the ice.

The most prominent feature of the acetic acid vibrational spectrum is the C=O stretching vibration found in the range 1650-1800 cm^{-1}. This feature is found to be particularly sensitive to the different physical forms of acetic acid following adsorption. On HOPG, the spectrum in figure 5.1 shows three main components at 1718 cm^{-1}, 1735 cm^{-1} and 1762 cm^{-1}. These are assigned, respectively, to acetic acid existing in the crystalline, dimeric and monomeric form. The transition at 1718 cm^{-1}, assigned to crystalline acetic acid, is at higher wavenumbers compared to other work in the literature (see table 5.1). However, a similar transition is shown to appear upon heating of the ice [129]. Considering its intermediate position between the polymer C=O stretching transition, at ~1640 cm^{-1} (not clearly evident in figure 5.1), and the dimer transition at 1735 cm^{-1}, the transition at 1718 cm^{-1} is assigned to the C=O stretching mode of acetic acid oligomers. The presence of features belonging to monomers not participating in the bulk structure, dimers and oligomers/polymers shows that all of the physical forms of solid acetic acid coexist in a multi-layered ice formed at low temperature. This is in agreement with what is shown in the TPD study of CH_3COOH desorption from the surface of water (chapter 4, section 4.3).

The second most prominent features are found at 1310 and 1286 cm^{-1} and are assigned, respectively, to C–O stretching of the dimeric and crystalline form of acetic acid. Other vibrational features are observed at 1365, 1417 and 1439 cm^{-1}. These are assigned to the bending modes of CH_3 and COH. Minor features associated with the CH_3 rocking mode are found at low wavenumbers, 1020 and 1055 cm^{-1}. Finally, figure 5.2 shows the RAIR spectra of acetic acid between 2500 and 3500 cm^{-1}.

Several small features are visible in figure 5.2. These are assigned to the first C–O stretch overtone (2582 cm^{-1}), a combination band of the C–O stretch and CH_3 and OH bending modes (2632 and 2692 cm^{-1}, respectively), to the CH_3 symmetric stretch (2929 cm^{-1}) and to the OH stretch (3103 cm^{-1}).

Figure 5.3 shows the thermal evolution of the RAIR spectrum when the ice is heated up to 160 K. Band assignments are made by comparison with the literature [119,129,135], see table 5.1.

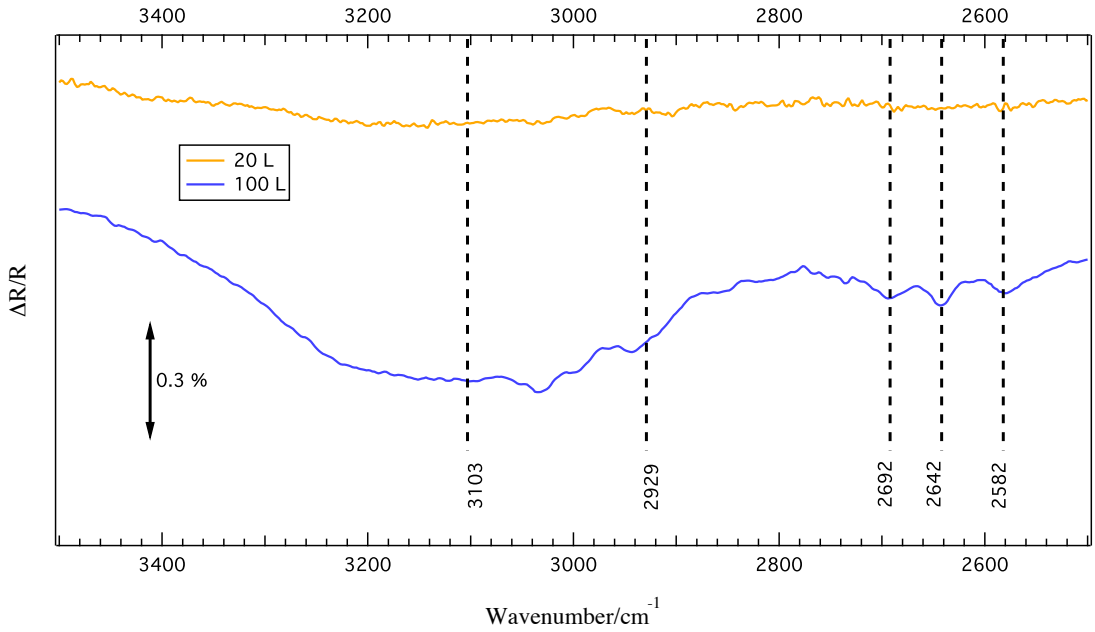

Figure 5.2. RAIR spectrum of CH_3COOH deposited on HOPG at 20 K. Comparison of two exposures: 20 L and 100 L, between 2500 and 3500 cm^{-1}.

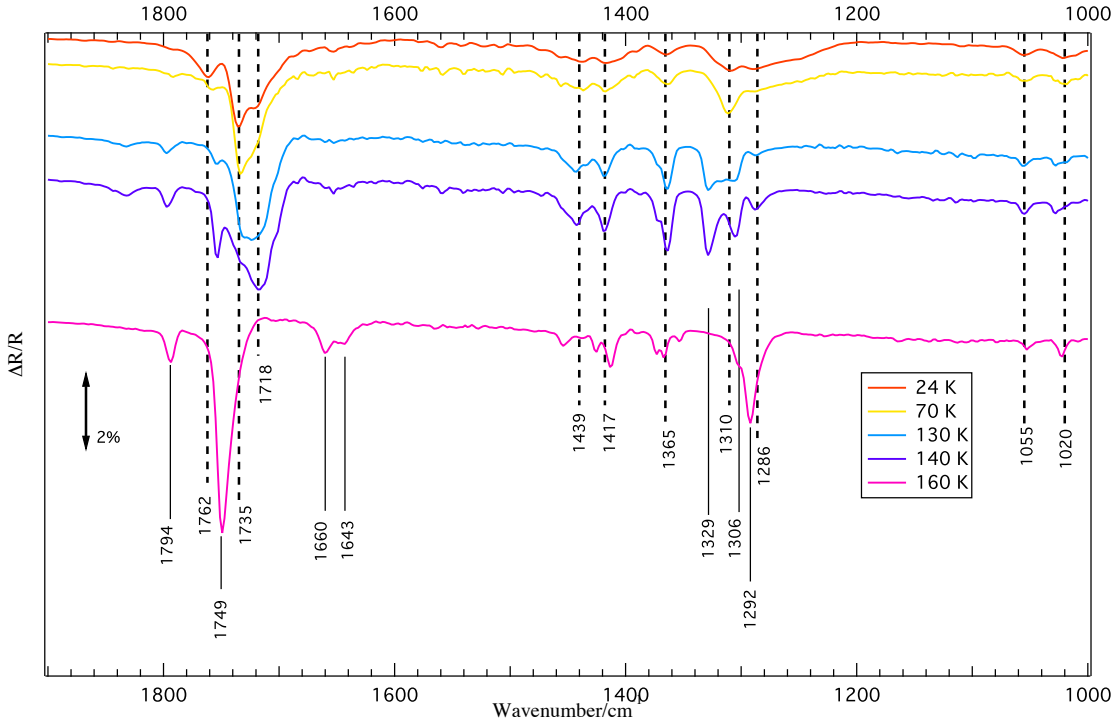

Figure 5.3. Thermal evolution of 100 L CH_3COOH deposited on HOPG, at 20 K, between 1000-1900 cm^{-1}. Temperature ranges from 24 K to 160 K.

It is immediately evident that heating causes a dramatic change in the ice configuration. Minimal changes in the spectrum in the C=O stretch wavenumber region are present already at 70 K, in the form of a small variation in the relative intensity of

the feature at 1735 cm^{-1} compared to the one at 1718 cm^{-1}. The spectrum undergoes a profound change at a temperature of 130 K that finishes at 160 K. In the C=O stretch region, the feature at 1718 cm^{-1} (acetic acid oligomers) increases in intensity until a temperature of 140 K is reached. At 140 K, this feature becomes more intense than the 1735 cm^{-1} feature (acetic acid dimers), which is consistent with a crystallization process. The band at 1762 cm^{-1} (acetic acid monomers) shifts towards lower wavenumbers (1749 cm^{1}) and a new feature appears at 1794 cm^{-1}. The new feature at 1794 cm^{-1} is assigned to the C=O stretch of acetic acid monomers on the surface of the ice, as opposed to the 1749 cm^{-1} feature that is assigned to monomers trapped in the bulk of the ice [129]. At 160 K the C=O stretch of bulk trapped monomers (1749 cm^{-1}) becomes the most prominent feature, this is consistent with the crystallization process [129]. Two new features appear at 1643 and 1660 cm^{-1} at 160 K. These are assigned to the C=O stretch of bulk polymers in the solid [119,129] and their increase is again consistent with a polymerisation/crystallization process.

At temperatures above 160 K, acetic acid desorbs and vibrational features are no longer visible. This is consistent with what is shown by the TPD study in section 4.2.

At 130 K, the C-O stretch feature at 1310 cm^{-1} evolves into a doublet at 1306 and 1329 cm^{-1} that becomes more pronounced at 140 K and finally disappears at 160 K. The feature at 1286 cm^{-1}, assigned to the C-O stretch of chainlike acetic acid, becomes more intense as the temperature increases. However, at 160 K, it shifts to 1292 cm^{-1}, merging with the 1306 cm^{-1} feature, and becomes the most intense feature in the C-O stretch region at that temperature.

The CH_3 and COH bending modes in the 1360-1450 cm^{-1} region (see table 5.1) increase in intensity and seem to show a more complex profile with the increase of the temperature up to 140 K. At 160 K, these features appear weakened. The features associated with the CH_3 rocking mode (1020 and 1055 cm^{-1}) increase in intensity up to 160 K.

Figure 5.4 shows the spectra of 100 L of acetic acid between 2500 and 3500 cm^{-1}, following annealing. The observed bands are assigned to the first C–O stretch overtone (2582 cm^{-1}), a combination of the C–O stretch and CH_3 and OH bending modes (2632 and 2692 cm^{-1}, respectively) and to the CH_3 symmetric stretch (2929 cm^{-1}). All of these modes increase in intensity up to 140 K and then weaken at 160 K. At this temperature, the C–O stretch overtone (2582 cm^{-1}) disappears, while the C-O combination bands at

2642 cm^{-1} (ν C-O + δ CH_3) and 2692 cm^{-1} (ν C-O + δ OH) shift to lower wavenumbers, respectively, 2628 cm^{-1} and 2679 cm^{-1} (see figure 5.4).

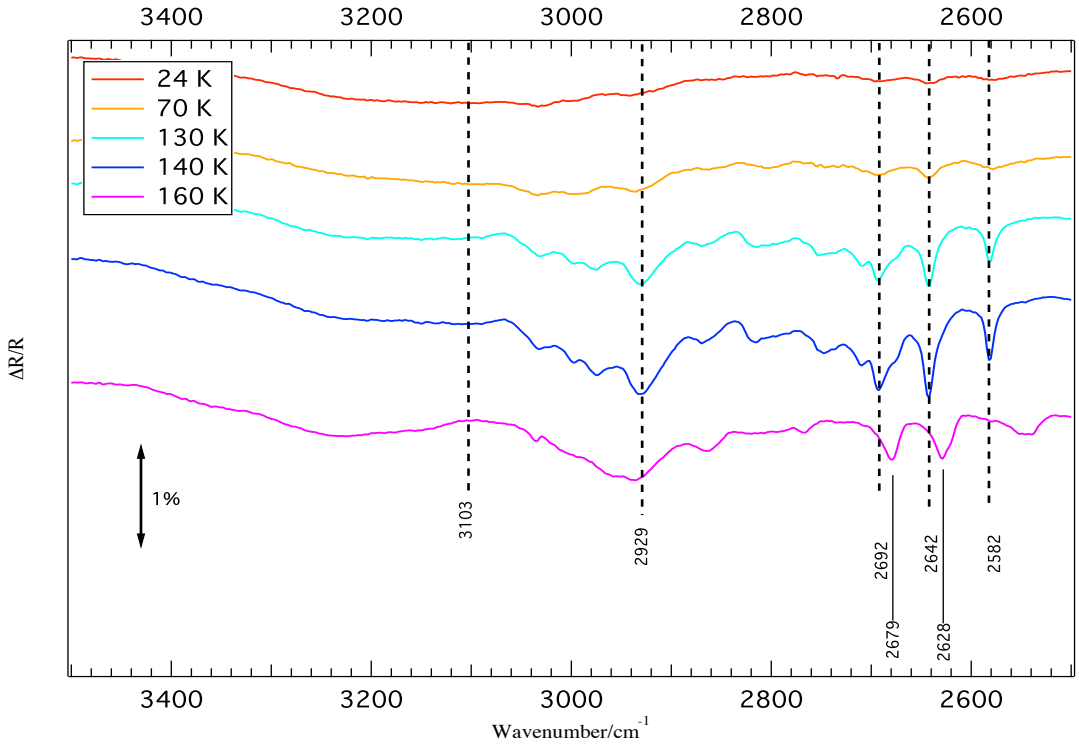

Figure 5.4. Thermal evolution of 100 L of CH_3COOH deposited on HOPG, at 20 K, between 2500-3000 cm^{-1}. Temperature ranges from 24 K to 160 K.

All the vibrational feature changes discussed above indicate clearly that a phase change, from amorphous to crystalline acetic acid ice composed predominantly of chain–like polymers, takes place upon heating of the ice. This phase change has been clearly showed by the TPD study of the desorption of acetic acid from an ASW surface (see section 4.3). The TPD study of acetic acid desorption does not show evidence of crystallization because the crystallization temperature is lower than the desorption temperature. Therefore, when acetic acid starts desorbing, it has already crystallized and it desorbs as multilayers of chain-like polymers.

5.2 RAIRS of Acetic Acid on H_2O

Figure 5.5 shows the thermal evolution of 40 L of acetic acid deposited on top of 100 L of ASW.

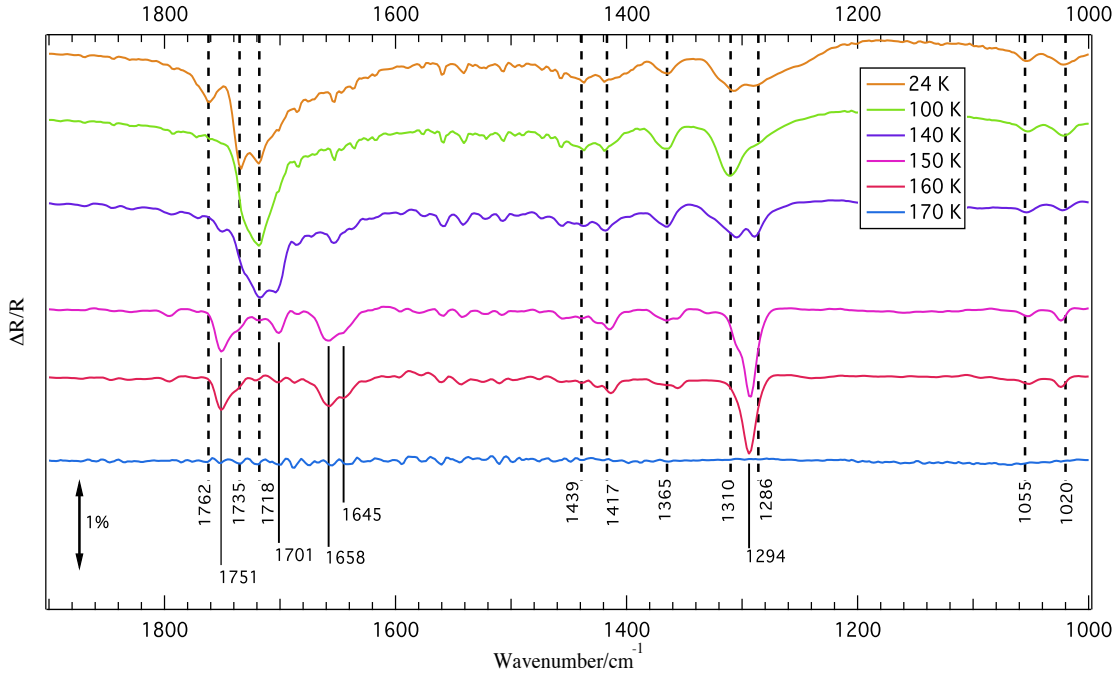

Figure 5.5. RAIR spectra of the thermal evolution of 40 L of CH_3COOH adsorbed on 100 L of pre-deposited ASW at 20 K, between 1000-1900 cm^{-1}.

The dashed vertical lines indicate the main vibrational transitions that are common with the spectrum of 100 L of acetic acid deposited on HOPG in figure 5.1. At 24 K, the vibrational features of acetic acid deposited on water are analogous to those of acetic acid deposited directly on HOPG. The differences between the 24 K spectra in figure 5.1 and the 24 K spectra in figure 5.5 are essentially due to the different absolute intensity of the transitions caused by the different amounts of acetic acid dosed onto the sample (100 L against 40 L).

Differences compared to acetic acid deposited directly onto HOPG begin to appear as the temperature increases. The first noticeable change in figure 5.5 is evident at 100 K. The peak at 1735 cm^{-1} subsides in favour of the peak at 1718 cm^{-1}. This behaviour is also observed when acetic acid is deposited on HOPG (figure 5.1), but in that case it happens at a higher temperature. The peak at 1718 cm^{-1} is assigned to the C=O stretch of crystalline acetic acid. The fact that this appears at lower temperatures is a strong indicator that the interaction with the underlying water ice affects the behaviour of acetic acid. This is in agreement with the TPD studies (chapter 4, section 4.3) of acetic acid deposited on water. Such studies showed evidence of strong interaction between acetic acid and water. At 150 K a new peak, not observed in the pure acetic acid study, appears in the C=O stretch region at 1701 cm^{-1}. This goes on to form a broad complex band combined with the features at 1718 cm^{-1} and 1735 cm^{-1}. At 150 K this

complex disappears leaving a single band at 1701 cm^{-1} and the peak at 1751 cm^{-1}, which is analogous (slightly shifted) to the 1749 cm^{-1} band observed in the range 140-160 K for acetic acid on HOPG. The peak at 1701 cm^{-1} is not reported in any previous study, therefore a precise assignment cannot be made. Bertin *et al.* [119] report a peak around 1700 cm^{-1} for acetic acid adsorbed on crystalline water, but its behaviour is more similar to the peak at 1718 cm^{-1}. It can be observed, however, that the 1701 cm^{-1} feature appears at 140 K, when water starts desorbing, and it disappears at 160 K, when water has completely desorbed. It is therefore possible that this peak is representative of the interaction between acetic acid and water. Consequently the 1701 cm^{-1} feature can be assigned to acetic acid hydrates. Further evidence supporting this assignment is discussed with reference to the acetic acid/water mixtures (next section).

The rest of the spectrum behaves very similarly to what is observed for acetic acid adsorbed on HOPG. The doublet due to polymeric acetic acid still appears at 160 K, although in a slightly shifted position: 1645 cm^{-1} and 1658 cm^{-1} compared to 1643 cm^{-1} and 1660 cm^{-1}. The C–O stretch peak (1294 cm^{-1}) becomes prominent at 150-160 K. Compared to the equivalent acetic acid on HOPG experiment (1292 cm^{-1}), this peak is slightly shifted and more intense with respect to the ν C=O (1749 cm^{-1}). The behaviour of the remaining features, including the ones at high wavenumbers (figure 5.6), is almost identical to that observed for acetic acid on HOPG. Desorption temperatures for acetic acid deposited on ASW are comparable to those of acetic acid deposited on HOPG. This is consistent with what is observed in the analogous TPD studies, where acetic acid always desorbs in the same range of temperatures (140-170 K) depending on the coverage.

The study of acetic acid adsorbed on ASW has revealed three important aspects of the interaction between acetic acid and water:

1. Water molecules can strongly interact with acetic acid molecules, as expected from the TPD analysis. This is indicated by the differences in the RAIR spectra upon annealing between the case of pure acetic acid ice and the case of acetic acid deposited on ASW. The strong CH_3COOH/H_2O interaction can potentially lead to the formation of hydrates as suggested by the feature at 1701 cm^{-1}, in figure 5.5.
2. The C=O stretch transition is again the feature most sensitive to the environment in which the molecule is situated.

3. Acetic acid undergoes crystallisation even when adsorbed on top of ASW and it remains on the surface of the sample even after the water has desorbed. This is consistent with the TPD study.

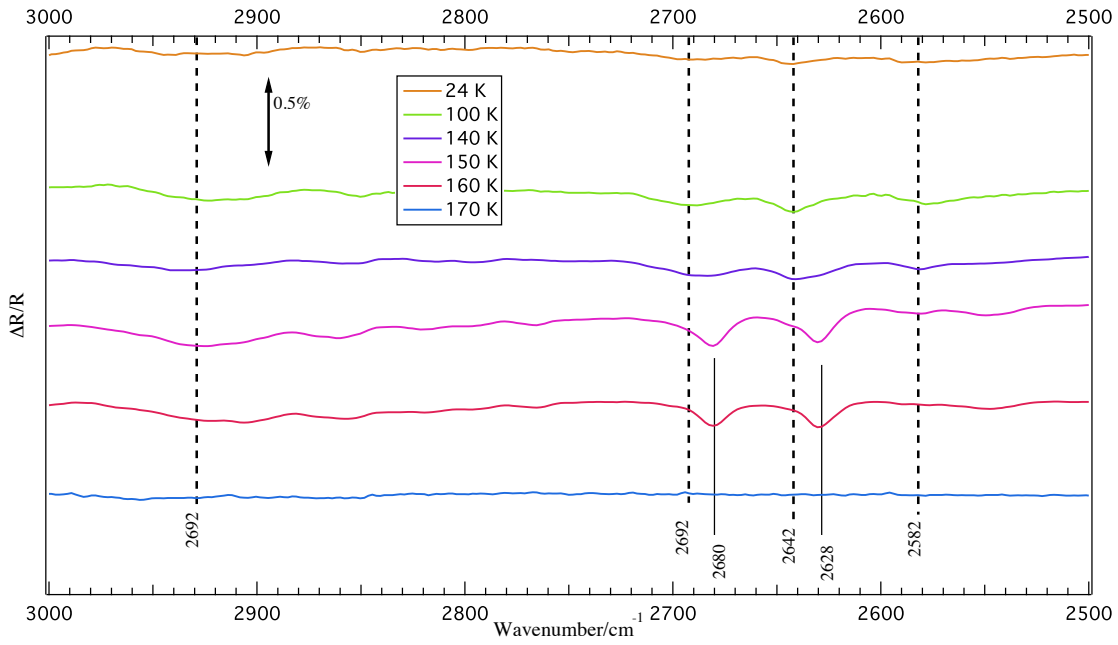

Figure 5.6. RAIR spectra of the thermal evolution of 40 L of CH_3COOH adsorbed on 100 L of pre-deposited ASW at 20 K, in the 2500-3000 cm^{-1} range.

5.3 RAIRS of Acetic Acid and H_2O mixtures

Figure 5.7 shows the comparison of two spectra corresponding to a 25% and 40% mixture of acetic acid and water, at 20 K. These concentrations are quite high to be of direct astrophysical relevance. They were chosen in order to be able to see the weak bands of acetic acid mixed with water. The dashed lines show the transitions of acetic acid deposited on bare HOPG. Several differences when compared to the IR spectra of acetic acid on HOPG and acetic acid on ASW are immediately evident, and this is a further demonstration that acetic acid interacts strongly with water.

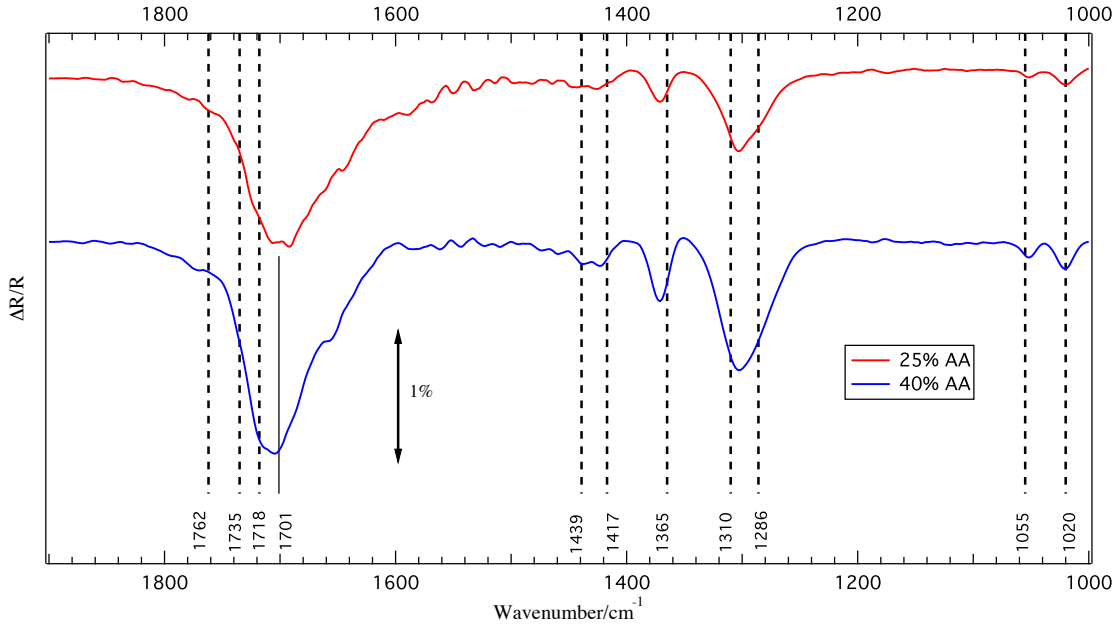

Figure 5.7. RAIR spectra of 25% and 40% mixtures of CH_3COOH and ASW at 20 K, in the 1000-1900 cm^{-1} range. Dashed lines represent the transitions of pure acetic acid on HOPG.

The most striking difference is shown in the ν C=O area where the three main features at 1718, 1735 and 1762 cm^{-1} are not the most prominent anymore. In their place there is a very broad (1600-1780 cm^{-1}) feature which in the case of the 25 % mixture, peaks at ~1701 cm^{-1}. In the previous section, a feature at 1701 cm^{-1} was tentatively assigned to acetic acid hydrates based on its thermal behaviour. The appearance of a broad feature, in the 25% CH_3COOH/H_2O mixture, that is centred on the same value is a further indication that this assignment is correct. For the higher concentration mixture (40%), the centre of the broad ν C=O peak moves slightly back towards the values belonging to anhydrous acetic acid (1718-1735 cm^{-1}). This is expected since increasing the amount of acetic acid increases the number of CH_3COOH/CH_3COOH bonds compared to the amount of CH_3COOH/H_2O bonds.

The ν C–O double feature at 1286 and 1310 cm^{-1} has also merged into a broader feature centred on ~1304 cm^{-1} in the acetic acid/water miture. The δ CH_3 (1365 cm^{-1}) band shifts to a higher wavenumber (1371 cm^{-1}). The remaining features are not noticeably changed compared to either acetic acid adsorbed on HOPG or adsorbed on ASW.

Figure 5.8 shows the behaviour of the 40% ice mixture when it is heated up to 150 K. The difference in the evolution of the bands compared to the spectra of acetic acid on HOPG (figure 5.3) and acetic acid on ASW (figure 5.5) is striking.

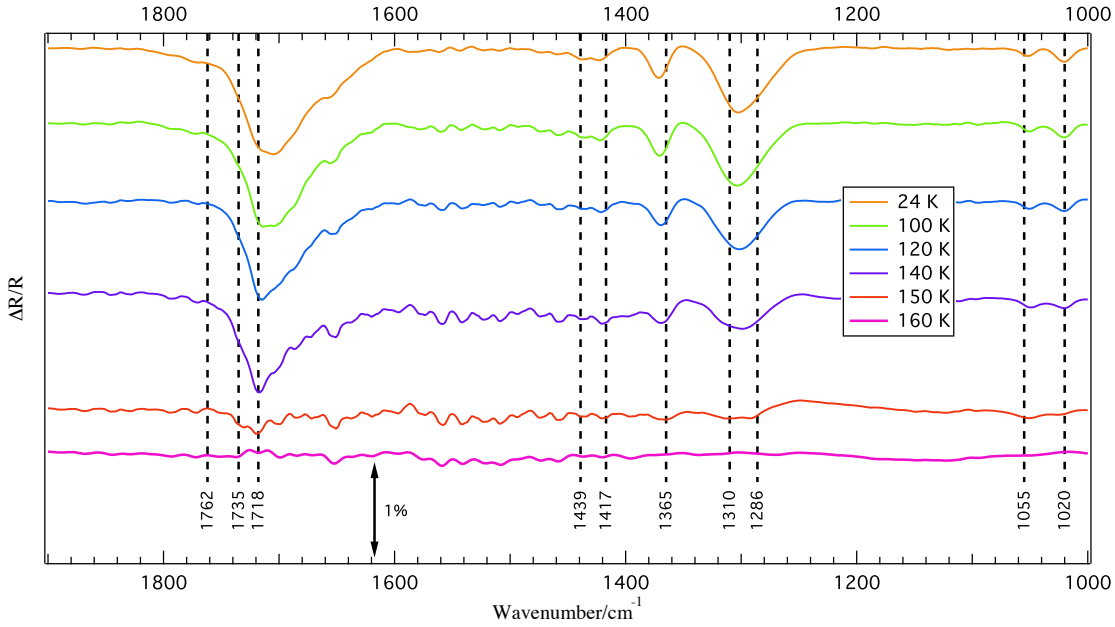

Figure 5.8. RAIR spectra of the thermal evolution of a 40% mixture of CH_3COOH and ASW, in the 1000-1900 cm^{-1} range.

While the latter spectra showed a variety of modifications (shifting, appearance of new features) during annealing, in figure 5.8 the only prominent modification is a shift of the broad ν C=O feature to 1718 cm^{-1}. The shift of the ν C=O feature is probably due to a partial polymerization of the acetic acid. However, the absence of the marked features that appear during heating (in the case of pure acetic acid and acetic acid on ASW) is an indication that acetic acid crystallization is substantially inhibited when it is diluted in a water matrix. This could be due to the fact that the interaction between water and acetic acid is so intense, as previously discussed in the TPD chapter and in the RAIRS sections shown above. Alternatively, considering that crystallization is a bulk effect, the amount of acetic acid in the water matrix might not be enough to effectively polymerize.

Once the water has desorbed (160 K), the acetic acid features disappear. This is expected since the TPD study of CH_3COOH/H_2O mixtures showed that acetic acid co-desorbs entirely with water.

5.4 RAIRS of pure Methyl Formate

Figure 5.9 shows the spectra of 40 L and 100 L of methyl formate deposited on top of HOPG at 20 K. These dosages correspond to multilayers of methyl formate as indicated by the TPD study in the previous chapter. The spectra show 6 vibrational bands. These were assigned by comparison with the pre-existing literature [95,119,123]

and are summarized in table 5.2. The most prominent vibrational band is, similarly to the case of acetic acid, the C=O stretch band at 1736 cm^{-1}. The second most intense vibrational bands appear at 1173 cm^{-1} and at 1227 cm^{-1} and are assigned to the CH_3 rocking and C–O stretch modes respectively. Two small peaks at 1435 and 1452 cm^{-1} are also visible. They are assigned to the symmetric and asymmetric CH_3 bending respectively. Finally a peak at 916 cm^{-1} is shown. This is assigned to the C–O stretching mode. No peaks above 1736 cm^{-1} are clearly detectable.

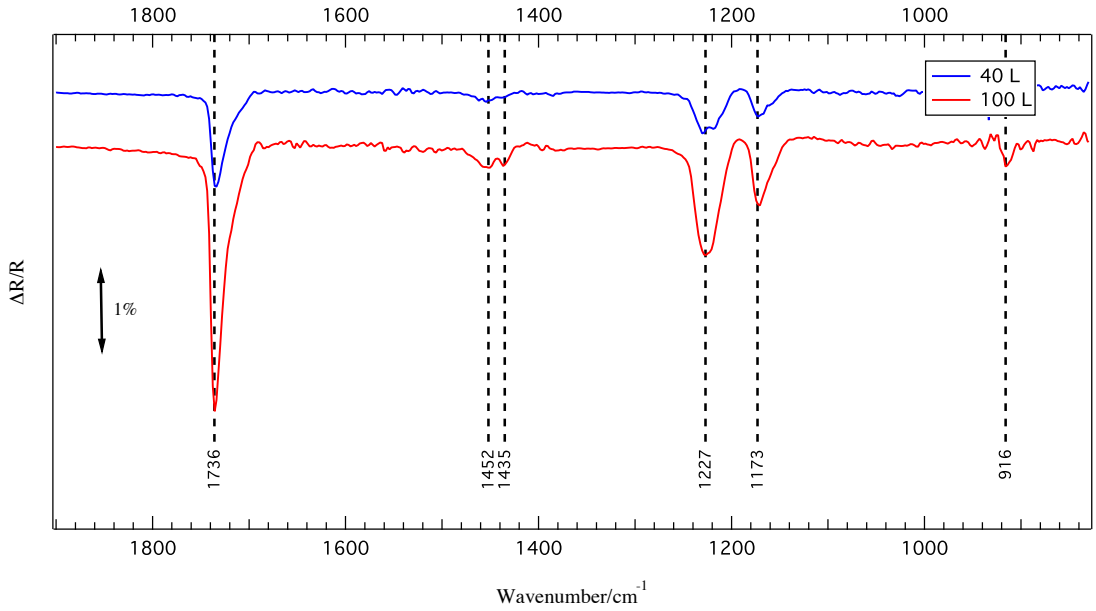

Figure 5.9. RAIR spectrum of $HCOOCH_3$ deposited on HOPG at 20 K. Comparison of two exposures: 40 L and 100 L.

Assignment	$HCOOCH_3$ on HOPG This work	$HCOOCH_3$ on crystalline water [119]	$HCOOCH_3$ on Ni [123]	Gas phase [95]
ν C-O	916		916	921
ρ CH_3	1173	1222	1182	1168
ν C_c–O	1227	1391	1262	1207
δ_s CH_3	1435	1433	1442	1445
δ_{as} CH_3	1452	1450	1458	1454
ν C=O	1736-1705	1726	1659	1754

Table 5.2. Assignment of the spectral features of multilayer $HCOOCH_3$ adsorbed on HOPG at 20 K. All values are in cm^{-1}. Abbreviations/symbols: ρ, rocking, ν, stretching, δ, bending; s, symmetric, as, asymmetric.

Figure 5.10 shows the evolution of the spectra of 100 L of methyl formate upon heating up to 115 K. Unlike acetic acid that exhibited dramatic changes upon heating, methyl formate only shows a change in the C=O stretch transition at 1736 cm^{-1}, which ends up shifting to a lower frequency (1705 cm^{-1}) at 105 K.

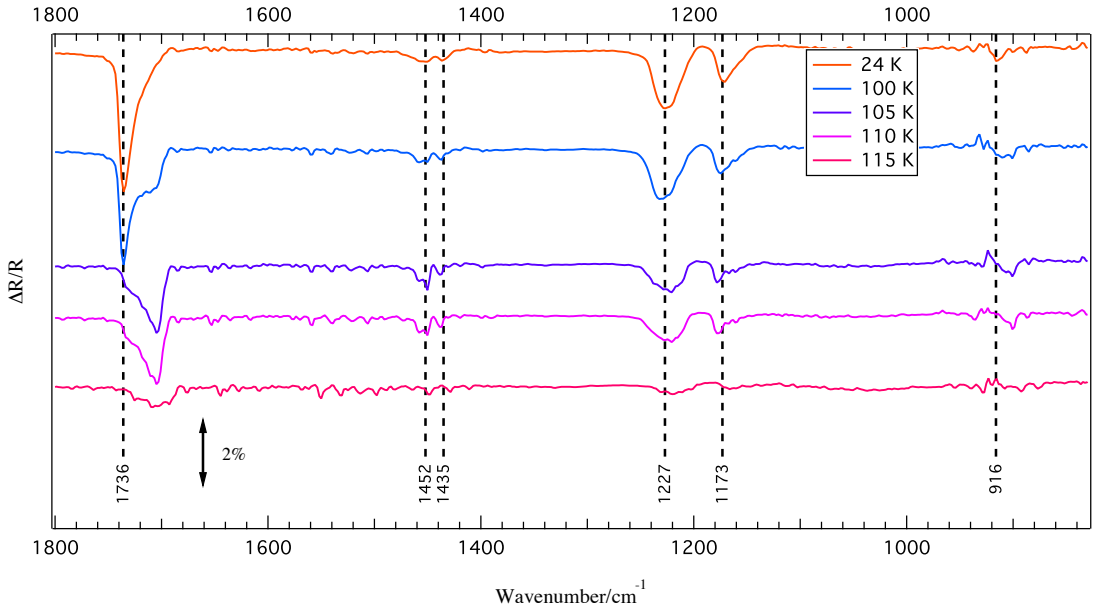

Figure 5.10. Thermal evolution of 100 L of $HCOOCH_3$ deposited on HOPG, at 20 K, in the range of 1000-1900 cm^{-1}. Temperature ranges from 24 K to 160 K.

The C=O stretch band begins to change shape at 100/105 K when the formation of a shoulder at 1705 cm^{-1} occurs. The C=O stretch feature is believed to be very sensitive to molecular interactions [119]. Its changing in shape with increasing temperature therefore indicates a change in the intermolecular interactions in the methyl formate ice, caused by the temperature increase. The shift in the C=O stretching mode from 1736 to 1705 cm^{-1} is therefore attributed to a phase change from an amorphous solid phase (grown on HOPG at 20 K) to a crystalline phase. This is supported by the similarity of the 1705 cm^{-1} band to the bands observed at 1710 and 1708 cm^{-1} for crystalline methyl formate [136]. The other vibrational features do not show remarkable changes due to the phase change. All the vibrational bands start weakening at ~100 K, this is due to the fact that methyl formate starts desorbing at that temperature. At 115 K, the vibrational features of methyl formate are still visible, although the majority of it has already desorbed. At higher temperature (120 K) methyl formate desorption is complete. This is in agreement with what observed in the TPD study of methyl formate desorption from HOPG. As in the case of acetic acid, the ν C=O transition is the most sensitive to changes in the arrangement of the molecules.

5.5 RAIRS of Methyl Formate on H_2O

Figure 5.11 shows the modifications that the methyl formate on water spectra undergo when the temperature is increased from 24 K to 130 K. The spectrum of 40 L

of methyl formate adsorbed on water at 20 K does not show discernable differences compared to the spectrum of 100 L of pure methyl formate adsorbed on HOPG. This can be appreciated in figure 5.11 where the dashed lines mark the position of the IR features of methyl formate adsorbed on HOPG.

Several changes are noticeable, mostly in the ν C=O area (1640-1750 cm^{-1}) and in the ρ CH_3 and ν C–O features (1227 and 1173 cm^{-1}, respectively). The C=O stretch feature shifts to 1719 cm^{-1} starting from 100 K. The peak at 1719 cm^{-1} is broadened compared to the feature at 1736 cm^{-1}, at 24 K, but it gets slightly sharper until 115 K. At temperatures above 115 K, the feature at 1736 cm^{-1} starts becoming stronger until, at 130 K, it becomes the dominant band (in the ν C=O region) because the feature at 1719 cm^{-1} disappears completely.

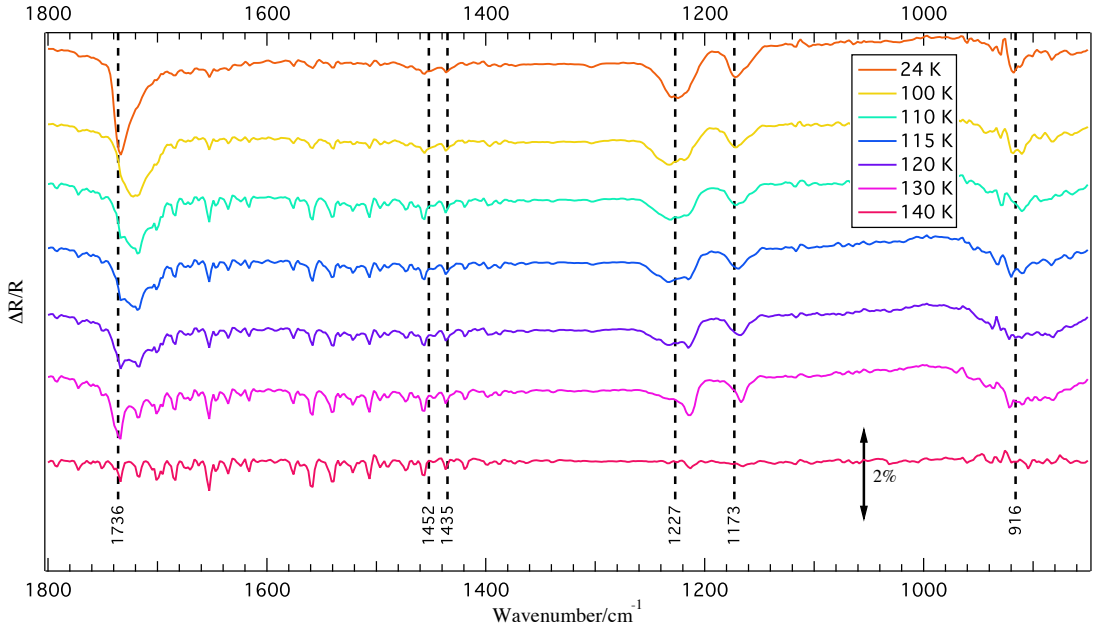

Figure 5.11. RAIR spectra of the thermal evolution of 40 L of $HCOOCH_3$ adsorbed on 100 L of pre-deposited ASW at 20 K.

The thermal behaviour of the vibrational band at 1719 cm^{-1} is analogous to that of the feature at 1705 cm^{-1} in the case of pure methyl formate (figure 5.10). Therefore, it can be assigned to ν C=O of crystallized methyl formate on the surface of the ASW. Its disappearance at temperatures higher than 120 K is due to the desorption of the methyl formate layer from the surface of the water. This is in agreement with the TPD results for the same ice configuration. The ν C=O transition is still visible at 130 K, while in the case of pure $HCOOCH_3$ ice it disappears for temperatures higher than 115 K. This is due to the fact that part of the methyl formate is trapped in the ASW and will only

desorb (volcano effect) at temperatures around 140 K when the ASW to CI phase transition occurs.

The ρ CH_3 (1227 cm^{-1}) and ν C–O (1173 cm^{-1}) peaks broaden from 100 to 115 K due to methyl formate crystallization. At higher temperatures, they shift to lower wavenumbers of 1213 and 1166 cm^{-1}, respectively. These features appear sharper at 130 K. The ρ CH_3 and ν C–O did not behave in this way in the case of methyl formate adsorbed on HOPG. Considering that at 130 K methyl formate has desorbed from the surface of the water, the new features at 1213 cm^{-1} and 1166 cm^{-1} are assigned to ρ CH_3 and ν C–O of methyl formate trapped in water. These features essentially disappear at 140 K when water crystallizes. Water crystallization is confirmed by examination of its O-H stretch feature between 3000 and 3600 cm^{-1}, figure 5.12.

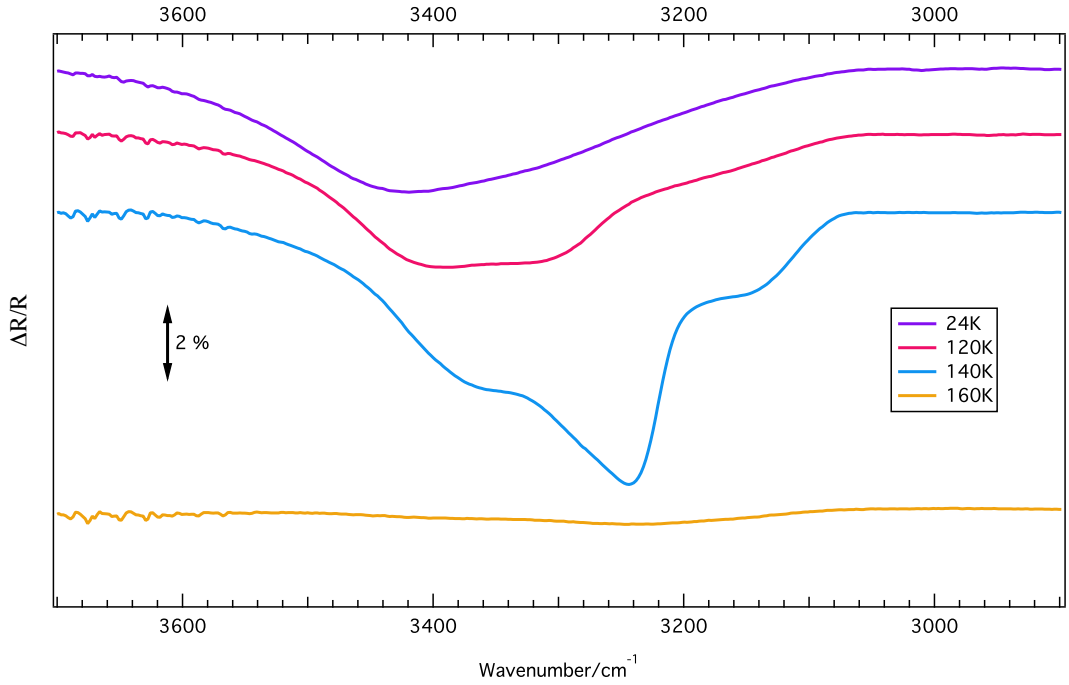

Figure 5.12. RAIR spectra of the thermal evolution of 100 L of H_2O between 2900 and 3700 cm^{-1}.

5.6 RAIRS of Methyl formate and H_2O mixtures

Figure 5.13 shows the RAIR spectra of a 30/70% mixture of methyl formate/water. The dashed lines represent the positions of the vibrational transitions in the case of pure methyl formate ice.

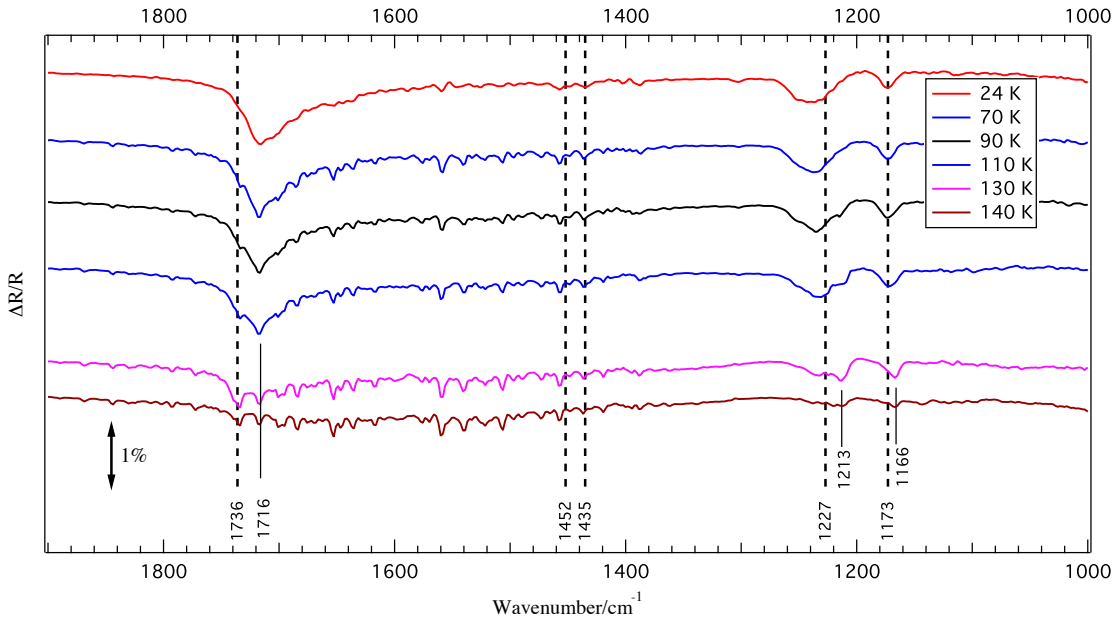

Figure 5.13. RAIR spectra of the thermal evolution of a 30% mixture of 100 L of $HCOOCH_3$ and ASW.

The ν C=O transition is very broad and shifted to 1716 cm^{-1}, compared to the pure ice value of 1736 cm^{-1}. Its position and shape remain fairly stable throughout the heating process up to 110 K. At 130 K, when the water ASW to CI transition begins to take place, the peak shifts to 1736 cm^{-1}.

The ρ CH_3 peak appears at 1242 cm^{-1}, compared to 1227 cm^{-1} in the pure methyl formate case. The ν C–O peak is in the same position as the pure ice case, 1173 cm^{-1}. Interestingly, the position of these two peaks shifts back to 1213 cm^{-1} and 1166 cm^{-1}, respectively, at a temperature of 130 K. These peak positions correspond to the methyl formate bands observed when layered methyl formate/water has been annealed to 130 K (figure 1.10). The assignment, made in the previous section, of the peaks at 1213 cm^{-1} and 1166 cm^{-1} to the ρ CH_3 and ν C–O modes of methyl formate trapped in water can therefore be confirmed.

5.7 RAIRS of pure Glycolaldehyde

Figure 5.14 shows the spectrum of 100 L of pure glycolaldehyde deposited on HOPG at 20 K, in the range 850-1900 cm^{-1}. This amount of glycolaldehyde corresponds to a multi-layered ice, as confirmed by TPD studies (chapter 4). Lower exposures are not shown because, given the intensity of even the strongest transitions, the signal to noise ratio is particularly low.

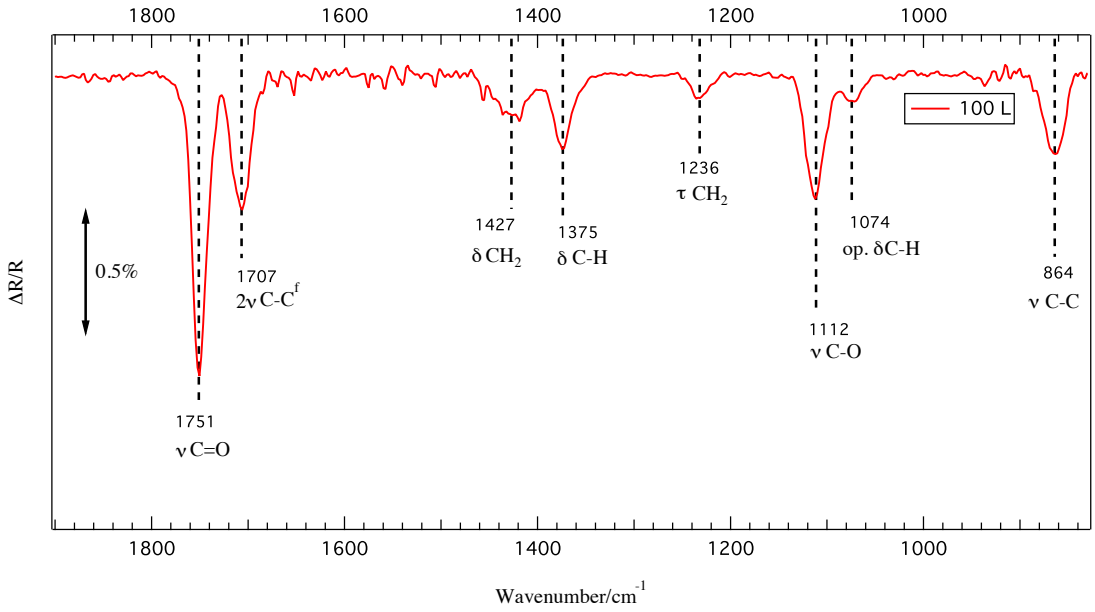

Figure 5.14. RAIR spectrum of 100 L of $HCOCH_2OH$ deposited on HOPG at 20 K, in the range from 1000 to 1900 cm^{-1}. The main vibrational frequencies and their assignments are also shown. Abbreviations/symbols: ρ, rocking, ν, stretching, δ, bending, τ, twisting.

The vibrational transitions have been assigned according to previous studies [126,137] and are summarized in table 5.3. As is the case for acetic acid and methyl formate, the most intense transition is assigned to the C=O stretching mode which is found at 1751 cm^{-1}. Very close, in terms of position, a vibrational band appears at 1707 cm^{-1}. This band is assigned to a C-C stretch overtone (the normal mode being at 864 cm^{-1}). Normally, an overtone should be less intense compared to the normal vibrational mode, which is not the case here. The intensity of this overtone band is due to the Fermi resonance between the 2ν C–C mode and the ν C=O mode [132] (the band will hereafter be referred to as 2ν $C–C^f$). Fermi resonances appear whenever a fundamental vibrational level lies very close to an overtone (or combination) level with the same wave function symmetry [138]. When this happens, the two original levels mix, producing two new levels whose wave functions are linear combinations of the initial ones. The net effect is that the energy of the fundamental mode is redistributed

between the two levels, increasing the intensity of the overtone (or combination) level, and the spectral separation between the two vibrational bands is increased [138]. The Fermi resonance in glycolaldehyde has been previously detected and computationally investigated both in the gas phase and the solid phase [126,132]. The positions of the ν C=O and the 2ν C–C^{f} band detected in this work are consistent with what is found in the literature, see table 5.3.

Assignment	$HCOCH_2OH$ on HOPG This work	$HCOCH_2OH$ on Al [126]	$HCOCH_2OH$ in pH_2 matrix [137]	Calculations MP2/6-311++G(d,p) [137]
ν C–C	864	861	859	867
op. δ C–H	1074	1073		1090
ν C–O	1112	1110	1110	1116
τ CH_2	1232	1231		1235
ip. δ C–H	1375	1372	1364	1378
δ CH_2	1427	1421	1424	1462
2ν C–C^{f}	1707	1706	1703	1711
ν C=O	1751	1747	1750	1753
ν CH_2	2873		2850/2880	2921
ν O–H	3390		3538	3624

Table 5.3. Assignment of the spectral features of multilayers of $HCOCH_2OH$ adsorbed onto HOPG at 20 K. All values are in cm^{-1}. Abbreviations/symbols: ρ, rocking, ν, stretching, δ, bending, τ, twisting; s, symmetric, as, asymmetric.

Other detected features (see figure 1.14) include a C–O stretching (1112 cm^{-1}) band, CH in-plane and out of plane bending modes (respectively, 1375 and 1074 cm^{-1}), CH_2 bending and twisting modes at 1427 and 1236 cm^{-1}, and the ν C–C stretch mode at 864 cm^{-1}.

Figure 5.15 shows the spectrum of 100 L of glycolaldehyde dosed onto HOPG at 20 K, in the wavenumber range 2650-3700 cm^{-1}.

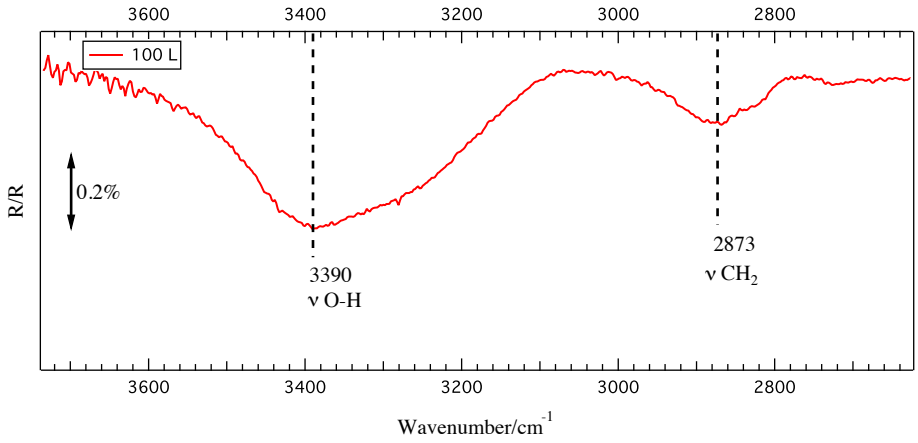

Figure 5.15. RAIR spectrum of 100 L of $HCOCH_2OH$ deposited on HOPG at 20 K, from 2659 to 3700 cm^{-1}. The main vibrational frequencies and their assignments are also shown. Abbreviations/symbols: ν, stretching.

Two additional vibrational features are visible at 2873 cm^{-1} (CH_2 stretching) and 3390 cm^{-1} (OH stretching). These features are very weak (0.2%) and they are in a region in which water has very intense vibrational bands. For these reasons, the study of the thermal behaviour of pure glycolaldehyde ices and in the presence of water will focus on the vibrational range spanning from 840 cm^{-1} to 1900 cm^{-1}.

Figure 5.16 shows the thermal evolution of the 100 L glycolaldehyde spectrum when the sample is sequentially heated to 160 K. In contrast to acetic acid and methyl formate, the spectra remain relatively unchanged during the annealing process. The only evident change is in the broadening of the 2 ν $C–C^f$ peak at 1707 cm^{-1}, at 140 K. This could be due to a phase change from amorphous to crystalline glycolaldehyde. The TPD study of glycolaldehyde adsorbed on HOPG also showed evidence of glycolaldehyde crystallization taking place between 145 and 150 K. The difference in the temperature compared to the RAIRS study is probably due to the difference in the heating procedure. Evidence of a glycolaldehyde phase change has also been previously shown in the literature by Hudson *et al.* [126].

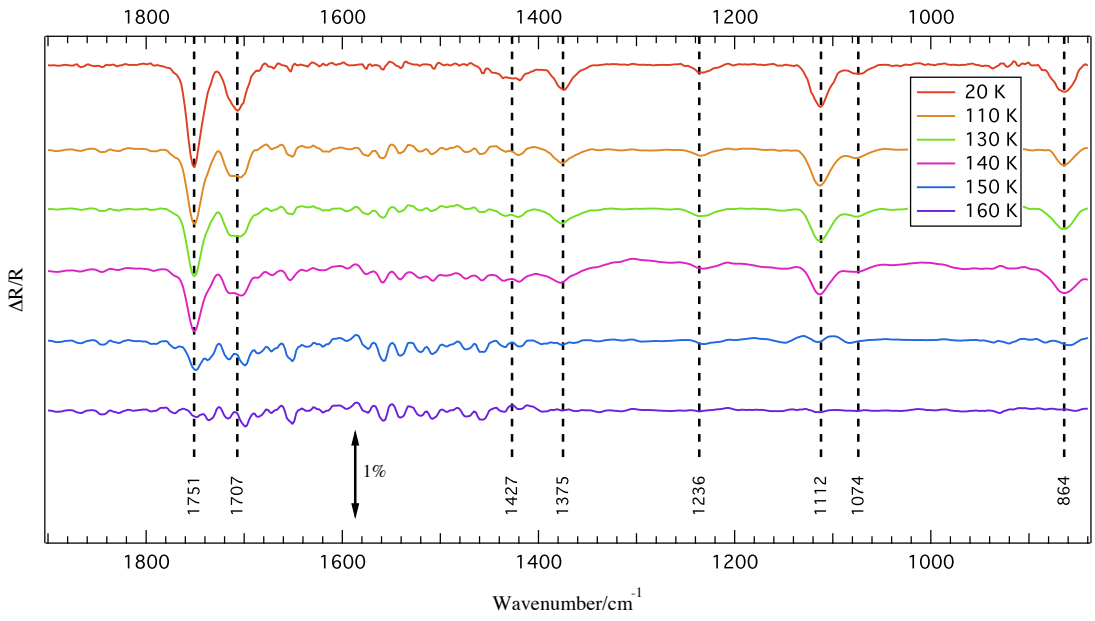

Figure 5.16. RAIR spectra of the thermal evolution of 100 L of pure $HCOCH_2OH$.

The remaining features do not undergo substantial modifications during the heating process. At 160 K, the desorption of glycolaldehyde is complete. This is in agreement with TPD studies that showed that high dosages of glycolaldehyde (≥ 50 L) desorb in the range 160-165 K.

5.8 RAIRS of Glycolaldehyde on H_2O

Figure 5.17 shows the behaviour of the IR spectrum of 40 L of glycolaldehyde deposited on the surface of water and heated up to 160 K. The dashed lines represent the vibrational bands of pure glycolaldehyde adsorbed on HOPG. The main IR features of glycolaldehyde adsorbed on water are analogous to those of glycolaldehyde adsorbed on HOPG. The main difference is in a wide shoulder between 1600 and 1700 cm^{-1}. This shoulder is visible at 20 K, but tends to disappear for temperatures higher than 100 K. This broad feature is due to the interaction of the lower layers of glycolaldehyde with the upper layers of ASW. That the interaction between glycolaldehyde and ASW is the cause of this feature will be confirmed by the RAIR study of glycolaldehyde/water mixtures shown in the next section.

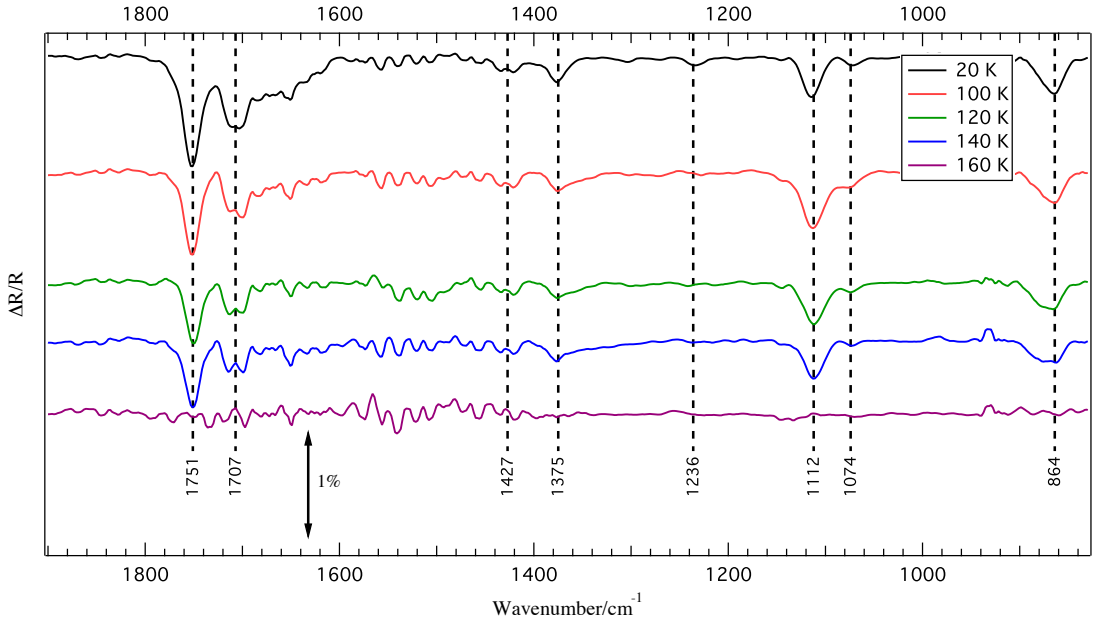

Figure 5.17. RAIR spectra of the thermal evolution of 40 L of $HCOCH_2OH$ adsorbed on 100 L of pre-deposited ASW at 20 K.

As in the case of the thermal processing of the pure glycolaldehyde ice, the spectral features remain unchanged. The only change appears to be in the 2 ν C–C^f peak profile at 1707 cm^{-1} that broadens and changes shape as the temperature increases. This could be due to the crystallization of glycolaldehyde, as observed for pure glycolaldehyde ice (previous section). However, given the smaller amount of glycolaldehyde deposited compared to 100 L, the signal to noise ratio in the case of 40 L of glycolaldehyde (on HOPG and on ASW) is really low. Therefore the changes in the shape of the feature at 1707 cm^{-1} could have been influenced by background noise.

The desorption of glycolaldehyde is again complete at 160 K. This is in agreement with the TPD study that showed a complete codesorption of water and glycolaldehyde. The desorption temperatures of glycolaldehyde and water are indeed very similar, therefore codesorption of the two species is expected.

5.9 RAIRS of Glycolaldehyde and H_2O mixtures

Figure 5.18 shows a comparison between the spectrum of 40 L of glycolaldehyde deposited on top of ASW and the spectrum of a 100 L 34% mixed $HCOCH_2OH/H_2O$ ice, at 20 K.

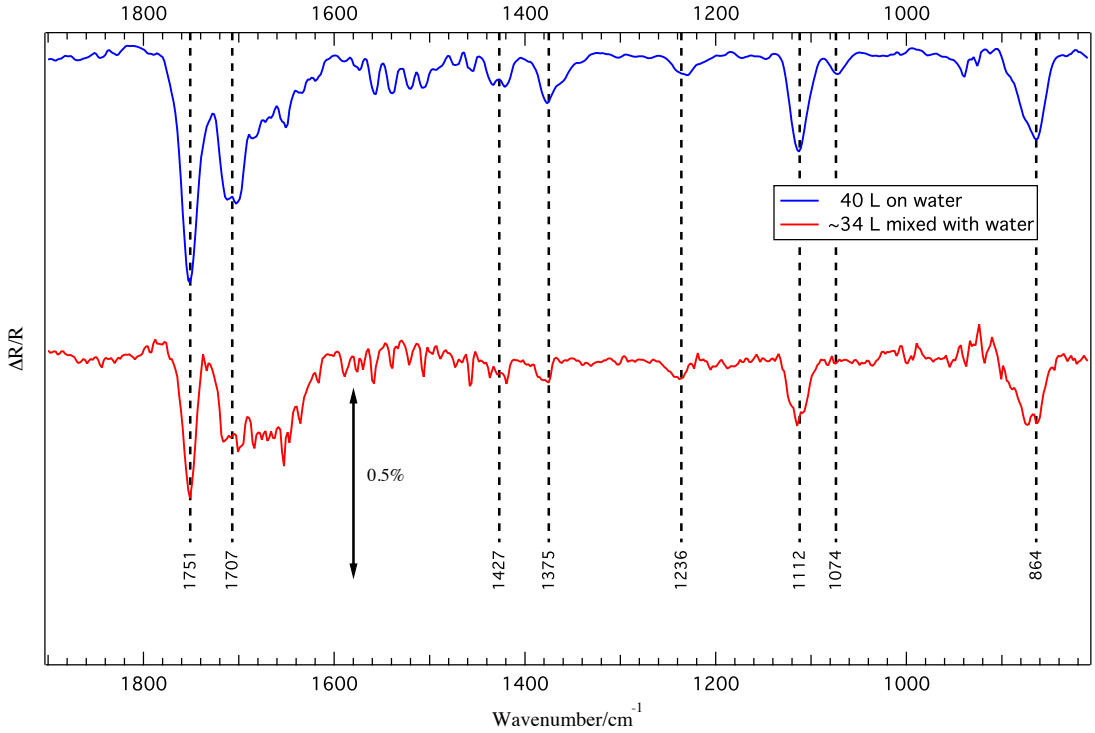

Figure 5.18. Comparison between the spectra of 40 L of $HCOCH_2OH$ deposited on top of ASW and the spectra of $HCOCH_2OH/H_2O$ 34% mixture, at 20 K.

The C=O stretch (1751 cm^{-1}) and its close Fermi resonance with the first C-C stretch overtone (1707 cm^{-1}) are, as expected, the prominent peaks. It is immediately evident that the overtone band profile is markedly different compared to the case of glycolaldehyde deposited on the surface of ASW. The overtone band is much broader and it has the appearance of a plateau extending from 1730 cm^{-1} to 1610 cm^{-1}. Considering that also the C-C stretch mode at 864 cm^{-1} appears broadened, it can be speculated that the embedding of the glycolaldehyde in the water matrix has a direct influence on the C-C stretch vibration and on its Fermi resonant overtone. As to how this happens, no indications can be easily inferred from the present study. A potential

cause could be the formation of different (and differently oriented in the ice) glycolaldehyde/water hydrates. Aviles-Moreno *et al.* [139] performed an *ab initio* study of glycolaldehyde water hydrates. They found several stable $HCOCH_2OH/H_2O$ conformers, the most stable of them involving two hydrogen bonds between the water molecule and the hydroxyl and aldehyde groups. They then proceeded to computationally simulate the vibrational spectra of the two most stable conformers, but the main differences were in the < 600 cm^{-1} region, not in the 1700 cm^{-1} region. This suggests that whatever is causing the broadening of the 2ν C–C^f is probably a bulk effect of the ice that was not simulated in the theoretical study.

Figure 5.19 shows the RAIR spectra of a 34% mixture of glycolaldehyde and water deposited on the sample at 20 K and then heated up to 150 K. As usual, the dashed lines mark the position of the vibrational transitions in the case of pure glycolaldehyde ice.

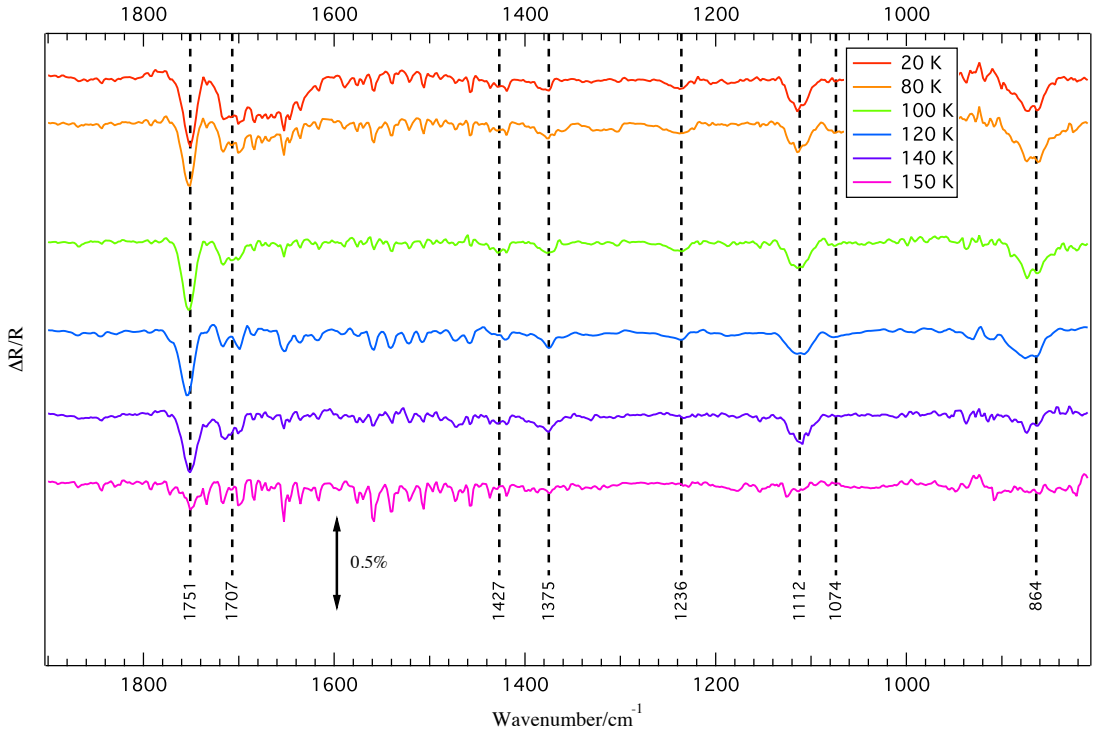

Figure 5.19. RAIR spectra of the thermal evolution of a 34% mixed $HCOCH_2OH/H_2O$, 100 L ice, dosed on HOPG.

The Fermi resonance band (1730-1610 cm^{-1}) broadness decreases at 100 K. At this temperature the ν C=O and the 2ν C–C^f doublet is more similar to the case of glycolaldehyde deposited on water. This is probably an indication of a structural change in the ice morphology, although it is not clear exactly how the ice is changing. The change cannot be assigned to the ASW to CI transition because the temperature is still

too low. The water phase change, in fact, happens at ~140 K and this is marked in figure 5.19 by the weakening of the C–C stretch band (864 cm^{-1}).

Apart from the variations in the C–C bands, the other vibrational bands simply decrease as the temperature increases. Complete desorption of glycolaldehyde happens at 150 K at the same time as the water desorbs. This is in agreement with what was seen in the TPD study of glycolaldehyde/water mixtures.

5.10 Concluding remarks

In summary, RAIR spectra of acetic acid, methyl formate and glycolaldehyde in their pure form, when deposited on top of a thick layer of ASW and when they were in mixtures with water have been collected. For each potential configuration, the spectral evolution upon annealing the sample has also been obtained in the present work.

It has been found that, despite some similarities, the spectra of the isomers are fairly different compared to each other. In the same way their behaviour upon annealing is quite different. In all experiments in which the isomers were embedded in a water matrix, no noticeable alterations to the water signal, between 3000 and 3900 cm^{-1}, due to the interaction with the isomers was observed.

Figure 5.20 shows a comparison between the spectra of 100 L of each of the studied molecules. The first noticeable thing is that all of the species have a prominent spectral feature in the 1680-1800 cm^{-1} region, associated with the C=O stretch. This spectral feature has been shown to be generally quite sensitive to the morphology of the ice (whether pure or in the presence of water). In the case of acetic acid, the ν C=O feature is complex (peaking at 1736 cm^{-1}) and is formed from the contributions of acetic acid molecules arranged as monomers, dimers and polymers. In the case of methyl formate, the C=O stretch is a very sharp and intense feature peaking at 1736 cm^{-1}. Finally, for glycolaldehyde the ν C=O band is blue shifted to 1751 cm^{-1} due to a Fermi resonance interaction with the C–C stretch overtone (1070 cm^{-1}).

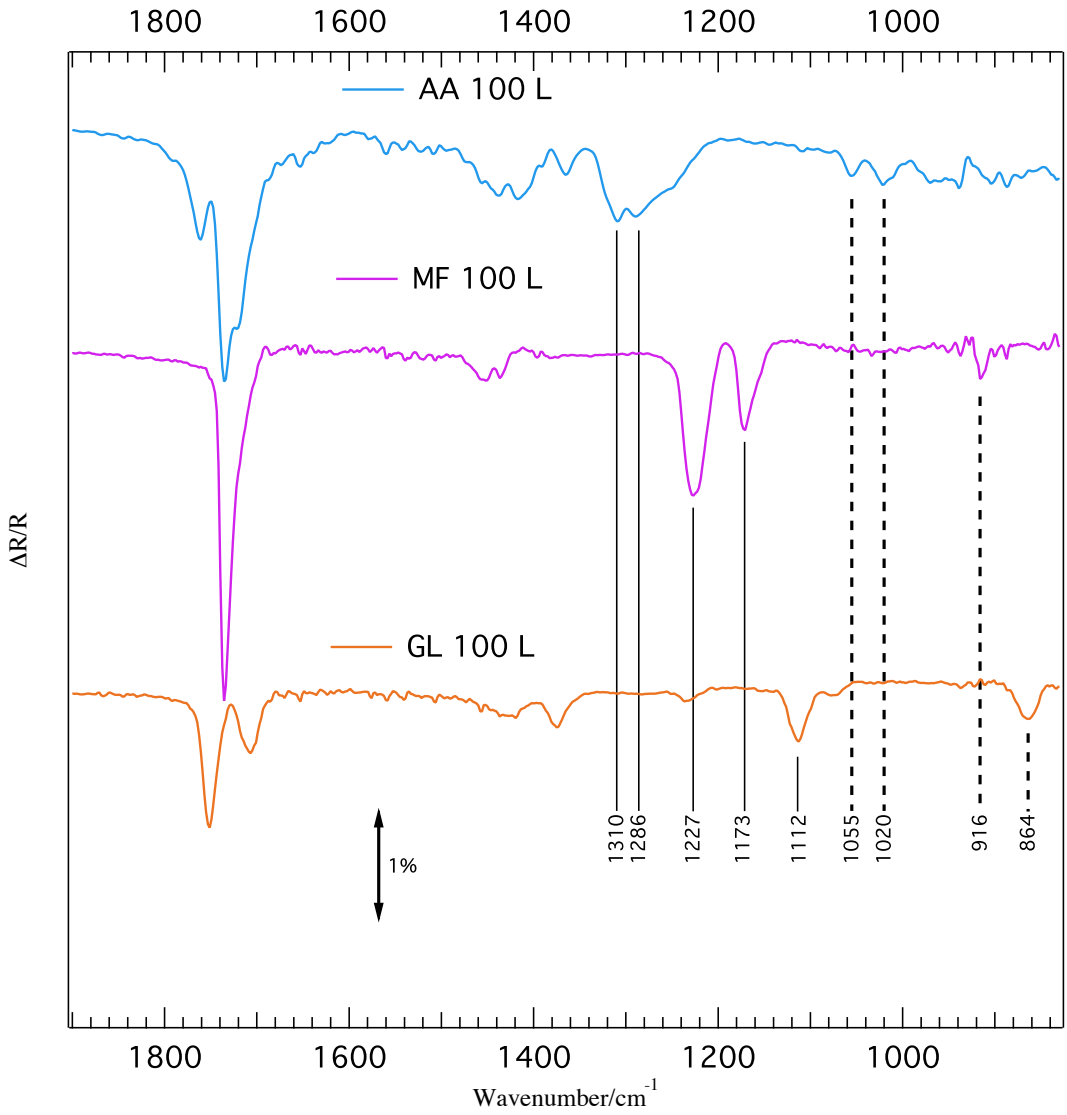

Figure 5.20. Comparison of RAIR spectra of pure acetic acid, methyl formate and glycolaldehyde. All the spectra correspond to 100 L dosage. The marked transitions represent "fingerprint" transitions (non overlapping) characterizing each species. Continuous lines mark the high intensity (HI) transitions, the dashed lines mark the low intensity (LI) transitions.

Apart from the main C=O stretch feature, the three molecules show overlapping features in the 1350-1530 cm^{-1} range involving generally CH_3, CH_2, C–H and COH bending modes.

The region from 1350 to 830 cm^{-1} is interesting because it is full of features that are characteristic of each individual species (figure 5.20), *i.e.*, there is almost no overlap between the vibrational modes belonging to the different isomers. In figure 5.20, these transitions are divided into two groups based on their relative intensities: high intensity (HI) transitions (continuous lines) and low intensity (LI) transitions (dashed lines). These transitions are very important, because they could be used to identify the presence of each molecule in ices containing two or more of the isomers. The HI

transitions should be preferred for this purpose because of their higher intensity compared to the LI transitions.

HI transitions include: ν C–O of acetic acid (1286/1310 cm^{-1}), ρ CH_3 and ν C_c–O (carbon belongs to the carbonyl group) of methyl formate (1173/1227 cm^{-1}) and ν C–O of glycolaldehyde. The transition at 1286 cm^{-1} of acetic acid and the ρ CH_3 mode of methyl formate are partially overlapping, but the transition of methyl formate seems to be much more intense at that specific wavenumber. For this reason they have been included in the group of characteristic transitions.

LI transitions include: ρ_s CH_3 and ρ_{as} CH_3 for acetic acid (1020 and 1055 cm^{-1}), ν C–O (C belongs to the aldehyde group) of methyl formate (916 cm^{-1}) and ν C–C of glycolaldehyde (864 cm^{-1}).

HI and LI bands are important because they could potentially be used to distinguish the isomers in an astrophysical environment. The already operational wide field infrared survey explorer (WISE) and the still to be launched James Webb space telescope (JWST) both possess observational capabilities in the mid-infrared. WISE can observe down to 22 μm (~500 cm^{-1}) [140] and JWST can reach 27 μm (~300 cm^{-1}) [141].

Figure 5.21 shows a comparison between the spectra corresponding to the deposition of 40 L of each species on top of ASW. In this plot only the HI transitions are shown, since the LI transitions are very faint at the lower exposures used in these experiments. Water seems to have a general broadening effect on the vibrational features, although this effect is not very pronounced due to the fact that only part of the isomer ice is interacting directly with water. The position of the vibrational bands does not change visibly compared to the pure ice case. The HI transitions are still in the same positions.

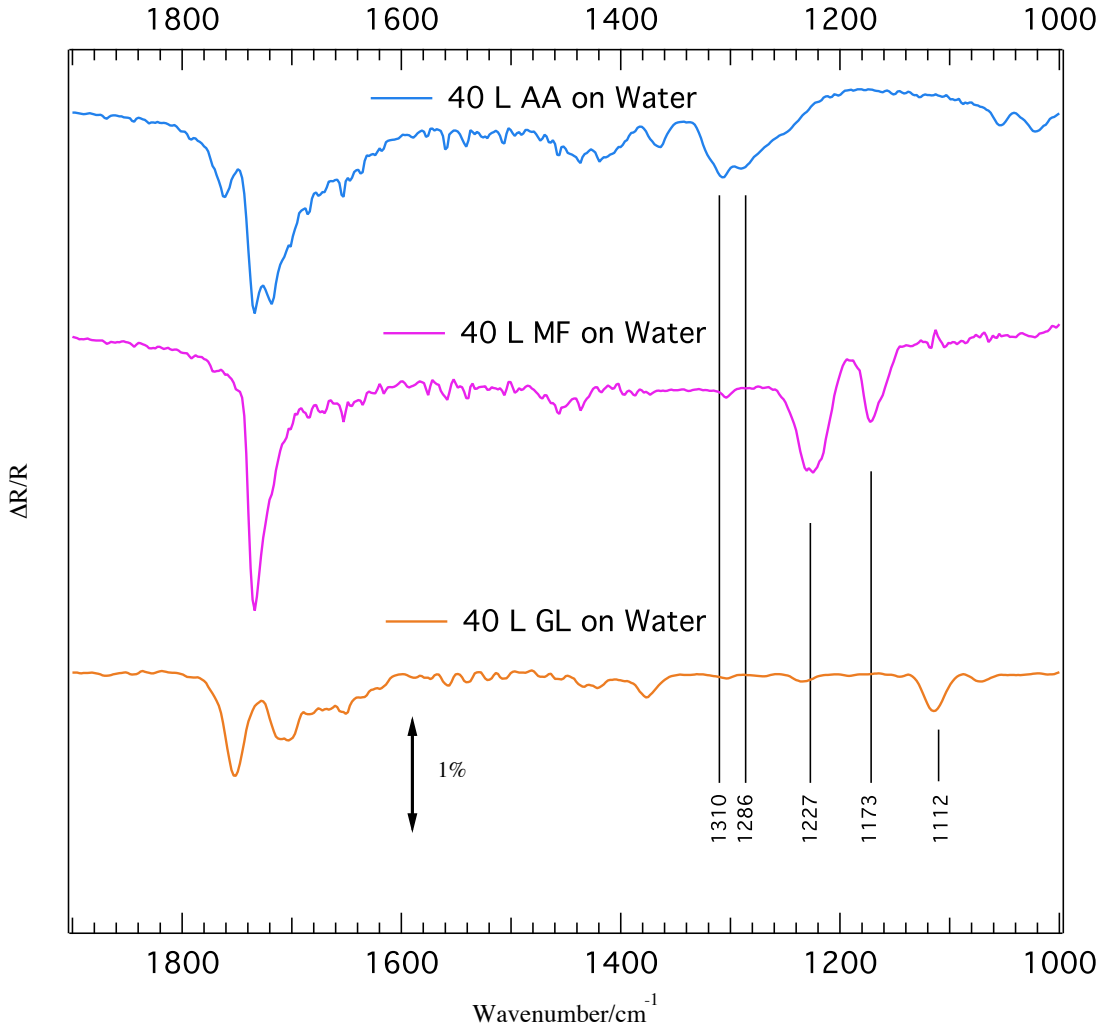

Figure 5.21. Comparison of 40 L dosages of acetic acid, methyl formate and glycolaldehyde deposited on 100 L of water. The marked transitions represent "fingerprint" transitions (non overlapping) characterizing each species. Continuous lines mark the high intensity (HI) transitions.

Figure 5.22 shows a comparison between comparable amounts of the isomers dosed in mixtures with water. In this case we can see that the interaction with water is causing the features to noticeably broaden. The broadening is much more pronounced compared to when the isomers are dosed on top of ASW (figure 5.21). This is expected because the interaction with water is more substantial given that the isomers are trapped inside the water matrix. Because of the interaction with water some of the HI peaks are shifted. The ν C–O peaks of acetic acid have merged into one peak at 1301 cm^{-1}, the ν C_c–O peak of methyl formate has shifted to 1240 cm^{-1}. Moreover, the ρ CH_3 transition of acetic acid at 1370 cm^{-1} is now a prominent peak at that particular wavenumber because the transition in the same region of the other two isomers is not detectable anymore.

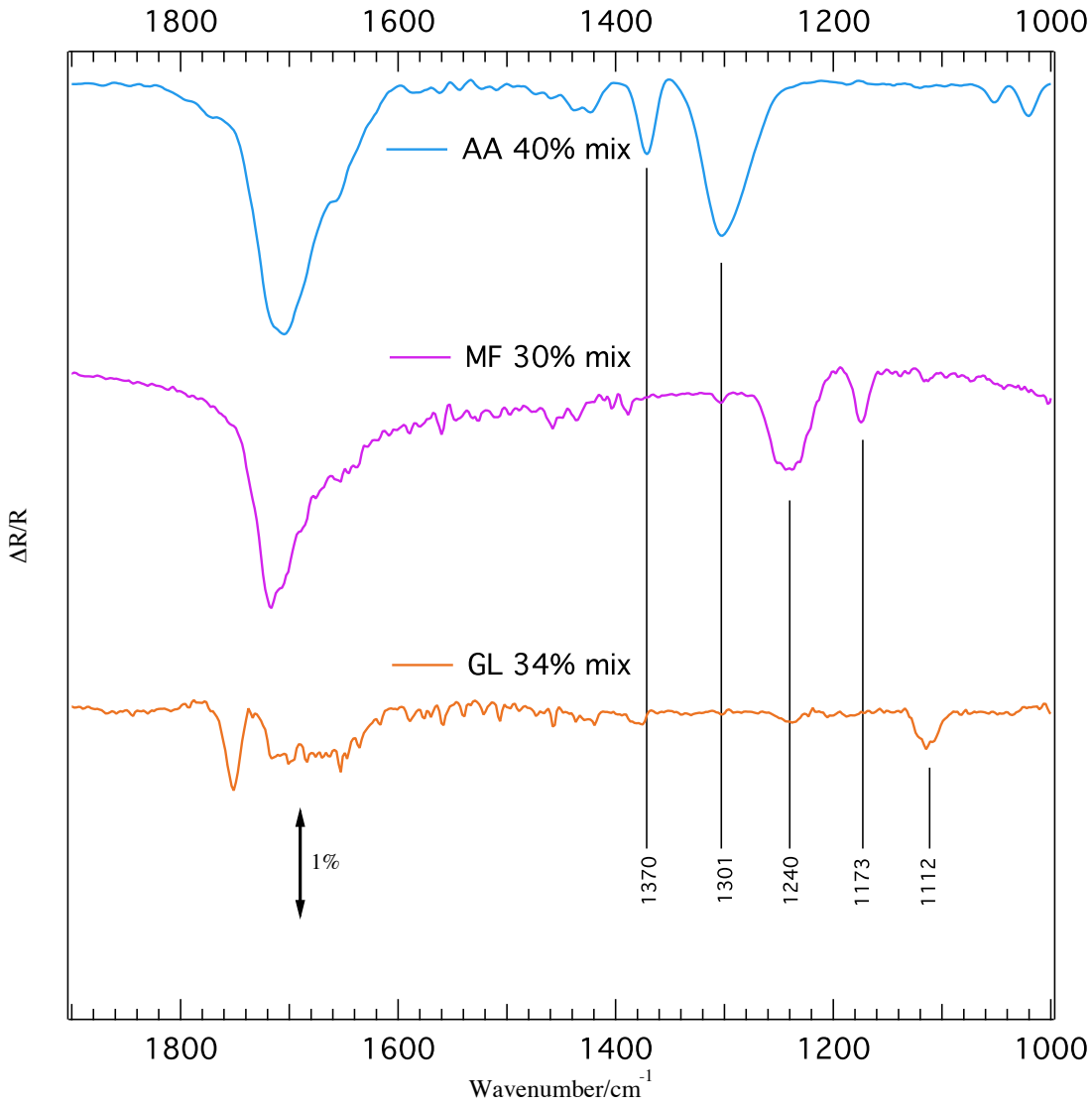

Figure 5.22. Comparison of pure acetic acid/water, methyl formate/water and glycolaldehyde/water mixtures. The marked transitions represent "fingerprint" transitions (non overlapping) characterizing each species. Continuous lines mark the high intensity (HI) transitions.

The thermal evolution of each species in each configuration (pure, on ASW, mixed with water) has also been studied. All pure ices show evidence of crystallization, although the changes in acetic acid are much more pronounced, with the appearance of new features and the shifting of already existing features. Signs of crystallization are also seen when the species are adsorbed on the surface of ASW, although due to the interaction with water and to the smaller amount of isomers dosed, the effects of crystallization are more subtle compared to the pure ices. When the species are trapped in water any form of crystallization is essentially impeded. The interaction with water and the isomers is very intense, possibly due to the formation of multiple hydrogen bonds. The relevance of hydrogen bonding between acetic acid and water, and between

methyl formate and water in the solid phase has been highlighted in the existing literature [119,121,129]. It has been computationally demonstrated that intermolecular hydrogen bonding is also important in the interaction between glycolaldehyde and water [139].

6 UV irradiation of glycolaldehyde

The chemical variety and the abundances of interstellar molecules is driven not just by the formation of ices on dust grains, but also by the processing that these ices go through [30]. Besides variations of the ice temperature due to the evolution of the surrounding star, the ices can be bombarded by several sources: electromagnetic radiation (typically UV from the interstellar radiation field and Ly-α radiation emitted by excited hydrogen), protons, electrons, heavy particles (such as He nuclei) and atoms (most noticeably hydrogen, but also N, C, O and D atoms) [20,142]. All of these effects can cause the ices to (photo)desorb and induce fragmentation or ionization of the ice. The species/fragments produced can then desorb and drive new chemistry in the gas phase, or recombine in the ice, forming new molecules [142].

For these reasons the processing of interstellar ices by radiation has been the object of study by a number of groups in the past 20 years.

Several groups studied the interaction of ices and atoms. Studies of hydrogenation of O, O_2 and O_3 have been thoroughly performed in Leiden, see for example [25,36], and have contributed to clarifying the viable routes of water formation in interstellar ices. H-atom bombardment of CO, CO_2, formic acid and CH_3CHO containing ices have also been performed [143,144]. Bombardment of CH_4 ices with superthermal O atoms has also been investigated and showed formation of CO_2, CH_3OH and CH_3CH_2OH. Proton bombardment of ethylene glycol and ethylene glycol containing ices showed the formation of glycolaldehyde [126]. Studies of proton irradiation have also been performed in Catania, for example, the irradiation of methanol containing ices with 200 keV H^+ showed the formation of methyl formate [28]. Several groups have also performed studies of the photochemistry of interstellar ices, such as the groups in Leiden, NASA Ames and Orsay [6]. Several important results arose from these studies. UV irradiation of CH_3OH containing ices showed the formation of complex molecules, such as CH_3CH_2OH and CH_3OCH_3 [43]. The irradiation of H_2S-bearing water ices showed the formation of more complex sulphur bearing species like H_2SO_4 [64]. UV photodestruction of some interstellar ices has also been studied (CH_4, CH_3OH, NH_3,…) [29]. Finally, the UV irradiation of a mixture of methanol, water, ammonia, CO and CO_2 showed the formation of a residue –known in the literature as "yellow stuff" [142]- that, after been analysed by gas chromatography, was shown to be composed of amino acids and other biologically relevant molecules [64].

From the results provided by the aforementioned studies, it is evident that understanding how radiation interacts with interstellar ices is of primary importance in order to elucidate how chemical networks evolve in the ISM.

Previous experiments on glycolaldehyde irradiation have mostly been performed in the gas phase, due to its relevance to atmospheric chemistry [73,125]. The study performed by Magneron *et al.* [125] showed evidence of glycolaldehyde UV photolysis in the gas phase, in air like mixtures. They suggest that the radicals HCO and CH_2OH are the most likely products of the photolysis. Their argument is based on the high yields obtained for CO and HCHO that originate in the reactions of the radicals with O_2. Hudson *et al.* [126] studied glycolaldehyde ice irradiation with 0.8 MeV protons. This study demonstrated that proton bombardment could convert glycolaldehyde into ethylene glycol and *vice versa*. UV irradiation of glycolaldehyde into an aqueous solution has also been studied. The results suggest that, upon irradiation of a solution of $HCOCH_2OH$ in D_2O, glycolaldehyde cleaves into a pair of formyl (HCO) and hydroxymethyl (CH_2OH) radicals that can recombine to form $HCOCH_2OH$ or $CO + CH_3OH$ [145].

Studies of the UV irradiation of glycolaldehyde in the solid phase are generally missing. This kind of study could provide insight into the destiny of glycolaldehyde in interstellar dust grains and provides quantitative information about the glycolaldehyde photodestruction/photodesorption cross section. For this reason, the effects of UV irradiation on glycolaldehyde ices have been studied.

The results presented in this chapter are preliminary to a more thorough comparative study of UV irradiated ices containing acetic acid and methyl formate. Such a study has, at the moment, yet to be performed.

6.1 Experimental methods

The experiments were performed in the experimental chamber CH1. The experimental setup used to perform the UV irradiation experiments has been described in chapter 2, section 2.2. Briefly, a combination of a power tuneable UV xenon arc lamp and a dual grating monochromator produced an UV beam that is then focused onto the sample *via* a series of quartz lenses. The UV flux coming from the lamp/monochromator/optics system was measured in a “bench configuration”

simulating the relative positions of the source, lenses and sample as in the actual experimental configuration.

The purpose of the experiment was to highlight any modification that a glycolaldehyde ice goes through due to interaction with UV radiation. Glycolaldehyde in the gas phase has been shown to have a peak in its absorption cross-section in the range 270-300 nm [73]. For this reason the irradiation wavelength was chosen as 285±27 nm. The UV flux was measured by positioning a UV detector at the same distance that the sample has with respect to the lenses. In this configuration, the detector measured a UV power of 0.9 mW. The resulting photon flux, considering an average photon wavelength of 285 nm, is ~$(1.9 \pm 0.1)\times10^{15}$ cm^{-2} s^{-1}.

In order to focus the UV beam onto the sample, the selected wavelength on the monochromator was temporarily increased in the 400-500 nm range, corresponding to visible violet/blue light. Once the focusing was satisfactory the wavelength reverted to the value used for irradiation.

Glycolaldehyde dosing was achieved as described in the previous chapters by heating the dimeric solid (Aldrich) to ~100 °C. Prior to dosing, the glycolaldehyde was pumped with a turbo-molecular pump in order to remove the trapped water.

6.2 Experimental results

Figure 6.1 shows the infrared spectra of glycolaldehyde ice (100 L) before and after 240 min UV irradiation has taken place. The C-C stretch band at 864 cm^{-1} has clearly decreased in intensity and so have all the other vibrational features in the 1000-1500 cm^{-1} range. The ν C=O and the Fermi resonance of the C-C stretch (1751 and 1707 cm^{-1}) have gone through some change, although it is difficult to pinpoint the nature of said change simply by observing the comparison of the two spectra. At around 2139 cm^{-1}, a new feature appears. This feature is assigned to the main vibrational mode of carbon monoxide.

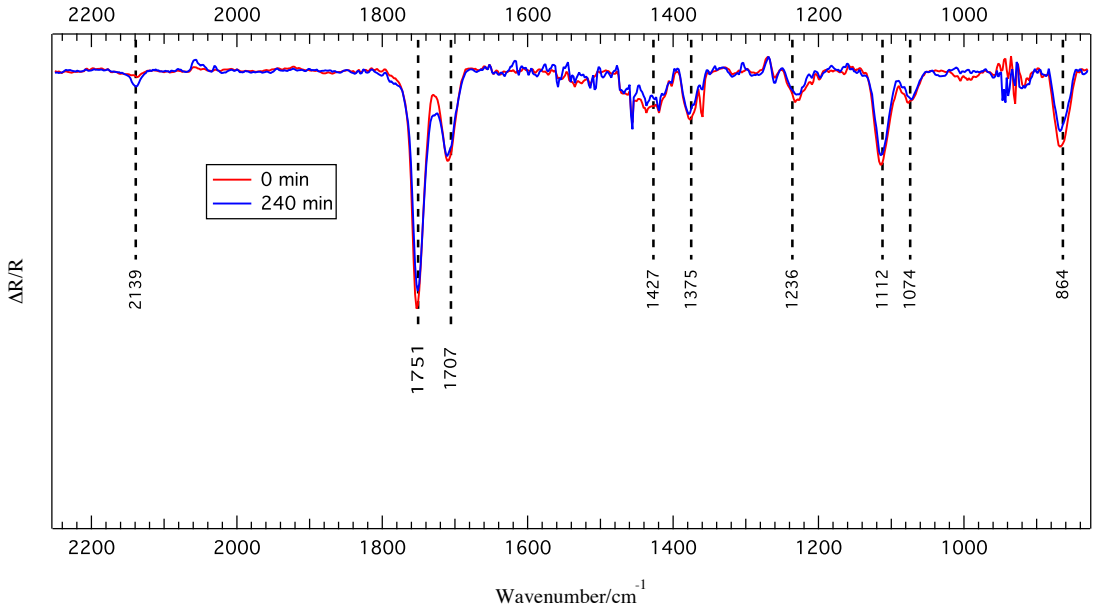

Figure 6.1. Spectra before (0 min) and after irradiation (240 min) of a 100 L glycolaldehyde ice.

In order to make the differences between the spectrum before and after UV irradiation more evident, a subtraction spectrum between the two has been plotted and this is shown in figure 6.2. The plot in figure 6.2 confirms that the transition at 2139 cm^{-1} (assigned to carbon monoxide stretching) is increasing in intensity, while the bands in the 1000-1500 cm^{-1} range and the C-C stretch band at 864 cm^{-1} are decreasing in intensity. It should be noted that the amount of noise from 1000 cm^{-1} to 1600 cm^{-1} is fairly high. This is due to a non-perfect functioning of the purge system whose purpose is to remove CO_2 and vapour H_2O from the IR beam path. The noise between 1000 and 1600 cm^{-1} is due to fluctuations of the amount of water vapour in the beam path.

The feature at 1751 cm^{-1} (ν C=O) appears to be decreasing, in the same way as the feature at 1707 cm^{-1}, which corresponds to the Fermi resonance between the C=O stretch and the first overtone of the C-C stretch. A new contribution seems to arise at 1730 cm^{-1}, although comparing figure 6.2 with figure 6.1, it can be noticed that the peak at 1730 cm^{-1} is more likely related to a variation of the relative positions and widths of the ν C=O and the Fermi resonance peak.

Besides the CO peak at 2139 cm^{-1}, two extra features have been identified, although with a degree of uncertainty. The assignment of these two features is based on the comparison with the work of Zhu & Zhu [146], which investigated the gas phase UV photolysis of glycolaldehyde. The feature at 1130 cm^{-1} is assigned to CH_3OH, while

the feature at 1560 cm^{-1} is assigned to H_2CO. These two assignments are uncertain due to the aforementioned fluctuations in the base line caused by the instability of the purge.

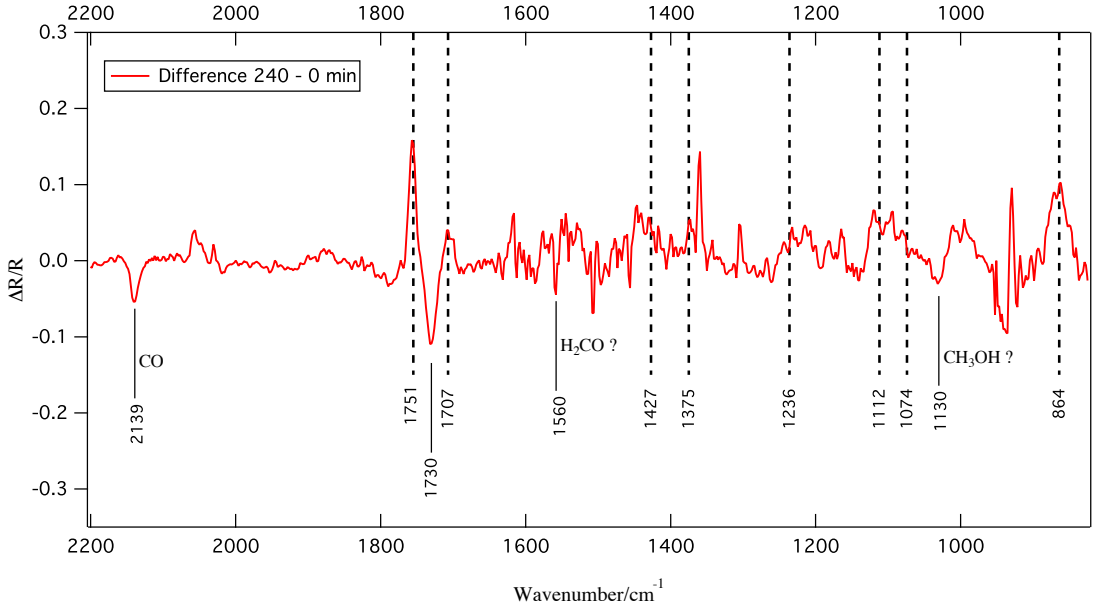

Figure 6.2. Difference spectrum between the post irradiation spectrum (240 min) and the pre irradiation spectrum (0 min), of 100 L of glycolaldehyde.

The decreasing of all of the peaks related to glycolaldehyde vibrational features suggests that glycolaldehyde is being photo-destroyed and/or photo-desorbed. The increase of the peak at 2139 cm^{-1} suggests that CO is being formed as a result of UV irradiation of glycolaldehyde. This implies that photo-destruction of the molecule is actually taking place. Considering that the band at 864 cm^{-1} (ν C-C) decreases markedly and that there is a variation in the relative width of the peaks at 1751 cm^{-1} and 1707 cm^{-1}, it is suggested that the photo-destruction of glycolaldehyde occurs by the cleavage of the C-C bond. This is in agreement with what is suggested for UV irradiation of glycolaldehyde in liquid solutions [145]. Figure 6.3 shows the variation of the area under the peak at 864 cm^{-1} (ν C-C) and at 2139 cm^{-1} (ν CO), in the subtraction spectra. A positive slope indicates that the feature is decreasing in intensity, and a negative slope indicates an increase in intensity. In figure 6.3, it is noted that the scatter of the points corresponding to the ν C-C peak is much higher compared to that of ν CO. This is due to the instability of the baseline in the region corresponding to the vibrations of water vapour.

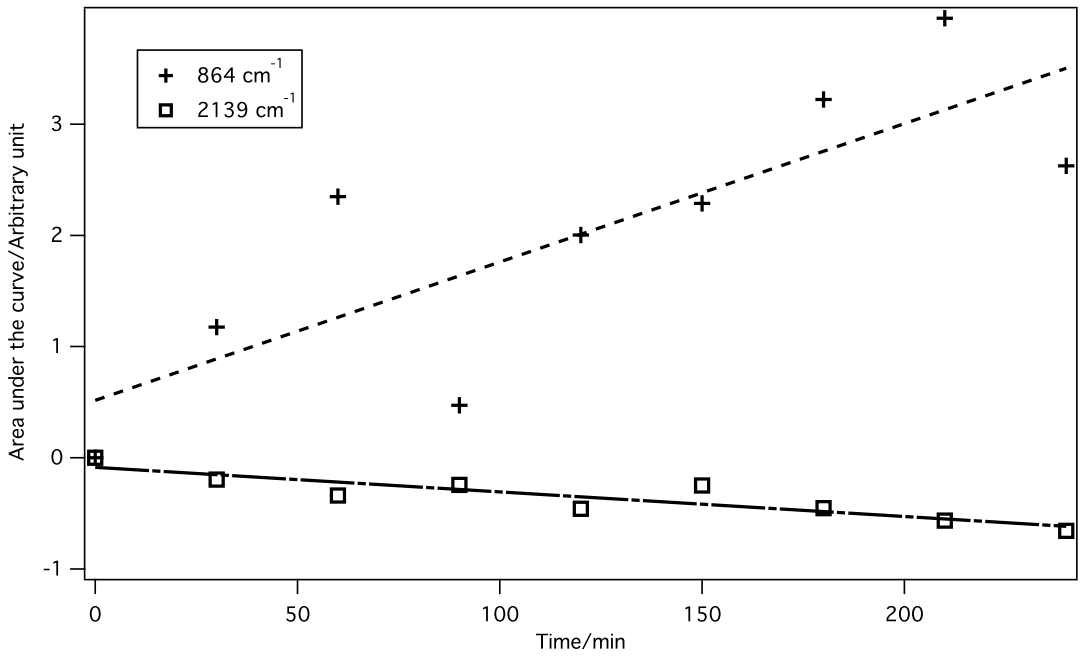

Figure 6.3. Variation of the area under the feature at 864 cm^{-1} (ν C-C) in the subtraction spectrum. A positive slope indicates that the area is decreasing as the irradiation time increases.

The variation in the ν C-C peak intensity discussed above, and the comparison with the literature concerning the irradiation of gas-phase and liquid glycolaldehyde [125,145,146], suggests that the reaction ensuing from the irradiation is:

$$HCOCH_2OH + h\nu \rightarrow HCO + CH_2OH$$

producing the formyl and hydroxymethyl radicals. The way that the radicals react afterwards cannot be fully understood from the available data. The increasing of the ν CO peak suggests CO formation. Two potential pathways that are able to produce CO are:

$$HCO + CH_2OH \rightarrow CH_3OH + CO \qquad (1)$$

$$HCO + HCO \rightarrow H_2CO + CO \qquad (2)$$

Reaction (1) is a direct recombination of the radicals that produces methanol and carbon monoxide, while reaction (2) is the result of the interaction of two formyl radicals producing formaldehyde and carbon monoxide. Both reactions have been found to be effective in previous studies of glycolaldehyde irradiation in the gas phase. In picture 6.2, two features were tentatively assigned to methanol (1130 cm^{-1}) and formaldehyde (1560 cm^{-1}). If these features are real and not due to the fluctuations of the baseline, both reactions (1) and (2) would be viable chemical pathways.

Using the way in which the area under the peak at 864 cm^{-1} varies with the UV irradiation, it is possible to estimate a value for the photodestruction/desorption cross-

section of glycolaldehyde. This is in the assumption that photo-desorption of the molecule is not negligible compared to the photo-destruction taking place and it is therefore affecting the decrease of the feature at 864 cm^{-1}.

Photodestruction of a molecule AB can be written as follows:

$$AB + h\nu \longrightarrow A^0 + B^0 \tag{6.1}$$

where A^0 and B^0 are the resulting fragments.

In the case of an optically thin ice, before back-reactions to reform AB become important, the UV destruction of AB is given by the formula:

$$N(\phi) = N(0)e^{-\phi\sigma_{des}^{\lambda}} \tag{6.2}$$

where N is the column density of the species AB in cm^{-2}, ϕ is the UV fluence in photons cm^{-2} and σ_{des}^{λ} is the photodestruction cross section (which is a function of the irradiating wavelength λ) in cm^2. Equation 6.2 can be rearranged as follows:

$$\ln\left(\frac{N(\phi)}{N(0)}\right) = -\sigma_{des}^{\lambda}\phi \tag{6.3}$$

Equation 6.3 describes the relationship between the ratio of the column densities before and during irradiation, and the fluence of UV photons hitting the sample. By plotting $\ln\left(\frac{N(\phi)}{N(0)}\right)$ against the fluence ϕ, it is possible to obtain the photodestruction cross section as the slope of the resulting line [43].

The intrinsic band strength I of an IR transition is given by [126]:

$$I = \frac{\int \tau(\nu)d\nu}{N} \tag{6.4}$$

where $\int \tau(\nu)d\nu$ is the band's integrated intensity, *i.e.*, the area of the band (A), and N is the column density. From equation 6.4 it follows that the area of the vibrational band is proportional to the column density. In the assumption that the irradiation does not change the intrinsic intensity of the vibration, for example, altering the geometry of the ice, and that the contribution to the variation of the band area due to photo-desorption is negligible, we can write:

$$\ln\left(\frac{A(\phi)}{A(0)}\right) = -\sigma_{des}^{\lambda}\phi \qquad (6.5)$$

where the logarithm of the ratio of the band areas is given as a function of the fluence. The photo-destruction cross section can be therefore estimated by plotting the logarithm of the ratio of the band areas against the fluence. Figure 6.4 shows a plot of $\ln\left(\frac{A(\phi)}{A(0)}\right)$ against the fluence for the ν C-C band, at 864 cm^{-1}. The figure shows a plot for two data sets. All of the points have been linearly fitted at the same time. Two data sets have been used for the fit because the baseline variation due to the instability of the purge causes undesired fluctuations in the area under the peak.

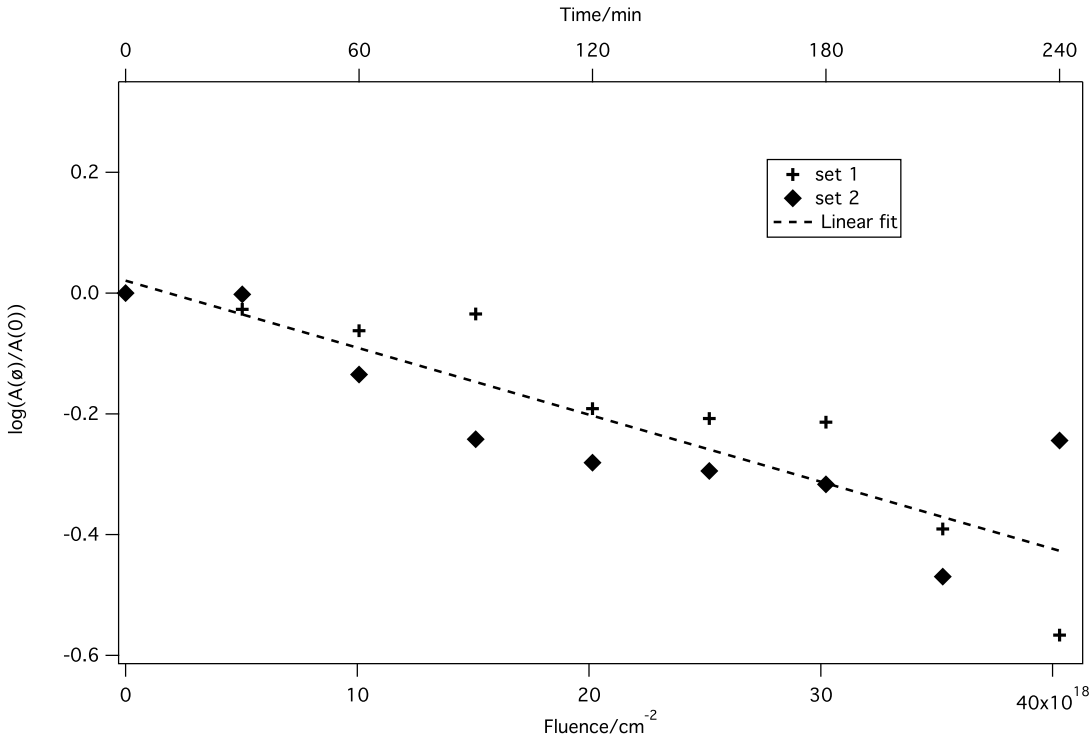

Figure 6.4. Logarithm of the normalized area under the 864 cm^{-1} band (C-C stretch) as a function of the UV fluence. The line represents the fit to the experimental points.

The photo-destruction cross-section for UV irradiated glycolaldehyde ice (the slope of the fitted line) has been found to be (1.1 ± 0.2) × 10^{-20} cm^2, where the uncertainty is the statistical uncertainty in the calculation of the slope. No previous values of glycolaldehyde ice photo-destruction have been found in the literature. However, as a comparison, the value obtained in this work is comparable with the gas phase glycolaldehyde UV cross-section at 280 nm (5 × 10^{-20} cm^{-2}) [125]. The two results are within the same order of magnitude. In the assumption that the absorption cross-section of gas phase glycolaldehyde is similar to that of the glycolaldehyde ice,

the value found for the photo-desorption/destruction cross-section seems to be reasonable.

As mentioned before, the value obtained with this calculation would correspond to the photo-destruction cross-section only in the assumption that the photo-desorption of glycolaldehyde is negligible compared to the photo-destruction. In order to properly argue whether this is the case, an at least qualitative estimation of the amount of glycolaldehyde photo-desorbed during the irradiation would be needed. This could, in principle, be achieved by monitoring the variation of the glycolaldehyde signal, during irradiation, with the QMS (mass 31). Unfortunately, this was not possible due to the fact that in this experimental setup (CH1) when the sample is in the RAIRS position it is not facing the QMS. This makes the detection of small amounts of molecules, such as the ones released during 3 hours of irradiation, extremely difficult. However, studies of UV irradiation (*via* a laser) of glycolaldehyde executed in the experimental setup CH2 by Dr Burke showed that photo-desorption of glycolaldehyde actually does take place (private communication). It is therefore reasonable to assume that the cross-section value found in this work is indeed due to both photo-desorption and photo-destruction, and it is therefore only an upper limit for the photo-destruction cross-section.

6.3 Final remarks

The effects of the UV irradiation of glycolaldehyde ices have been preliminarily studied. In this work, attention was focused on the 285±27 nm range where glycolaldehyde has a peak in the absorption cross-section in the gas phase. The results showed that the ice goes through some processing characterized essentially by a decrease in the intensity of all the main vibrational features and by the appearance of a new feature (2139 cm^{-1}), assigned to carbon monoxide. Two more features may be present at 1130 cm^{-1} (methanol) and at 1560 cm^{-1} (formaldehyde), but the poor baseline behaviour impedes a certain assignment.

This behaviour suggests that photo-destruction and/or photo-desorption of the ice is taking place. Using the variation of the feature at 864 cm^{-1} (ν C-C) an estimation of the photo-desorption + photo-destruction cross section has been obtained. The value found for this combined cross-section is $(1.1 \pm 0.2) \times 10^{-20}$ cm^2. Some considerations need to be made on this value. The uncertainty provided on the combined cross section (0.2) is purely statistical and does not take into consideration other experimental sources of uncertainty. The greatest source of error/uncertainty comes from the potential

variation of the UV flux due to window absorption and incorrect focusing of the beam onto the sample. As mentioned at the beginning of the chapter, the flux was measured in a "bench configuration" simulating the relative positions of the source, lenses and sample as in the actual experimental configuration. Although great care was taken in trying to precisely emulate the position and distance of the sample respect to the focusing lenses, a certain amount of error is unavoidable. This is essentially due to adjustments made on the sample position to maximise the IR signal and to adjustments made to the lens positions in order to maximise the UV beam focusing on the sample. Considering that a measurement of the UV flux, direct or indirect, on the sample has not been performed, it is not possible to determine how much the error on the sample/beam alignment and the absorption of the window affect the actual UV flux. However, a general argument can be made. If the flux (fluence) of UV photons bombarding the sample were actually lower than that estimated, the actual cross-section would be higher (the reaction should be more effective to produce the same result). Therefore, in the assumption that the errors due to window absorption and beam misalignment are not negligible, the value provided in this work is to be considered a lower limit for the actual cross-section.

In an astrophysical environment, the interstellar radiation field is characterized by UV radiation at the wavelength of the hydrogen Lyα transition, which is 121 nm. The UV wavelength used in this work is 285 nm. Below 180 nm the absorption cross-section of gas-phase glycolaldehyde is higher than that at 285 nm [73,125]. Assuming that the overall behaviour of the absorption cross section remains similar for glycolaldehyde ice and considering the higher energy of the Lyα photons, it is reasonable to infer that the photo-destruction of glycolaldehyde can effectively take place in astrophysical conditions. This could have important implications for the probability of survival of this molecule in environments that are not shielded from UV radiation or that are characterised by intense UV radiation, such as the proximity of newly born stars.

7 Concluding remarks

This thesis has focused on the investigation of the adsorption and desorption of a range of astrophysically relevant molecules from the surface of an interstellar dust grain analogue, at 20 K. Investigation *via* temperature programmed desorption (TPD) is an important tool to obtain information on the kinetics of the desorption process, which can subsequently be used in astrochemical simulations. Using infrared spectroscopy to determine the structure and environment of these ices provides an important way to characterise the ices in the interstellar medium.

In chapter 3, the infrared properties and desorption of H_2S were the object of study. The TPD analysis of pure H_2S ice distinguished monolayer and multilayer desorption. Quantitative analysis of the TPD spectra was performed in order to obtain the desorption energy and pre-exponential factor for both desorption regimes. The TPD study of H_2S deposited on water and in a mixture showed that H_2S desorbs from the surface of the ice, *via* volcano desorption, and also that it co-desorbs with water. A reflection absorption infrared (RAIR) study showed that amorphous H_2S has a bulk vibrational band at 2535 cm^{-1} that evolves into two separate bands (symmetric stretch at 2551 cm^{-1} and asymmetric stretch at 2526 cm^{-1}) upon thermal annealing of the ice, due to crystallization. The bending mode appears in crystalline H_2S at 1169 cm^{-1}. RAIR experiments of H_2S embedded in water showed a broadening of the main feature at 2525 cm^{-1} and no signs of crystallization.

In chapters 4 and 5, a comparative TPD and RAIR study of acetic acid (CH_3COOH), methyl formate ($HCOOCH_3$) and glycolaldehyde ($HCOCH_2OH$) was presented. A quantitative analysis of the TPD spectra for the pure ices was performed for each molecule. Acetic acid and glycolaldehyde were found to desorb exclusively *via* multilayer desorption, while methyl formate showed monolayer, bi-layer and multilayer desorption. The desorption energies and pre-exponential factors were calculated for multilayer acetic acid and glycolaldehyde desorption, and for monolayer and multilayer methyl formate desorption. When adsorbed on water, acetic acid and methyl formate showed the effects of a strong interaction with water. Because of this interaction, their spectra showed complex features whose behaviour is dependent on the temperature and the amount of the adsorbed species. Glycolaldehyde was shown to entirely co-desorb with water. When in mixtures, acetic acid and glycolaldehyde mostly co-desorb with

water, while methyl formate shows great mobility inside the ice and desorbs mainly as volcano desorption during the amorphous to crystalline water transition.

The RAIR investigation provided the vibrational spectra of the three molecules in their pure form, when adsorbed on top of water and when embedded in a water ice. For the three molecules, the most intense features are the ones related to C=O stretch, between 1680 and 1800 cm^{-1}. This feature has been shown to be very sensitive to the changes in the ice morphology, for example, due to crystallization of the ice. In the case of acetic acid, the C=O stretch feature allowed the distinguishing of monomers, dimers and chain-like polymer configurations. All molecules showed evidence of crystallization upon annealing, although the changes in the respective IR spectra were very different depending on the considered molecule. Acetic acid spectra showed the greatest change due to crystallization. All of its features, besides the ones assigned to CH_3 rocking at low wavenumbers, changed in intensity, profile shape and/or position. In the case of methyl formate, the most remarkable variation due to crystallization was a shift in the C=O stretch. Finally, glycolaldehyde showed only a very small change in the peak assigned to the Fermi resonance between the C=O stretch and the overtone of the C-C stretch.

When interacting with water, both in the case of adsorption onto a water substrate and in mixtures, the spectra of the three isomers showed a general broadening of the vibrational peaks. The broadening was more marked in the case of $C_2H_4O_2$/water mixtures. This is expected since the interaction with water is more important when the species are embedded in the water matrix, compared to when they are adsorbed on top of amorphous solid water (ASW) and only the upper layers of ASW are effectively interacting with the isomer. The C=O stretch peak shown is the one to be most affected by this interaction, for acetic acid and methyl formate, while the 2ν C-C^f was the most affected in the case of glycolaldehyde.

The comparative study of the IR spectra of the three isomers allowed the identification of specific transitions that are characteristic of each species, in all of the configurations studied in this work (pure on HOPG, on ASW, in mixtures with water). The fingerprint features for each molecule are: the C-O stretch (1286 and 1310 cm^{-1}) for acetic acid, the C-O stretch (1227/1240 cm^{-1}) and CH_3 rocking (1173 cm^{-1}) for methyl formate, and the C-O stretch (1112 cm^{-1}) for glycolaldehyde. This is an important result because these characteristic transitions can aid the identification of mixed isomer ices both in the laboratory and in the interstellar medium.

Finally, in chapter 6, the results of experiments involving the UV irradiation of glycolaldehyde (at 285 nm) were discussed. Evidence was shown that photolysis, *via* cleavage of the C-C bond, takes place. Further laser UV irradiation experiments performed by Dr Burke (private communication) showed that photo-desorption of glycolaldehyde can also take place, although evidence for this was not seen in the study presented here. Using the variation of the C-C stretch peak area as a function of the fluence, a calculation of the photo-destruction/desorption cross-section of glycolaldehyde at 285 nm was performed. The value of the cross-section is dependent on the estimation of the flux of UV photons bombarding the surface of the sample. As mentioned in chapter 6, this estimation is based on measurements made outside of the chamber with a lens configuration similar to the one actually used for the experiments. In order to obtain a more reliable value of the cross section, a more precise determination of the flux is in order. This could be performed by positioning a detector (photo-diode) on the cold finger, at the same position as the sample during experiments. Alternatively, an indirect measurement could be performed, in which a species with a known cross section (at 285 nm) is irradiated.

The quality of the RAIR spectra taken during the irradiation experiments was affected by the instability of the purge system. This has been an issue throughout all the $C_2H_4O_2$ experiments, but more so during the UV irradiation of glycolaldehyde. The instability of the purge affects the spectrum baseline between 900 and 1600 cm^{-1}. This becomes a problem for the irradiation experiments because the fluctuations of the baseline in that range hinder the identification of small vibrational features. This makes the positive identification of reaction products, such as CH_3OH and H_2CO, uncertain. Ideally, a new run of experiments on glycolaldehyde irradiation with a stabilized purge could lead to a more robust identification of potential reaction products.

The purpose of these irradiation experiments was to test the interaction of glycolaldehyde ice with UV radiation. The experiments showed that glycolaldehyde ice can dissociate in the presence of UV radiation. This is an important result, because it can potentially contribute to the explanation of the anomaly of the distribution of the isomers in Sgr B2(LMH). In this source, glycolaldehyde was found to be situated on the outskirts of the central object, while acetic acid and methyl formate are found towards the centre [65,112]. The UV radiation field in this environment is stronger in the centre, compared to on the outskirts (due to shielding from the gases or simply due to distance). Therefore, if glycolaldehyde UV dissociates more efficiently with respect to the other

two isomers, it would be removed from the centre region. Of course, this is a speculation. In order to properly answer this question, the UV irradiation of all the isomers needs to be investigated.

7.1 Future work

The natural evolution of the study on the $C_2H_4O_2$ isomers is the study of ices made with mixtures of two and then three of the isomers. This would shed light on the interactions of the species when they are embedded in the same ice. Moreover it would allow the possibility to test whether the fingerprint transitions remain characteristic even in these configurations. The setup CH1 allows for the dosing of a maximum of 2 species at the same time, from two different leak valves. Therefore, a mixture consisting of three isomers would need to be prepared beforehand and then injected into the chamber. This would be difficult to realize in the standard gas line used during the experiments, especially because of the low vapour pressure of glycolaldehyde. The construction of a dedicated mixing manifold would therefore be ideal in order to obtain a precise control on the isomer ratios in the mixtures.

A good amount of future work will be related to UV irradiation of ices. The study of irradiated ices (UV, X-ray, energetic particles) has become one of the main topics of modern laboratory astrochemistry. The first thing that needs to be addressed is a more precise characterization of the UV flux of the lamp at the sample position. As mentioned in the previous chapter, the precise estimation of the UV flux in the sample position is necessary to obtain sound quantitative results. This can be achieved by using a photo-diode located in the same position of the sample. In order to achieve this, a diode mount needs to be designed and temporarily put in the place of the sample mount. Considering that the majority of the UV radiation in space is H Lyman α, it would be interesting to study how this particular wavelength interacts with the ices. The UV flux of the Xe lamp plus monochromator setup, at 121 nm, is not high enough to allow effective bombardment of the ices. Therefore, the acquisition of a hydrogen lamp would be necessary in order to pursue this particular kind of investigation.

One of the problems encountered during the experiments was the instability of the purge system for the IR setup. This instability resulted in a non-optimal quality of the IR spectra, which affected the quality of the experimental data. In order to study the effects of UV irradiation on the ices (photo-destruction/desorption and formation of new species) a noiseless background is of paramount importance.

Once the UV setup is characterized and the RAIR system is stable a series of experiments on $C_2H_4O_2$ ices can be performed. The irradiation of each species can be studied in function of time and temperature. This would provide information on the photo-destruction cross sections, formation of new species and on the recombination rate of the fragments. After this kind of study is performed on the single species, it can be repeated for ices formed with mixtures of the isomers, in order to understand whether some selective process can favour the photo-processing of one or two of these species.

Bibliography

1. Tielens, A. G. G. M. The molecular universe. *Rev. Mod. Phys.* **85**, 1021–1081 (2013).

2. Gibb, E. L., Whittet, D. C. B., Boogert, A. C. A. & Tielens, A. G. G. M. Interstellar Ice: The Infrared Space Observatory Legacy. *Astrophys. J. Suppl. Ser.* **151**, 35–73 (2004).

3. http://www.astro.uni-koeln.de/cdms/molecules.

4. Tielens, A. G. G. M. *The physics and chemistry of the Interestellar Medium*. (New York: Cambridge University Press, 2005).

5. Stecher, T. P. & Williams, D. A. Interstellar Molecule Formation. *Astrophys. J.* **146**, 88 (1966).

6. Herbst, E. & van Dishoeck, E. F. Complex Organic Interstellar Molecules. *Annu. Rev. Astron. Astrophys.* **47**, 427–480 (2009).

7. Shu, F. H. *The Physical Universe: An Introduction to Astronomy*. **6**, 584 (University Science Books, 1982).

8. Habing, H. J. The interstellar radiation density between 912 A and 2400 A. *Bull. Astron. Institutes Netherlands* **19**, (1968).

9. Field, G. B., Goldsmith, D. W. & Habing, H. J. Cosmic-Ray Heating of the Interstellar Gas. *Astrophys. J.* **155**, L149 (1969).

10. McKee, C. F. & Ostriker, J. P. A theory of the interstellar medium - Three components regulated by supernova explosions in an inhomogeneous substrate. *Astrophys. J.* **218**, 148 (1977).

11. Dickey, J. M. & Garwood, R. W. The mass spectrum of interstellar clouds. *Astrophys. J.* **341**, 201 (1989).

12. Swings, P. & Rosenfeld, L. Considerations Regarding Interstellar Molecules. *Astrophys. J.* **86**, 483 (1937).

13. Dame, T. M. *et al.* A composite CO survey of the entire Milky Way. *Astrophys. J.* **322**, 706 (1987).

14. Greenberg, J. M. & Shen, C. Cosmic Dust in the 21st Century. *Astrophys. Space Sci.* 33–55 (1999).doi:10.1023/A:1017003503904

15. Williams, D. A. & Herbst, E. It's a dusty Universe: surface science in space. *Surf. Sci.* **500**, 823–837 (2002).

16. Fitzpatrick, E. L. Correcting for the Effects of Interstellar Extinction. *Publ. Astron. Soc. Pacific* **111**, 63–75 (1999).

17. Salpeter, E. E. Formation and Destruction of Dust Grains. *Annu. Rev. Astron. Astrophys.* **15**, 267–293 (1977).

18. Draine, B. T. Interstellar Dust Grains. *Annu. Rev. Astron. Astrophys.* **41**, 46 (2003).

19. Spitzer, L. J. & Fitzpatrick, E. L. Composition of interstellar clouds in the disk and halo. I - HD 93521. *Astrophys. J.* **409**, 299 (1993).

20. Gibb, E. L. *et al.* An Inventory of Interstellar Ices toward the Embedded Protostar W33A. *Astrophys. J.* **536**, 347–356 (2000).

21. Adriaens, D. a., Goumans, T. P. M., Catlow, C. R. A. & Brown, W. A. Computational Study of Carbonyl Sulphide Formation on Model Interstellar Dust Grains. *J. Phys. Chem. C* **114**, 1892–1900 (2010).

22. Terzieva, R. . & Herbst, E. The Sensitivity of Gas-Phase Chemical Models of Interstellar Clouds to C and O Elemental Abundances and to a New Formation Mechanism for Ammonia. *Astrophys. J.* **509**, 932–932 (1998).

23. Millar, T. J. ., Farquhar, P. R. A. . & Willacy, K. . The UMIST Database for Astrochemistry 1995. *A & A Suppl. Ser.* **121**, (1997).

24. Vidali, G. H2 Formation on Interstellar Grains. *Chem. Rev.* (2013).doi:10.1021/cr400156b

25. Ioppolo, S., Cuppen, H. M. & Linnartz, H. Surface formation routes of interstellar molecules: hydrogenation reactions in simple ices. *Rend. Lincei* **22**, 211–224 (2011).

26. Prasad, S. S. & Tarafdar, S. P. UV radiation field inside dense clouds: its possible existence and chemical implications. *Astrophys. J.; (United States)* **267:2**, (1983).

27. Moore, M. H., Donn, B., Khanna, R. & A'Hearn, M. F. Studies of proton-irradiated cometary-type ice mixtures. *Icarus* **54**, 388–405 (1983).

28. Modica, P., Palumbo, M. E. & Strazzulla, G. Formation of methyl formate in comets by irradiation of methanol-bearing ices. *Planet. Space Sci.* **73**, 425–429 (2012).

29. Cottin, H., Moore, M. H. & Benilan, Y. Photodestruction of Relevant Interstellar Molecules in Ice Mixtures. *Astrophys. J.* **590**, 874–881 (2003).

30. Burke, D. J. & Brown, W. A. Ice in space: surface science investigations of the thermal desorption of model interstellar ices on dust grain analogue surfaces. *Phys. Chem. Chem. Phys.* **12**, 5947–69 (2010).

31. Smith, I. W. M. Laboratory Astrochemistry: Gas-Phase Processes. *Annu. Rev. Astron. Astrophys.* **49**, 29–66 (2011).

32. Vidali, G. *et al.* Analysis of molecular hydrogen formation on low-temperature surfaces in temperature programmed desorption experiments. *J. Phys. Chem. A* **111**, 12611–9 (2007).

33. Pirronello, V., Biham, O., Liu, C., Shen, L. & Vidali, G. Efficiency of Molecular Hydrogen Formation on Silicates. *Astrophys. J.* **483**, L131–L134 (1997).

34. Burke, D. J., Wolff, A. J., Edridge, J. L. & Brown, W. A. The adsorption and desorption of ethanol ices from a model grain surface. *J. Chem. Phys.* **128**, 104702 (2008).

35. Bolina, A. S., Wolff, A. J. & Brown, W. A. Reflection absorption infrared spectroscopy and temperature-programmed desorption studies of the adsorption and desorption of amorphous and crystalline water on a graphite surface. *J. Phys. Chem. B* **109**, 16836–45 (2005).

36. Ioppolo, S., Cuppen, H. M., Romanzin, C., van Dishoeck, E. F. & Linnartz, H. Water formation at low temperatures by surface O2 hydrogenation I: Characterization of ice penetration. *Phys. Chem. Chem. Phys.* **12**, 12065–76 (2010).

37. Sandford, S. A. & Allamandola, L. J. The condensation and vaporization behavior of H2O: CO ices and implications for interstellar grains and cometary activity. *Icarus* **76**, 201–224 (1988).

38. Andrade, D. P. P. *et al.* Frozen methanol bombarded by energetic particles: Relevance to solid state astrochemistry. *Surf. Sci.* **603**, 1190–1196 (2009).

39. Ward, M. Reactions of hydrogen and oxygen atoms on interstellar grain analogues. (2012).

40. Collings, M. P. *et al.* A laboratory survey of the thermal desorption of astrophysically relevant molecules. *Mon. Not. R. Astron. Soc.* **354**, 1133–1140 (2004).

41. Sandford, S. A. & Allamandola, L. J. The condensation and vaporization behavior of ices containing SO2, H2S, and CO2: implications for Io. *Icarus* **106**, 478–88 (1993).

42. Bolina, A. S. & Brown, W. A. Studies of physisorbed ammonia overlayers adsorbed on graphite. *Surf. Sci.* **598**, 45–56 (2005).

43. Öberg, K. I., Garrod, R. T., van Dishoeck, E. F. & Linnartz, H. Formation rates of complex organics in UV irradiated CH 3 OH-rich ices. *Astron. Astrophys.* **504**, 891–913 (2009).

44. Garozzo, M., Fulvio, D., Kanuchova, Z., Palumbo, M. E. & Strazzulla, G. The fate of S-bearing species after ion irradiation of interstellar icy grain mantles. *Astron. Astrophys.* **509**, A67 (2009).

45. MOORE, M., HUDSON, R. & CARLSON, R. The radiolysis of SO2 and H2S in water ice: Implications for the icy jovian satellites. *Icarus* **189**, 409–423 (2007).

46. Kenzo Hiraoka, Toshikazu Takayama, Atsuko Euchi, Hiroko Handa, A. T. S. Study of the reactions of H and D atoms with solid C2H2, C2H4, and C2H6 at cryogenic temperatures. *Astrophys. J.* **532**, 1029–1037 (2000).

47. Charnley, S. B. Sulfuretted Molecules in Hot Cores. *Astrophys. J.* **481**, 396–405 (1997).

48. Zasowski, G. *et al.* Spitzer infrared spectrograph observations of class I/II objects in Taurus: composition and thermal history of the circumstellar ices. *Astrophys. J.* **694**, 459–478 (2009).

49. Boogert, A. C. A., Schutte, W. A., Helmich, F. P., Tielens, A. G. G. M. & Wooden, D. H. Infrared observations and laboratory simulations of interstellar CH_4_ and SO_2_. *Astron. Astrophys.* (1997).

50. Palumbo, M. E., Tielens, A. G. G. M. & Tokunaga, A. T. Solid Carbonyl Sulphide (OCS) in W33A. *Astrophys. J.* **449**, 674 (1995).

51. Palumbo, M. E., Geballe, T. R. & Tielens, A. G. G. M. Solid Carbonyl Sulfide (OCS) in Dense Molecular Clouds. *Astrophys. J.* **479**, 839–844 (1997).

52. Geballe, T. R., Baas, F., Greenberg, J. M. & Schutte, W. New infrared absorption features due to solid phase molecules containing sulfur in W 33 A. *Astron. Astrophys. (ISSN 0004-6361)* **146**, (1985).

53. Van der Tak, F. F. S., Boonman, A. M. S., Braakman, R. & van Dishoeck, E. F. Sulphur chemistry in the envelopes of massive young stars. *Astron. Astrophys.* **412**, 133–145 (2003).

54. Jiménez-Escobar, A. & Muñoz Caro, G. M. Sulfur depletion in dense clouds and circumstellar regions. *Astron. Astrophys.* **536**, A91 (2011).

55. Charnley, S., Rodgers, S. & Ehrenfreund, P. Gas-grain chemical models of star-forming molecular clouds as constrained by ISO and SWAS observations. *Astron. Astrophys.* **1036**, 1024–1036 (2001).

56. Wakelam, V., Caselli, P., Ceccarelli, C., Herbst, E. & Castets, A. Astrophysics Resetting chemical clocks of hot cores based on S-bearing molecules. *Astronomy* **169**, 159–169 (2004).

57. Pineau des Forets, G., Roueff, E., Schilke, P. & Flower, D. R. Sulphur-bearing molecules as tracers of shocks in interstellar clouds. *Mon. Not. R. Astron. Soc. (ISSN 0035-8711)* **262**, 915–928 (1993).

58. Duley, W. W., Millar, T. J. & Williams, D. A. Interstellar chemistry of sulphur. *Mon. Not. R. Astron. Soc.* **192**, 945–957 (1980).

59. Doty, S. D., Schöier, F. L. & van Dishoeck, E. F. Physical-chemical modeling of the low-mass protostar IRAS 16293-2422. *Astron. Astrophys.* **418**, 1021–1034 (2004).

60. Irvine, W. M., Goldsmith, P. F. & Hjalmarson, A. Chemical abundances in molecular clouds. *Interstellar Process. Proc. Symp.* 561–609 (1987).

61. Vogel, S. N., Genzel, R. & Palmer, P. The dispersal of dense protostellar material - NH3 hot cores and outflows in Sagittarius B2. *Astrophys. J.* **316**, 243 (1987).

62. Snyder, L. E. Interferometric observations of large biologically interesting interstellar and cometary molecules. *Proc. Natl. Acad. Sci. U. S. A.* **103**, 12243–8 (2006).

63. Ehrenfreund, P. & Charnley, S. B. ORGANIC MOLECULES IN THE INTERSTELLAR MEDIUM , COMETS, AND METEORITES : A Voyage from Dark Clouds to the Early Earth. *Annu. Rev. Astron. Astrophys.* **38**, 427–483 (2000).

64. Muñoz Caro, G. M. *et al.* Amino acids from ultraviolet irradiation of interstellar ice analogues. *Nature* **416**, 403–6 (2002).

65. Hollis, J. M., Jewell, P. R., Lovas, F. J. & Remijan, A. Interstellar glycolaldehyde: the first sugar. *Astrophys. J.* (2000).

66. Hollis, J. M., Lovas, F. J., Jewell, P. R. & Coudert, L. H. Interstellar Antifreeze: Ethylene Glycol. *Astrophys. J.* **571**, L59–L62 (2002).

67. Edridge, J. L. Adsorption and desorption of model interstellar ices on a dust grain analogue surface. 197 (2010).

68. Perry, J. S. A. & Price, S. D. Detection of rovibrationally excited H2 formed through the heterogeneous recombination of H atoms on a cold HOPG surface. *Astrophys. Space Sci.* **285**, 769–776 (2003).

69. Perry, J. S. A., Gingell, J. M., Newson, K. A., To, J. & Price, S. D. An apparatus to determine the rovibrational distribution of molecular hydrogen formed by the heterogeneous recombination of H atoms on cosmic dust analogues. *Meas. Sci. Technol.* **13**, 1414–1424 (2002).

70. Hornekær, L. *et al.* Clustering of Chemisorbed H(D) Atoms on the Graphite (0001) Surface due to Preferential Sticking. *Phys. Rev. Lett.* **97**, 186102 (2006).

71. Chen, C. *et al.* Self-Assembled Free-Standing Graphite Oxide Membrane. *Adv. Mater.* **21**, 3007–3011 (2009).

72. Stabel, A., Rabe, J. P. & Gonza, A. R. Surface Defects and Homogeneous Distribution of Silver Particles on HOPG. 7324–7326 (1998).

73. Bacher, C. The Atmospheric Chemistry of Glycolaldehyde. 171–189 (2001).

74. Heidberg, J., Warskulat, M. & Folman, M. Fourier-transform-infrared spectroscopy of carbon monoxide physisorbed on highly oriented graphite. doi:10.1016/0368-2048(90)80287-K

75. Leitner, T., Kattner, J. & Hoffmann, H. Infrared Reflection Spectroscopy of Thin Films on Highly Oriented Pyrolytic Graphite. *Appl. Spectrosc.* **57**, 1502–1509 (2003).

76. King, D. A. Thermal desorption from metal surfaces: A review. *Surf. Sci.* **47**, 384–402 (1975).

77. FALCONER, J. Desorption rate isotherms in flash desorption analysis. *J. Catal.* **48**, 262–268 (1977).

78. Green, S. D. *et al.* Applying laboratory thermal desorption data in an interstellar context: sublimation of methanol thin films. *Mon. Not. R. Astron. Soc.* **398**, 357–367 (2009).

79. Thaddeus, P., Kutner, M. L., Penzias, A. A., Wilson, R. W. & Jefferts, K. B. Interstellar Hydrogen Sulfide. *Astrophys. J.* **176**, L73 (1972).

80. Dalgarno, A. & Black, J. H. Molecule formation in the interstellar gas. *Reports Prog. Phys.* **39**, 573–612 (1976).

81. Vastel, C., Phillips, T. G., Ceccarelli, C. & Pearson, J. First Detection of Doubly Deuterated Hydrogen Sulfide. *Astrophys. J.* **593**, L97–L100 (2003).

82. Druard, C. & Wakelam, V. Polysulphanes on interstellar grains as a possible reservoir of interstellar sulphur. *Mon. Not. R. Astron. Soc.* **426**, 354–359 (2012).

83. Stevenson, K. P. Controlling the Morphology of Amorphous Solid Water. *Science (80-.).* **283**, 1505–1507 (1999).

84. Smith, R., Huang, C., Wong, E. & Kay, B. The Molecular Volcano: Abrupt CCl4 Desorption Driven by the Crystallization of Amorphous Solid Water. *Phys. Rev. Lett.* **79**, 909–912 (1997).

85. Michalak, W., Broitman, E., Alvin, M. a., Gellman, a. J. & Miller, J. B. Interactions of SO2 and H2S with amorphous carbon films. *Appl. Catal. A Gen.* **362**, 8–13 (2009).

86. I.A. Doleva, A.V. Kiselev, Y. I. Y. No Title. *Zhurnal Fiz. Khimii* (1974).

87. Bagreev, A., Rahman, H. & Bandosz, T. J. Thermal regeneration of a spent activated carbon previously used as hydrogen sulfide adsorbent. *Carbon N. Y.* **39**, 1319–1326 (2001).

88. Ulbricht, H., Zacharia, R., Cindir, N. & Hertel, T. Thermal desorption of gases and solvents from graphite and carbon nanotube surfaces. *Carbon N. Y.* **44**, 2931–2942 (2006).

89. De Jong, A. M. & Niemantsverdriet, J. W. Thermal desorption analysis: Comparative test of ten commonly applied procedures. *Surf. Sci.* **233**, 355–365 (1990).

90. Ehrenfreund, P. *et al.* Physics and chemistry of icy particles in the universe: answers from microgravity. *Planet. Space Sci.* **51**, 473–494 (2003).

91. Ayotte, P. *et al.* Effect of porosity on the adsorption, desorption, trapping, and release of volatile gases by amorphous solid water. *J. Geophys. Res.* **106**, 33387 (2001).

92. Nelson, R. D. J., Lide, D. R. & Maryott, A. A. Selected values of electric dipole moments for molecules in the gas phase. *Natl. Stand. Ref. Data Ser.* (1967).

93. Salama, F. *et al.* The 2.5–5.0 μm spectra of Io: Evidence for H2S and H2O frozen in SO2. *Icarus* **83**, 66–82 (1990).

94. Anderson, A., Binbrek, O. S. & Tang, H. C. Raman and infrared study of the low temperature phase of solid H2S and D2S. *J. Raman Spectrosc.* **6**, 213–220 (1977).

95. Takehiko, S. Tables of Molecular Vibrational Frequenies. *Natl. Stand. Ref. Data Ser.* (1972).

96. Viti, S., Collings, M. P., Dever, J. W., McCoustra, M. R. S. & Williams, D. A. Evaporation of ices near massive stars: models based on laboratory temperature programmed desorption data. *Mon. Not. R. Astron. Soc.* **354**, 1141–1145 (2004).

97. Brown, W. A. & Bolina, A. S. Fundamental data on the desorption of pure interstellar ices. *Mon. Not. R. Astron. Soc.* **374**, 1006–1014 (2007).

98. Fraser, H. J., Collings, M. P., McCoustra, M. R. S. & Williams, D. A. Thermal desorption of water ice in the interstellar medium. *Mon. Not. R. Astron. Soc.* **327**, 1165–1172 (2001).

99. Cesaroni, R., Hofner, P., Araya, E. & Kurtz, S. The structure of hot molecular cores over 1000 AU. *Astron. Astrophys.* **509**, A50 (2010).

100. Bennett, C. J. & Kaiser, R. I. On the Formation of Glycolaldehyde (HCOCH 2 OH) and Methyl Formate (HCOOCH 3) in Interstellar Ice Analogs. *Astrophys. J.* **661**, 899–909 (2007).

101. Remijan, A., Shiao, Y. -S., Friedel, D. N., Meier, D. S. & Snyder, L. E. A Survey of Large Molecules of Biological Interest toward Selected High-Mass Star-forming Regions. *Astrophys. J.* **617**, 384–398 (2004).

102. Mehringer, D. M., Snyder, L. E., Miao, Y. & Lovas, F. J. Detection and Confirmation of Interstellar Acetic Acid. *Astrophys. J.* **480**, L71–L74 (1997).

103. Cazaux, S. *et al.* The Hot Core around the Low-Mass Protostar IRAS 16293-2422: Scoundrels Rule! *Astrophys. J.* **593**, L51–L55 (2003).

104. Remijan, A. J., Wyrowski, F., Friedel, D. N., Meier, D. S. & Snyder, L. E. A Survey of Large Molecules toward the Proto–Planetary Nebula CRL 618. *Astrophys. J.* **626**, 233–244 (2005).

105. Huang, Y. *et al.* Molecular and compound-specific isotopic characterization of monocarboxylic acids in carbonaceous meteorites. *Geochim. Cosmochim. Acta* **69**, 1073–1084 (2005).

106. Brown, R. D. *et al.* Discovery of interstellar methyl formate. *Astrophys. J.* **197**, L29 (1975).

107. Requena-Torres, M. A. *et al.* Organic molecules in the Galactic center. *Astron. Astrophys.* **455**, 971–985 (2006).

108. Krishnamurthy, R., Arrhenius, G. & Eschenmoser, A. Formation of Glycolaldehyde Phosphate from Glycolaldehyde in Aqueous Solution. *Orig. Life Evol. Biosph.* 333–354 (1999).

109. Weber, A. L. Sugars as the Optimal Biosynthetic Carbon Substrate of Aqueous Life Throughout the Universe. *Orig. life Evol. Biosph.* **30**, 33–43 (2000).

110. Collins, P. M. & Ferrier, R. J. Monosaccharides: their chemistry and their roles in natural products. (1996).

111. Beltrán, M. T., Codella, C., Viti, S., Neri, R. & Cesaroni, R. FIRST DETECTION OF GLYCOLALDEHYDE OUTSIDE THE GALACTIC CENTER. *Astrophys. J.* **690**, L93–L96 (2009).

112. Hollis, J. M., Vogel, S. N., Snyder, L. E., Jewell, P. R. & Lovas, F. J. The Spatial Scale of Glycolaldehyde in the Galactic Center. *Astrophys. J.* **554**, L81–L85 (2001).

113. Puletti, F., Malloci, G., Mulas, G. & Cecchi-Pestellini, C. Large prebiotic molecules in space: photo-physics of acetic acid and its isomers. 8 (2009).

114. Garrod, R., Hee Park, I., Caselli, P. & Herbst, E. Are gas-phase models of interstellar chemistry tenable? The case of methanol. *Faraday Discuss.* **133**, 51 (2006).

115. Garrod, R. T., Weaver, S. L. W. & Herbst, E. Complex Chemistry in Star-forming Regions: An Expanded Gas-Grain Warm-up Chemical Model. *Astrophys. J.* **682**, 283–302 (2008).

116. Woods, P. M. *et al.* On the formation of glycolaldehyde in dense molecular cores. *Astrophys. J.* **750**, 19 (2012).

117. Woods, P. M. *et al.* GLYCOLALDEHYDE FORMATION *VIA* THE DIMERIZATION OF THE FORMYL RADICAL. *Astrophys. J.* **777**, 90 (2013).

118. Bennett, C. J. & Kaiser, R. I. The Formation of Acetic Acid (CH 3 COOH) in Interstellar Ice Analogs. *Astrophys. J.* **660**, 1289–1295 (2007).

119. Bertin, M., Romanzin, C., Michaut, X., Jeseck, P. & Fillion, J.-H. Adsorption of Organic Isomers on Water Ice Surfaces: A Study of Acetic Acid and Methyl Formate. *J. Phys. Chem. C* **115**, 12920–12928 (2011).

120. Bahr, S. *et al.* Interaction of acetic acid with solid water. *J. Phys. Chem. B* **110**, 8649–56 (2006).

121. Allouche, A. & Bahr, S. Acetic acid-water interaction in solid interfaces. *J. Phys. Chem. B* **110**, 8640–8 (2006).

122. Schwaner, A. L., Fieberg, J. E. & White, J. M. Methyl Formate on Ag(111). 1. Thermal Adsorption−Desorption Characteristics and Alignment in Monolayers. *J. Phys. Chem. B* **101**, 11112–11118 (1997).

123. Zahidi, E., Castonguay, M. & McBreen, P. RAIRS and TPD Study of Methyl Formate, Ethyl Formate, and Methyl Acetate on Ni(111). *J. Am. Chem. Soc.* **116**, 5847–5856 (1994).

124. Sexton, B. A., Hughes, A. E. & Avery, N. R. A spectroscopic study of the adsorption and reactions of methanol, formaldehyde and methyl formate on clean and oxygenated Cu(110) surfaces. *Surf. Sci.* **155**, 366–386 (1985).

125. Magneron, I. *et al.* Photolysis and OH-Initiated oxidation of glycolaldehyde under atmospheric conditions. *J. Phys. Chem. A* **109**, 4552–61 (2005).

126. Hudson, R. L., Moore, M. H. & Cook, A. M. IR characterization and radiation chemistry of glycolaldehyde and ethylene glycol ices. *Adv. Sp. Res.* **36**, 184–189 (2005).

127. Michelsen, H. & Klaboe, P. Spectroscopic studies of glycolaldehyde. *J. Mol. Struct.* **4**, 293–302 (1969).

128. Lattelais, M. *et al.* Differential adsorption of complex organic molecules isomers at interstellar ice surfaces. *Astron. Astrophys.* **532**, A12 (2011).

129. Gao, Q. & Leung, K. T. Thermal evolution of acetic acid nanodeposits over 123-180 K on noncrystalline ice and polycrystalline ice studied by FTIR reflection-

absorption spectroscopy: hydrogen-bonding interactions in acetic acid and between acetic acid and ice. *J. Phys. Chem. B* **109**, 13263–71 (2005).

130. Xi, M., Yang, M. X., Jo, S. K., Bent, B. E. & Stevens, P. Benzene adsorption on Cu(111): Formation of a stable bilayer. *J. Chem. Phys.* **101**, 9122 (1994).

131. Garrod, R. T. & Herbst, E. Formation of methyl formate and other organic species in the warm-up phase of hot molecular cores. *Astron. Astrophys.* **457**, 927–936 (2006).

132. Jetzki, M., Luckhaus, D. & Signorell, R. Fermi resonance and conformation in glycolaldehyde particles. *Can. J. Chem.* **82**, 915–924 (2004).

133. Bertagnolli, H. The structure of liquid acetic acid-an interpretation of neutron diffraction results by geometrical models. *Chem. Phys. Lett.* **93**, 287–292 (1982).

134. Bellamy, L. J., Lake, R. F. & Pace, R. J. Hydrogen bonding in carboxylic acids—II. Monocarboxylic acids. *Spectrochim. Acta* **19**, 443–449 (1963).

135. Haurie, M. & Novak, A. Spectres de vibration des molecules CH3COOH, CH3COOD, CD3COOH et CD3COOD—III. Spectres infrarouges des cristaux. *Spectrochim. Acta* **21**, 1217–1228 (1965).

136. Katon, J. E. & Ranieri, N. L. The Infrared Spectrum of Crystalline Methyl Formate. *Spectrosc. Lett.* **11**, 367–373 (1978).

137. Ceponkus, J. *et al.* Infrared study of glycolaldehyde isolated in parahydrogen matrix. *J. Chem. Phys.* **133**, 094502 (2010).

138. Kondratyuk, P. Analytical formulas for Fermi resonance interactions in continuous distributions of states. *Spectrochim. Acta Part A Mol. Biomol. Spectrosc.* **61**, 589–593 (2005).

139. Aviles-Moreno, J.-R., Demaison, J. & Huet, T. R. Conformational flexibility in hydrated sugars: the glycolaldehyde-water complex. *J. Am. Chem. Soc.* **128**, 10467–73 (2006).

140. Wright, E. L. *et al.* THE WIDE-FIELD INFRARED SURVEY EXPLORER (WISE): MISSION DESCRIPTION AND INITIAL ON-ORBIT PERFORMANCE. *Astron. J.* **140**, 1868–1881 (2010).

141. Gardner, J. P. *et al.* The James Webb Space Telescope. *Space Sci. Rev.* **123**, 485–606 (2006).

142. Allodi, M. A. *et al.* Complementary and Emerging Techniques for Astrophysical Ices Processed in the Laboratory. *Space Sci. Rev.* (2013).doi:10.1007/s11214-013-0020-8

143. Bisschop, S. E., Fuchs, G. W., van Dishoeck, E. F. & Linnartz, H. H-atom bombardment of CO2, HCOOH and CH3CHO containing ices. (2007).

144. Fuchs, G. W. *et al.* Hydrogenation reactions in interstellar CO ice analogues. (2009).

145. Seifert, K.-G. & Bargon, J. CIDNP-Detection of a Photocatalyzed C?C Cleavage upon UV Irradiation of Glycolaldehyde in Aqueous Solution. *Angew. Chemie Int. Ed. English* **12**, 763–764 (1973).

146. Zhu, C. & Zhu, L. Photolysis of glycolaldehyde in the 280-340 nm region. *J. Phys. Chem. A* **114**, 8384–90 (2010).